

Semi-classical description of near-field driven attosecond photoemission from nanostructures

Dissertation zur Erlangung des akademischen Grades
doctor rerum naturalium
der Mathematisch-Naturwissenschaftlichen Fakultät
der Universität Rostock



vorgelegt von
Lennart Seiffert
aus Rostock

August 2018

Betreuer: Prof. Dr. Thomas Fennel (Universität Rostock)

Gutachter: Prof. Dr. Thomas Fennel (Universität Rostock)
Prof. Dr. Misha Ivanov (Max-Born-Institut Berlin)
Prof. Dr. Claus Ropers (Georg-August-Universität Göttingen)

Eingereicht: 24.08.2018

Verteidigung: 21.12.2018

Short summary

Excitation of nanostructures with ultrashort waveform-controlled laser pulses makes it possible to generate strongly enhanced near-fields that may be localized to dimensions far below the wavelength. Adjusting their spatio-temporal evolution on nanometer length- and attosecond timescales enables precise control of the near-field mediated electron dynamics and thus constitutes a key challenge for realizing ultrafast light-driven nanoelectronics.

This thesis aims at exploring attosecond electron dynamics in the near-fields of laser-excited nanostructures theoretically to develop so far lacking physical pictures for explaining recent experiments. Thereto, the light-matter interaction is modeled via classical, semi-classical and quantum simulations. In particular, three key issues are addressed in this work. The first part is dedicated to investigating the quantum aspects of coherent photoemission from metallic nanotips under bichromatic laser fields. Second, the strong-field electron emission from dielectric nanospheres under optical few-cycle pulses will be analyzed. Nanospheres provide ideal model systems to investigate the combined impacts of field propagation, electron transport and many-electron effects, which are of particular interest in this work. In the third part, the ultrafast electron transport dynamics within dielectrics is studied, which can be probed via attosecond streaking spectroscopy.

Kurzzusammenfassung

Die Anregung von Nanostrukturen mit ultrakurzen Wellenform-kontrollierten Laserpulsen ermöglicht die Erzeugung von verstärkten Nahfeldern, die weit unterhalb der Wellenlänge lokalisiert sein können. Das gezielte Einstellen ihrer raumzeitlichen Entwicklung auf Nanometer Längen- und Attosekunden Zeitskalen erlaubt die präzise Kontrolle der Nahfeld-getriebenen Elektronendynamik und stellt damit eine zentrale Herausforderung für die Realisierung ultraschneller lichtgetriebener Nanoelektronik dar.

Ziel dieser Arbeit ist die theoretische Beschreibung der Attosekunden-Elektronendynamik in den Nahfeldern Laser-angeregter Nanostrukturen mit dem Ziel, ein physikalisches Verständnis der Ergebnisse hochaktueller Experimente zu entwickeln. Im Rahmen der Arbeit wird dazu die Licht-Materie Wechselwirkung mit Hilfe von klassischen, semi-klassischen und Quantensimulationen modelliert. Insbesondere werden drei zentrale Fragestellungen untersucht. Der erste Teil der Arbeit behandelt die Quanten-Aspekte von kohärenter Elektronenemission am Beispiel metallischer Nanospitzen unter Zweifarben-Laserfeldern. Der zweite Teil widmet sich der Starkfeld-getriebenen Elektronenemission von dielektrischen Nanokugeln in optischen Wenigzyklen-Pulsen. Nanokugeln bieten ideale Modellsysteme für die Untersuchung der kombinierten Einflüsse von Feldpropagation, Elektronentransport und Vielteilchen-Effekten, die in dieser Arbeit von besonderem Interesse sind. Im dritten Teil wird die ultraschnelle Transportdynamik von Elektronen in Dielektrika untersucht, die experimentell mit der Methode des 'Attosekunden Streaking' zugänglich ist.

Contents

List of Own Publications	III
List of Presentations	V
List of Figures	VII
List of Tables	IX
1. Introduction	1
1.1. Basic features in atomic strong field physics	2
1.2. Strong-field nanophysics	4
1.3. Investigated scenarios and aims of this thesis	5
1.3.1. Strong-field photoemission from metal nanotips	6
1.3.2. Near-field driven photoemission from dielectric nanospheres	6
1.3.3. Attosecond streaking on dielectric nanospheres	7
2. Theoretical framework	11
2.1. The semi-classical model	11
2.2. Description of the spatio-temporal near-fields	13
2.2.1. The linear near-field	14
2.2.2. The nonlinear mean-field	19
2.3. Field-driven ionization	24
2.3.1. Tunnel ionization	26
2.3.2. Photoionization	27
2.4. Propagation and scattering of photoelectrons	27
2.4.1. Description of electron scattering in dielectrics	28
2.5. Numerical details: Optimization & Parallelization	32
2.6. Simplified quantum description	34
2.6.1. Time evolution and Crank-Nicolson method	34
2.6.2. Ground state preparation via imaginary time propagation	35
2.6.3. Extracting energy spectra by the window operator method	35
3. Photoemission from metal nanotips in bichromatic laser fields	37
3.1. The one-dimensional nanotip model	37
3.1.1. Spatio-temporal near-field	37
3.1.2. Quantum description	39
3.2. Coherent photoemission from metal nanotips	40
3.2.1. Influence of the spatial near-field profile	41
3.2.2. Two-color effects on the electron emission	42
4. Strong-field electron emission from small dielectric nanospheres	45
4.1. Few-cycle driven ionization of small nanospheres	45
4.1.1. Time-resolved ionization response	46

4.1.2. Selective analysis of photoelectron spectra	47
4.1.3. Temporally resolved electron emission	49
4.1.4. Impact of the field waveform on the electron emission	50
4.2. Charge interaction effects	51
4.2.1. Trapping field assisted backscattering	52
4.2.2. Quenching of the material dependence	57
5. Field propagation effects at large dielectric nanospheres	61
5.1. Strong-field photoemission from nanospheres – from small to large	61
5.1.1. Characterization of the linear near-fields	62
5.1.2. Field propagation mediated directional electron emission	64
5.1.3. Phase-dependent directional switching	66
5.1.4. Systematic comparison of simulation and experiment	67
5.2. Tangential field effects and double recollisions	70
5.2.1. Evolution of electron yields and cut-off energies with size	71
5.2.2. Trajectory analysis of single and double rescattering	73
5.2.3. Selective energy gains for single and double rescattering	74
5.2.4. Emission directionality of single and double rescattering	75
6. Attosecond streaking on dielectric nanospheres	79
6.1. The attosecond streaking experiment	79
6.1.1. Data discrimination	80
6.1.2. Extraction of streaking spectrograms and delays	82
6.2. Semi-classical streaking simulations	83
6.2.1. Contributions to the relative streaking delay	85
6.2.2. Near-field induced contributions to the streaking delay	86
6.2.3. Impact of the XUV chirp	89
6.3. The collisional streaking delay	90
6.3.1. Impact of internal streaking	90
6.3.2. Intuitive physical picture for the collisional streaking delay	92
6.3.3. Selective impacts of elastic and inelastic scattering in M^3C	94
6.3.4. Intercycle averaging and wavelength dependence	95
6.3.5. Extracted IMFP in comparison with literature	97
7. Conclusions and outlook	99
Appendix	103
A. Quiver motion & ponderomotive energy	103
B. Derivation of the spectral photoionization cross section	103
C. Impact of anisotropic elastic scattering in typical simulations	104
D. Impact of charge interaction on attosecond streaking	105
E. Transport cross sections for SiO_2 , ZnS , Fe_3O_4 and PS	106
Bibliography	107
Academic curriculum vitae	119
Statement of authorship	121
Acknowledgments	123

List of Own Publications

- [LS1] M. F. Ciappina, J. A. Pérez-Hernández, A. S. Landsman, W. Okell, S. Zherebtsov, B. Förg, J. Schötz, L. Seiffert, T. Fennel, T. Shaaran, T. Zimmermann, A. Chacón, R. Guichard, A. Zair, J. W. G. Tisch, J. P. Marangos, T. Witting, A. Braun, S. A. Maier, L. Roso, M. Krüger, P. Hommelhoff, M. F. Kling, F. Krausz and M. Lewenstein, *Attosecond physics at the nanoscale*, *Rep. Prog. Phys.* **80**, 054401 (2017).
- [LS2] L. Seiffert, T. Paschen, P. Hommelhoff and T. Fennel, *High-order above-threshold photoemission from nanotips controlled with two-color laser fields*, *J. Phys. B: At. Mol. Opt. Phys.* **51**, 134001 (2018).
- [LS3] L. Seiffert, P. Henning, P. Rupp, S. Zherebtsov, P. Hommelhoff, M. F. Kling and T. Fennel, *Trapping field assisted backscattering in strong-field photoemission from dielectric nanospheres*, *J. Mod. Opt.* **64**, 1096–1103 (2017).
- [LS4] P. Rupp, L. Seiffert, Q. Liu, F. Süßmann, B. Ahn, B. Förg, C. G. Schäfer, M. Gallei, V. Mondes, A. Kessel, S. Trushin, C. Graf, E. Rühl, J. Lee, M. S. Kim, D. E. Kim, T. Fennel, M. F. Kling and S. Zherebtsov, *Quenching of material dependence in few-cycle driven electron acceleration from nanoparticles under many-particle charge interaction*, *J. Mod. Opt.* **64**, 995–1003 (2017).
- [LS5] F. Süßmann, L. Seiffert, S. Zherebtsov, V. Mondes, J. Stierle, M. Arbeiter, J. Plenge, P. Rupp, C. Peltz, A. Kessel, S. A. Trushin, B. Ahn, D. Kim, C. Graf, E. Rühl, M. F. Kling and T. Fennel, *Field propagation-induced directionality of carrier-envelope phase-controlled photoemission from nanospheres*, *Nat. Commun.* **6**, 7944 (2015).
- [LS6] L. Seiffert, F. Süßmann, S. Zherebtsov, P. Rupp, C. Peltz, E. Rühl, M. F. Kling and T. Fennel, *Competition of single and double rescattering in the strong-field photoemission from dielectric nanospheres*, *Appl. Phys. B* **122**, 1–9 (2016).
- [LS7] L. Seiffert, Q. Liu, S. Zherebtsov, A. Trabattoni, P. Rupp, M. C. Castrovilli, M. Gallei, F. Süßmann, K. Wintersperger, J. Stierle, G. Sansone, L. Poletto, F. Frassetto, I. Halfpap, V. Mondes, C. Graf, E. Rühl, F. Krausz, M. Nisoli, T. Fennel, F. Calegari and M. F. Kling, *Attosecond chronoscopy of electron scattering in dielectric nanoparticles*, *Nat. Phys.* **13**, 766–770 (2017).
- [LS8] Q. Liu, L. Seiffert, A. Trabattoni, M. C. Castrovilli, M. Galli, P. Rupp, F. Frassetto, L. Poletto, M. Nisoli, E. Rühl, F. Krausz, T. Fennel, S. Zherebtsov, F. Calegari and M. F. Kling, *Attosecond streaking metrology with isolated nanoparticles*, *J. Opt.* **20**, 024002 (2018).
- [LS9] L. Seiffert, T. Fennel, F. Calegari and M. F. Kling, *Attosekunden-Stoppuhr für inelastische Elektronenstöße*, *Phys. unserer Zeit* **48**, 217–218 (2017).

List of Own Publications

- [LS10] Q. Liu, P. Rupp, B. Förg, J. Schötz, F. Süßmann, W. Okell, J. Passig, J. Tiggesbäumker, K.-H. Meiwes-Broer, [L. Seiffert](#), T. Fennel, E. Rühl, M. Förster, P. Hommelhoff, S. Zherebtsov and M. F. Kling, *Photoemission from Nanomaterials in Strong Few-Cycle Laser Fields*, Chapter in [Nano-Optics: Principles Enabling Basic Research and Applications](#), 283–299, Springer Netherlands (2017).
- [LS11] [L. Seiffert](#), J. Köhn, C. Peltz, M. F. Kling and T. Fennel, *Signatures and mechanisms of plasmon-enhanced electron emission from clusters in few-cycle laser fields*, *J. Phys. B: At. Mol. Opt. Phys.* **50**, 224001 (2017).

List of Presentations

Talks

- 06.03.2013 DFG-SFB 652 GK Workshop, Sievershagen
'Phase-controlled electron acceleration from dielectric nanoparticles in intense few-cycle laser pulses'
- 22.03.2013 DPG Spring Meeting (AMOP), Hannover
'Phase-controlled electron acceleration from dielectric nanoparticles in intense few-cycle laser pulses'
- 28.10.2013 3rd SPP 1391 School, Mühlheim a.d. Ruhr
'Imaging sub-wavelength optical near-fields of isolated nanosystems'
- 17.04.2014 DPG Spring Meeting (AMOP), Berlin
'Imaging sub-wavelength optical near-fields of isolated nanosystems'
- 29.09.2014 3rd SPP 1391 Student Seminar, Bronnbach
'Attosecond controlled photoemission tailored by sub-wavelength nanofocussing'
- 20.09.2015 Clustertreffen, Lindow
'Field propagation-induced directionality of CEP-controlled photoemission from nanospheres'
- 18.10.2015 4th International Workshop on Ultrafast Nanooptics, Bad Dürkheim
'Field propagation-induced directionality of CEP-controlled photoemission from nanospheres'
- 03.11.2015 Theory Seminar, Rostock
'Field propagation-induced directionality of CEP-controlled photoemission from nanospheres'
- 07.12.2016 QUTIF Young Researcher Meeting at Mariaspring, Göttingen
'Attosecond electron scattering in dielectrics'
- 19.01.2017 DFG-SFB 652 GK Seminar, Rostock
'Attosecond electron scattering in dielectrics'
- 08.03.2017 DPG Spring Meeting (AMOP), Mainz
'Attosecond electron scattering in dielectrics'
- 06.03.2018 DPG Spring Meeting (AMOP), Erlangen
Invited talk: *'Attosecond streaking in dielectrics'*

Posters

- 06.10.2013 Clustertreffen, Herzogenhorn
'Phase-controlled electron acceleration from metal clusters in few-cycle laser pulses'
- 16.06.2014 Annual SPP 1391 Meeting, Bad Dürkheim
'Short-Wavelength Photon and Electron Emission in Free and Deposited Nanoparticles by Controlled Ultrafast Laserinduced Nanolocalized Fields'
- 24.11.2014 14th International Workshop on Atomic Physics, Dresden
'Attosecond controlled photoemission tailored by sub-wavelength nanofocussing'
- 23.03.2015 DPG Spring Meeting (AMOP), Heidelberg
'Attosecond controlled photoemission tailored by sub-wavelength nanofocussing'
- 14.09.2015 3rd International Conference on Correlation Effects in Radiation Fields, Rostock
'Field propagation induced directionality of carrier-envelope phase-controlled photoemission from nanospheres'
- 29.02.2016 DPG Spring Meeting (AMOP), Hannover
'Simulation of attosecond-streaking in dielectric nanospheres'
- 17.05.2016 Annual SPP 1840 Meeting, Jena
'Controlling the photoemission from dielectric nanospheres and metal nanotips with two-color laser fields'
- 23.08.2016 2nd Summer Workshop on Ultrafast Cluster Dynamics, Berlin
'Attosecond clocking of inelastic scattering in dielectrics'
- 26.09.2016 1st Summer School of the DFG Priority Program 1840, Rostock
'Attosecond clocking of inelastic scattering in dielectrics'
- 26.02.2017 Annual SPP 1840 Meeting, Dresden
'Attosecond electron scattering in dielectrics'
- 15.06.2017 Final SFB 652 Symposium, Rostock
'Attosecond chronoscopy of electron scattering in dielectric nanoparticles'
- 05.09.2017 QUTIF International Conference, Bad Honnef
'Attosecond chronoscopy of electron scattering in dielectrics'
- 25.09.2017 Clustertreffen, Bacharach
'Attosecond chronoscopy of electron scattering in dielectrics'

List of Figures

1.1.	Three-step model of strong-field physics	1
1.2.	Strong-field experiments	2
1.3.	Electron emission within the Simple Man's Model	3
1.4.	Enhanced near-field at a tungsten nanotip	4
1.5.	Coherent photoemission from a tungsten nanotip in two-color laser fields	6
1.6.	Electron emission from silica nanospheres	7
1.7.	Attosecond streaking	8
1.8.	Attosecond streaking on gas targets and surfaces	9
1.9.	Radiation-induced DNA damage	10
2.1.	The M ³ C model	12
2.2.	Spectral pulse decomposition	18
2.3.	Wigner distributions of unchirped and chirped XUV pulses	19
2.4.	Numerical implementation of the multipole expansion	23
2.5.	Required lookup tables in dependence of the multipole expansion order.	23
2.6.	Photoionization regimes	24
2.7.	Photoelectron spectrum measured from SiO ₂ nanoparticles	25
2.8.	Tunneling from the surface of a dielectric	26
2.9.	Complex refractive index of SiO ₂	27
2.10.	Elastic electron-atom collisions	29
2.11.	Inelastic electron scattering in SiO ₂	30
2.12.	Scattering properties of SiO ₂ as used in M ³ C	31
2.13.	Parallel LUT-based multipole expansion	32
2.14.	Parallel efficiency of M ³ C simulations	33
3.1.	Schematic representation of the one-dimensional nanotip model	38
3.2.	Quantum nanotip model	39
3.3.	Coherent photoemission from metal nanotips	41
3.4.	Interplay of temporal and spatial field profiles	42
3.5.	Photoelectron spectra from metal nanotips in two-color fields	43
3.6.	Phase-dependent photoelectron spectra with selectively activated 2 ω -fields	44
4.1.	Linear near-field at a small dielectric nanosphere	46
4.2.	Ionization of small dielectric nanospheres	46
4.3.	Photoelectron spectra from small dielectric nanospheres	47
4.4.	Typical recollision trajectories	48
4.5.	Correlation of generation times and final energies	49
4.6.	Phase-dependent electron emission from small nanospheres	51
4.7.	Charge interaction effects in strong-field photoemission from nanospheres	52
4.8.	Evolution of the mean-field potential	53

List of Figures

4.9.	Trapping field effects on the electron emission from surfaces	54
4.10.	Pulse length and CEP dependence of TRAB	55
4.11.	Trajectory analysis of trapping field assisted backscattering	56
4.12.	Cut-off energies vs. ionization energy and surface field intensity	57
4.13.	Material and intensity-dependent cut-off energies	59
5.1.	Near-field enhancement at large dielectric nanospheres	62
5.2.	Linear near-field evolution at small and large nanospheres	62
5.3.	Characterization of the linear near-fields	63
5.4.	Measured CEP-averaged momentum distributions from silica nanospheres	64
5.5.	Emission from small and large SiO ₂ nanospheres predicted by M ³ C	65
5.6.	Directionality and phase-dependent switching	66
5.7.	Evolution of characteristic emission parameters with diameter	68
5.8.	Time evolution of the selective kinetic energy gains	70
5.9.	Near-field polarization at dielectric nanospheres	70
5.10.	Recollision-resolved selective electron energy spectra	71
5.11.	Single and double recollision electron yields	72
5.12.	Cut-off energies of single and double recollision electrons	73
5.13.	Trajectory analysis of single and double rescattering	74
5.14.	Energy absorption for single and double recollisions	75
5.15.	Correlation analysis of electron emission from nanospheres	76
5.16.	Directionality and switching for single and double recollisions	77
6.1.	Schematic setup of the streaking experiment	79
6.2.	Discrimination of measured streaking data	80
6.3.	Hit statistic correlation maps	81
6.4.	Averaged VMI images	82
6.5.	Extraction of streaking spectrograms from VMI data	82
6.6.	Measured streaking spectrograms and extracted delays	83
6.7.	Comparison of measured and simulated streaking delays	84
6.8.	Near-fields and birth angle distribution	86
6.9.	Near-field mediated streaking delays	87
6.10.	Evolution of near-field induced delays with nanoparticle size	89
6.11.	XUV chirp induced streaking delay	89
6.12.	Systematic analysis of the collisional streaking delay	91
6.13.	Simplified model for the collisional streaking delay	92
6.14.	Cancellation of the momentum gain via elastic scattering	93
6.15.	Population depletion due to inelastic collisions.	94
6.16.	Impact of elastic an inelastic scattering on the streaking delay	95
6.17.	Intracycle averaging and wavelength dependence of the streaking delays	96
6.18.	Energy-dependent IMFPs	97
B.1.	Absorption of a plane wave by a box of atoms	104
C.1.	M ³ C simulations with isotropic and anisotropic elastic scattering	105
D.1.	Impact of charge-interaction on the streaking delays from silica	106
E.1.	Transport cross sections for different materials	106

List of Tables

4.1. Properties of nanoparticle samples and parameters for the simulations . . .	58
--	----

1. Introduction

Exposing an atom or molecule to a strong laser pulse can result in the liberation of electrons by the nonlinear absorption of energy from the laser field. Two conceptually different physical pictures for this process are multiphoton and tunnel ionization, where the Keldysh parameter is typically used to associate a specific scenario with the prevailing picture [1]. Being further driven by the laser field, a liberated electron can be accelerated back towards the parent ion to recollide. Upon such a recollision, the electron might (i) scatter elastically and escape or (ii) recombine under the emission of a short burst of radiation. This intuitive picture (Fig. 1.1) was suggested by Paul Corkum in 1993 [2] and is typically referred to as the 'three-step model' or 'simple man's model' (SMM) of strong-field science. Its importance for the field of attosecond physics is reflected by the recent special issue 'celebrating 25 years of recollision physics' [3] and results from the provided intuitive and unifying physical picture of high-order above-threshold ionization (HATI) [4–6] and high harmonic generation (HHG) [2, 7–12].

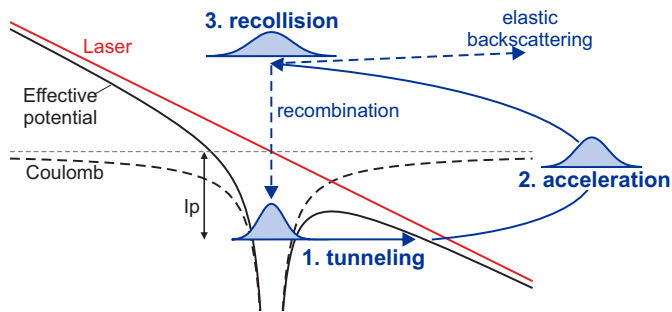


Figure 1.1. Three-step model of strong-field physics. An electron can (1) tunnel through the finite barrier of the effective potential (solid black curve), (2) be accelerated by the laser field (red curve), and (3) recollide with the ion resulting in elastic backscattering or recombination.

Recent experiments revealed that the concepts of atomic strong field physics are applicable to a large extent also to the photoemission from nanostructures or nanostructured solids. There non-resonant excitation enables the generation of strongly enhanced near-fields that can be confined far below the wavelength without losing the shortness of the pulses. For example, clear signatures from energetic electron emission via near-field driven elastic backscattering have been observed for isolated dielectric nanospheres [13, 14], metal nanotips [15–19] and surface-assembled nanoantennas [20]. The idea to utilize near-fields to enhance, localize and modify the above described attosecond phenomena has received remarkable attention within the last couple of years and even led to the emergence and rapid development of a new research field termed 'attosecond nanophysics' [21, LS1]. A key motivator and promising future perspective is the realization of protocols for ultrafast light-wave driven nanoelectronics [22]. However, due to the large number of additional effects, such as near-field inhomogeneity, collisional dynamics and collective phenomena, the physical mechanisms are not fully understood. To understand and harness the implications of attosecond science with nanostructures – which will be at the heart of this thesis – it is essential to clarify the combined action and modifications of the elementary physical processes of (i) tunneling, (ii) propagation, and (iii) recollision in the presence of a nanostructure.

1.1. Basic features in atomic strong field physics

Following the successful concept of the three-step model, the analysis of classical trajectories and characteristic cut-off features associated with specific trajectory classes will be a central tool to uncover the physical mechanisms of photoemission from nanostructures in this thesis. The resulting qualitative and quantitative predictive capabilities can be illustrated in a very convincing way by the historic examples from atomic strong-field physics in Fig. 1.2. The agreement of the two pronounced step-like features in the photoelectron spectrum in Fig. 1.2(a) with the predicted cut-offs at $2U_p$ and $10U_p$ from the three-step model enables an unambiguous assignment of the low and high energy signals to direct electron emission [23] and elastic backscattering [5]. Further, the cut-off of the harmonic emission in Fig. 1.2(b) around $3.17U_p + I_p$ can be associated with the maximal return energy of electrons prior to recombination [2]. Here, the ponderomotive energy U_p reflects the characteristic energy scale of the electron's oscillation in the field¹ and I_p is the ionization energy of the atom.

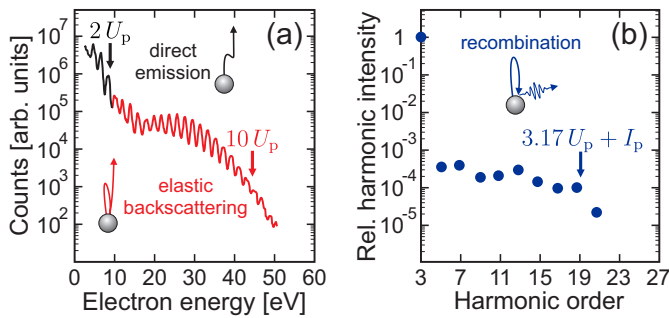


Figure 1.2. Strong-field experiments. (a) HATI spectrum from Ar under 40 fs 630 nm pulses at $I = 1.2 \times 10^{14} \text{ W/cm}^2$. Data from [4]. (b) Intensities of harmonics of 1064 nm pulses generated in Xe at $I \approx 3 \times 10^{13} \text{ W/cm}^2$. Data from [8]. Arrows indicate the spectral cut-offs as predicted by the three-step model.

Schematic representations of the characteristic electron trajectories for these three cases are shown as insets in Fig. 1.2. Specific properties of the three trajectory classes can be extracted from the quantitative analysis of representative realizations of the trajectories in Fig. 1.3(a).

Directly emitted electrons result from ionization before the peak of a laser half-cycle as such trajectories cannot return to the origin (black curves in Fig. 1.3(a)). Their maximal yield is reached for emission at the peak of the laser field, where, however, the vector potential and thus also the final kinetic energy vanish (cf. Fig. 1.3(b)). On the other hand, for the optimal direct trajectory (bold black curve labeled with ①) with maximal kinetic energy of $2U_p$, the ionization probability vanishes due to the negligible electric field.

The second relevant class are recollision electrons which are generated after the peak of the laser half-cycle and escape after elastic backscattering at the origin (red curves in Fig. 1.3(a)). The optimal backscattering trajectory (bold red curve with label ②) returns close to minimum of the vector potential and corresponds to a final energy of $\approx 10U_p$. Shorter and longer trajectories with respective earlier and later recollisions result in lower final energies and contribute to the spectral plateau [5]. The possibility to acquire the same energy via two different trajectories can lead to signatures from

¹The ponderomotive energy $U_p = e^2 \mathcal{E}_0^2 / (4m_e \omega^2)$ reflects the mean kinetic energy of the quiver motion of an electron in a continuous field with field strength \mathcal{E}_0 and frequency ω (for a short derivation see Appendix A). Here, e and m_e are the elementary charge and the electron mass, respectively.

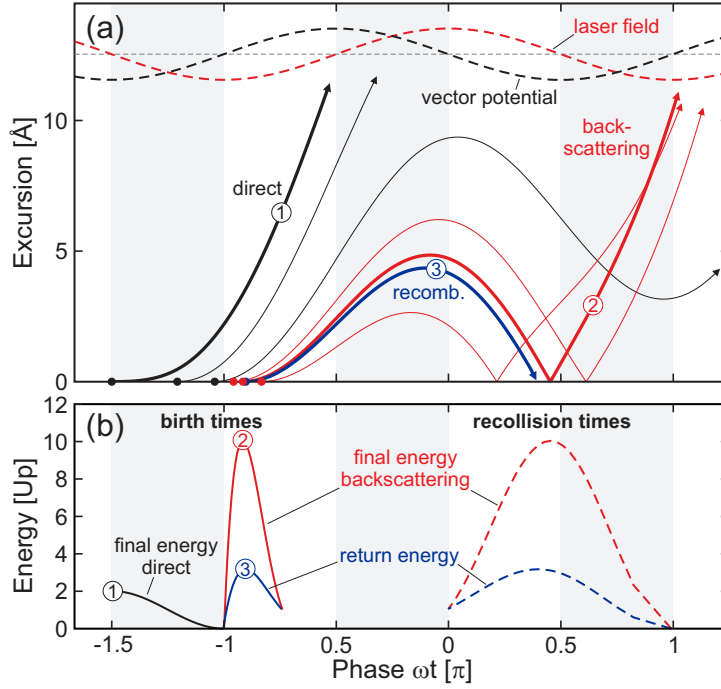


Figure 1.3. Electron emission within the SMM². (a) Trajectories for direct emission (black) and with one recollision (red) for different birth times (colored dots). Bold curves reflect optimal trajectories for direct emission ①, elastic backscattering ② and recombination ③. Dashed red and black curves show the evolution of laser electric field and its vector potential. White and gray areas visualize quarter-cycles of the field. (b) Birth time-dependent final energies for direct emission (black curve) and backscattering (solid red), and recollision energies (solid blue). Recollision timings are indicated by respective dashed curves.

intracycle interference [24]. The sensitivity of the backscattering process to the field waveform enables the characterization of the carrier-envelope phase (CEP) of few-cycle laser pulses [25]. Waveform-controlled backscattering has also been demonstrated utilizing multi-color [26, 27] and bicircular laser fields [28, 29].

The third relevant class of trajectories reflects recollision electrons that recombine with the parent ion. The respective optimal trajectory (bold blue curve with label ③) leads to the highest return energy of $\approx 3.17 U_p$ and together with the released ionization energy upon recombination directly yield the famous HHG cut-off law [2] $E_c^{\text{HHG}} = 3.17 U_p + I_p$. A particularly important aspect of HHG is the generation of attosecond pulses, that enable metrologies for tracing electronic processes on their natural timescale [30–32]. As the possible timings of electron recollisions leading to a specific photon energy are confined to short time intervals (see dashed blue curve in Fig. 1.3(b)) the generated radiation is emitted in short bursts. For a long pulse, recollisions take place in each half cycle, leading to the emission of an attosecond pulse train. The corresponding spectrum forms a frequency comb of odd harmonics [33–35]. The interference of electron trajectories resulting from adjacent harmonics and coupled by the additional absorption/emission of an infrared (IR) photon enables the reconstruction of the attosecond pulse train. This concept constitutes the well-known RABBITT³ technique [34, 36] that also allows the characterization of attosecond delays in the photoemission from atoms [34, 35], molecules [37] and recently also solids [38, 39] and liquids [40]. In fact, almost 20 years ago Hentschel *et al.* stated that

²For the SMM simulations, electrons are generated at the origin with zero initial velocity and are accelerated by a long laser pulse $\mathcal{E}(t) = \mathcal{E}_0 \cos(\omega t)$ with peak field strength \mathcal{E}_0 and angular frequency ω . Here, the pulse is assumed long enough to justify the neglect of different field strengths in subsequent cycles but vanishes at $t \rightarrow \pm\infty$. Electron trajectories are calculated in one dimension by integrating the classical equation of motion $\ddot{x}(t) = -\frac{e}{m_e} \mathcal{E}(t)$. For electrons returning to the origin elastic backscattering ($\dot{x} \rightarrow -\dot{x}$) is considered.

³Reconstruction of Attosecond Bursts By Interference of Two-photon Transitions

1. Introduction

a 'straightforward interpretation of spectroscopic data requires isolated, single (attosecond) pulses' [30]. Today, such pulses can be generated routinely in many attosecond labs based on a variety of gating techniques that rely on different approaches. For example, first isolated attosecond pulses have been generated by selection of the cut-off harmonics generated by employing CEP-stabilized [41–43] few-cycle pulses [30, 44, 45]. An alternative approach is to restrict the generation of attosecond bursts to only one half-cycle of the driving field, which can be achieved via polarization gating [46] or ionization gating [47, 48]⁴. The availability of isolated attosecond pulses enabled unprecedented possibilities to probe ultrafast electronic dynamics, e.g. by the well-established attosecond streaking technique [30, 45, 50–52].

1.2. Strong-field nanophysics

The three crucial processes of electron liberation, propagation and collisions can be substantially modified when moving from atomic targets to nanostructures. The physical motivation results from three key aspects that strongly affect the photoemission and are explained and motivated in the following.

The probably most obvious aspect are the enhanced, inhomogeneous and localized near-fields, see Fig. 1.4. Here, the first crucial factor is the pure near-field enhancement that on the one hand, allows to initiate HATI processes already at much lower laser intensities when compared to the atomic case and thus enables to study recollision phenomena at much lower intensities, often below the damage threshold of the nanostructure. On the other hand, it enables to substantially enhance the acceleration of both direct and backscattered electrons. Experiments on metal nanotips [15, 18] and isolated dielectric nanospheres [13, 14] have shown that the near-field enhanced photoemission can still be modified by the CEP of short pulses. Novel applications of tip-based photoemission include for example the complete characterization of the optical phase of focused few-cycle laser pulses [53] and controlled high-contrast switching of photocurrents via terahertz fields [54, 55]. Another intriguing application is the generation of coherent attosecond electron pulses that can be employed for near-field mediated quantum coherent manipulation and reconstruction of free-electron beams [56, 57]. Besides the pure enhancement effect, also the near-field inhomogeneities can strongly affect the photoemission. Their decisive impact could be demonstrated experimentally via the quenching of elastic backscattering if the electrons quiver amplitude exceeds the extension of the local near-field [16, 58] and via ponderomotive shifts in the emission spectra of direct electrons [59].

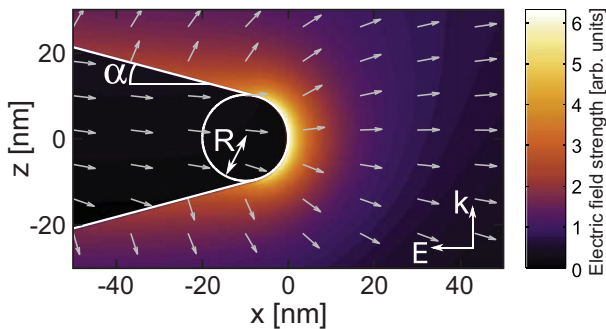


Figure 1.4. Near-field at a tungsten nanotip with 10 nm apex radius and opening angle $\alpha = 15^\circ$ under a 5 fs 800 nm few-cycle laser pulse propagating in z -direction and polarized in x -direction. Gray arrows indicate the local orientation of the field at the instant of maximal enhancement. Adapted from [60].

⁴A detailed overview of the various attosecond pulse generation techniques is given in [49].

The second aspect are charge interaction effects. As compared to atomic strong-field photoemission, where typically less than one electron is emitted per atom, the liberation of multiple electrons from a nanostructure within the same laser-shot can lead to strong many-electron effects. For example, loss of intercycle coherence was observed for metal nanotips and dielectric nanospheres in the case of emission of multiple electrons [13, 14, 58]. Another crucial charge interaction effect is the generation of trapping fields that result from the separation of liberated electrons and residual ions at the surface of a nanostructure. Previous experiments on dielectric nanospheres support that trapping fields lead to quenching of direct emission but can result in substantial enhancement of the energies for electrons emitted via elastic backscattering [13, 14].

The third crucial aspect is the collisional dynamics within the nanostructures. For example, experiments on metal nanotips revealed that the contrast of HATI peaks is much smaller as compared to atomic photoemission [15], which is a clear hint at decoherence phenomena and electron collision processes. In addition, the impact of collisions can be particularly large for electrons that are generated within the volume, as for example in the case of linear photoemission by extreme ultraviolet (XUV) fields. Hence, nanostructures can enable the study of the ultrafast electron transport dynamics within solids, for example via attosecond streaking.

1.3. Investigated scenarios and aims of this thesis

In this thesis, the implications of the above introduced crucial aspects of photoemission from nanostructures will be studied via three selected scenarios which are motivated by recent experiments.

- The first scenario addresses strong-field photoemission from metal nanotips under two-color laser fields. Here, the specific focus will be on the impacts of the enhancement, inhomogeneity, and waveform of the near-field on the coherent electron emission.
- As a second scenario, few-cycle driven electron emission from dielectric nanospheres will be considered in order to inspect the combined impacts of near-fields, charge interaction and the collisional dynamics.
- In the third scenario, the emission from nanospheres excited by XUV laser pulses will be studied, where the central aim is to identify the specific impacts of near-field inhomogeneities and the attosecond electron transport dynamics within the material on photoemission delays that can be extracted via attosecond streaking.

In the following, the three scenarios are described briefly to motivate the central scientific questions relevant for this thesis.

1. Introduction

1.3.1. Strong-field photoemission from metal nanotips

In the first scenario, the photoemission from metal nanotips under waveform-controlled optical two-color fields will be investigated. This scenario is motivated by a recent nanotip experiment where almost perfect coherent control of the photoemission was demonstrated [61, 62]. In particular, the emission current could be strongly modulated via the relative phase between the two spectral components of a two-color laser field composed of a fundamental and its second harmonic, see Fig. 1.5(a). Already with a very weak second harmonic of less than 3% relative intensity with respect to the fundamental, high phase-contrast up to 97.5% could be observed, see Fig. 1.5(b). However, so far it is unclear under which circumstances the modulation is caused by the impact of the second harmonic on the (quantum) tunneling process or on the (classical) electron propagation. This motivates to study the quantum and classical aspects of two-color driven electron rescattering in the enhanced and inhomogeneous near-fields of metal nanotips, which presents the first particular aim for this thesis.

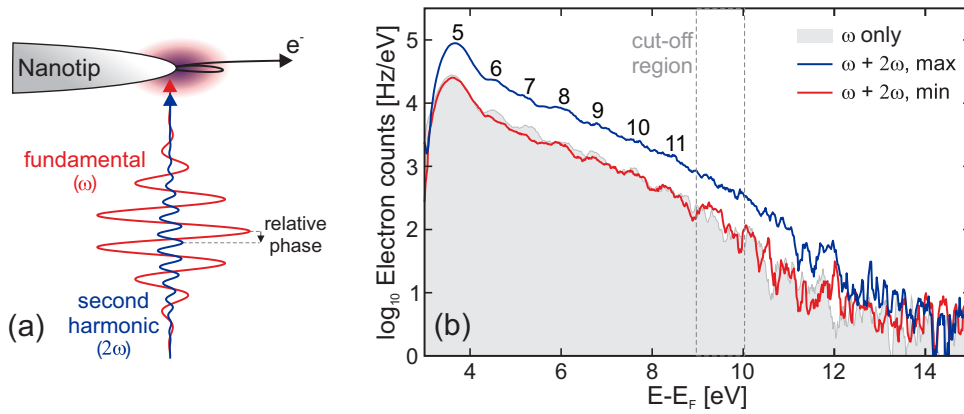


Figure 1.5. Coherent photoemission from a tungsten nanotip in two-color laser fields. (a) Schematic setup of the nanotip experiment. (b) Electron energy spectra measured from a tungsten nanotip in a two-color laser field composed of an intense 1560 nm pulse and its weak second harmonic (2.6% rel. intensity). Gray area: only fundamental. Red/blue curves: two-color field with relative phase locked at the photocurrent minimum/maximum. Numbers indicate multi-photon orders of the fundamental. Adapted from [LS2].

1.3.2. Near-field driven photoemission from dielectric nanospheres

In the second scenario, the CEP-controlled strong-field electron emission from isolated dielectric nanospheres will be investigated. In fact, elastic backscattering from nanostructures has first been demonstrated for silica nanoparticles [13]. A crucial motivation for this scenario are previous experiments by Zharebtsov *et al.* that – besides the impact of the enhanced near-field – also revealed clear evidence for nonlinear many-particle charge interaction effects on the CEP-controlled photoemission [13, 14]. In particular, the increasing energy enhancement with intensity far beyond the prediction of the SMM could only be explained when taking into account charge interaction in corresponding semi-classical simulations (compare red to black curve in Fig. 1.6(b)). Although the observations could be associated with charge interaction, the physical picture underlying the additional energy

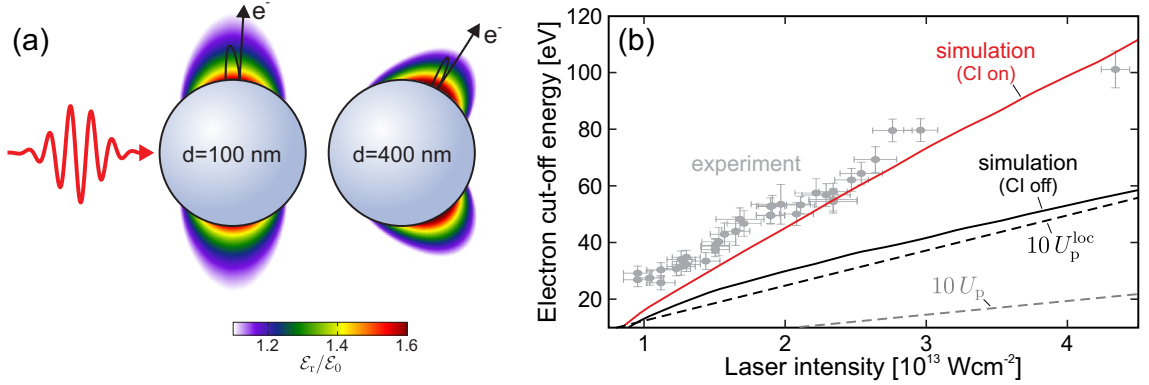


Figure 1.6. Electron emission from silica nanospheres under 720 nm 5 fs few-cycle pulses. (a) Maximum enhancements of the radial near-fields at small and large spheres with respect to the peak field strength of the incident field (Mie calculations). Black curves illustrate backscattering trajectories. (b) Intensity-dependence of the measured cut-off energies of electrons emitted from $d \approx (100 \pm 50)$ nm silica spheres (gray symbols). Curves show respective simulation results excluding (black) and including charge interaction (red). Dashed gray and black lines illustrate the classical cut-offs of backscattered electrons for the ponderomotive energies of the incident field U_p and the maximally enhanced local field $U_p^{loc} = \gamma_0^2 U_p$, with peak field enhancement $\gamma_0 = 1.6$. Data from [13].

gain is not yet fully understood. The present thesis addresses this problem with the aim to identify how the generation of local trapping fields at the surface of the sphere as well as the interaction among emitted electrons affect the emission dynamics.

Another open question is how the electron dynamics is affected by propagation effects of the local near-fields. Theoretical investigations of the electron emission from droplets revealed that field propagation effects can significantly modify the electron emission (including its directionality) and enable the generation of relativistic attosecond electron bunches [63, 64]. Former experiments, however, were performed only on dielectric nanoparticles small compared to the driving wavelength, where field propagation effects are negligible. In this case, pronounced electron emission was observed along the laser polarization direction. An interesting perspective is to extend these studies to a size regime where field propagation effects set in and where the near-field localization can be substantially modified, see Fig. 1.6(a). A central aim for this thesis is to study the resulting modifications of the photoemission, especially with respect to its directionality.

1.3.3. Attosecond streaking on dielectric nanospheres

The combination of isolated attosecond pulses with phase-stabilized optical fields enables the precise analysis of the electron dynamics following linear photoemission via attosecond streaking, where a particularly intriguing aspect is the accurate characterization and interpretation of photoemission delays [65, 66]. The physical relevance of such delays for the streaking at nanostructures is still an open question and will be investigated in this thesis. In the last couple of years, attosecond streaking was utilized extensively to investigate photoemission delays from atomic [67, 68] and molecular [69] targets. Several experimental and theoretical studies revealed that the delays essentially arise from the atomic potentials

1. Introduction

and thus contain target-specific information such as Eisenbud-Wigner-Smith-type (EWS) photoemission delays [70–72] as well as contributions from post-interaction dynamics due to Coulomb-laser coupling (CLC) [73–75].

The idea of the underlying spectroscopic method is illustrated in Fig. 1.7(a) and can be described classically via the following simplified picture. First, the absorption of a photon (with energy $\hbar\omega$, where \hbar is Planck’s constant) from the attosecond XUV pulse leads to liberation of an electron at time t_0 with an initial momentum p_0 that corresponds to the excess energy $E_0 = \hbar\omega - I_p$. After its liberation, the electron is accelerated (‘streaked’) by a synchronized optical streaking field $\mathcal{E}(t)$. For a finite pulse (i.e. $\mathcal{E}(t) = 0$ for $t \rightarrow \pm\infty$) and neglecting the atomic potential, the final photoelectron momentum

$$p_f(t_0) = p_0 - eA(t_0) \quad (1.1)$$

depends only on the initial momentum p_0 and the vector potential $A(t) = \int_t^\infty \mathcal{E}(t')dt'$ at the generation time t_0 , see blue and red arrow in Fig. 1.7(b). Scanning the XUV-optical pulse delay Δt , which corresponds to scanning the generation time t_0 , therefore enables to map the vector potential to the experimentally accessible final photoelectron momenta $p_f(\Delta t)$ or kinetic energies $E_f(\Delta t) = p_f(\Delta t)^2/(2m_e)$. Hence, attosecond streaking enables

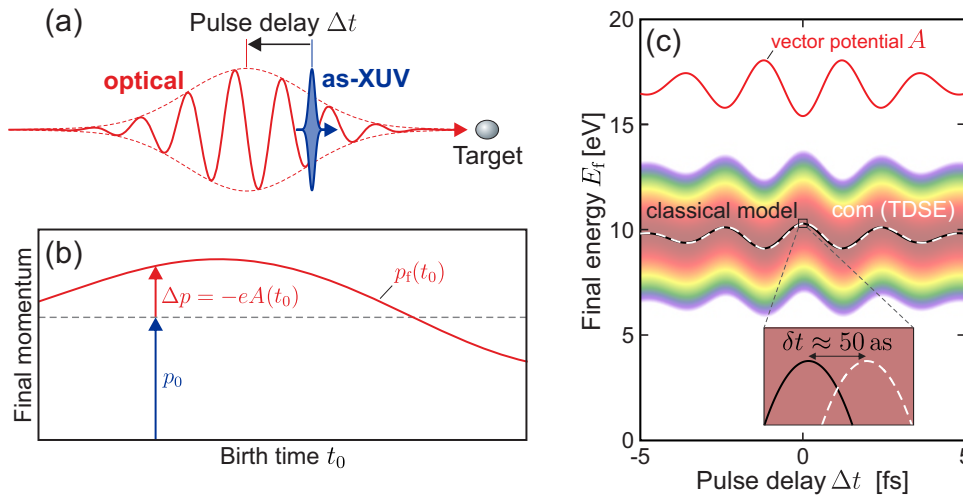


Figure 1.7. Attosecond streaking. (a) Schematic illustration of the streaking principle. The target is exposed to an attosecond XUV-pulse (blue) and a synchronized optical pulse (red) with adjustable delay Δt . (b) Initial momentum p_0 of a liberated photoelectron (blue arrow) and asymptotic momentum gain $\Delta p = -eA(t_0)$ from the streaking field (red arrow) for a selected birth time t_0 . The red curve shows the respective final momentum in dependence of the generation time t_0 . (c) Pulse-delay dependent final energies of photoelectrons with $E_0 = 10$ eV streaked by a weak streaking pulse as predicted by the simplified classical model (black curve) and a corresponding quantum simulation⁵(false color plot). The white dashed curve shows the respective energetic center of mass. The inset shows the relative streaking delay δt .

⁵For the quantum simulations, the ground state wave function is determined for a Coulombic potential $V_0(x)$ and propagated by numerical integration of the time-dependent Schrödinger equation $i\hbar \frac{\partial}{\partial t} \Psi(x, t) = \left[-\frac{\hbar^2}{2m} \frac{\partial^2}{\partial x^2} + V_0(x) + e\mathcal{E}_{\text{XUV}}(t + \Delta t) + e\mathcal{E}(t) \right] \Psi(x, t)$ taking into account the streaking field $\mathcal{E}(t)$ and the delayed XUV pulse $\mathcal{E}_{\text{XUV}}(t + \Delta t)$. Asymptotic energy spectra are extracted from the emitted part of the wave function. The numerical details are described in Section 2.6.

the direct measurement of light waves of optical fields, which was first demonstrated experimentally by Goulielmakis *et al.* [42] and Kienberger *et al.* [45]. Streaking further provides a powerful tool to accurately characterize the employed XUV fields via the FROG-CRAB⁶ technique [76, 77].

Besides the characterization of both employed fields, attosecond streaking also opens the door to investigate the dynamics of the target’s valence electrons on their natural time-scale via photoemission- or streaking-delays [65, 66]. How such delays affect a streaking measurement or simulation can be demonstrated instructively via the following simple example. While the above described classical picture predicts a streaking trace that directly reflects the vector potential (black curve in Fig. 1.7(c)), a corresponding quantum simulation that accounts for the atomic potential yields a more complex streaking spectrogram (false color plot in Fig. 1.7(c)). The latter exhibits a spectral broadening that is attributed to the spectral width of the attosecond pulse, and also shows delay-dependent oscillations similar to the classical prediction. A typical way to analyze such a streaking spectrogram is to extract its energetic center of mass (white dashed curve) that reveals a delay of around 50 as with respect to the classical result. This delay includes contributions from EWS and CLC delays and directly reflects the impact of the potential.

At nanostructures, streaking delays can be substantially modified due to near-field inhomogeneities and the attosecond electron transport dynamics in the material. In contrast to the atomic case, where the streaking field is homogeneous and affects the photoelectron directly after its liberation (see Fig. 1.8(a)), streaking from a surface may be fundamentally different. For example, for a metal, where the external streaking field is screened⁷, the streaking begins only after the electron has escaped from the surface, see Fig. 1.8(c). In this case, the final electron momentum $p_f(t_0) = p_0 - eA(t_0 + t_{\text{trans}})$ is determined by the vector potential at the escape time and results in a streaking delay $\delta t = t_{\text{trans}}$ that is associated with the transport to the material’s surface. Such transport delays have been demonstrated experimentally for clean and adlayer-covered metallic surfaces [78–80] and only recently also for a semi-conductor [81]. However, the microscopic aspects of the material-specific transport, for example the impacts of elastic and inelastic electron-atom collisions, were so far not explored in detail for such streaking experiments.

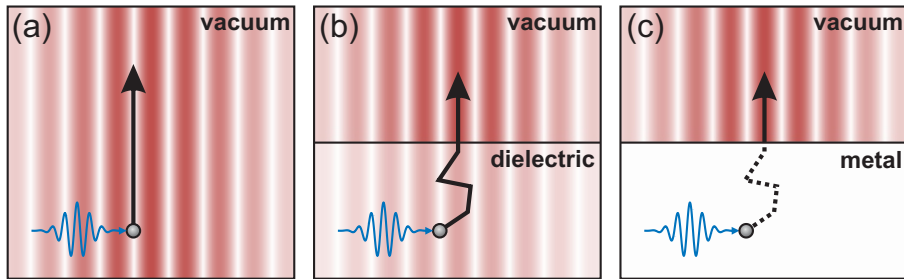


Figure 1.8. Schematic illustration of attosecond streaking on an atomic target (a) and on the surfaces of a dielectric (b) and a metal (c). After ionization by the XUV pulse (blue) the electron is streaked by the (near-)field of the optical pulse (red).

⁶Frequency-Resolved Optical Gating for Complete Reconstruction of Attosecond Bursts

⁷More precisely, the field component normal to the surface.

1. Introduction

In this thesis it will be shown that streaking by the internal fields within a dielectric is important (see Fig. 1.8(b)) and enables to draw conclusions about the inelastic mean free path (IMFP) of electrons in the material. This can be of large relevance for many research fields ranging from material science to biology or medicine. For example, the impact of inelastic electron-atom scattering and specifically the associated generation of secondary electrons via impact ionization are key for laser nanomachining [82] but can also restrict light-driven electronics due to rapid carrier multiplication [22]. The latter can also cause radiation-induced DNA damage [83–86]. As illustrated in Fig. 1.9, inelastic scattering of photoelectrons that are generated in the tissue by incident high energy radiation results in so-called 'low energy electron tracks' that can severely damage the DNA helix. However, direct experimental characterization of IMFPs in the relevant low energy range ($\lesssim 50$ eV) has so far not been demonstrated.

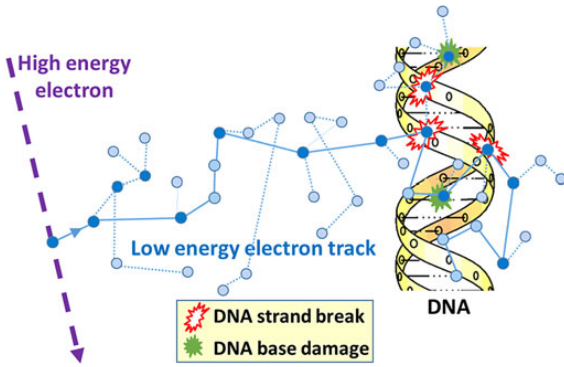


Figure 1.9. Schematic illustration of radiation-induced DNA damage. Ionizing radiation (high energy electrons or photons, purple) can generate low-energy electron tracks (blue). Dark blue circles mark inelastic scattering events resulting in the generation of secondary charges via impact ionization. Tracks ending at and interacting with the DNA double helix can cause strand breaks or base damage (as indicated). From [86].

So far, a major obstacle for streaking experiments on dielectric surfaces was space-charge accumulation which impedes or at least contaminates the required delay resolved measurement of streaking spectrograms. Only recently the space-charge problem has been resolved in experiments performed by the groups of Matthias F. Kling and Francesca Calegari, who employed a jet of isolated dielectric nanospheres to provide fresh targets for each laser shot, enabling the first measurement of attosecond streaking at a dielectric. The physical interpretation of the observed streaking delays is subject of the theoretical analysis presented in this thesis. The central aim is to identify how and to what extend the near-fields at and the collisional dynamics within a nanosphere affect the observed streaking delays. A particularly relevant aspect of the analysis will be to explore how IMFPs can be characterized directly via streaking experiments and if this method is generally applicable to arbitrary materials.

Structure of the thesis

As a starting point, the theoretical framework for the employed semi-classical and quantum simulations is described in Chapter 2. Classical and quantum signatures of coherent photoemission from metal nanotips in two-color fields are investigated in Chapter 3. Key aspects of strong-field driven electron dynamics in small dielectric nanospheres are analyzed in Chapter 4 for a typical reference scenario. In addition, charge interaction effects on the strong-field electron emission are discussed. Chapter 5 is dedicated to field propagation of the linear near-fields at large dielectric nanospheres and their translation to the electron emission directionality. The studies of the charge transport dynamics within dielectric nanospheres via attosecond streaking are presented in Chapter 6. Finally, Chapter 7 contains a summary of the key results and develops an outlook for future research.

2. Theoretical framework

This chapter is dedicated to the theoretical methods employed to simulate the ultrafast electron dynamics in dielectric nanoparticles and metal nanotips under intense near-infrared (NIR) and XUV laser pulses. In general, such systems are fully described by highly correlated many-particle wave functions and their dynamics is determined by the time-dependent Schrödinger equation (TDSE). However, for the considered scenarios numerical solutions of the TDSE for the full problems are neither possible (even on modern supercomputers) nor insightful as it is unclear if the relevant physics can be extracted from the highly correlated wave functions. Hence, instructive theoretical models require reasonable approximations. Based on the idea of Corkum’s three-step model, a common approximation in strong-field physics is to treat the dynamics of liberated electrons classically and include quantum effects (e.g. the tunneling step) via appropriate rates that can be extracted from simplified quantum models or experiments.

Following the above approach, in this work the electron dynamics in dielectric nanospheres is modeled semi-classically, where a classical electron trajectory reflects the motion of the respective quantum wave packet’s center of mass. For the considered scenarios with many active electrons, the neglect of quantum interferences is justified, as interaction will lead to rapid dephasing of individual quantum trajectories. This assumption is substantiated by the lack of HATI features in the spectra measured in receptive nanoparticle experiments¹. The comprehensive semi-classical description requires addressing three key challenges: First, the evaluation of the local near-fields including field propagation and charge interaction. Second, a proper treatment of near-field driven ionization as well as electron impact ionization. Third, the description of charge transport within the dielectric material. After a brief description of the main ingredients for the semi-classical model in [Section 2.1](#), the approaches used to meet these requirements are discussed in detail in [Section 2.2](#) to [Section 2.4](#). [Section 2.5](#) contains an outline of technical details regarding optimization and parallelization of the simulation code for efficient utilization of modern supercomputers. Note that most of the descriptions will be exemplified for the case of SiO₂ that is mainly studied in this work. Finally, [Section 2.6](#) is dedicated to the description of a simplified quantum model that is employed to investigate the quantum aspects of coherent electron emission from metal nanotips.

2.1. The semi-classical model

The electron dynamics at the dielectric nanospheres is simulated via the semi-classical trajectory-based Mean-field Mie Monte-Carlo (M³C) model. The latter provides a continuum description of the local near-fields at a laser-excited nanosphere and a quasi-

¹Only in the regime with $\lesssim 1$ electron per pulse experimental results from nanotips support substantial quantum coherence [15].

2. Theoretical framework

microscopic description of the electron motion via classical trajectories. Quantum effects such as ionization of the initially neutral dielectric sphere via tunneling or single-photon ionization as well as electron-atom scattering within the material are included via effective rates extracted from simplified quantum models. Please note that conceptually similar simulation models have been utilized also for studying metallic nanotips [87]. A typical simulation scenario and the implementation of the model are illustrated schematically in Fig. 2.1. Before describing the details of the model its three key ingredients are briefly outlined in the following.

The first part of the model addresses the description of the local near-fields within and outside of the dielectric sphere (① in Fig. 2.1) that include two separate contributions. First, the linear near-field including the incident (NIR or XUV) laser pulse as well as the induced linear-response polarization field of the sphere. This contribution is calculated by a spectral decomposition of the respective incident laser pulse in modes which are then treated with the analytic Mie solution of Maxwell's equations for a sphere. The second contribution includes the Coulomb fields among free charges (liberated electrons and residual ions) and the sphere's polarization that is induced by the free charges. This nonlinear contribution to the near-field is included as an effective mean-field that is evaluated in electrostatic approximation via high-order multipole expansion. Hence, field retardation is only included in the linear-response contribution.

The second key ingredient of M³C is the generation of classical electron trajectories via three different ionization channels (② in Fig. 2.1). First, tunneling of electrons from the dielectrics surface that is driven by the combined linear NIR near-field and the nonlinear mean-field. Second, XUV mediated photoionization within the sphere volume and third, impact ionization due to inelastic interband excitations, resulting in the generation of secondary electrons.

The third part addresses the classical motion of liberated electrons (③ in Fig. 2.1). Their dynamics is mediated by the combined NIR near-field and the mean-field. Material-specific transport is taken into account via elastic and inelastic electron-atom scattering inside the dielectric.

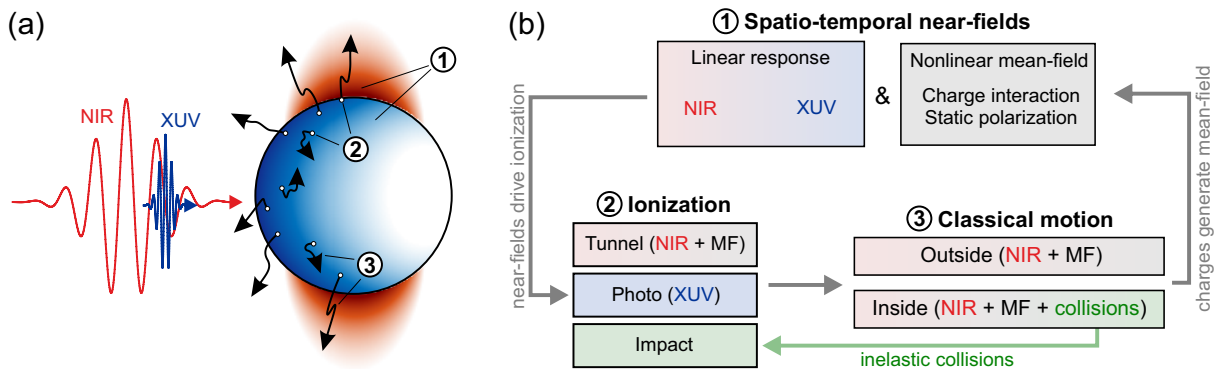


Figure 2.1. The M³C model. (a) Illustration of a typical simulation scenario. Linear near-fields (blue, red) generated by non-resonant excitation via XUV and NIR laser pulses. White dots mark ionization sites of electron trajectories (black arrows). (b) Visualization of the M³C model.

2.2. Description of the spatio-temporal near-fields

In general, the evolution of the electric field $\boldsymbol{\mathcal{E}}(\mathbf{r}, t)$ and magnetic flux density $\mathbf{B}(\mathbf{r}, t)$ of an electromagnetic field is described by the microscopic Maxwell equations [88]

$$\nabla \cdot \boldsymbol{\mathcal{E}} = \frac{\rho}{\varepsilon_0} \quad (2.1) \quad \nabla \times \boldsymbol{\mathcal{E}} = -\dot{\mathbf{B}} \quad (2.3)$$

$$\nabla \cdot \mathbf{B} = 0 \quad (2.2) \quad \nabla \times \mathbf{B} = \mu_0 \left[\mathbf{j} + \varepsilon_0 \dot{\boldsymbol{\mathcal{E}}} \right], \quad (2.4)$$

with vacuum permittivity ε_0 , vacuum permeability μ_0 , charge density $\rho(\mathbf{r}, t)$ and current density $\mathbf{j}(\mathbf{r}, t)$. To model the considered scenario of a dielectric sphere under a strong laser pulse it is necessary to describe both its polarization mediated by the incident field as well as effects induced by free charges. Therefore, it is convenient to separate the charge and current densities

$$\rho = \rho_b^{\text{fast}} + \rho_b^{\text{slow}} + \rho_f \quad (2.5) \quad \mathbf{j} = \mathbf{j}_b^{\text{fast}} + \mathbf{j}_b^{\text{slow}} + \mathbf{j}_f \quad (2.6)$$

into contributions from bound and free charges, indicated with subscripts 'b' and 'f', respectively. The key idea is to further separate the bound charge and current densities into two contributions based on the timescale of the processes that cause the corresponding polarization. The first contribution is associated with the fast polarization (and magnetization) of the material by the incident laser field. The second contribution reflects the slow response of the sphere to the free charges. Similarly, also the fields can be separated into two contributions via $\boldsymbol{\mathcal{E}} = \boldsymbol{\mathcal{E}}^{\text{fast}} + \boldsymbol{\mathcal{E}}^{\text{slow}}$ and $\mathbf{B} = \mathbf{B}^{\text{fast}} + \mathbf{B}^{\text{slow}}$. The linearity of the Maxwell equations (or more precisely the linearity of the divergence and curl operators) allows to associate the 'slow' bound charges with the 'slow' fields and the 'fast' bound charges and the free charges with the 'fast' fields. This yields two separate sets of Maxwell equations, where the first set

$$\nabla \cdot \boldsymbol{\mathcal{E}}^{\text{fast}} = \frac{\rho_b^{\text{fast}}}{\varepsilon_0} \quad (2.7) \quad \nabla \times \boldsymbol{\mathcal{E}}^{\text{fast}} = -\dot{\mathbf{B}}^{\text{fast}} \quad (2.9)$$

$$\nabla \cdot \mathbf{B}^{\text{fast}} = 0 \quad (2.8) \quad \nabla \times \mathbf{B}^{\text{fast}} = \mu_0 \left[\mathbf{j}_b^{\text{fast}} + \varepsilon_0 \dot{\boldsymbol{\mathcal{E}}}^{\text{fast}} \right] \quad (2.10)$$

describes the evolution of the incident laser field and the respective fast polarization response. Within this work, this first set of equations is treated in linear response, yielding the linear near-field as discussed in detail in [Sec. 2.2.1](#). The second set

$$\nabla \cdot \boldsymbol{\mathcal{E}}^{\text{slow}} = \frac{\rho_b^{\text{slow}} + \rho_f}{\varepsilon_0} \quad (2.11) \quad \nabla \times \boldsymbol{\mathcal{E}}^{\text{slow}} = -\dot{\mathbf{B}}^{\text{slow}} \quad (2.13)$$

$$\nabla \cdot \mathbf{B}^{\text{slow}} = 0 \quad (2.12) \quad \nabla \times \mathbf{B}^{\text{slow}} = \mu_0 \left[\mathbf{j}_b^{\text{slow}} + \mathbf{j}_f + \varepsilon_0 \dot{\boldsymbol{\mathcal{E}}}^{\text{slow}} \right] \quad (2.14)$$

reflects the Coulomb fields induced by the free charges as well as the spheres slow polarization response to the free charges. As outlined in detail in [Sec. 2.2.2](#) the respective electric field is approximated as an effective nonlinear mean-field that reflects the additional charge interaction effects. Please note that from here on the superscripts 'slow' and 'fast' will be skipped for the sake of readability.

2. Theoretical framework

2.2.1. The linear near-field

The first set of Maxwell equations (Eq. 2.7–2.10) describes the evolution of the linear response fields of a (neutral) medium without free charges in the presence of an external electromagnetic field. The charge and current densities of the bound charges are connected to the polarization \mathbf{P} and magnetization \mathbf{M} of the material via

$$\rho_b = -\nabla \cdot \mathbf{P} \quad (2.15) \quad \mathbf{j}_b = \nabla \times \mathbf{M} + \dot{\mathbf{P}}. \quad (2.16)$$

Inserting Eq. 2.15 and Eq. 2.16 into the Maxwell equations (Eq. 2.7–2.10) and using the definitions of the displacement \mathbf{D} and magnetic field \mathbf{H}

$$\mathbf{D} = \varepsilon_0 \boldsymbol{\mathcal{E}} + \mathbf{P} \quad (2.17) \quad \mathbf{H} = \frac{\mathbf{B}}{\mu_0} - \mathbf{M} \quad (2.18)$$

yields the macroscopic Maxwell equations in the absence of free charges and currents

$$\nabla \cdot \mathbf{D} = 0 \quad (2.19) \quad \nabla \times \boldsymbol{\mathcal{E}} = -\dot{\mathbf{B}} \quad (2.21)$$

$$\nabla \cdot \mathbf{B} = 0 \quad (2.20) \quad \nabla \times \mathbf{H} = \dot{\mathbf{D}}. \quad (2.22)$$

Considering a homogeneous, linear, and isotropic medium, the fields $\boldsymbol{\mathcal{E}}$ and \mathbf{B} can be related to the (generating) fields \mathbf{D} and \mathbf{H} via the constitutive relations

$$\mathbf{D} = \varepsilon_0 \varepsilon_r \boldsymbol{\mathcal{E}} \quad (2.23) \quad \mathbf{B} = \mu_0 \mu_r \mathbf{H}, \quad (2.24)$$

with constant (scalar) relative permittivity ε_r and relative permeability μ_r . Making use of the vector identity $\nabla \times \nabla \times \mathbf{V} = \nabla(\nabla \cdot \mathbf{V}) - \nabla^2 \mathbf{V}$ allows to derive the Helmholtz equations

$$\left[\nabla^2 - \frac{1}{c^2} \frac{\partial^2}{\partial t^2} \right] \boldsymbol{\mathcal{E}} = 0 \quad (2.25) \quad \left[\nabla^2 - \frac{1}{c^2} \frac{\partial^2}{\partial t^2} \right] \mathbf{H} = 0, \quad (2.26)$$

where $c = 1/\sqrt{\varepsilon_0 \varepsilon_r \mu_0 \mu_r}$ is the speed of light in the medium. It is easy to show that plane waves

$$\boldsymbol{\mathcal{E}}(\mathbf{r}, t) = \boldsymbol{\mathcal{E}}_0 e^{i(\mathbf{k}\mathbf{r} \pm \omega t)} \quad (2.27) \quad \mathbf{H}(\mathbf{r}, t) = \mathbf{H}_0 e^{i(\mathbf{k}\mathbf{r} \pm \omega t)} \quad (2.28)$$

solve the wave equations if they fulfill the dispersion relation $k = \omega/c$ between wave number k and angular frequency ω . In that case the wave equations can be expressed as

$$[\nabla^2 + k^2] \boldsymbol{\mathcal{E}} = 0 \quad \text{and} \quad [\nabla^2 + k^2] \mathbf{H} = 0. \quad (2.29)$$

Scattering of a plane wave by a sphere

Scattering of a plane wave at a sphere is a fundamental problem in electromagnetic scattering theory. In contrast to the general problem of light scattering at arbitrary particles, spherical symmetry allows for an analytical solution to Maxwell's equations as introduced in the famous work by Gustav Mie [89] published in 1908. Since then, the solution to the problem has been thoroughly discussed in many electromagnetic theory books (see e.g. Stratton [90] or Bohren & Huffman [91]) and will therefore not be described in detail here. However, for the sake of completeness, the main steps are briefly outlined in close analogy to the discussion in [91]. For convenience, the following discussion is tailored to

2.2. Description of the spatio-temporal near-fields

the specific scenarios investigated within this thesis where the sphere is considered to be non-magnetizable ($\mu_r = 1$) and in vacuum.

Starting point is the problem of finding an electromagnetic field that satisfies the wave-equations [Eq. 2.29](#) in a linear, isotropic, and homogeneous medium. It can be shown that this difficult problem can be translated to a simpler one by introducing a scalar function ψ and two vector functions

$$\mathbf{M} = \nabla \times (\mathbf{c}\psi) \quad \text{and} \quad \mathbf{N} = \frac{\nabla \times \mathbf{M}}{k} \quad (2.30)$$

with an arbitrary constant vector \mathbf{c} . The trick is that both vector functions satisfy vector wave equations similar to [Eq. 2.29](#) if ψ is a solution to the scalar wave equation

$$[\nabla^2 + k^2] \psi = 0. \quad (2.31)$$

The comparably much simpler task of finding a solution for ψ then also generates the two vector functions. The generating function ψ and a useful choice for the constant vector \mathbf{c} depend on the symmetry of the particular problem. For spherical symmetry, choosing $\mathbf{c} = \mathbf{r}$ results in the vector functions being solutions to the vector wave equation in spherical coordinates. The remaining task then boils down to finding solutions to the respective scalar wave equation also expressed in spherical coordinates. The typical textbook ansatz for problems with spherical symmetry via separation of the variables

$$\psi(r, \theta, \phi) = R(r)\Theta(\theta)\Phi(\phi) \quad (2.32)$$

yields two linearly independent odd and even solutions

$$\psi_{\text{e}ml} = \frac{\sin}{\cos}(m\phi)P_l^m(\cos\theta)J_l(kr). \quad (2.33)$$

Here, $P_l^m(\cos\theta)$ are the associated Legendre functions of first kind with degree l and order m and $J_l(kr)$ are spherical Bessel functions of either first, second or third type. The spherical Bessel functions of second and third type are often referred to as Neumann and Hankel functions and are denoted as $Y_l(kr)$ and $H_l(kr)$, respectively. The choice of the particular type depends on the boundary conditions of the considered problem. Plugging the solutions for the generating function into the definitions of the vector functions in [Eq. 2.30](#) yields the respective vector spherical harmonics²

$$\mathbf{M}_{\text{e}l} = \pm \frac{1}{\sin\theta} J_l P_l^{\cos\phi} \mathbf{e}_r - J_l \frac{\partial P_l}{\partial\theta} \frac{\sin\phi}{\cos\phi} \mathbf{e}_\theta \quad (2.34)$$

$$\mathbf{N}_{\text{e}l} = \frac{l(l+1)}{kr} J_l P_l^{\sin\phi} \mathbf{e}_r + \frac{1}{kr} [kr J_l]' \frac{\partial P_l}{\partial\theta} \frac{\sin\phi}{\cos\phi} \mathbf{e}_\theta \pm \frac{1}{kr \sin\theta} [kr J_l]' P_l^{\cos\phi} \mathbf{e}_\phi, \quad (2.35)$$

expressed in components of the spherical coordinate unit vectors \mathbf{e}_r , \mathbf{e}_θ and \mathbf{e}_ϕ . Any solution to the wave equations can be expanded into an infinite series of the above four solutions³.

²Here, only solutions for $m = 1$ are shown, as all other solutions vanish in the considered scenario.

³This follows from the completeness of the \sin , \cos , associated Legendre and spherical Bessel functions.

2. Theoretical framework

For the considered scenario of a plane wave scattered by a sphere it is convenient to decompose the electric and magnetic fields into the incident parts ($\boldsymbol{\mathcal{E}}_i, \boldsymbol{\mathcal{H}}_i$) and reflected parts ($\boldsymbol{\mathcal{E}}_r, \boldsymbol{\mathcal{H}}_r$) outside the sphere and the transmitted parts ($\boldsymbol{\mathcal{E}}_t, \boldsymbol{\mathcal{H}}_t$) inside the sphere and to express all fields as expansions into vector spherical harmonics. For an incident plane wave propagating in z -direction (i.e. $\mathbf{k} = k\mathbf{e}_z$) and being polarized in x -direction the expansions of the electric and magnetic fields read

$$\boldsymbol{\mathcal{E}}_i = e^{ikz} \mathbf{e}_x = \sum_{l=1}^{\infty} i^l \frac{2l+1}{l(l+1)} (\mathbf{M}_{ol} - i\mathbf{N}_{el}) \quad (2.36)$$

$$\boldsymbol{\mathcal{H}}_i = \frac{k}{\mu\omega} e^{ikz} \mathbf{e}_y = \frac{-k}{\mu\omega} \sum_{l=1}^{\infty} i^l \frac{2l+1}{l(l+1)} (\mathbf{M}_{el} + i\mathbf{N}_{ol}). \quad (2.37)$$

Similarly, the reflected and transmitted fields can be expressed as

$$\boldsymbol{\mathcal{E}}_r = \sum_{l=1}^{\infty} i^l \frac{2l+1}{l(l+1)} (ia_l \mathbf{N}_{el}^{(3)} - b_l \mathbf{M}_{ol}^{(3)}) \quad (2.38)$$

$$\boldsymbol{\mathcal{H}}_r = \frac{k}{\mu\omega} \sum_{l=1}^{\infty} i^l \frac{2l+1}{l(l+1)} (ib_l \mathbf{N}_{ol}^{(3)} + a_l \mathbf{M}_{el}^{(3)}) \quad (2.39)$$

$$\boldsymbol{\mathcal{E}}_t = \sum_{l=1}^{\infty} i^l \frac{2l+1}{l(l+1)} (c_l \mathbf{M}_{ol} - id_l \mathbf{N}_{el}) \quad (2.40)$$

$$\boldsymbol{\mathcal{H}}_t = \frac{-\sqrt{\varepsilon_r} k}{\mu\omega} \sum_{l=1}^{\infty} i^l \frac{2l+1}{l(l+1)} (d_l \mathbf{M}_{el} + ic_l \mathbf{N}_{ol}). \quad (2.41)$$

For the transmitted fields the wavenumber is replaced by the wavenumber in the medium $\sqrt{\varepsilon_r} k$ in the prefactor for $\boldsymbol{\mathcal{H}}_t$ and in the vector spherical harmonics. For the incident and transmitted fields, Bessel function of first type (J_l) are required to assure finite solutions at $r \rightarrow 0$ as the Neumann and Hankel functions diverge at the origin. The reflected fields must vanish at infinity ($r \rightarrow \infty$) which is a property of the Hankel functions H_l . Their usage is denoted by the superscript (3) at the respective vector spherical harmonics in Eq. 2.38 and Eq. 2.39. The expansion coefficients for the reflected fields (a_l and b_l) and the transmitted fields (c_l and d_l) are calculated from the interface conditions

$$[\boldsymbol{\mathcal{E}}_i + \boldsymbol{\mathcal{E}}_r] \times \mathbf{e}_r = \boldsymbol{\mathcal{E}}_t \times \mathbf{e}_r \quad \text{and} \quad [\boldsymbol{\mathcal{H}}_i + \boldsymbol{\mathcal{H}}_r] \times \mathbf{e}_r = \boldsymbol{\mathcal{H}}_t \times \mathbf{e}_r \quad (2.42)$$

that reflect the continuity of the tangential fields at the surface of the sphere. Plugging the six expansions (Eq. 2.36 – Eq. 2.41) into the boundary conditions results in two pairs of inhomogeneous equations (one for the θ and ϕ components of each field). Solving this system yields the expansion coefficients

$$a_l = \frac{\varepsilon_r J_l(\sqrt{\varepsilon_r} \varrho) [\varrho J_l(\varrho)]' - J_l(\varrho) [\sqrt{\varepsilon_r} \varrho J_l(\sqrt{\varepsilon_r} \varrho)]'}{\varepsilon_r J_l(\sqrt{\varepsilon_r} \varrho) [\varrho H_l(\varrho)]' - H_l(\varrho) [\sqrt{\varepsilon_r} \varrho J_l(\sqrt{\varepsilon_r} \varrho)]'} \quad (2.43)$$

$$b_l = \frac{J_l(\sqrt{\varepsilon_r} \varrho) [\varrho J_l(\varrho)]' - J_l(\varrho) [\sqrt{\varepsilon_r} \varrho J_l(\sqrt{\varepsilon_r} \varrho)]'}{J_l(\sqrt{\varepsilon_r} \varrho) [\varrho H_l(\varrho)]' - H_l(\varrho) [\sqrt{\varepsilon_r} \varrho J_l(\sqrt{\varepsilon_r} \varrho)]'} \quad (2.44)$$

$$c_l = \frac{J_l(\varrho) [\varrho H_l(\varrho)]' - H_l(\varrho) [\varrho J_l(\varrho)]'}{J_l(\sqrt{\varepsilon_r}\varrho) [\varrho H_l(\varrho)]' - H_l(\varrho) [\sqrt{\varepsilon_r}\varrho J_l(\sqrt{\varepsilon_r}\varrho)]'} \quad (2.45)$$

$$d_l = \frac{\sqrt{\varepsilon_r} J_l(\varrho) [\varrho H_l(\varrho)]' - \sqrt{\varepsilon_r} H_l(\varrho) [\varrho J_l(\varrho)]'}{\varepsilon_r J_l(\sqrt{\varepsilon_r}\varrho) [\varrho H_l(\varrho)]' - H_l(\varrho) [\sqrt{\varepsilon_r}\varrho J_l(\sqrt{\varepsilon_r}\varrho)]'}, \quad (2.46)$$

where $[\dots]'$ denotes the derivative of the expression within the brackets with respect to the argument of the respective Bessel function. The coefficients signify that the linear near-field

$$\mathcal{E}^{\text{Mie}}(\mathbf{r}, \omega, R, \varepsilon_r) = \begin{cases} \mathcal{E}_i + \mathcal{E}_r & \text{for } r > R \\ \mathcal{E}_t & \text{for } r \leq R \end{cases} \quad (2.47)$$

at a dielectric sphere (for a given frequency) only depends on the relative permittivity ε_r of the sphere and the dimensionless propagation parameter

$$\varrho = kR = \frac{2\pi R}{\lambda} \quad (2.48)$$

that sets the sphere's radius R in proportion to the incident fields wavelength λ .

Spectral decomposition for finite pulses

The obtained Mie solutions \mathcal{E}^{Mie} reflect the spatial mode structure of the linear near-field for a single frequency. In order to describe the linear near-field of a sphere under finite laser pulses, the Mie solutions are combined with a spectral decomposition of the incident field. Therefore, the incident pulses are described by spectral mode decomposition based on the complex electric field in the Fourier domain

$$\mathcal{E}(\mathbf{r}, \omega) = \mathcal{E}_0 f(\omega) e^{i\mathbf{k}\mathbf{r}} e^{-i\varphi(\omega)}, \quad (2.49)$$

where \mathcal{E}_0 reflects the field's peak amplitude and with spectral amplitude profile $f(\omega)$, spectral phase $\varphi(\omega)$ and the spatial mode $e^{i\mathbf{k}\mathbf{r}}$. In this work, pulses are considered to have a Gaussian amplitude spectrum

$$f(\omega) = \frac{1}{\sigma_\omega} e^{-\frac{1}{2}\left(\frac{\omega-\omega_0}{\sigma_\omega}\right)^2} \quad (2.50)$$

with spectral width $\sigma_\omega = \frac{2\sqrt{\ln 2}}{\tau}$ defined by the full-width at half-maximum (FWHM) τ of the temporal intensity envelope. The spectral phase

$$\varphi(\omega) = \varphi_{\text{ce}} + \frac{\zeta}{2}(\omega - \omega_0)^2 \quad (2.51)$$

includes the CEP φ_{ce} and a linear chirp⁴ quantified by the chirp parameter ζ . Similar to the incident field, also the linear near-field of a sphere can be expressed via spectral decomposition when replacing the plane wave spatial modes by the previously discussed Mie-solutions.

The spatio-temporal evolution of the electric field is obtained by the Fourier transform

$$\mathcal{E}(\mathbf{r}, t) = \frac{1}{2} \frac{1}{\sqrt{2\pi}} \int_{-\infty}^{\infty} \mathcal{E}(\mathbf{r}, \omega) e^{-i\omega t} d\omega + c.c. \quad (2.52)$$

⁴Note that a linear temporal chirp corresponds to a parabolic spectral phase.

2. Theoretical framework

and allows to calculate the local instantaneous field strength. In the numerical simulations, the integral is evaluated by discretizing frequency space (see Fig. 2.2(a)) such that all relevant spectral components are included and with spectral resolution $\Delta\omega$ being sufficiently small to suppress short revival times $\Delta T_{\text{rev}} = 2\pi/\Delta\omega$ of the pulses (cf. Fig. 2.2(b)).

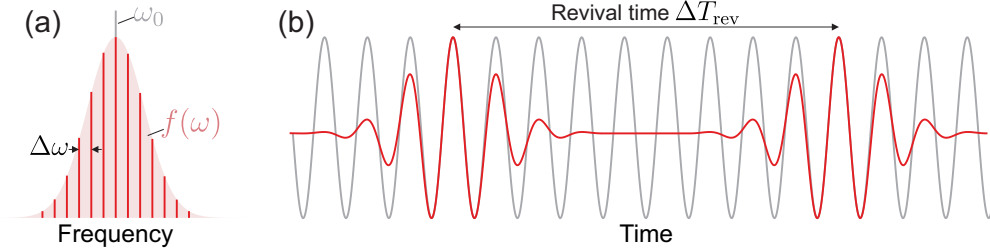


Figure 2.2. Schematic representation of the spectral pulse decomposition. **(a)** Spectral profile $f(\omega)$ of a finite pulse (red shaded) and for a continuous wave (gray line). Red lines visualize the discretization for the numerical implementation. The spectral resolution $\Delta\omega = 2\pi/\Delta T_{\text{rev}}$ determines the revival time ΔT_{rev} of the corresponding pulses in the time-domain. Please note that recurring pulses are only an artifact of the discretization. In the continuous limit $\Delta\omega \rightarrow 0$ the revival time becomes infinite, i.e. the spectrum $f(\omega)$ corresponds to one isolated pulse. **(b)** Corresponding time-dependent fields.

The instantaneous NIR near-field is calculated when evaluating tunnel ionization (cf. Sec. 2.3.1) and for the integration of the classical trajectories (cf. Sec. 2.4). The evaluation of XUV-induced photoionization (cf. Sec. 2.3.2) also requires the instantaneous spectral profile. Therefore, the combined spectral and temporal evolution of the local intensity is characterized by the Wigner distribution [92–94]

$$W(\mathbf{r}, t, \omega) = \frac{\varepsilon_0 c_0}{2} \frac{1}{2\pi} \int_{-\infty}^{\infty} \mathcal{E}(\mathbf{r}, \omega + \frac{\omega'}{2}) \mathcal{E}^*(\mathbf{r}, \omega - \frac{\omega'}{2}) e^{-i\omega' t} d\omega'. \quad (2.53)$$

Typical Wigner distributions for unchirped and chirped XUV pulses propagating in vacuum are visualized in Fig. 2.3(a,b). While the distribution is symmetric in the unchirped case, the Wigner distribution for the chirped pulse exhibits a clear distortion that can be quantified via the spectral and temporal centers of mass (dashed and solid black curves). The latter reflects the spectral arrival time $\Delta t_{\text{vac}}^{\text{XUV}}(E_{\text{ph}})$ of the intensity envelope and reveals that low frequency components arrive before high frequency components for the selected chirp. In the unchirped case all frequency components arrive at the same time. The local intensity evolution (Fig. 2.3(c,d)) and spectral intensity profile (Fig. 2.3(e))

$$I(\mathbf{r}, t) = \int_{-\infty}^{\infty} W(\mathbf{r}, t, \omega) d\omega \quad (2.54)$$

$$I(\mathbf{r}, \omega) = \int_{-\infty}^{\infty} W(\mathbf{r}, t, \omega) dt \quad (2.55)$$

follow from frequency and time integration over the respective Wigner distributions. The Wigner distributions will be used to evaluate the spectral photoionization rate (cf. Sec. 2.3.2) and to analyze the impact of the XUV chirp on the attosecond streaking from nanospheres (cf. Sec. 6.2.3).

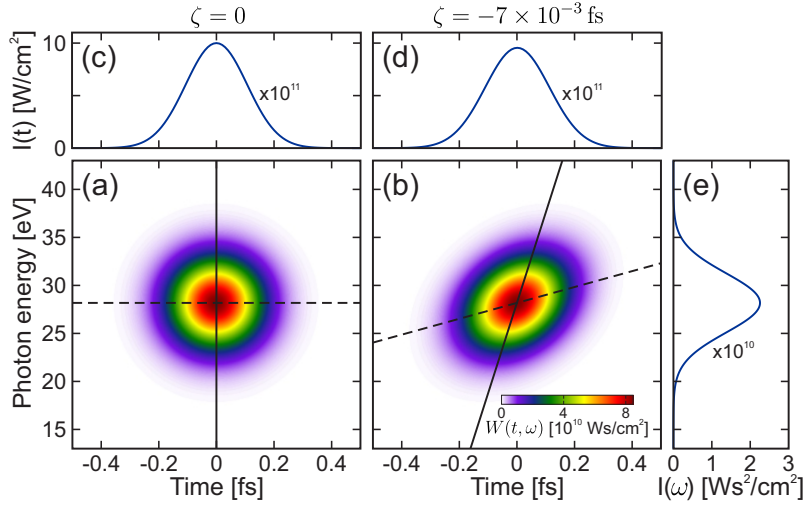


Figure 2.3. Wigner distributions. (a,b) Wigner distributions for unchirped (a) and chirped (b) $\tau = 250$ as XUV pulses at photon energy $\hbar\omega_0 = 28$ eV sampled at the origin. Solid and dashed black curves indicate the temporal and spectral centers of mass, respectively. (c,d) Corresponding intensity evolutions. (e) Spectral intensity profiles (identical for both pulses).

2.2.2. The nonlinear mean-field

So far, only the strategy for evaluating the linear near-field at a neutral dielectric sphere under an external laser field has been described. However, free charges (liberated electrons and residual ions) that are generated upon ionization of the sphere generate two additional nonlinear contributions to the near-field: First, the Coulomb fields among the free charges and second, the additional polarization of the dielectric sphere mediated by the free charges. In this work, the interaction of free charges is evaluated in mean-field approximation. Hence, evaluating both Coulomb interaction and sphere polarization requires to solve the second set of Maxwell equations (Eq. 2.11 – Eq. 2.14). Under the assumption that field retardation effects are negligible for the considered scenarios this problem can be treated in electrostatic approximation. In this case the problem reduces to finding solutions to the divergence equation for the electric displacement field that (using Eq. 2.15 and Eq. 2.17) can be expressed as

$$\nabla \cdot \mathbf{D} = \rho_f. \quad (2.56)$$

When considering the dielectric sphere as a linear medium with spatially inhomogeneous permittivity $\varepsilon_r(\mathbf{r})$ (such that $\mathbf{D} = \varepsilon_0 \varepsilon_r(\mathbf{r}) \mathbf{E}$, cf. Eq. 2.23), the divergence equation can be written in the form

$$\nabla \cdot [\varepsilon_r(\mathbf{r}) \mathbf{E}] = \frac{\rho_f}{\varepsilon_0}. \quad (2.57)$$

For a homogeneous dielectric sphere with radius R and surrounded by vacuum the relative permittivity can be written as

$$\varepsilon_r(\mathbf{r}) = \begin{cases} \varepsilon_r & \text{for } r \leq R \\ 1 & \text{for } r > R \end{cases} \quad (2.58)$$

and leads to the two divergence equations

$$\nabla \cdot \mathbf{E}_{\text{out}} = \frac{\rho_f}{\varepsilon_0} \quad (2.59)$$

$$\nabla \cdot \mathbf{E}_{\text{in}} = \frac{\rho_f}{\varepsilon_0 \varepsilon_r} \quad (2.60)$$

for the fields outside and inside of the sphere, respectively. In electrostatic approximation, where the electric field is conservative, introducing the electrostatic potential $\Phi(\mathbf{r})$ via $\mathbf{E} = -\nabla\Phi$ leads to the two corresponding Poisson equations

2. Theoretical framework

$$\Delta\Phi_{\text{out}} = -\frac{\varrho_f}{\varepsilon_0} \quad (2.61)$$

$$\Delta\Phi_{\text{in}} = -\frac{\varrho_f}{\varepsilon_0\varepsilon_r}. \quad (2.62)$$

The electrostatic potential is generated by the free charges and also includes the static polarization of the medium induced by the free charges via the relative permittivity. It has to fulfill the respective Poisson equation in and outside of the sphere and must match the interface conditions⁵

$$\Phi_{\text{in}}(\mathbf{R}) = \Phi_{\text{out}}(\mathbf{R}) \quad (2.63) \quad \varepsilon_r \frac{\partial}{\partial r} \Phi_{\text{in}}(\mathbf{R}) = \frac{\partial}{\partial r} \Phi_{\text{out}}(\mathbf{R}) \quad (2.64)$$

at the surface. In the following, an efficient approximate solution to the Poisson equation via high-order multipole expansion, the matching at the interface, and the numerical aspects of the implementation are briefly outlined.

Solution to the Laplace equation in spherical coordinates

An electrostatic potential $\Phi(\mathbf{r})$ that is a solution to the Poisson equation Eq. 2.61 also has to solve the Laplace equation $\Delta\Phi = 0$ at any point where $\varrho_f = 0$. Therefore, instead of directly solving the Poisson equation, it is convenient to first find a solution to the Laplace equation. A separation ansatz similar to Eq. 2.32 yields that the formal solution of the Laplace equation (in spherical coordinates) can be expressed as the series expansion

$$\Phi(\mathbf{r}) = \sum_{l=0}^{\infty} [A_l r^l + B_l r^{-(l+1)}] P_l(\cos\theta), \quad (2.65)$$

where $P_l(\cos\theta)$ are the Legendre polynomials and θ reflects the angle between \mathbf{r} and the z -axis. The expansion coefficients A_l and B_l depend on the boundary conditions of the particular problem.

Potential of a point charge as series expansion

To derive the potential of a free point charge q_i located at \mathbf{r}_i within a homogeneous medium with permittivity ε_r , the expansion coefficients A_l and B_l can be evaluated by matching the solution of the Laplace equation to the electrostatic potential following from Coulomb's law $\Phi(r) = \frac{1}{4\pi\varepsilon_0\varepsilon_r} \frac{q_i}{|r-r_i|}$. The obtained potential solves the Poisson equation and can be expressed via

$$\Phi(\mathbf{r}, \mathbf{r}_i) = \frac{q_i}{4\pi\varepsilon_0\varepsilon_r} \sum_{l=0}^{\infty} \frac{r_{<}^l}{r_{>}^{l+1}} P_l(\cos\theta_{rr_i}). \quad (2.66)$$

In this notation, the subscripts $<$ and $>$ indicate the respective smaller and larger radius, i.e. $r_{<} = r$ and $r_{>} = r_i$ for $r < r_i$ and vice versa. The angle θ_{rr_i} reflects the angle between the vectors to the charge and the sample point. Following from the solution for a single point charge, the solution for an ensemble of n point charges q_i located at \mathbf{r}_i is given by

⁵These conditions follow directly from the well-known interface conditions of Maxwell's equations $\mathbf{e}_r \times (\mathcal{E}_{\text{out}} - \mathcal{E}_{\text{in}}) = 0$ and $\mathbf{e}_r \cdot (\mathbf{D}_{\text{out}} - \mathbf{D}_{\text{in}}) = 0$ (in the absence of surface charges).

superposition of the individual potentials

$$\Phi(\mathbf{r}) = \sum_{i=0}^n \Phi(\mathbf{r}, \mathbf{r}_i) \quad (2.67)$$

$$= \frac{1}{4\pi\epsilon_0\epsilon_r} \sum_{l=0}^{\infty} \left[\sum_{\substack{r_i \leq r \\ r_i \leq R}} q_i \frac{r_i^l}{r^{l+1}} + \sum_{\substack{r_i > r \\ r_i > R}} q_i \frac{r^l}{r_i^{l+1}} \right] P_l(\cos \theta_{rr_i}), \quad (2.68)$$

where the left and right sum within the brackets include all charges with $r_i \leq r$ and $r_i > r$, respectively.

Transition to the potential in the vicinity of a dielectric sphere

Having found a particular solution of Poisson's equation for point charges within a homogeneous medium, the remaining task is to derive the solution for a distribution of point charges in and outside of a dielectric sphere that is surrounded by vacuum. In order to fulfill the interface conditions at the sphere surface, the solution is constructed from the particular solution of Poisson's equation (Eq. 2.68) and the general solution of Laplace's equation (Eq. 2.65). As the solution needs to vanish for $r \rightarrow \infty$, the coefficient A_l in Eq. 2.65 must be zero when sampling the potential outside of the sphere (due to the r^l dependence of the respective term). Similarly, B_l needs to be zero when sampling the inside potential to ensure finite solutions for $r \rightarrow 0$. With these requirements, the constructed solutions for the potential in- and outside of the sphere read

$$\Phi_{\text{in}}(\mathbf{r}) = \sum_{l=0}^{\infty} \left[\underbrace{\sum_{\substack{r_i \leq R \\ r_i \leq r}} \frac{q_i}{4\pi\epsilon_0\epsilon_r} \frac{r_i^l}{r^{l+1}} + \sum_{\substack{r_i \leq R \\ r_i > r}} \frac{q_i}{4\pi\epsilon_0\epsilon_r} \frac{r^l}{r_i^{l+1}}}_{\text{charges inside}} + \sum_{r_i \leq R} A_{l,i} r^l + \underbrace{\sum_{r_i > R} C_{l,i} r^l}_{\text{charges outside}} \right] P_l(\cos \theta_{rr_i}) \quad (2.69)$$

and

$$\Phi_{\text{out}}(\mathbf{r}) = \sum_{l=0}^{\infty} \left[\underbrace{\sum_{\substack{r_i > R \\ r_i \leq r}} \frac{q_i}{4\pi\epsilon_0} \frac{r_i^l}{r^{l+1}} + \sum_{\substack{r_i > R \\ r_i > r}} \frac{q_i}{4\pi\epsilon_0} \frac{r^l}{r_i^{l+1}}}_{\text{charges outside}} + \sum_{r_i > R} D_{l,i} r^{-(l+1)} + \underbrace{\sum_{r_i \leq R} B_{l,i} r^{-(l+1)}}_{\text{charges inside}} \right] P_l(\cos \theta_{rr_i}). \quad (2.70)$$

The four expansion coefficients

$$A_{l,i} = \frac{q_i}{4\pi\epsilon_0} \frac{(l+1)(\epsilon_r - 1)}{(1 + \epsilon_r)l + 1} \frac{r_i^l}{R^{2l+1}} \quad (2.71) \quad C_{l,i} = \frac{q_i}{4\pi\epsilon_0} \frac{2l+1}{(1 + \epsilon_r)l + 1} \frac{1}{r_i^{l+1}} \quad (2.73)$$

$$B_{l,i} = \frac{q_i}{4\pi\epsilon_0} \frac{2l+1}{(1 + \epsilon_r)l + 1} r_i^l \quad (2.72) \quad D_{l,i} = \frac{q_i}{4\pi\epsilon_0} \frac{l(1 - \epsilon_r)}{(1 + \epsilon_r)l + 1} \frac{R^{2l+1}}{r_i^{l+1}} \quad (2.74)$$

can be derived from the interface conditions (Eq. 2.63 and Eq. 2.64). With these coefficients, the potential for a given distribution of charges and thus also the mean-field $\mathcal{E}_{\text{mf}}(\mathbf{r}) = -\nabla\Phi(\mathbf{r})$ can be calculated at any point \mathbf{r} . Obviously, this requires the summation over

2. Theoretical framework

all charges and one evaluation of the Legendre polynomial $P_l(\cos \theta_{rr_i})$ per charge which is numerically particularly demanding. In a typical simulation, where the potential needs to be evaluated at the positions of all n charges, the direct evaluation of the potential thus results in unfeasible numerical effort of the order $\mathcal{O}(n^2)$. The strategy for a more efficient numerical implementation is based on lookup tables (LUTs) and is now briefly outlined. The Legendre polynomials can be written as

$$P_l(\alpha_i) = \sum_{s=0}^{l/2} (-1)^s \underbrace{\frac{(2l-2s)!}{(l-s)! (l-2s)! s! 2^l}}_{L_{ls}} \alpha_i^k, \quad (2.75)$$

with $\alpha_i = \cos(\theta_{rr_i}) = \frac{xx_i + yy_i + zz_i}{rr_i}$ and $k = l - 2s$. Hence, the only task is to evaluate α_i^k which can be achieved via the multinomial expansion

$$\alpha_i^k = \left(\frac{xx_i + yy_i + zz_i}{rr_i} \right)^k \quad (2.76)$$

$$= \sum_{q=0}^k \sum_{p=0}^q \underbrace{\binom{k}{q} \binom{q}{p}}_{M_{kqp}} \frac{x^{k-q} y^{q-p} z^p}{r^k} \frac{x_i^{k-q} y_i^{q-p} z_i^p}{r_i^k}, \quad (2.77)$$

with the multinomial coefficient $M_{kqp} = \frac{k!}{(k-q)!(q-p)!p!}$. Using this, the first term of the potential in Eq. 2.69 (this term is chosen here for simplicity, all other terms follow analogously) can be written in the form

$$\Phi_{\text{in}}^1(\mathbf{r}) = \frac{1}{4\pi\epsilon_0\epsilon_r} \sum_{l=0}^{\infty} \sum_{s=0}^{l/2} \sum_{q=0}^{k=l-2s} \sum_{p=0}^q L_{ls} M_{kqp} \frac{x^{k-q} y^{q-p} z^p}{r^{l+k+1}} \underbrace{\sum_{\substack{r_i \leq R \\ r_i \leq r}} q_i \frac{x_i^{k-q} y_i^{q-p} z_i^p}{r_i^{k-l}}}_{S_{lkqp}(r)}. \quad (2.78)$$

This representation reveals why the multipole expansion is very attractive for numerical simulations. In principle, all variables related to the charges (x_i, y_i, z_i and q_i) are 'decoupled' from the position where the potential is evaluated (x, y and z). The only coupling appears in the summation, where in this case only charges with $r_i \leq r$ are taken into account. For a given distribution of charges, the sum $S_{lkqp}(r)$ for a specific set of $[l, k, q, p]$ only depends on the radial coordinate r . Hence, it is very convenient to precalculate $S_{lkqp}(r)$ in dependence of r , store the results in radial lookup tables, and extract the necessary table entry upon evaluation of the potential for a specific r . The strategy for the implementation is schematically sketched in Fig. 2.4 and visualizes the three required steps. First, all charges are injected into the lookup table, i.e. $q_i x_i^{k-q} y_i^{q-p} z_i^p / r_i^{k-l}$ is added to the respective radial bin for each charge. This operation obviously requires one loop through the full list of charges and thus scales linearly with the number of charges ($\mathcal{O}(n)$). In the second step, a cumulative sum of the LUT is calculated in order to reflect the summation over the charges with $r_i \leq r$ for each individual bin of the LUT. A second LUT containing the cumulative sum from the right needs to be calculated in order to store the summation over charges with $r_i > r$. Evaluation of the two cumulative sums requires to loop over the number of LUT entries, which is in typical simulations one or two orders of magnitude

2.2. Description of the spatio-temporal near-fields

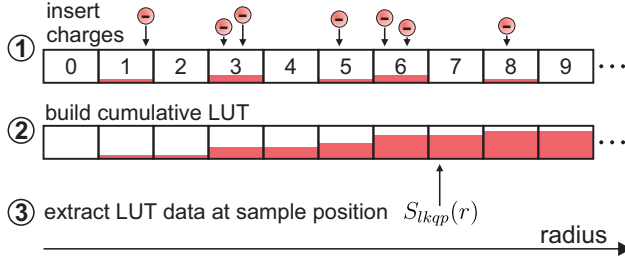


Figure 2.4. Sketch of the numerical implementation of the multipole expansion. First, all charges are injected into the respective LUT bins for their radii r_i . Second, a cumulative sum is built. Third, to evaluate the potential $\Phi(\mathbf{r})$ the required value of $S_{lkqp}(r)$ can be extracted from the respective bin of the cumulative LUT.

lower than the number of charges and thus negligible for the numerical effort. In the third step, upon evaluation of the potential at a given position \mathbf{r} the respective LUT entries are extracted. The evaluation of the potential for each charge in the simulation obviously also scales linear with the number of charges, such that the overall computational cost is of the order $\mathcal{O}(2n)$.

Numerical restrictions of the multipole expansion

The numerical implementation of the multipole expansion requires to cut the expansion at a finite maximal order l_{\max} . While a higher maximal order decreases truncation errors in the calculated mean-field, both calculation time and required physical memory increase rapidly since the number of required LUTs scales nonlinear with l_{\max} , see Fig. 2.5. Hence, the efficient numerical evaluation of the mean-field requires to determine the sweet-spot between accuracy and numerical effort. For the simulations in this work a maximal expansion order of $l_{\max} = 10$ was used and it was checked that all simulation results were converged with respect to the expansion order.

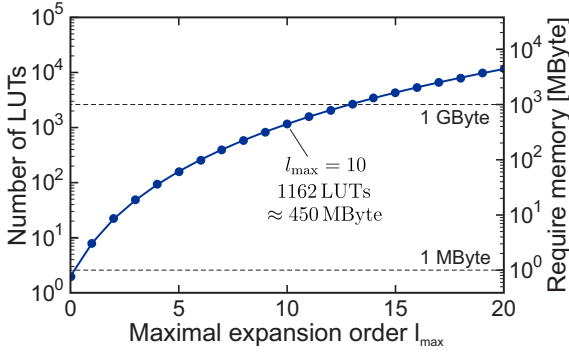


Figure 2.5. Total number of lookup tables in dependence of the maximal multipole expansion order (blue dots). The blue curve is a guide to the eye. The right axis indicates the corresponding required amount of physical memory for lookup tables with 50,000 entries (storing 64 bit double-precision floating-point values) as used in typical simulations. The dashed black lines indicate 1 MByte and 1 GByte of memory.

2.3. Field-driven ionization

When an atom is exposed to a laser field with photon energy $\hbar\omega$ larger than the atoms ionization energy I_p , the atom may be ionized by absorption of a single photon. Upon such single-photon ionization, an electron is liberated with excess energy $\hbar\omega - I_p$. If the photon energy is below the ionization energy, absorption of a single photon is insufficient to lift a bound electron into the continuum. However, when applying strong laser fields, ionization is still possible. In this case the typical picture to describe the ionization mechanism depends strongly on the laser intensity I_0 . For low intensities, where the strength of the laser electric field is small compared to the field that binds the electron to its ion, the absorption of n photons is necessary to overcome the binding potential ($n\hbar\omega > I_p$), see Fig. 2.6(a). This multiphoton ionization can be described conveniently by means of perturbation theory that predicts an ionization rate proportional to I_0^n .

The perturbative picture breaks down when the electric field strengths of laser and ion become comparable. In this case, the effective potential $V_{\text{eff}} = V_{\text{ion}} + V_{\text{las}}$ formed by the combined ionic potential V_{ion} and the potential V_{las} mediated by the laser field, can be substantially deformed such that a finite barrier is formed, see Fig. 2.6(b). The probability for a bound electron to tunnel through this barrier depends mainly on the shape of the potential and particularly on the barrier width. For arbitrary shapes the respective ionization rate can be derived within WKB approximation. For atomic tunneling a widely utilized tunneling rate has been derived by Ammosov, Delone and Krainov [95], where the respective ADK rate⁶ $\Gamma^{\text{ADK}} \sim \exp\left(-\frac{2^{5/2}I_p^{3/2}}{3\mathcal{E}}\right)$ scales highly nonlinear with the field-strength.

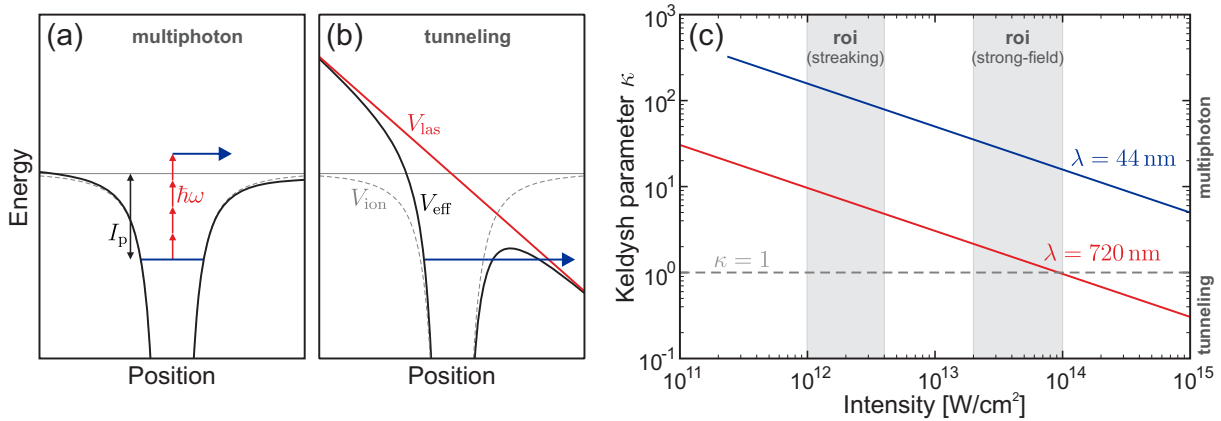


Figure 2.6. Photoionization regimes. (a) Multiphoton regime, where electrons are liberated from the ionic potential (dashed black) by absorption of multiple photons (red arrows). The laser field only acts as a weak perturbation to the ionic field, resulting in an almost unperturbed effective potential (solid black). (b) Tunneling regime, where the strong laser field deforms the ionic potential creating a finite tunneling barrier in the effective potential. (c) Keldysh parameter κ in dependence of laser intensity for $I_p = 9$ eV for two wavelength (as indicated). The dashed gray line separates the multiphoton regime ($\kappa \gg 1$) and the tunneling regime ($\kappa \lesssim 1$). Gray areas indicate the regions of interest (roi) for the strong-field and streaking scenarios considered in this work.

⁶Note that the rate is given in atomic units.

Atomic photoemission is often described following the famous work of Keldysh [1] that connects the regimes of multiphoton ionization and ionization via field-induced tunneling. Introducing the dimensionless Keldysh parameter

$$\kappa = \sqrt{\frac{I_p}{2U_p}}, \quad (2.79)$$

that sets the relevant energy scales of atom (I_p) and laser field (U_p) into proportion, allows to roughly estimate the relevant regime for a specific scenario. Typically, ionization is treated in the multiphoton regime for $\kappa \gg 1$, while tunneling is considered for $\kappa \lesssim 1$.

Near-field driven ionization in dielectric nanospheres

In M³C, atomic ionization is considered for a convenient description of the ionization of the initially neutral dielectric spheres. Potential ionization sites are sampled randomly within the sphere volume and the ionization probability is determined from the local near-field. For the scenarios investigated in this work, the XUV near-field is considered to drive single-photon ionization with the respective rate scaling proportional to the local instantaneous intensity. Ionization by the combined NIR near-field and the nonlinear mean-field is treated in the tunneling picture and the ionization probability is determined from the ADK rate calculated from the local instantaneous near-field. These assumptions are substantiated by the respective Keldysh parameters at the relevant laser wavelength and for the considered intensities, see Fig. 2.6(c). Here, an effective ionization energy of $I_p = 9$ eV is assumed to approximate the wide band gap of the SiO₂ nanoparticles (cf. Fig. 2.7). For the strong-field simulations, NIR pulses with peak intensities around 10¹³ W/cm² are considered, corresponding to a Keldysh parameter close to unity when taking into account a field enhancement of (≈ 2) at the nanosphere surface (cf. red curve and right shaded area in Fig. 2.6(c)). For the attosecond streaking simulations, both fields have intensities of around 10¹² W/cm². For these intensities NIR-driven tunneling can be safely neglected due to vanishing ionization probabilities. Ionization from the XUV near-field can be treated in the multiphoton regime as the respective Keldysh parameter is > 100 (cf. blue curve and left shaded area in Fig. 2.6(c)).

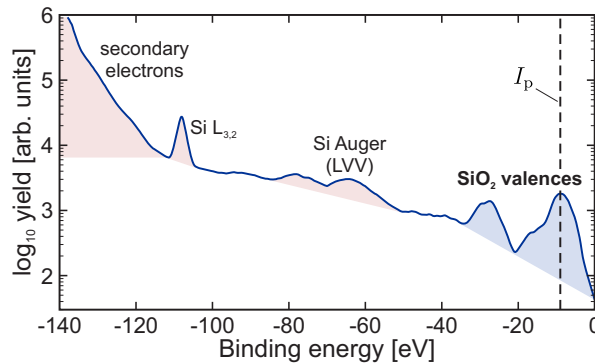


Figure 2.7. Photoelectron spectrum measured for 50 nm SiO₂ nanoparticles under soft X-rays at photon energy $\hbar\omega = 137.9$ eV. The vertical dashed line indicates the effective ionization energy of around 8.5 – 9 eV as considered for the semi-classical simulations. Adapted from [96].

2.3.1. Tunnel ionization

For the intensities considered in this work, the description of tunnel ionization in the dielectric nanospheres is restricted to tunneling from the surface into the surrounding vacuum. Tunneling within the volume can be neglected, as the local field strengths within the spheres are substantially lower and the tunneling probabilities vanish due to the highly nonlinear ADK rate. In the atomic case, the starting point of a classical electron trajectory is typically chosen as the classical tunneling exit $x_{te} = I_p/|\mathcal{E}_{las}|$ (see dashed black curve and blue arrow in Fig. 2.8) and their statistical weight is determined by the tunneling probability calculated from the lased field.

For an atom that is located close to the surface within a dielectric material (see Fig. 2.8) the case is fundamentally different. Here, the effective potential that provides the tunneling barrier is determined by the local near-field instead of the laser field alone. When considering only an enhanced linear near-field, the effective potential exhibits a steeper slope in the vacuum region (compare solid red to dashed black curve in Fig. 2.8). This results in (i) a shorter classical tunneling exit and (ii) an increased tunneling probability. For this reason, tunneling can be expected to be most pronounced at localized field hot spots at the nanosphere surface. Taking into account the full near-field (linear near-field & mean-field, see blue curve in Fig. 2.8) can result in a reduced tunneling probability and may even lead to complete quenching of tunnel ionization if the mean-field becomes comparable to the linear near-field. Most importantly, the simple straight-forward approach to determine the classical tunneling exit and the tunneling rate from the laser field breaks down. Therefore, in the simulations the tunneling path is sampled along the effective near-field (cf. blue curve in Fig. 2.8(b)) and the tunneling exit and tunneling rate are determined from the average field along the path.

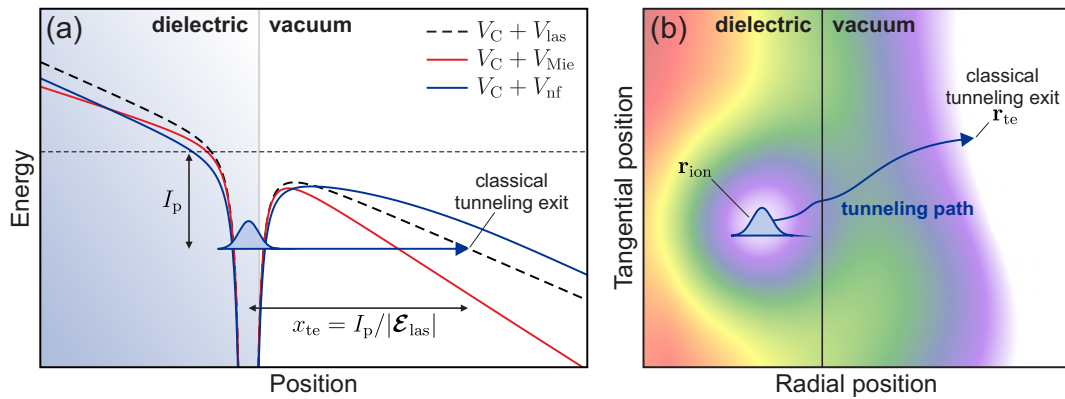


Figure 2.8. Schematic representation of tunneling from the surface of a dielectric. (a) The dashed black curve reflects the effective potential for the atomic case (Coulomb + Laser), cf. Fig. 1.1. Solid red and blue curves represent the effective potentials when considering the enhanced linear (Mie) near-field and the full near-field for an atom located near the surface of a dielectric, respectively. (b) Visualization of the potential landscape at the surface of a dielectric in a 2D-cut (false color plot). The blue curve illustrates the tunneling path ending at the classical tunneling exit.

2.3.2. Photoionization

Photoionization is implemented via Monte-Carlo sampling of the photoionization rate at randomly sampled points inside the sphere. In order to account for the spectral width and the chirp of the attosecond XUV pulses the local instantaneous total photoionization rate

$$\Gamma(\mathbf{r}, t) = \int_{-\infty}^{\infty} \gamma(\omega, \mathbf{r}, t) d\omega, \quad (2.80)$$

is determined from the spectral photoionization rate

$$\gamma(\omega, \mathbf{r}, t) = \frac{\sigma(\omega)W(\mathbf{r}, t, \omega)}{\hbar\omega}. \quad (2.81)$$

Here, the Wigner distribution $W(\mathbf{r}, t, \omega)$ reflects the spectral intensity profile of the XUV pulse. Further, the spectral rate depends on the spectral molecular photoionization cross section⁷

$$\sigma(\omega) = \frac{2n_i\omega}{n_{\text{mol}}c_0} \quad (2.82)$$

that can be extracted from the extinction coefficient n_i (i.e. the imaginary part of the complex refractive index $n = n_r + in_i$, see Fig. 2.9) and includes the density n_{mol} of potential ionization sites. Here, a molecular density of $n_{\text{mol}} = 0.022 \text{ \AA}^{-3}$ is considered to reflect the density of effective SiO₂ 'molecules' within a silica sphere. Upon a successful ionization event the initial energy of the generated electron is sampled randomly according to the local instantaneous spectral intensity and reduced by the ionization energy. The direction of the corresponding initial momentum is initialized randomly.

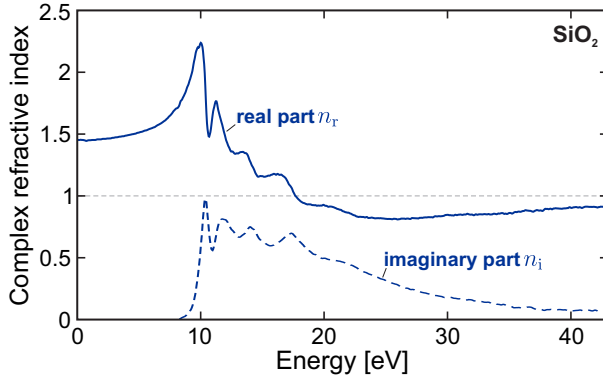


Figure 2.9. Energy-dependent complex refractive index $n = n_r + in_i$ of SiO₂ in the relevant energy range as considered for the attosecond streaking simulations. Solid and dashed blue curves reflect the real and imaginary parts, as indicated. Adapted from [97].

2.4. Propagation and scattering of photoelectrons

Photoelectron trajectories are calculated via integration of the classical equation of motion

$$m\ddot{\mathbf{r}} = -e\mathcal{E}_{\text{nf}}(\mathbf{r}, t), \quad (2.83)$$

where the effective electron mass m is considered to be m_e in the relevant energy range [98] and $\mathcal{E}_{\text{nf}}(\mathbf{r}, t) = \mathcal{E}_{\text{NIR}}(\mathbf{r}, t) + \mathcal{E}_{\text{mf}}(\mathbf{r}, t)$ is the effective near-field including contributions

⁷The derivation of the spectral photoionization rate is given in Appendix B.

2. Theoretical framework

from the NIR near-field and the charge interaction induced mean-field. The Lorentz force $\mathbf{F}_L = -e\mathbf{v} \times \mathbf{B}$ is neglected in Eq. 2.83 as the impact of magnetic fields becomes relevant only for much higher intensities, where relativistic effects start to play a role.

The numerical integration is performed utilizing the well-known Velocity-Verlet algorithm [99, 100] that follows directly from Taylor expanding the position and momentum vectors of a charge around time $t + \Delta t$, yielding

$$\mathbf{r}(t + \Delta t) = \mathbf{r}(t) + \underbrace{\frac{\partial \mathbf{r}}{\partial t}}_{\mathbf{p}/m} \Delta t + \frac{1}{2} \underbrace{\frac{\partial^2 \mathbf{r}}{\partial t^2}}_{\mathbf{F}/m} \Delta t^2 + \mathcal{O}(\Delta t^3) \quad (2.84)$$

for the position and

$$\mathbf{p}(t + \Delta t) = \mathbf{p}(t) + \underbrace{\frac{\partial \mathbf{p}}{\partial t}}_{\mathbf{F}} \Delta t + \frac{1}{2} \underbrace{\frac{\partial^2 \mathbf{p}}{\partial t^2}}_{\partial \mathbf{F} / \partial t} \Delta t^2 + \mathcal{O}(\Delta t^3) \quad (2.85)$$

for the momentum, respectively. It is obvious that the position can be updated directly, since the right hand side of Eq. 2.84 only depends on the time t . The momentum update, however, requires evaluating the time-derivative of the force which can be expressed via the Taylor expansion

$$\frac{\partial \mathbf{F}}{\partial t} = \frac{\mathbf{F}(t + \Delta t) - \mathbf{F}(t)}{\Delta t} + \mathcal{O}(\Delta t) \quad (2.86)$$

and depends on the force at the new time step $t + \Delta t$. Thus, in every time step of the classical simulations the Velocity-Verlet scheme requires the three successive steps of (i) updating the positions of all charges, (ii) calculating the forces at these new positions (i.e. recalculating the local near-fields), and (iii) updating all momenta.

2.4.1. Description of electron scattering in dielectrics

For electrons propagating inside the dielectric sphere, elastic and inelastic electron-atom collisions are taken into account as instantaneous scattering events and are treated via Monte Carlo methods. Therefore, both scattering processes are quantified via their respective energy-dependent mean free paths (MFP)

$$L_{\text{el/inel}}(E) = \frac{1}{n_{\text{mol}} \sigma_{\text{el/inel}}(E)} \quad (2.87)$$

that describe the average distance an electron propagates between two adjacent collision events (of the same type) and that depend on the respective scattering cross sections $\sigma_{\text{el/inel}}$ and the density of scattering centers n_{mol} . The MFPs are directly related to the corresponding scattering times

$$\tau_{\text{el/inel}}(E) = \frac{L_{\text{el/inel}}(E)}{v(E)} \quad (2.88)$$

that quantify the time it takes an electron to travel the mean free path at a given velocity v . For the numerical implementation, the effective mean free path

$$L_{\text{eff}} = \left(\frac{1}{L_{\text{inel}}} + \frac{1}{L_{\text{el}}} \right)^{-1} \quad (2.89)$$

that characterizes the average distance between two collisions of arbitrary kinds is considered for the Monte Carlo sampling as follows. During the integration of a trajectory inside the material, in each time step a streaming length $L_{\text{stream}} = L_{\text{eff}} \ln\left(\frac{1}{1-r}\right)$ is calculated, where r is sampled from a uniform distribution in the interval $[0, 1]$. This streaming length characterizes the travel distance until the next collision for that specific trajectory. For an ensemble of trajectories the distribution of streaming lengths thus decays with $e^{-\frac{l}{L_{\text{eff}}}}$ to reflect the statistics of scattering process. If the displacement $|\mathbf{r}(t + \Delta t) - \mathbf{r}(t)|$ predicted for a specific trajectory in the current time step is larger than the streaming length, a scattering event is evaluated. The type of scattering (elastic or inelastic) is sampled randomly, taking into account the scattering probabilities of the two possible branches. In the following, the scattering cross section for the elastic and inelastic collisions are discussed in more detail.

Elastic scattering

In general, elastic electron-atom collisions are fully quantified by the energy-dependent differential cross section (DCS) $\frac{d\sigma}{d\Omega}(E, \theta)$. The latter characterizes the probability of an incoming electron that impinges the differential area $d\sigma$ to be scattered into the differential solid angle element $d\Omega$, cf. Fig. 2.10(a). Here, cylindrical symmetry is considered, such that the azimuthal angle remains unchanged in the scattering process. To model elastic scattering within the materials investigated in this work, effective DCS are defined by superposition of the specific DCS of the relevant atoms⁸ that are weighted by the respective

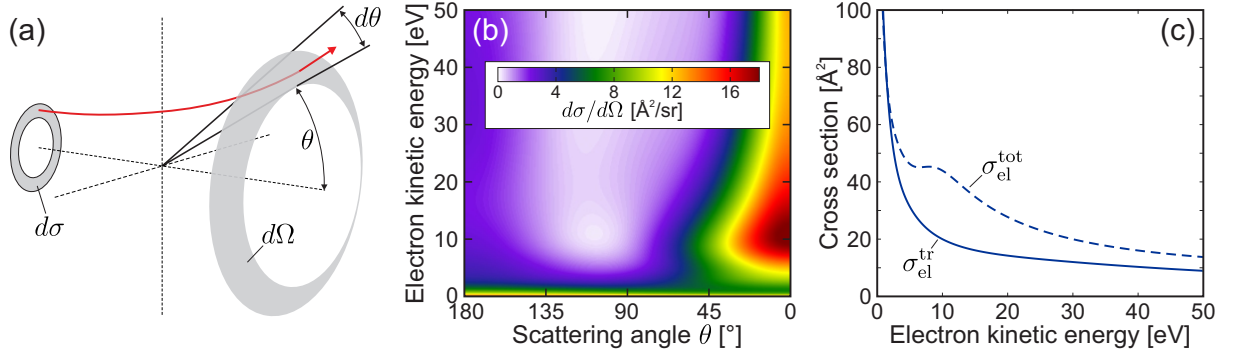


Figure 2.10. Elastic electron-atom collisions. (a) Schematic representation of the elastic scattering process. The red curve visualizes the deflected trajectory of an incoming electron that passes the cross section element $d\sigma$ and is scattered into the solid angle element $d\Omega$ under the angle θ . Adapted from [101]. (b) Effective differential cross section for SiO_2 in dependence of the incoming electron's energy E and the scattering angle θ . (c) Total (dashed) and transport (solid) cross sections corresponding to the DCS in (b).

⁸The atomic DCS are extracted from quantum mechanical electron-atom scattering simulations for the atomic potentials. The latter are calculated via density functional theory (DFT) including exchange and self-interaction correction.

2. Theoretical framework

stoichiometric ratios. For example, for SiO_2 the effective DCS follows from combining the specific DCS for silicon and oxygen, weighted by the ratio 1 to 2, see Fig. 2.10(b). In the limit of low energies of the incoming electrons ($E \lesssim 3 \text{ eV}$) the effective DCS is nearly constant, corresponding to isotropic scattering. For higher energies, forward scattering ($\theta \rightarrow 0$) dominates. The total scattering cross section

$$\sigma_{\text{el}}^{\text{tot}}(E) = \int \frac{d\sigma}{d\Omega}(E, \theta) d\Omega \quad (2.90)$$

follows from integration over the full solid angle $d\Omega$, see dashed curve in Fig. 2.10(c). For the numerical implementation of the anisotropic scattering processes, the MFP corresponding to the total scattering cross section is sampled. Upon an elastic scattering event the scattering angle is sampled randomly from the effective DCS.

For the scenarios presented in this work, however, it is sufficient to approximate the anisotropic scattering by an isotropic model scattering process⁹. This description is very convenient, as the latter is fully characterized by the transport cross section (solid curve in Fig. 2.10(c))

$$\sigma_{\text{el}}^{\text{tr}}(E) = \int \frac{d\sigma}{d\Omega}(E, \theta)(1 - \cos \theta) d\Omega \quad (2.91)$$

that reflects the same loss of forward momentum in the isotropic scattering process when compared to the anisotropic process with the corresponding total scattering cross section. Thus, when forward rescattering prevails the DCS, the transport cross section is smaller than the total cross section (compare solid to dashed curve for $E \gtrsim 3 \text{ eV}$ in Fig. 2.10(c)). Obviously, for smaller energies, both cross sections become similar, as the DCS becomes flat in this region, i.e. reflects isotropic scattering.

Inelastic scattering & impact ionization

In the range of kinetic energies relevant for the scenarios considered in this work, inelastic scattering of the free electrons inside the dielectric is dominated by interband

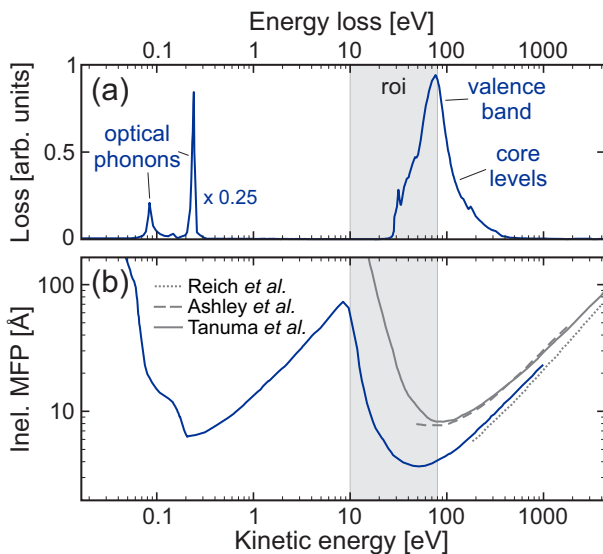


Figure 2.11. Inelastic electron scattering in SiO_2 . (a,b) Loss function (a) and inelastic mean free path (b) in SiO_2 in dependence of the electrons kinetic energy (blue curves). Adapted from Kuhr *et al.* [102]. Inelastic MFP data published by Tanuma *et al.* [103], Ashley *et al.* [104] and Reich *et al.* [105] is shown for comparison (gray curves, as indicated). The gray area indicates the energy region of interest for the scenarios studied in this work.

⁹For a comparison of simulation results for isotropic and anisotropic elastic scattering see Appendix C.

2.4. Propagation and scattering of photoelectrons

excitations [102], see gray areas in Fig. 2.11. These interband excitations are modeled via impact ionization of the effective SiO₂ molecules and the respective inelastic scattering cross section is calculated via the simplified Lotz-formula [106]

$$\sigma_{\text{inel}}(E) = s 450 (\text{\AA eV})^2 \frac{\log(E/I_p)}{EI_p}. \quad (2.92)$$

Here, E is the incoming electron's kinetic energy and $I_p = 9 \text{ eV}$ reflects the ionization potential to model the effective band gap of SiO₂ (cf. Fig. 2.7). The additional scaling factor s is varied to best reproduce the data of the streaking experiments, where optimal agreement is found for $s = 2.1$ (cf. Chapt. 6). Upon an inelastic scattering event, a new pair of one free electron and one residual ion is generated and the energy of the incoming electron is reduced by the effective ionization potential.

Finally, an overview of the scattering cross sections, mean free paths, and scattering times for both elastic and inelastic collisions as used in the semi-classical simulations for SiO₂ is provided in Fig. 2.12.

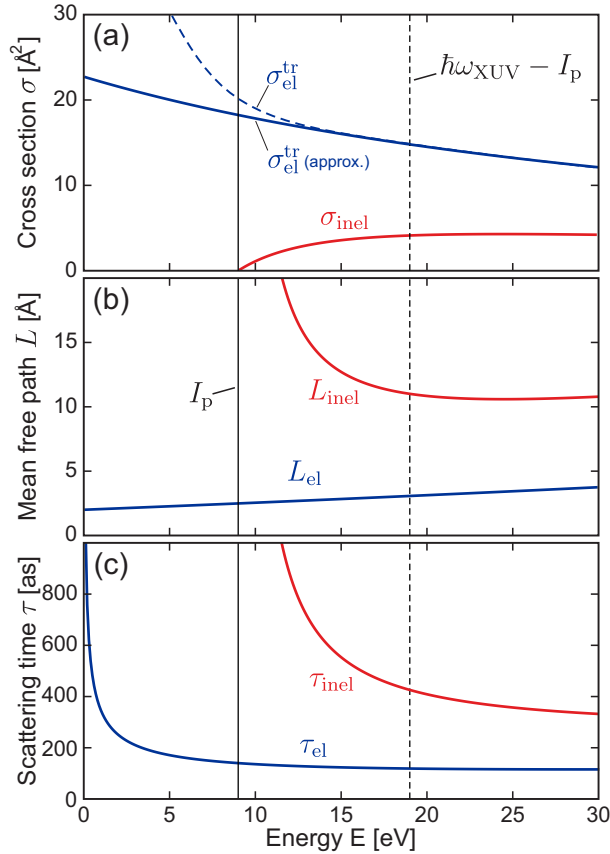


Figure 2.12. Scattering properties of SiO₂ as used in the M³C simulations. **(a-c)** Energy-dependent scattering cross sections (a), mean free paths (b), and scattering times (c) for the elastic (blue curves) and inelastic (red curves) collisions. The solid black line indicates the considered ionization energy of 9 eV. The dashed black line represents the mean initial energy of the generated photoelectrons in the attosecond streaking simulations. Note that the transport cross section for the elastic collisions has been artificially reduced for low energies (compare solid to dashed blue curve in (a), cf. Fig. 2.10(c)) in order to prevent rapid evaluation of elastic scattering in the numerical simulations. It was checked that the impact of this approximation on the relevant dynamics is negligible. Adapted from [LS7].

2.5. Numerical details: Optimization & Parallelization

Key requirement for investigating the scenarios presented in this thesis are (i) simulations with high statistics (i.e. sufficiently high numbers of photoelectron trajectories to generate smooth electron energy spectra) and (ii) scans over large parameter spaces (including for example laser intensity, wavelength, pulse length or phase as well as material, size, ionization energy, optical and scattering properties of the nanoparticles). To meet these requirements, the simulation code was thoroughly optimized. Most importantly, evaluating the local Mie- and mean-fields (which requires $\gtrsim 95\%$ of the overall calculation time in typical simulations) could be sped up by up to two orders of magnitude. To further benefit from the availability of high performance supercomputers, in addition to the optimizations the code was efficiently parallelized¹⁰. Therefore, in a simulation run the ensemble of trajectories is evenly split into N micro-ensembles that are distributed onto N processes. Thus, each process has to treat only a fraction $1/N$ of the total trajectories, reducing the numerically particularly 'expensive' evaluations of the near-fields by a factor $1/N$. However, when including charge interaction, each process needs to calculate the effective mean-field for the full ensemble.

The strategy for efficient combination of the multi-ensemble method with the mean-field solver is visualized schematically in Fig. 2.13 for the example of two micro-ensembles distributed on two parallel processes. For the multipole expansion, each process injects only 'its own' charges into the radial LUTs (depicted in blue and red). Before calculating the cumulative sums, the processes communicate the LUTs (by summation over all LUT entries) such that eventually the LUTs of all processes include all charges. This communication step is the main opponent for reaching high parallel efficiency, as the amount of data that needs to be communicated between the individual processes increases rapidly with the number of processes. Thus, efficient utilization of the available supercomputers required to identify the sweet spot for a speed up $S = T_1/T_N$ of the calculation time at a reasonable parallel efficiency S/N . Here, T_1 and T_N are the required calculation times using 1 and N processes, respectively. For typical simulations, the parallel efficiency decreases to around 50% for $N = 24$ processes (see Fig. 2.14) enabling efficient utilization

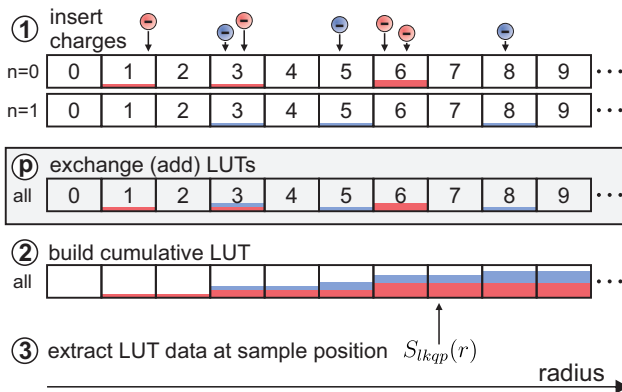


Figure 2.13. Schematic visualization of the parallel LUT-based multipole expansion (cf. Fig. 2.4). In step one, charges from two micro-ensembles (red and blue) are injected into respective LUTs handled by two parallel processes ($n = 0$ and 1). Before building cumulative LUTs in step two the LUTs of both processes are added in an intermediate communication step (gray area), such that both process have access to the full information (i.e. all charges).

¹⁰Here, MPI parallelization was used, where (in contrast to shared memory parallelization methods) each process operates on its own memory, such that all processes need to communicate the relevant data during the simulation.

of the supercomputers provided by the North-German Supercomputing Alliance¹¹ (HLRN) that exhibit hundreds of computation nodes with 24 processes, respectively. In scenarios where charge interaction is negligible (e.g. for the attosecond streaking¹² discussed in [Chapt. 6](#)) the simulations can be performed with 100 % parallel efficiency.

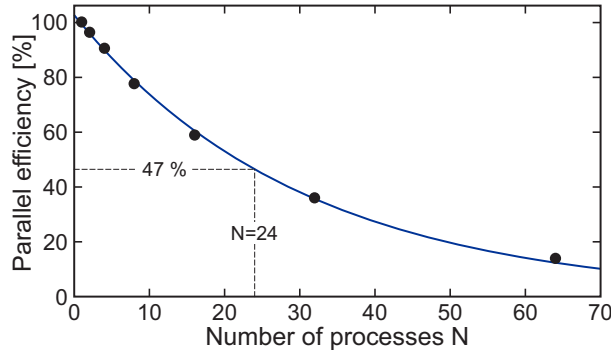


Figure 2.14. Parallel efficiency $S/N = T_1/(T_N N)$ in dependence of the number of utilized processes N for a typical M³C simulation run including charge interaction. Black dots show the results for $N = 2, 4, 8, 16, 32$ and 64 processes. The blue line is a guide to the eye.

Please note that M³C is based on the model described in [13, 14] and was extended to account for the physics relevant for this thesis. The utilized simulation code was implemented from scratch. Key modifications as compared to the previous model include:

- Mie description of the linear near-fields to account for field propagation, material dispersion and chirped pulses
- Efficient evaluation of the mean-field via high-order multipole expansion
- Improved description of surface tunneling
- XUV-photoionization
- Impact ionization
- Anisotropic elastic scattering
- Parallelization of the simulation code

¹¹<https://www.hlrn.de>

¹²For a comparison of streaking simulations ex- and including charge interaction see [Appendix D](#).

2.6. Simplified quantum description

For the comparison of quantum and classical features, in addition to classical SMM simulations and semi-classical M³C simulations, corresponding quantum simulations are performed by considering the one-dimensional single-electron TDSE

$$i\hbar \frac{\partial}{\partial t} \Psi(x, t) = \hat{H} \Psi(x, t). \quad (2.93)$$

Here, the Hamilton operator

$$\hat{H} = -\frac{\hbar^2}{2m} \frac{\partial^2}{\partial x^2} + V(x, t) \quad (2.94)$$

contains the effective potential $V(x, t) = V_0(x) + V_{\text{ext}}(x, t)$ including contributions from the time-independent ground state potential $V_0(x)$ and the external (typically laser-induced) time-dependent interaction potential $V_{\text{ext}}(x, t)$. The particular definitions for the potentials are given later. In the following, the strategy for the numerical solution of the TDSE, the preparation of the ground state, and the extraction of energy spectra is briefly discussed. Please note that the discussion is included here only for convenience as the utilized techniques are well-established, see e.g. [107].

2.6.1. Time evolution and Crank-Nicolson method

For the numerical treatment of the TDSE the wave function $\Psi(x, t)$ is discretized on a spatio-temporal grid. To distinguish the discretized wave function from the continuous one it is in the following denoted as Ψ_t^x , where the sub- and superscripts indicate the grid points in time and space, respectively. Further, for the description of electrons it is convenient to express the TDSE in atomic units (where $\hbar = m = 1$), such that the discretized TDSE reads

$$\frac{\partial}{\partial t} \Psi_t^x = -i\hat{H}\Psi_t^x. \quad (2.95)$$

Calculating the evolution of the discretized wave function in time requires an appropriate numerical time propagator. Typically, for TDSE calculations, the Crank-Nicolson propagator [108]

$$\Psi_{t+1}^x = \Psi_t^x + \left[-i\hat{H}\Psi_t^x - i\hat{H}\Psi_{t+1}^x \right] \frac{\Delta t}{2} \quad (2.96)$$

is the propagator of choice, as it is unitary, i.e. conserves the norm of the discretized wave function (up to numerical errors), and is unconditionally stable. Rearranging Eq. 2.96 yields the representation

$$\underbrace{\left[1 + \frac{i\hat{H}\Delta t}{2} \right]}_{\hat{A}^-} \Psi_{t+1}^x = \underbrace{\left[1 - \frac{i\hat{H}\Delta t}{2} \right]}_{\hat{A}^+} \Psi_t^x, \quad (2.97)$$

that nicely shows that the time propagation reduces to the two matrix operations $\tilde{\Psi} = \hat{A}^+ \Psi_t^x$ and $\hat{A}^- \Psi_{t+1}^x = \tilde{\Psi}$ where the propagation matrices \hat{A}^\pm follow from discretizing the Hamilton

operator. This can for example be done by using a three-point stencil (to numerically express the second derivative with respect to x) resulting in

$$\hat{H} = -\frac{1}{2\Delta x^2} \begin{pmatrix} -2 & 1 & & & & \\ 1 & -2 & 1 & & & \\ & & \ddots & \ddots & \ddots & \\ & & & 1 & -2 & 1 \\ & & & & 1 & -2 \end{pmatrix} + \begin{pmatrix} V^1 & & & & & \\ & V^2 & & & & \\ & & \ddots & & & \\ & & & V^{N-1} & & \\ & & & & V^N & \end{pmatrix}. \quad (2.98)$$

When implementing the numerical scheme, the spatial grid is chosen large enough to accommodate all spectral components that are relevant to the specific problem for a sufficiently long time to ensure convergence of the final electron spectra. Further, in order to prevent spurious reflections of the discretized wave function at the sides of the spatial grid, absorbing boundary conditions are implemented by including an imaginary potential with exponential increase towards the ends of the numerical arena [109]. The strength of the increase (i.e. the value of the exponent) is chosen such that the wave function is significantly damped before reaching the end of the grid but not notably reflected on the imaginary potential itself.

2.6.2. Ground state preparation via imaginary time propagation

Before propagating the wave function according to the TDSE, the initial wave function needs to be prepared. In this work, the latter is chosen to be the ground state wave function of the considered potential $V_0(x)$ and is determined via imaginary time propagation (see e.g. [107]). For the numerical implementation, the imaginary time propagation method is particularly convenient since the Crank-Nicholson scheme (when already implemented for solving the TDSE) can be reused with only substituting the time step $\Delta t \rightarrow -i\Delta t$. The initial wave function for the imaginary time propagation can be chosen randomly and higher bound states can also be determined successively by projecting out the previously determined lower energy states during the propagation.

2.6.3. Extracting energy spectra by the window operator method

Having prepared a reasonable ground state and calculated its evolution in time, the remaining task is to extract the energy spectrum of the final wave function. This can conveniently be achieved by applying the window operator method [110, 111]. Therefore, consider a window operator to be defined as

$$\hat{W}_\gamma^n(E) = C_\gamma^n \frac{\gamma^{2n}}{(\hat{H}_0 - E)^{2n} + \gamma^{2n}} \quad (2.99)$$

with operator order n , energy width parameter γ , normalization constant $C_\gamma^n = \frac{2^n \sin(\pi/2^n)}{2\pi\gamma}$, and E representing the sample energy. Applying this operator to a superposition of eigenstates $|\Psi\rangle = \sum_i c_i |\Psi_i\rangle$ and calculating the expectation values in dependence of

2. Theoretical framework

energy E yields the energy spectrum

$$W_\gamma^n(E) = \langle \Psi | \hat{W}_\gamma^n(E) | \Psi \rangle \quad (2.100)$$

$$= \langle \Psi | \Psi_W \rangle \quad (2.101)$$

$$= C_\gamma^n \sum_i |c_i|^2 \frac{\gamma^{2^n}}{(\varepsilon_i - E)^{2^n} + \gamma^{2^n}}. \quad (2.102)$$

Obviously, the spectrum represents a superposition of peaks at the eigenenergies ε_i , with heights determined by the eigenstate populations $|c_i|^2$ and broadened by γ . The shape of the individual peaks is determined by the operator order, reaching from Lorentzian-like for $n = 1$ to rectangular in the limit $n \rightarrow \infty$. The FWHM of the individual peaks is 2γ , irrespective of their particular shape (i.e. the operator order). Further, the normalization constant C_γ^n assures that $\int W_\gamma^n(E) dE = \sum_i |c_i|^2$, i.e. the area under the spectrum reflects the total population.

For the numerical implementation, the result of applying the window operator to the final discretized wave function $|\Psi_f^x\rangle$

$$|\Psi_W^x\rangle = C_\gamma^n \frac{\gamma^{2^n}}{(\hat{H}_0 - E)^{2^n} + \gamma^{2^n}} |\Psi_f^x\rangle \quad (2.103)$$

needs to be calculated. Since the unperturbed Hamilton operator \hat{H}_0 appears in the denominator, the equation can be rewritten to

$$(\hat{H}_0 - E)^{2^n} + \gamma^{2^n} |\Psi_W^x\rangle = C_\gamma^n \gamma^{2^n} |\Psi_f^x\rangle. \quad (2.104)$$

However, solving this equation for the desired $|\Psi_W^x\rangle$ numerically is impractical as the operator on the left hand side is not tridiagonal. This hurdle can be overcome by utilizing the clever factorization

$$(\hat{H}_0 - E)^{2^n} + \gamma^{2^n} = \prod_{k=1}^{2^{n-1}} \underbrace{\left[\hat{H}_0 - E + \gamma e^{i\nu_k^n} \right]}_{\hat{P}_1} \underbrace{\left[\hat{H}_0 - E - \gamma e^{i\nu_k^n} \right]}_{\hat{P}_2} \quad (2.105)$$

with phases $\nu_k^n = (2k - 1)\pi/2^n$ [107]. In this way the problem is translated to 2^{n-1} successive iterations of solving two matrix equations of the form $\hat{P} |\Psi_W^x\rangle = |\Psi_f^x\rangle$ which are very efficient since \hat{P}_1 and \hat{P}_2 are tridiagonal.

3. Photoemission from metal nanotips in bichromatic laser fields

This chapter is dedicated to strong-field photoemission from metallic nanotips, which provide a powerful model system to explore the impact of the linear near-field as charge interaction effects are expected to be suppressed due to the ultrafast screening by the delocalized valence-electrons. In particular, nanotips have turned out to be suited to study coherent photoemission and resulting quantum interferences in the photoelectron spectra (HATI peaks). Motivated by two-color experiments on tungsten nanotips performed in the group of Peter Hommelhoff [61, 62] (cf. Fig. 1.5 in the introduction), the goal of the current analysis is to theoretically study two effects. First, the impact of the spatial profile of the near-field on the coherent photoemission and second, the variation of the photoelectron spectra with the relative phase of the two-color field which is composed of a fundamental and its weak second harmonic. Therefore, the electron emission is simulated utilizing a one-dimensional quantum nanotip model and compared to predictions by the classical SMM. The assumptions for both models are described in Section 3.1. In the first part of Section 3.2 the coherent photoemission is inspected via systematically analyzing photoelectron spectra with respect to the parameters of the near-field from the fundamental. In the second part, the impact of the second harmonic component of the bichromatic field is identified by comparison of the quantum simulation results to respective SMM predictions. Note that the results shown in this chapter have been published in [LS2]. The discussion follows the presentation of these published results and contains additional details where appropriate.

3.1. The one-dimensional nanotip model

In this first section, the assumptions for the one-dimensional nanotip model are motivated and the quantum mechanical description utilizing the numerical solution of the TDSE is briefly discussed.

3.1.1. Spatio-temporal near-field

The metal nanotip is considered to be aligned along the x -axis with the tip apex located at $x = 0$, see Fig. 3.1. Along this axis the effective spatio-temporal near-field

$$\mathcal{E}_{\text{nf}}(x, t) = \gamma(x)\mathcal{E}_{\text{inc}}(t) \tag{3.1}$$

is considered as a superposition of the spatial enhancement profile $\gamma(x)$ and the incident laser field $\mathcal{E}_{\text{inc}}(t)$. Inside the nanotip ($x < 0$) the near-field is assumed to vanish due to

3. Photoemission from metal nanotips in bichromatic laser fields

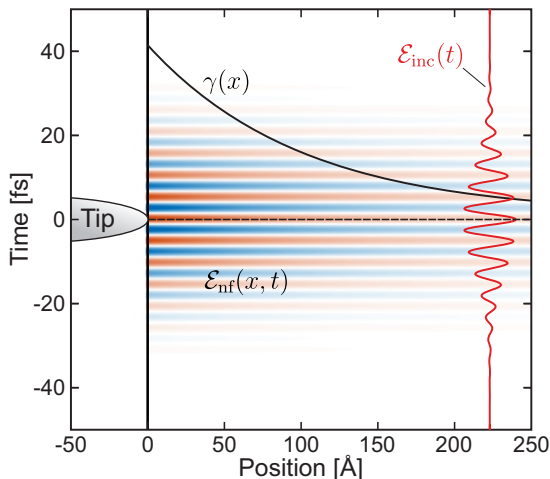


Figure 3.1. Schematic representation of the one-dimensional nanotip model. The tip is aligned along the x -axis with the apex located at $x = 0$. Red and black curves represent the incident laser field $\mathcal{E}_{\text{inc}}(t)$ and the exponentially decaying field-enhancement profile $\gamma(x)$, respectively. The false color map visualizes the effective spatio-temporal near-field $\mathcal{E}_{\text{nf}}(x, t) = \gamma(x)\mathcal{E}_{\text{inc}}(t)$ that is assumed to be perfectly screened inside the tip ($x < 0$). Published in [LS2].

perfect screening while an exponential decay is assumed for the outside region, such that the spatial enhancement profile is defined as

$$\gamma(x) = \begin{cases} 0 & \text{for } x < 0 \\ 1 + (\gamma_0 - 1)e^{-x/\lambda_{\text{nf}}} & \text{for } x \geq 0, \end{cases} \quad (3.2)$$

where γ_0 is the peak field enhancement at the tip apex and λ_{nf} is the decay length, see black curve in Fig. 3.1. The incident two-color laser field including the fundamental (ω -component) and the second harmonic (2ω -component) is defined as

$$\mathcal{E}_{\text{inc}}(t) = \mathcal{E}_0 f(t) \left[\cos(\omega t) + \sqrt{\beta} \cos(2\omega t + \varphi_{\text{tc}}) \right], \quad (3.3)$$

see red curve in Fig. 3.1. Here, \mathcal{E}_0 describes the peak field strength of the fundamental, $f(t)$ reflects a normalized Gaussian envelope (considered identical for both field components for the sake of simpler analysis¹, β is the intensity-ratio of the second harmonic with respect to the fundamental and φ_{tc} is the relative two-color phase (TCP).

In the following, the fundamental of the incident field is considered to have wavelength 1560 nm, pulse duration $\tau = 20$ fs, and intensity $I = 1 \times 10^{11}$ W/cm². The relative intensity of the second harmonic is assumed to be $\beta = 0.01$. The common peak field enhancement of both spectral components is chosen as $\gamma_0 = 7$ [60, 112]. In this case, the intensities of the maximally enhanced surface fields are $\approx 5 \times 10^{12}$ W/cm² for the fundamental and $\approx 5 \times 10^{10}$ W/cm² for the second harmonic, in good agreement with the parameters as in the two-color experiment. The respective ponderomotive energies of the dominant fundamental are $U_p = 0.02$ eV for the incident field and $U_p^{\text{loc}} = \gamma_0^2 U_p = 1.14$ eV for the maximally enhanced near-field at the tip apex. Please note that within this thesis energies will often be scaled with respect to the local ponderomotive energy to clearly illustrate effects beyond the acceleration in the linear near-fields. The corresponding quiver amplitude (cf. Appendix A) of an electron in the maximally enhanced near-field is $x_q = 7.4$ Å.

¹Note that for the experiment the field enhancements are estimated as $\gamma_0^\omega \approx 7$ and $\gamma_0^{2\omega} \approx 6$ (see e.g. [60, 112]).

3.1.2. Quantum description

The quantum description of the coherent photoemission from the metal nanotips is based on solving the one-dimensional one-electron TDSE. The numerical details of the method are discussed in Sec. 2.6. Here, only the specific aspects of the considered scenario, in particular the preparation of a suitable ground state, are briefly discussed. For the description of the metal-vacuum interface the field-free ground state wave function is determined for a square-well potential defined as

$$V_0(x) = \begin{cases} \tilde{V}_0 & \text{for } -d < x < 0 \\ 0 & \text{otherwise,} \end{cases} \quad (3.4)$$

with width d and depth \tilde{V}_0 (black curve in Fig. 3.2(a)) that are chosen in order to reflect the properties of the material. On the one hand, the energy of the ground state E_0 has to fulfill $E_0 = \tilde{V}_0 + E_F$, to reproduce the Fermi level of the material (where E_F is the respective Fermi energy). On the other hand, the binding energy needs to correspond to the material's work function W , i.e. $E_0 = -W$. In order to describe tungsten (in [310]-direction), here work function and Fermi energy are assumed to be $W = 4.3$ eV [113] and $E_F = 7.0$ eV [114], resulting in the parameters $d = 0.99$ Å and $\tilde{V}_0 = -11.3$ eV for the square-well potential. This particular construction of the initial state not only correctly describes the material parameters, but also suppresses states with binding energies below the ground state, emulating Pauli-blocking of transitions to occupied final states below the Fermi level.

To simulate the photoionization dynamics induced by the two-color laser field, the wave function $\Psi(x, t)$ is integrated by numerically solving the TDSE

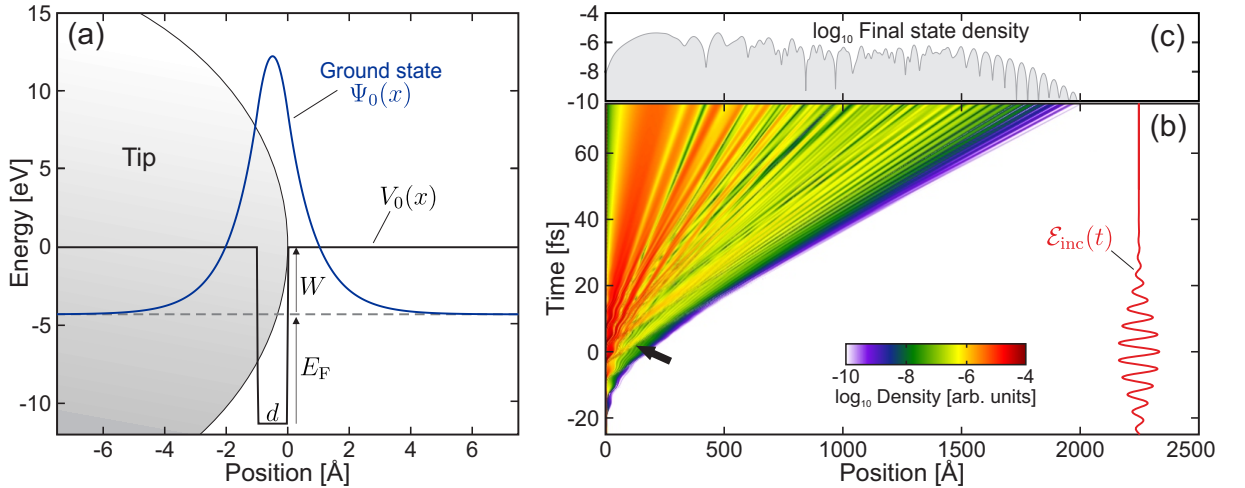


Figure 3.2. Quantum nanotip model. (a) One-dimensional square-well potential $V_0(x)$ (black curve) inside the metal nanotip for the active electron with ground state energy E_0 (dashed black line) matching Fermi energy E_F and work function W of the tungsten tip. The blue curve shows the ground state wave function. From [LS2]. (b) Time-evolution of the electron density $\varrho(x, t) = |\Psi(x, t)|^2$ in the vacuum calculated by numerically solving the TDSE including only the fundamental field (red curve). (c) Density at the end of the simulation.

3. Photoemission from metal nanotips in bichromatic laser fields

$$i\hbar\frac{\partial}{\partial t}\Psi(x,t) = \left[-\frac{\hbar^2}{2m}\frac{\partial^2}{\partial x^2} + V(x,t)\right]\Psi(x,t). \quad (3.5)$$

Here, the time-dependent effective potential

$$V(x,t) = V_0(x) + e \int_0^x \mathcal{E}_{\text{nf}}(x',t)dx' \quad (3.6)$$

$$= V_0(x) + e\mathcal{E}_{\text{inc}}(t) \int_0^x \gamma(x')dx'. \quad (3.7)$$

includes the time-independent square-well potential $V_0(x)$ defined in Eq. 3.4 and the laser induced spatio-temporal near-field $\mathcal{E}_{\text{nf}}(x,t)$ as introduced in Eq. 3.1 in length gauge. As an example, the time evolution of the density $\varrho(x,t) = |\Psi(x,t)|^2$ in the vacuum region outside the nanotip is shown in Fig. 3.2(b) for a typical scenario. The density shows a clear fringe structure that is attributed mainly to intercycle interference, i.e. the coherent superposition of electron wave packets emitted in different field cycles. Energy spectra are calculated for electrons emitted into vacuum (by applying the window operator method to the part of the wave function at $x > 0$) sufficiently late in the simulation, to ensure convergence (cf. respective density in Fig. 3.2(c)). The corresponding classical dynamics is described in the scope of the SMM and assuming the same spatio-temporal near-fields as in the TDSE simulations.

3.2. Coherent photoemission from metal nanotips

To explore the impacts of the individual field components and their combined effect on the coherent photoemission, Fig. 3.3(a) shows photoelectron spectra extracted from TDSE runs including only the fundamental (gray area), only the second harmonic (blue area), and the combined two-color field for two different relative phases (red and blue curves). The spectra show that the second harmonic component alone results in comparably weak HATI peaks with negligible overall electron yield compared to the spectrum when including only the fundamental field (compare blue and gray areas). Furthermore, the second harmonic induced spectrum exhibits an exponential decrease of the HATI peak intensities (i.e. a linear decrease on the logarithmic scale) that is characteristic for the perturbative regime. In contrast to that, the spectrum corresponding to the fundamental reveals signatures typical for strong-field electron emission such as a pronounced contribution in the spectral region below $2U_{\text{p}}^{\text{loc}}$ connected with directly emitted electrons and the backscattering-plateau with a pronounced cut-off around $10U_{\text{p}}^{\text{loc}}$. The spectrum extracted from a corresponding SMM simulation (black curve) exhibits cut-offs around 2 and $10U_{\text{p}}^{\text{loc}}$ but naturally lacks the HATI peaks. Despite the weak impact of the second harmonic alone, its effect on the emission spectra calculated with the full two-color field is far from being negligible. When including the second harmonic, variation of the relative two-color phase strongly affects the emission spectra over the full spectral range. In particular, both the high energy cut-off and the electron yields over the full spectral region can be suppressed or enhanced by varying the relative phase. Moreover, this effect is not uniform for the whole spectrum, i.e. the yield is not suppressed or enhanced for the full energy range for a selected value of the relative phase. Instead, for the phases selected here, the yield is enhanced in the low and high energy ranges and suppressed in the plateau region or vice versa. A detailed analysis of the relative phase-dependence is discussed in Sec. 3.2.2.

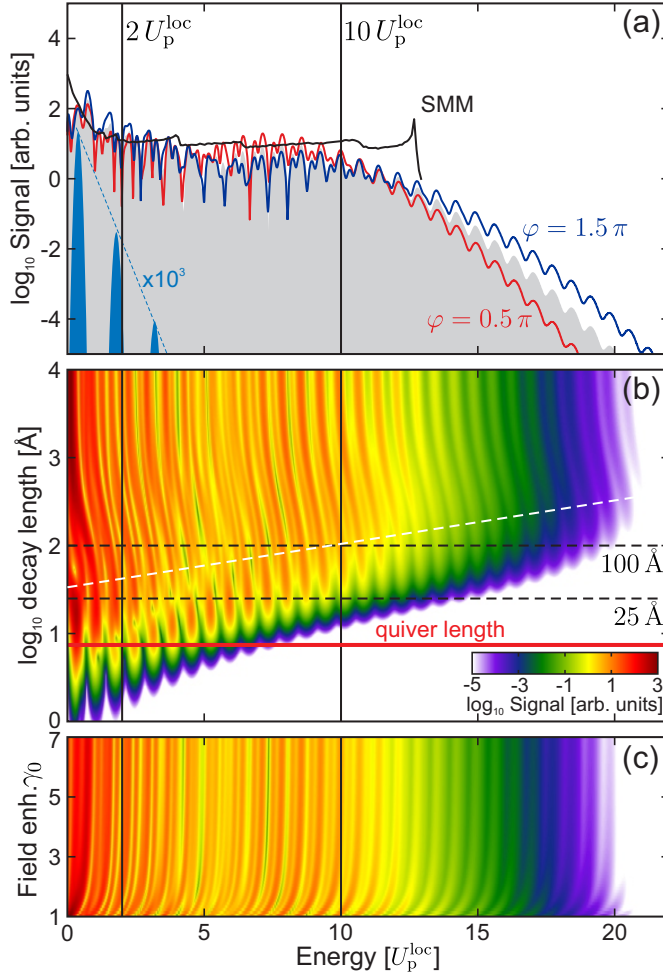


Figure 3.3. Coherent photoemission from metal nanotips calculated via TDSE. (a) Energy spectra when including only the second harmonic (blue area), only the fundamental (gray area), and the full two-color field for two relative phases (blue and red curves, as indicated). The black curve represents the spectrum from a corresponding SMM calculation including only the fundamental. Vertical black lines indicate the conventional cut-off energies. Energies are scaled to the ponderomotive energy of the maximally enhanced near-field. (b) Evolution of HATI spectra with the near-fields decay length λ_{nf} for the fundamental only. The red horizontal line indicates the quiver amplitude x_q of an electron in the maximally enhanced field. The white dashed line visualizes the onset of the ponderomotive downshift. (c) HATI spectra in dependence of the enhancement γ_0 for $\lambda_{\text{nf}} = 100$ Å and with local peak intensity fixed at 5×10^{13} W/cm² by adjusting the intensity of the incident field. From [LS2].

3.2.1. Influence of the spatial near-field profile

In order to inspect the effect of the spatial near-field profile, photoelectron spectra are calculated under systematic variation of the decay length λ_{nf} , see Fig. 3.3(b). Their evolution reveals the following trends. First, towards the limit of strong field localization, with decay lengths around the electrons quiver amplitude (horizontal red line), the spectra collapse as recollisions are first suppressed and eventually quenched [16, 59]. In this regime, the spectral positions of the HATI orders are essentially independent of the decay length. In contrast, for large decay length above $\gtrsim 100$ Å the overall spectrum persists. However, with increasing decay length the positions of the HATI orders gradually shift towards lower energies with a magnitude of roughly the local ponderomotive energy U_p^{loc} . This shows the successive vanishing of the ponderomotive acceleration of electrons escaping the enhanced near-field as the latter is terminated by the temporal pulse profile before the electrons can leave the inhomogeneous enhancement profile [115]. Finally, in the intermediate range of decay length around 100 Å, the electrons experience the full decaying spatial profile of the local near-field before the temporal field envelope ceases and can therefore accumulate the local ponderomotive energy while escaping. The interplay of the spatial and temporal field profiles also explains why lower HATI orders begin to shift already at lower decay length compared to orders at higher energies (the onset is visualized by the white dashed line in Fig. 3.3(b)). While faster electrons can still escape

3. Photoemission from metal nanotips in bichromatic laser fields

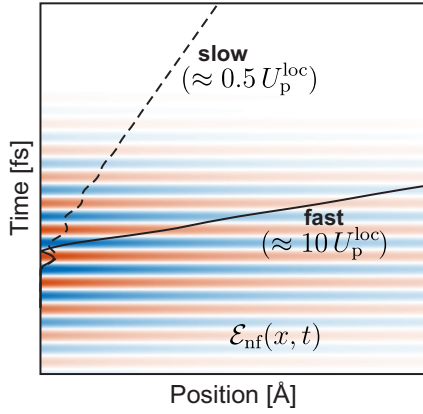


Figure 3.4. Interplay of temporal and spatial field profiles. Slow (dashed) and fast (solid) SMM trajectories.

from the enhanced near-field and thus experience the ponderomotive energy gain, the acceleration of slower electrons is terminated by the temporal profile (compare solid to dashed SMM trajectories in Fig. 3.4). This energy-dependent quenching of the ponderomotive acceleration constitutes a clear and characteristic fingerprint of the near-field inhomogeneity. Although the near-field profile could be utilized as a parameter for the experimental verification of the effect, it is more practical to vary the pulse duration instead.

In addition to the variation of the decay length, the field inhomogeneity effects can also be modified via adjusting the peak enhancement γ_0 . The systematic analysis of the enhancement-dependent spectra (for constant decay length of $\lambda_{\text{nf}} = 100 \text{ \AA}$) in Fig. 3.3(c) clearly shows the ponderomotive downshift of HATI orders with decreasing enhancement in the region $\gamma_0 \lesssim 2$. For larger enhancements, the spectra as function of γ_0 remain robust. Note that for this analysis the peak intensity of the local enhanced field has been kept constant by adjusting the peak intensity of the incident laser field.

3.2.2. Two-color effects on the electron emission

After analyzing the impact of the spatial near-field profile on the photoelectron spectra for the fundamental alone, the electron emission will now be analyzed systematically with respect to the relative phase of the full two-color field. Therefore, phase-dependent HATI spectra for three selected values of the near-field decay length are displayed in Fig. 3.5(a-c). All three spectra clearly show strong modulations of the yields of the individual HATI orders in dependence of the two-color phase. To quantify the energy-resolved phase-dependence, the yields are fitted with harmonic functions $Y_{\text{fit}}(E, \varphi_{\text{tc}}) = A(E) + B(E) \cos[\varphi_{\text{tc}} - \varphi_{\text{tc}}^{\text{crit}}(E)]$. The resulting energy-dependent critical phases $\varphi_{\text{tc}}^{\text{crit}}(E)$, which represent maximal two-color yield (black curves in Fig. 3.5(a-c)), show a trend that is similar for all three selected values of the decay length. First, the critical phases start around 1.2π in the low energy region ($\lesssim 2U_p^{\text{loc}}$) and decrease to 0.8π for the plateau before finally increasing to $\approx 1.5\pi$ at the cut-off. This observation is supported by the comparison of selective yields that are calculated by integration over the three relevant spectral regions (blue, green and red curves in Fig. 3.5(g-i) for the low, intermediate and high energy range as indicated at the top of panel Fig. 3.5(a)). Note that while the global structure of the spectra remains qualitatively unchanged for different values of the decay length, the cut-off decreases when the near-field becomes more localized.

3.2. Coherent photoemission from metal nanotips

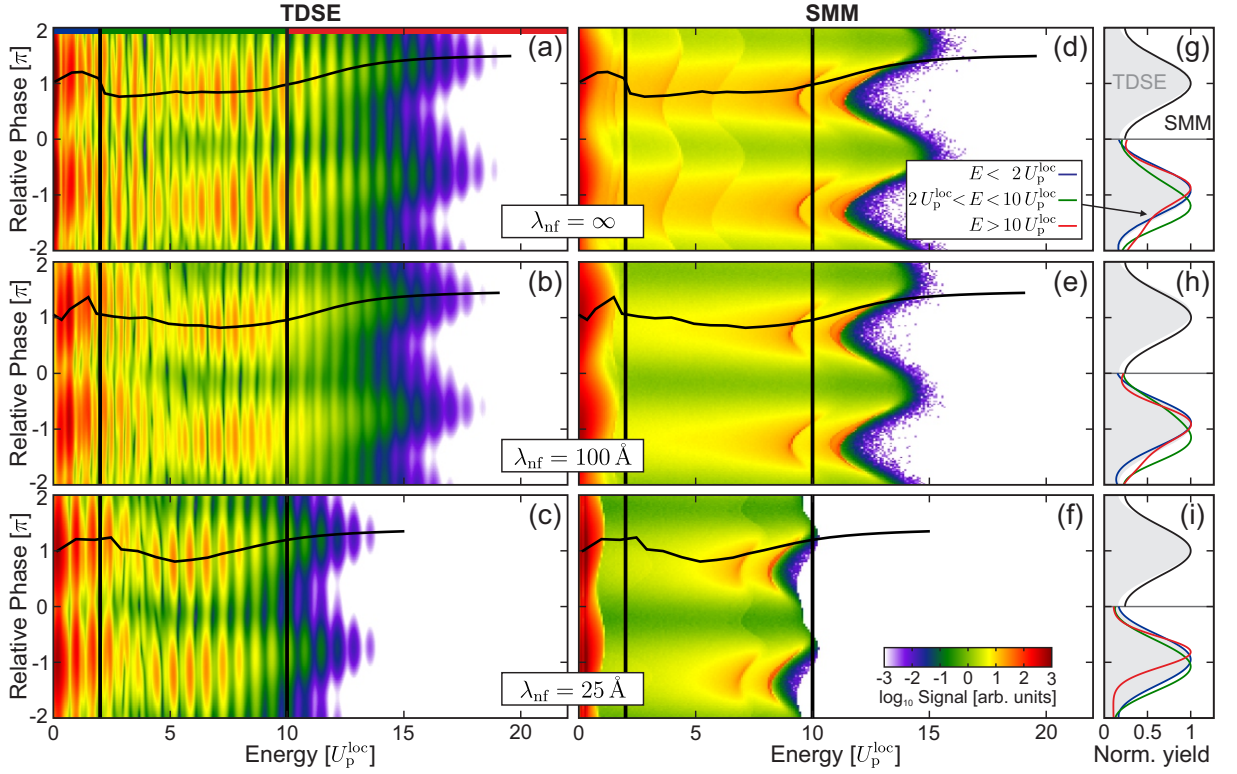


Figure 3.5. Photoelectron spectra from metal nanotips in two-color fields. **(a-c)** Spectra as function of relative two-color phase for three values of the decay length (as indicated) predicted by TDSE. Black curves indicate the spectral critical phases $\varphi_{tc}^{\text{crit}}(E)$. Vertical lines mark the conventional cut-offs. **(d-f)** Respective spectra predicted by the classical SMM. For comparison, black curves show the critical phases extracted from the TDSE results. **(g-i)** Relative phase-dependent total electron yields extracted from TDSE (gray areas) and SMM (black curves) and selective yields from TDSE for the energy regions as indicated (cf. panel (d)) and visualized by the respective colors at the top of panel (a). All curves are normalized to their peak values. Published in [LS2].

Although the TDSE results reveal the main trends of the phase-dependent two-color emission, they do not allow a clear identification of the underlying physical mechanisms and cannot explain the spectral dependence of the critical phases. Therefore, to help developing an intuitive physical picture, the TDSE results are compared to corresponding SMM calculations, see Fig. 3.5(d-f). Similar to the TDSE, the SMM photoelectron spectra exhibit clear signatures from direct electrons below $2U_p^{\text{loc}}$ and from recollision electrons forming the spectral plateau up to a cut-off around $10U_p^{\text{loc}}$. The step-like features in the plateau regions are attributed to electron emission from the individual field half-cycles close to the pulse peak. Moreover, in good agreement with the TDSE results the cut-off energies decrease for strong field localization. Most importantly though, the phase-dependent modulation of the yields qualitatively reproduces the TDSE results in all spectral regions (the black curves in Fig. 3.5(d-f) reflect the critical phases extracted from the corresponding TDSE spectra and are shown for convenience).

Selective impact of the second harmonic component

The good qualitative agreement of the SMM and TDSE results justifies the detailed analysis of the selective impacts of the second harmonic field on the ionization and acceleration processes. In contrast to the quantum description, this is easily achievable in the SMM description, as the second harmonic component can be selectively turned on and off in both the evaluation of the ionization rate and the trajectory propagation. The results of this selective analysis are shown in Fig. 3.6 for the same parameters as in Fig. 3.5(e). First, the second harmonic component is only turned on in the ionization rate but neglected for the trajectory propagation, see Fig. 3.6(a). In this case, the SMM predicts strong variation of the yields with the two-color phase in the low and intermediate energy regions. The additional small variation of the yield in the cut-off region is attributed to the statistical weight of the trajectories but exhibits a different two-color phase-dependence when compared to the TDSE results. Including the second harmonic field only in the trajectory integration but not in the ionization rate (Fig. 3.6(b)) results in a very pronounced modulation of the cut-off energies with a similar phase-dependence as in the TDSE prediction, but does not affect the lower spectral regions significantly. Hence, the analysis reveals that the two-color contrast in the spectral range of direct emission and the recollision plateau is determined by the effect of the 2ω -component on the ionization rate while the cut-off modulation is governed by its effect on the electron trajectories. The robustness of the latter effect with respect to the specific value of the decay length supports that the phase-dependent modulation of the spectral cut-off could be utilized to characterize the relative phase of two-color fields.

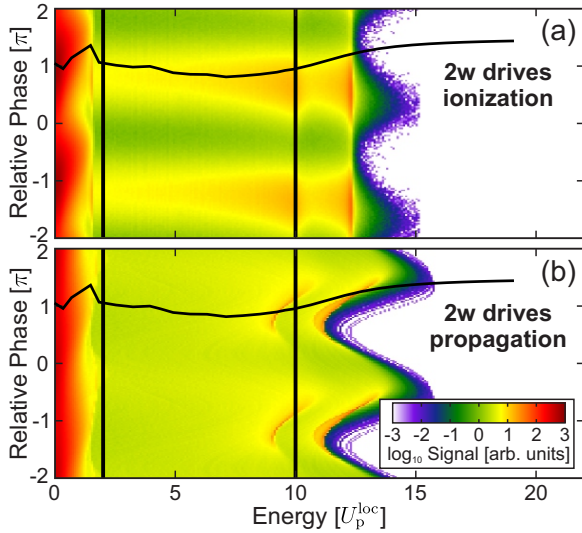


Figure 3.6. Relative two-color phase-dependent photoelectron spectra predicted by the SMM for decay length $\lambda_{\text{nf}} = 100 \text{ \AA}$ (cf. Fig. 3.5(e)) and with selectively activated 2ω -fields. (a) Spectra extracted from simulations with the 2ω -field included only in the evaluation of the ionization rate. (b) Spectra from simulations with the second harmonic field only included for the integration of the trajectories. Vertical black lines mark the conventional SMM cut-offs. Black curves indicate the critical phases extracted from the TDSE result in Fig. 3.5(b). From [LS2].

The fact that semi-classical trajectory simulations can partly (but not completely) reproduce the spectral phase-dependence shows that both classical contributions such as field-dependent trajectory modifications as well as tunneling rate effects and quantum interference contribute to the modulation of the photoelectron spectra. Further clarification of the intertwining of these classical and quantum effects as well as the impact of transport dynamics and nonlinear plasmonic effects in phase-controlled nanotip emission provide a challenging goal for future research where a promising strategy could be the combination of strong-field photoemission and attosecond streaking.

4. Strong-field electron emission from small dielectric nanospheres

This chapter focuses on the electron emission from small isolated dielectric nanospheres under non-resonant excitation with intense optical few-cycle pulses. In particular, the following three key issues are addressed: First, the identification of relevant acceleration mechanisms for the emitted electrons. Second, their individual contributions to the photoelectron energy spectra and their dependence on the field waveform. Third, the impact of charge interaction on the electron emission. To start the discussion, a typical reference scenario is presented in [Section 4.1](#). After a brief analysis of the linear near-fields, the time-resolved ionization dynamics and the features of typical photoelectron energy spectra are inspected. Finally, a detailed discussion of charge interaction effects on the ionization dynamics and the electron acceleration is provided in [Section 4.2](#). Substantial parts of the presented results have already been published [[LS3](#), [LS4](#)] and are revisited here for convenience. The discussion is close to that in the original publications with extra information given where appropriate.

4.1. Few-cycle driven ionization of small nanospheres

As a starting point of the analysis, the general evolution of the strong-field driven electron dynamics is illustrated for a typical reference scenario. Therefore, a small nanosphere with diameter $d = 100$ nm, ionization energy $I_p = 9$ eV [[96](#)], and relative permittivity $\varepsilon_r = 2.12$ [[116](#)] serves as a model system to mimic the SiO₂ nanoparticles in respective experiments. The nanosphere is irradiated by an intense NIR few-cycle pulse with pulse length $\tau = 4$ fs, central wavelength $\lambda = 720$ nm, peak intensity $I = 3 \times 10^{13}$ W/cm², and CEP $\varphi_{ce} = 0$, that is considered to propagate in positive x -direction and is linearly polarized in y -direction. The geometry is illustrated schematically in [Fig. 4.1\(a\)](#). The linear near-field exhibits pronounced hot spots with particularly strong field enhancement at the poles, i.e. in the polarization direction of the incident field. The spatial enhancement profile sampled along the polarization direction (red curve in [Fig. 4.1\(b\)](#)) indicates a maximum field enhancement of $\gamma_0 \approx 1.6$. With increasing distance from the surface, the enhancement decays to unity (i.e. the near-field decays to the incident field) on the order of a few tens of nanometers, providing a pronounced inhomogeneous enhancement profile. At the interfaces, the field jumps by the relative permittivity such that the field strength inside the sphere is suppressed below that of the incident field. For spheres that are small compared to the laser wavelength the linear near-field can be described reasonably within dipole approximation (compare dashed black to solid red curve in [Fig. 4.1\(b\)](#)) as considered in previous studies [[13](#)]. This underpins the vanishing effect of field propagation within the small spheres.

4. Strong-field electron emission from small dielectric nanospheres

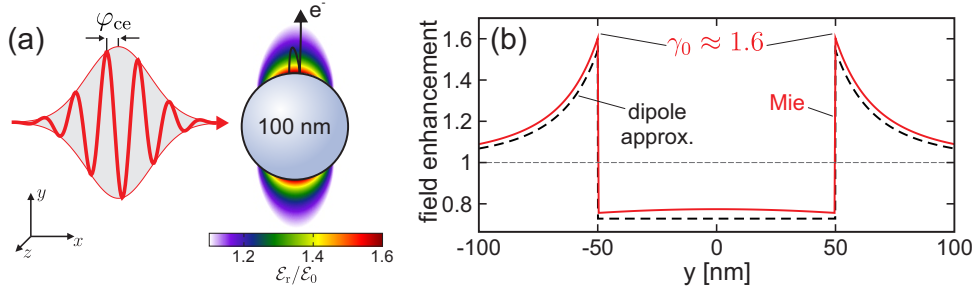


Figure 4.1. Linear near-field at a small $d = 100$ nm silica sphere in an intense NIR few-cycle laser pulse ($\lambda = 720$ nm, $\tau = 4$ fs, $I = 3 \times 10^{13}$ W/cm², $\varphi_{ce} = 0$). **(a)** Maximum enhancement of the radial near-field relative to the peak field strength of the incident pulse (red curve) in the propagation-polarization ($x - y$) plane for $z = 0$ (Mie calculation). The black curve illustrates a typical trajectory of an electron emitted after a recollision at the surface. **(b)** Field enhancement profile $\gamma(y)$ along the y -axis in (a) extracted from Mie calculations (solid red) and as predicted in dipole approximation (dashed black). The horizontal line indicates unity enhancement.

4.1.1. Time-resolved ionization response

To identify the specific contributions of different ionization mechanisms to the overall yield of liberated electrons, the selective yields of electrons generated via tunnel and impact ionization are traced in the simulation. Their time evolutions are illustrated in Fig. 4.2(b) and reveal that the majority of electrons is generated via tunneling during the three main half-cycles of the laser field (solid red curve and dark shaded red area). In particular, ionization is most pronounced close to the respective minima and maxima of the laser electric field (cf. Fig. 4.2(a)) resulting in a pronounced step-like increase of the yield. Impact ionization provides an additional small contribution that develops after the maximum of the pulse and is not directly correlated with the waveform (dark shaded gray area). A closer analysis of the time-resolved tunnel ionization indicates that despite the similar field strength during the two dominant negative half-cycles (at $\approx \pm 1.2$ fs), more electrons are liberated during the first of these two half-cycles (see red arrows). This is a first hint at the impact of charge interaction and can be understood as follows. In the earlier half-cycle, generation of tunnel electrons in the vacuum and residual ions in the material results in a surface field that counteracts the linear near-field and

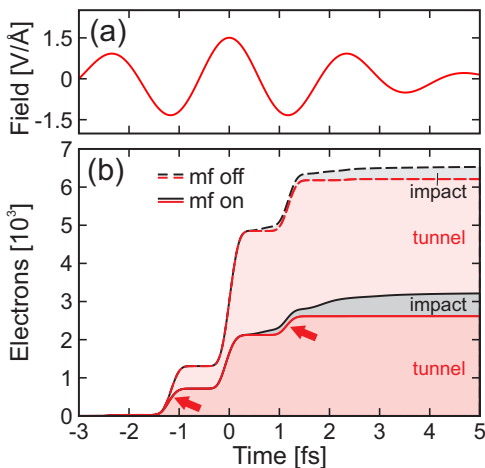


Figure 4.2. Ionization of small dielectric nanospheres in intense few-cycle laser pulses. **(a)** Field strength of the incident few-cycle laser pulse. **(b)** Yields of electrons generated at the surface of the nanosphere via tunnel ionization (red shaded areas) and inside the sphere due to impact ionization (gray shaded areas) predicted by M³C simulations with the mean-field turned off (dashed curves and light shaded areas) and on (solid curves and dark shaded areas).

hence limits ionization in the second half-cycle. To further inspect the effects of charge interaction, the results are compared to a corresponding simulation with the mean-field turned off (solid vs. dashed curves in Fig. 4.2(b)). The comparison allows two conclusions. First, without charge interaction tunneling is stronger, producing roughly twice as many electrons as in the case with charge interaction. Second, neglecting charge interaction leads to a symmetric yield of tunnel electrons for the two negative half-cycles as opposed to the weaker ionization in the second half-cycle when including the mean-field. These two observations strongly substantiate the quenching due to an emerging surface field. A detailed analysis of the quenching effect is presented in Section 4.2.2 for a variety of dielectric materials.

4.1.2. Selective analysis of photoelectron spectra

Having identified the impact of charge interaction on the electron yield, its effect on the energy spectra of emitted electrons¹ will now be investigated. For the case without charge interaction, the energy spectrum (gray shaded area in Fig. 4.3(a)) reveals a global shape similar to the spectra recorded from atomic targets (cf. Fig. 1.2(a)). It exhibits a high yield at low energies with a cut-off around $2U_p^{\text{loc}}$ followed by a plateau region with a second cut-off around $10U_p^{\text{loc}}$. Similar to the atomic case and the emission from nanotips, also here the two prominent signatures can be connected unambiguously with direct emission (solid black curve) and elastic backscattering (solid red curve). Note that the ponderomotive energy $U_p^{\text{loc}} = \gamma_0^2 U_p \approx 3.72 \text{ eV}$ is defined with respect to the maximally enhanced linear near-field and is a factor of $\gamma_0^2 \approx 2.6$ larger than the ponderomotive energy $U_p = 1.45 \text{ eV}$

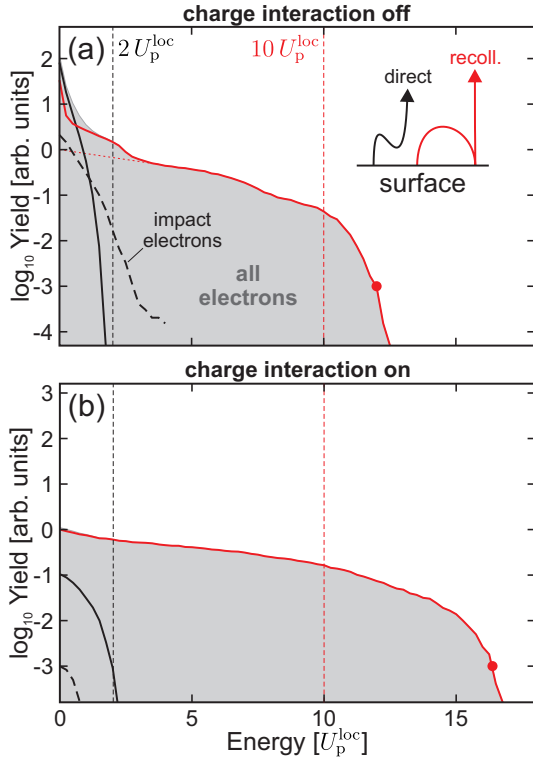


Figure 4.3. Photoelectron spectra from 100 nm silica nanospheres under NIR few-cycle laser pulses predicted by M³C. **(a,b)** Full (gray areas) and selective (curves) energy spectra from simulations without (a) and with charge-interaction (b). Black curves represent direct electrons generated via tunnel ionization (solid) and via impact ionization (dashed). Red curves indicate backscattered electrons. Vertical dashed lines mark the classical 2 and $10U_p^{\text{loc}}$ SMM cut-offs for direct end backscattered electrons, respectively. The energies are scaled to the ponderomotive energy of the maximally enhanced linear near-field. Red symbols indicate the cut-offs for backscattered electrons, defined as the energy where the normalized yields have dropped by three orders of magnitude compared to the yield at $E = 0$. Note that for the charge interaction free case the plateau was extrapolated to neglect spurious contributions at low energies for the cut-off evaluation (dashed red line).

¹Electrons are considered to be emitted if they are outside of the nanosphere with positive radial momentum and positive single particle energy sufficiently late in the simulation (to assure convergence).

4. Strong-field electron emission from small dielectric nanospheres

of the incident laser pulse. This signifies that the well-known pictures from atomic strong-field physics can be transferred to the electron acceleration in the enhanced near-field of dielectric nanoparticles. The low portion of electrons exceeding $10 U_p^{\text{loc}}$ can be attributed to the finite classical tunneling exit. Furthermore, electrons generated via impact ionization (dashed black curve) result in an additional small contribution to the overall yield that only affects the low-energy spectral region and is thus neglected in the further analysis.

While the energy spectrum extracted from the simulation excluding charge interaction can be explained well by the acceleration of direct and recollision electrons in the enhanced linear near-field, the simulation including charge interaction reveals a completely different scenario, see Fig. 4.3(b). In this case, direct emission of tunnel and impact electrons (solid and dashed black) is suppressed by around three orders of magnitude compared to the charge interaction free case. The positions of the respective cut-offs, however, remain effectively unchanged. In stark contrast, the cut-off of backscattered electrons exceeds the classical cut-off by around 50 % in good agreement with the results of previously published studies [13]. The physical mechanisms behind this cut-off enhancement are discussed in detail in Section 4.2.

Typical recollision trajectories

Analyzing the energy spectra revealed that charge interaction can significantly enhance the maximum energies of electrons emitted after elastic backscattering. To investigate the effects of charge interaction on the underlying recollision process, representative recollision trajectories predicted by SMM simulations and M³C simulations ex- and including the mean-field are compared in Fig. 4.4. All trajectories start close to the field's minimum and recollide when the latter flips sign. While the SMM trajectory (black) starts and recollides at the surface, both M³C trajectories (gray and red) are launched at their respective classical tunneling exits and penetrate the material for a finite time before their final escape. Within the M³C model, a recollision is therefore defined as a return to the surface and the subsequent emission and can include multiple microscopic collisions within the material. The smooth evolution in the material results from the averaging over multiple similar trajectories. The respective recollision time (defined as the average of the entry and escape times) is similar to the SMM prediction. When comparing M³C to SMM, even without charge interaction the finite tunneling exit and possible effects from the near-field inhomogeneity result in a slightly higher escape velocity (compare gray to black curve). Including charge interaction (red curve) results in an even steeper slope of the trajectories

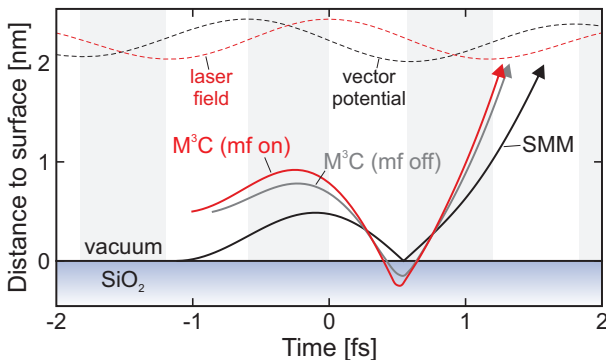


Figure 4.4. Typical recollision trajectories predicted by the SMM (black curve) and M³C simulations ex- and including charge interaction (gray and red curves). The M³C trajectories represent averaged trajectories of electrons close to the respective cut-off energies (cf. red symbols in Fig. 4.3). Dashed red and black curves indicate the laser field and its vector potential, respectively.

during the approach to and escape from the surface. The corresponding higher velocity leads to an additional energy gain that will be analyzed in more detail in [Section 4.2.1](#).

4.1.3. Temporally resolved electron emission

To resolve how electrons that are liberated at different times contribute to the previously inspected energy spectra, the correlations of their generation times and final energies are analyzed in [Fig. 4.5](#). The correlation map extracted from the simulation neglecting charge interaction (false color map in [Fig. 4.5\(a\)](#)) reveals signatures similar to the results of a corresponding SMM calculation (solid curves). The comparison allows to clearly identify signatures corresponding to direct emission (solid black curves) and elastic backscattering (solid red curves)². In both cases, electrons are generated in short bursts close to the peaks of the incident laser field (dashed red curve) supporting that direct emission and elastic backscattering from nanospheres are driven by the near-field. The additional 'smeared out' (i.e. non field-driven) contribution after the pulse maximum ($t > 0$) is attributed to electrons generated via impact ionization. Most importantly, the results signify that without charge interaction the ionization dynamics and the cut-offs of directly emitted and backscattered electrons can be described reasonably well within the classical three-step model when taking the enhanced near-field into account.

When including the mean-field, the correlation map in [Fig. 4.5\(b\)](#) clearly shows three effects that are induced by charge interaction. First, ionization is suppressed after the peak of the pulse and for both emission directions only one half-cycle contributes significantly to the overall electron yield. This can be explained by the build-up of trapping fields on each side of the nanoparticle in the earlier half-cycles leading to suppressed ionization in the following half-cycles. Second, due to the emerging trapping fields the emission of

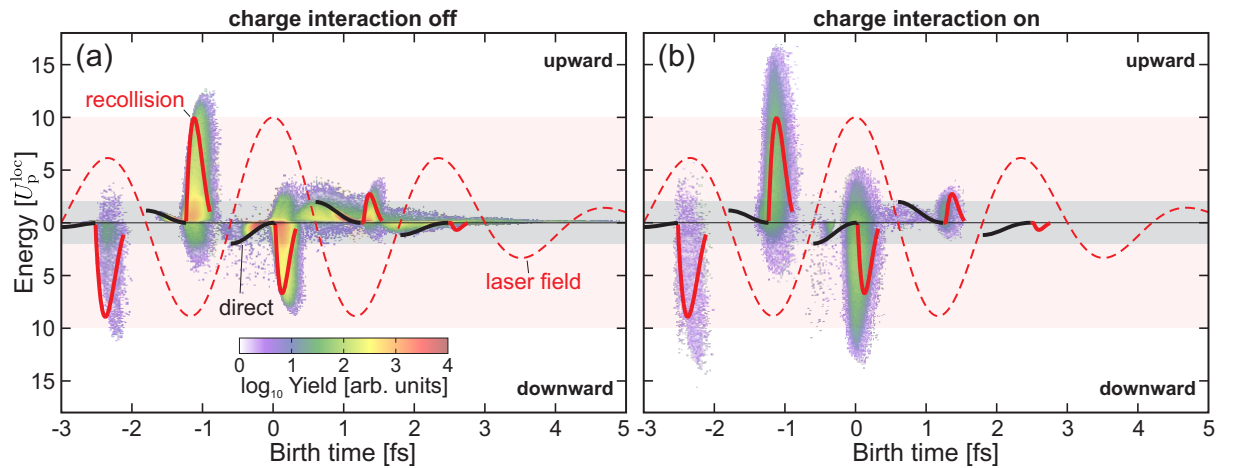


Figure 4.5. Correlation of generation times and final energies. (a,b) Distribution of final electron energies against birth times of electrons emitted into upward and downward direction (as indicated). Solid black and red curves show respective SMM results. Gray and red shaded areas indicate the classical 2 and $10 U_p^{\text{loc}}$ cut-offs. Dashed red curves reflect the laser field.

²The signatures can also be connected to the respective emission mechanisms from the M³C simulations alone by analyzing selective correlation maps.

4. Strong-field electron emission from small dielectric nanospheres

direct electrons is almost completely quenched. Third, the maximum energies of recollision electrons are significantly enhanced beyond the $10 U_p^{\text{loc}}$ cut-off as already observed in the respective energy spectrum. However, the general signatures of the correlation map and especially the generation times of recollision electrons are essentially unchanged. This underpins the robustness of the rescattering mechanism under the impact of charge interaction.

4.1.4. Impact of the field waveform on the electron emission

Besides revealing the effects of charge interaction on the build-up of the final energy spectra, the correlation map in Fig. 4.5(b) also shows a clear asymmetry of the emission into up- and downward direction. For the considered value of the CEP, electrons emitted into upward direction exhibit a significantly higher cut-off energy of $\approx 17 U_p^{\text{loc}}$ compared to downward emission ($\approx 12 U_p^{\text{loc}}$). This directional asymmetry is a strong hint at the applicability of waveform control and motivates a detailed analysis of the energy spectra in dependence of the driving fields waveform. Therefore, CEP-dependent energy spectra of electrons emitted into up- and downward direction are analyzed systematically in Fig. 4.6(a). Although the spectra reveal variations of the electron yield in the full energy range, the modulation is most pronounced at the energy cut-off. While the fastest electrons are emitted into upward direction for values of the CEP close to zero, downward emission is preferred for $\varphi_{\text{ce}} \approx \pi$. The phase-dependence can be visualized best in a respective map of the up–down emission asymmetry (Fig. 4.6(d)) as commonly used in experimental studies [13, 14, 117–122]. In this representation, asymmetry parameters of ± 1 correspond to exclusive emission into upward (indicated in red) and downward (indicated in blue) direction, respectively.

In the present scenario, the asymmetry map reveals three key features. First, largest asymmetries occur in the cut-off region which can be explained by the exclusive emission of electrons with energies close to the cut-off into one direction for certain CEPs (cf. Fig. 4.5(b)). Second, with decreasing energy the regions with maximum and minimum asymmetry values shift to lower CEPs. Third, the map reveals a pronounced low energy feature ($\lesssim 3 U_p^{\text{loc}}$) that – at first sight – might be attributed to directly emitted electrons due to its energy scale. For a clear comparison of the phase-dependencies for direct emission and backscattering, selective energy spectra and corresponding asymmetry maps are shown in Fig. 4.6(b,c,e,f). While direct emission (b,e) and elastic backscattering (c,f) are strongly phase-dependent with pronounced up-down asymmetries in their respective cut-off regions, their critical phases (defined via the maximum energy for upward emission) are different. For direct emission, the most energetic electrons are emitted in upward direction for $\varphi_{\text{ce}} \approx 0.9\pi$, as opposed to the low energy feature in the full asymmetry map. The map for backscattered electrons reveals two separated features with similar critical phases of $\varphi_{\text{ce}} \approx 0$ in the cut-off region and at low energies. This signifies that the low energy feature observed in the full asymmetry map is attributed to recollision electrons that are generated in a different cycle. The small offset of the critical phase of the low energy feature with respect to the cut-off region is attributed to charge interaction effects.

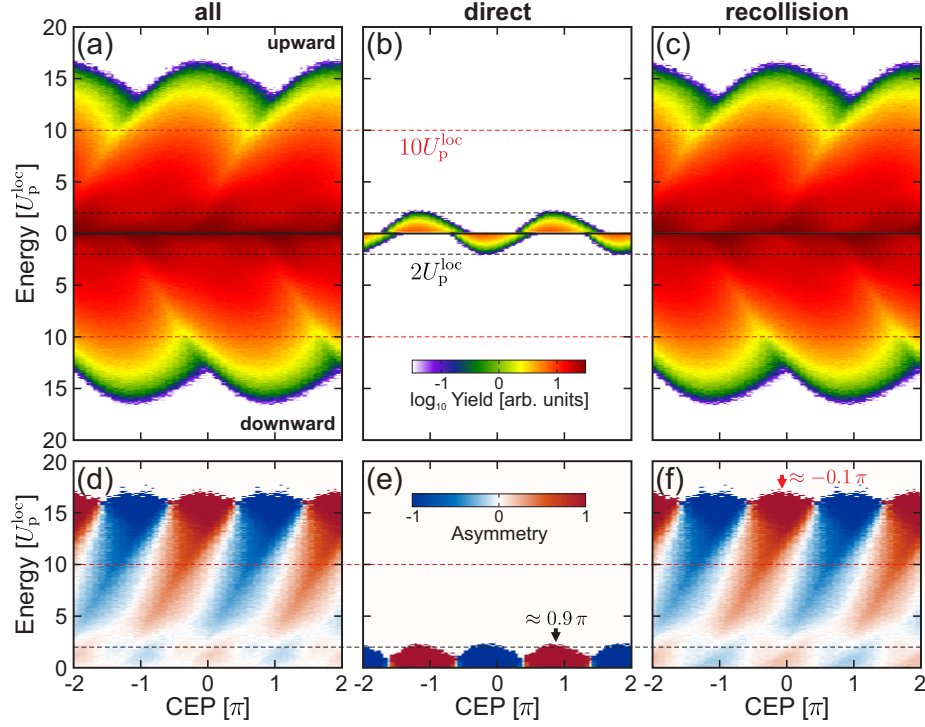


Figure 4.6. Phase-dependent electron emission from small nanospheres. (a) Energy spectra $Y(E, \varphi_{ce})$ of electrons emitted into upward (Y_{up}) and downward (Y_{down}) direction (as indicated) in dependence of the carrier-envelope phase φ_{ce} . (b,c) Respective selective spectra of directly emitted electrons (b) and recollision electrons (c). (d-f) Asymmetry maps $A = (Y_{up} - Y_{down}) / (Y_{up} + Y_{down})$ calculated from the respective energy spectra in (a-c). Horizontal dashed lines indicate the classical 2 and $10 U_p^{loc}$ cut-off energies. Arrows in (e,f) mark the respective phases of maximal asymmetry.

4.2. Charge interaction effects

The previous comparison of the results from M^3C simulations excluding and including the mean-field revealed several effects of charge interaction on the photoemission. The quenching of ionization in later cycles of the driving field and the suppression of direct emission can be understood intuitively by the generation of an attractive trapping field. On the one hand, such a field acts against the linear near-field and the lower effective field leads to a reduced tunneling probability. On the other hand, the trapping field constitutes an additional hurdle that the slow direct electrons cannot overcome. Most importantly though, the cut-off of recollision electrons is enhanced, which is counter-intuitive at first glance.

To unravel the mechanisms behind the charge interaction induced cut-off enhancement, the time evolution of the kinetic energies of representative fast electrons is compared in Fig. 4.7(a) for simulations excluding (black curve) and including (red curve) the mean-field. The fast electrons are selected from those with final energies close to the cut-offs of the respective energy spectra (black and red symbols in the inset of Fig. 4.7(a)). The comparison shows that although the overall structure of the evolution is similar in both cases, it exhibits two additional energy gains that develop on very different time scales when including the mean-field. The first gain occurs during the recollision phase (between 0 and 2 fs) and is attributed to the potential of the attractive trapping field (cf. blue

4. Strong-field electron emission from small dielectric nanospheres

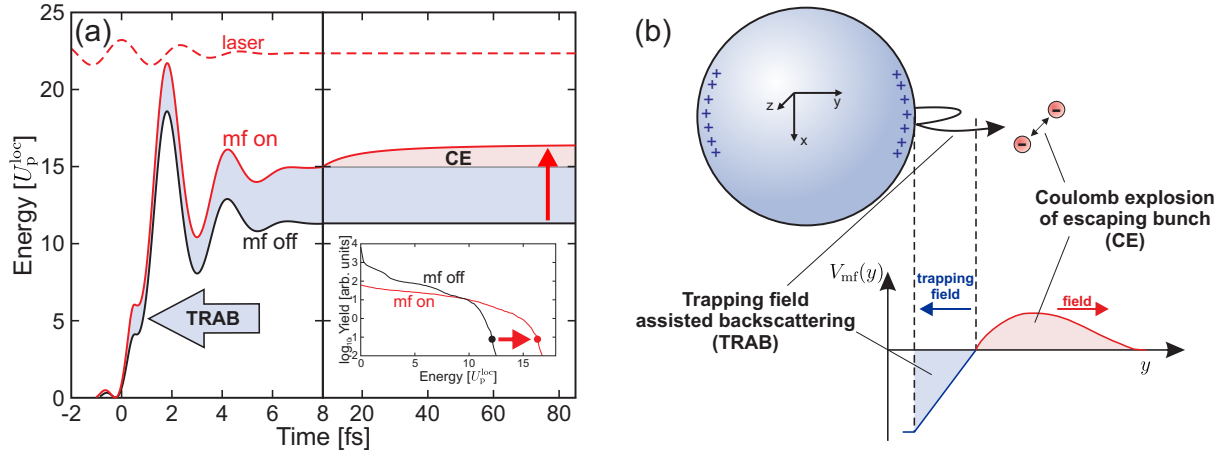


Figure 4.7. Charge interaction effects in strong-field photoemission from dielectric nanospheres. (a) Evolution of the kinetic energies of typical recollision trajectories corresponding to the cut-off energies of spectra extracted from M³C simulations without (black) and with (red) charge interaction. The cut-offs are defined as the energies where the spectra of single recollision electrons drop by three orders of magnitude (symbols in the inset). Blue and red shaded areas indicate energy gains due to trapping field assisted backscattering (TRAB) and Coulomb explosion of the escaping electron bunch (CE), respectively. (b) Top: Blue plus signs represent positive surface charges from residual ions. Red spheres indicate escaping electrons under the effect of space charge repulsion. Bottom: Attractive trapping potential near the surface mediated by residual ions and emitted electrons (blue) and additional repulsive component (red) due to space-charge repulsion among the escaping electrons. Adapted from [LS3].

shaded are in Fig. 4.7(b)). The second gain takes place on a much longer time scale and starts after the laser pulse is off ($\gtrsim 8$ fs), when the emitted electrons have left the vicinity of the surface. This second contribution is attributed to the Coulomb explosion (CE) of the escaping electrons due to the repulse forces within the bunch (cf. red shaded are in Fig. 4.7(b)). The trapping field assisted backscattering (TRAB) will now be investigated in detail.

4.2.1. Trapping field assisted backscattering

The clear separation of the two charge interaction driven enhancement effects (TRAB and CE) by their timescales motivates to identify the relevant regions of the spatio-temporal mean-field potential V_{mf} (see Fig. 4.8(a)). The mean-field potential $V_{mf} = -e\Phi_{mf}$ describes the potential energy of an electron in the electrostatic potential Φ_{mf} and includes two contributions. First, negative areas in the potential landscape (blue) that correspond to the attractive trapping field and result from the charge separation at the surface, i.e. residual ions inside and emitted electrons outside of the material. Second, positive areas (red) representing the space charge repulsion among the emitted electrons. Since the trapping field assisted backscattering takes place during the recollision phase (cf. Fig. 4.7(a)), the evolution of the mean-field potential on this time-scale (indicated by the gray rectangle in Fig. 4.8(a)) is analyzed in more detail, see Fig. 4.8(b). The analysis reveals that the trapping potential develops around -1 fs (i.e. during the first half-cycle of the laser field that significantly contributes to the ionization, cf. Fig. 4.2(b)) and varies only weakly

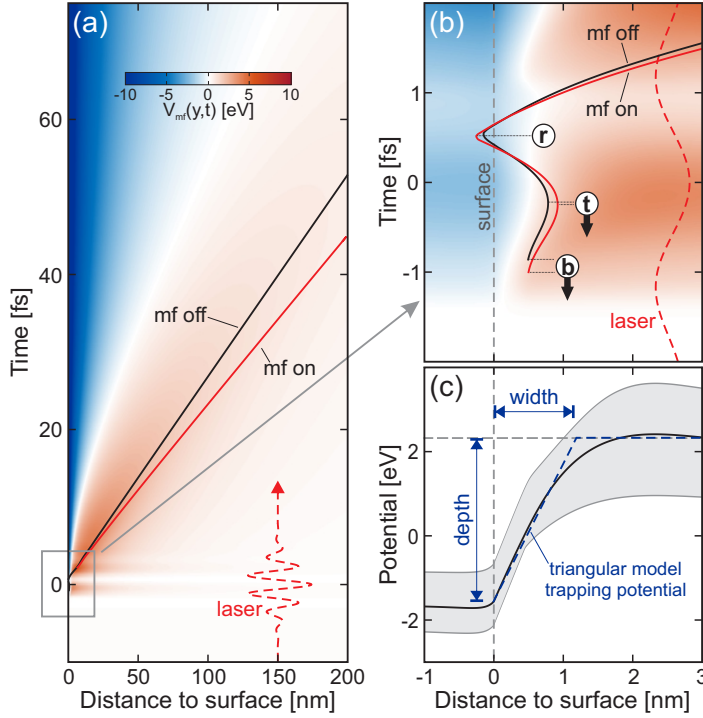


Figure 4.8. Evolution of the mean-field potential $V_{mf}(y, t)$ along the polarization axis. Solid and dashed curves represent trajectories of recollision electrons from Fig. 4.7(a), in- and excluding charge interaction. (b) Zoomed view of the recollision process, cf. gray rectangle in (a). Labeled circles mark birth (b), outer turning point (t) and recollision (r). Arrows show the change of the timings when including charge interaction. (c) Mean-field potential averaged between -1 and 1 fs (black) and its variation within the interval (gray area). Triangular model trapping potential (dashed blue curve). From [LS3].

during the recollision process (between -1 and 1 fs). This weak variation (visualized by the gray area in Fig. 4.8(c)) justifies the following analysis of TRAB via a simplified model considering a static model trapping potential $V(x)$. The shape of the potential, averaged within the above described time-interval (solid black curve in Fig. 4.8(c)), motivates to consider a triangular model trapping potential (dashed blue curve).

Simple Man's Model with static trapping potential

In order to investigate the trapping field assisted backscattering systematically, the conventional SMM is extended to include the trapping field. Trajectories of electrons born at the origin with zero initial velocity are calculated by integration of the one-dimensional classical equation of motion (EOM)

$$\ddot{x}(t) = -\frac{e}{m_e} \mathcal{E}_0 [f(t) \cos(\omega t + \varphi_{ce}) + \epsilon(x)], \quad (4.1)$$

where the effective field contains the laser and the additional trapping field $\mathcal{E}_0 \epsilon(x)$. For generalization (i.e. making the dynamics independent of the specific laser parameters) it is useful to express the equation of motion in terms of scaled variables. By introducing the scaled time (i.e. phase) $\tau = \omega t$ and the scaled displacement $\xi = x/x_q$, where $x_q = \frac{e\mathcal{E}_0}{m_e \omega^2}$ is the quiver amplitude, the generalized EOM reads

$$\ddot{\xi}(\tau) = -[f(\tau) \cos(\tau) + \epsilon(\xi)]. \quad (4.2)$$

The corresponding kinetic energy is then given by $\xi^2/2$ and the ponderomotive energy simply is $1/4$. The electric field of the considered triangular trapping potential is defined as

$$\epsilon(\xi) = \begin{cases} \epsilon_0 & \text{if } \xi < \alpha \\ 0 & \text{otherwise,} \end{cases} \quad (4.3)$$

4. Strong-field electron emission from small dielectric nanospheres

with field strength ϵ_0 and extension (i.e. width of the potential) α . For trajectories returning to the surface ($\xi = 0$) within a full laser cycle after their generation elastic backscattering is assumed. In this simplified model the birth time fully characterizes the trajectory and determines if it corresponds to an electron being emitted directly or after elastic backscattering (cf. Fig. 1.3(b)).

Systematic analysis of the trapping field effect

For the systematic analysis of TRAB, the cut-off energies for direct emission and backscattering as well as the maximal recollision energies are determined from the extended SMM simulations in dependence of the trapping field parameters. The evolution of the three cut-off energies with the trapping field strength and extension is shown in Fig. 4.9 for the limit of long pulses in order to suppress the impact of additional CEP effects. For direct emission (Fig. 4.9(a)) the well-known cut-off energy of $2U_p$ is reproduced in the limit of a vanishing trapping field that can be achieved for either $\epsilon_0 \rightarrow 0$ or $\alpha \rightarrow 0$. For increasing strength and extension of the trapping field, the direct emission cut-off energy is first reduced and eventually direct emission is quenched completely (white area). Also for backscattered electrons (Fig. 4.9(b)) the conventional $10U_p$ cut-off energy is reproduced in the vanishing trapping field limit. However, as opposed to direct emission, increasing the trapping field strength and extension does not result in a reduction of the cut-off. Instead, for a large parameter range (triangular area) the cut-off can be substantially enhanced up to a maximum of $\approx 14.5U_p$ (white arrow). Also the maximal recollision energies (Fig. 4.9(c)) can be enhanced up to $\approx 9U_p$, almost tripling the conventional $3.17U_p$ cut-off for vanishing trapping fields. This strong enhancement effect could be of interest for future nanostructure-based HHG. Note that similar effects have been studied also for HHG in atomic systems in combination with static electric fields [123, LS1].

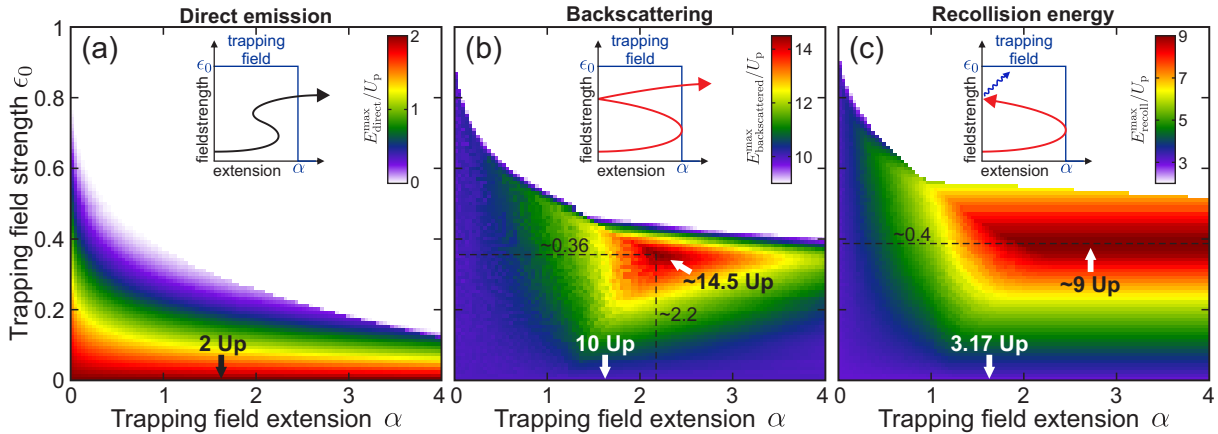


Figure 4.9. Trapping field induced quenching and enhancement of the electron emission from surfaces. (a,b) Final energies of optimal trajectories of electrons emitted directly (a) and after elastic backscattering (b) in dependence of the field strength ϵ_0 and extension α of a triangular trapping potential. (c) Recollision energies of optimal backscattering trajectories in dependence of the trapping field parameters as in (a) and (b). Insets in (a-c) visualize the respective processes. Dashed black lines in (b) and (c) indicate the optimal parameters for the maximal cut-off and recollision energy, respectively. From [LS3].

Pulse length and CEP dependence

The previously discussed results have been obtained in the limit of long pulses, where the predicted maximal enhancements of the backscattering and recollision energies are unaffected by the variation of the field amplitude between the adjacent half-cycles involved in the recollision process. In the case of few-cycle pulses, as used in the reference M³C simulations, the cut-offs are expected to depend strongly on the pulse length and the CEP. To investigate these dependencies, the optimal cut-offs for backscattering and the recollision energies are calculated in dependence of both parameters, see Fig. 4.10. In the limit of long pulses, the cut-offs approach the previously found values of $\approx 14.5 U_p$ for the final energy of backscattered electrons and $\approx 9 U_p$ for the recollision energy (red and blue curves) and variations with the CEP (shaded areas) vanish. For short pulses, with $\lesssim 3$ cycles of the electric field both cut-off energies depend strongly on pulse length and CEP. For extremely short pulses with less than one cycle of the electric field the cut-offs can even be reduced below the conventional values of 10 and $3.17 U_p$. For the pulse parameters in the reference scenario (4 fs and 720 nm, see vertical dashed line in Fig. 4.10) and for $\varphi_{ce} = 0$ the simplified model predicts a cut-off energy for the backscattered electrons of $\approx 13.7 U_p$. This enhancement of around 37% is in reasonable agreement with the enhancement of $\approx 30\%$ found for the reference scenario (cf. Fig. 4.7(a)) and supports that the backscattering process in the full M³C simulations is close to realizing the optimal TRAB process.

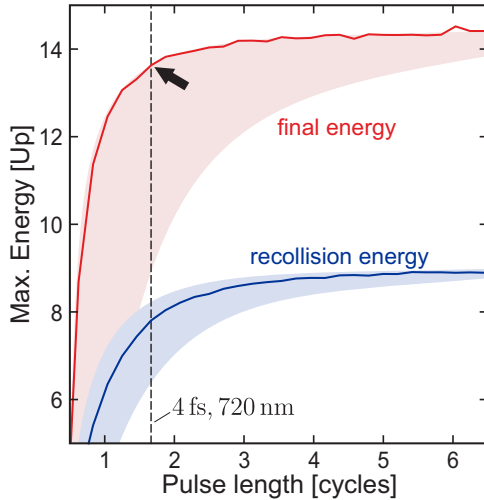


Figure 4.10. Pulse length and CEP dependence of TRAB. Maximal final energy for backscattering (red) and recollision energy (blue) for optimal trapping field parameters (cf. white arrows and dashed lines in Fig. 4.9(b,c)) as function of the pulse length, measured in cycles of the laser field. Solid curves show the results for $\varphi_{ce} = 0$. Red and blue shaded areas indicate the variation of the energies with the CEP. The vertical dashed line indicates the number of cycles (≈ 1.7) corresponding to a 4 fs pulse at 720 nm. Adapted from [LS3].

Impact of TRAB on the optimal backscattering trajectories

So far, the effect of TRAB has only been studied 'empirically' and a clear physical picture of the enhancement mechanism is lacking. To provide this picture, in Fig. 4.11 the optimal backscattering trajectory for optimal trapping field parameters ($\epsilon_0 = 0.36$ and $\alpha = 2.2$, cf. dashed lines in Fig. 4.9(b)) is compared to the conventional optimal trajectory for a vanishing trapping field (compare red vs black curves). The comparison shows that the trapping field leads to an earlier birth time (compare red to black circles labeled with (b)) and an outer turning point that is located further away from the surface and is reached slightly earlier (see (t)). The recollision timing (see (r)) remains the same and is close to the zero-crossing of the electric field at $\pi/2$. These changes of the three characteristic

4. Strong-field electron emission from small dielectric nanospheres

points are in excellent agreement with the results from the reference simulations ex- and including charge interaction (cf. Fig. 4.8(b)).

To finally reveal the mechanism behind the TRAB mediated additional energy gain, the evolutions of the single particle energies

$$E_{\text{sp}}(t) = E_{\text{kin}}(t) + E_{\text{pot}}(t) \quad (4.4)$$

corresponding to the trajectories in Fig. 4.11(a) are compared in Fig. 4.11(b), where the potential energy $E_{\text{pot}}(t) = V(x(t))$ is determined from the local model trapping potential. In both cases, the single-particle energy is zero at the outer turning point. Note that in the case including the trapping field, the outer turning point is located at the end of the trapping potential for the optimal trajectory. The analysis further reveals that in the TRAB process the additional energy is gained during the approach of the electron to the surface (compare energy gains of black and red curve between \textcircled{t} and \textcircled{r}). This can be explained when considering that the single particle energy gain rate [124, 125, LS5, LS11]

$$\frac{d}{dt}E_{\text{sp}}(t) = -e\dot{x}(t)\mathcal{E}(t) + \frac{\partial}{\partial t}V(x, t) \quad (4.5)$$

scales linearly with the electrons velocity $\dot{x}(t)$ and the laser field for a static potential. Since an additional trapping field results in a higher velocity during both approach and departure (compare slopes of red and black trajectories before and after the recollision in Fig. 4.11(a)), the overall energy gain is enhanced.

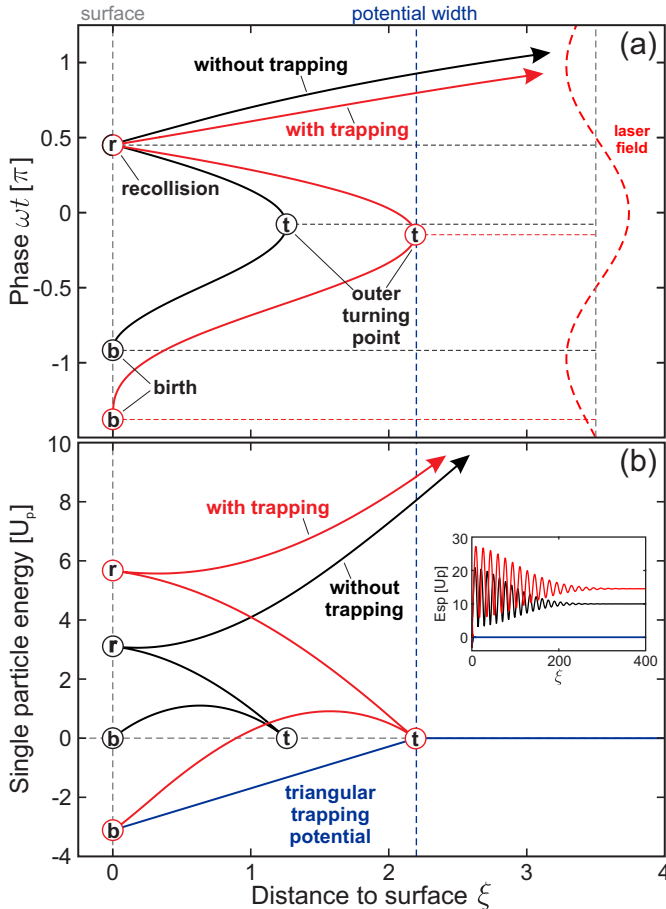


Figure 4.11. Trajectory analysis of TRAB. (a) Optimal recollision trajectories calculated in the long pulse limit via the conventional SMM (solid black curve) and the SMM extended to account for a triangular trapping potential (solid red curve) with strength $\epsilon_0 = 0.36$ and extension $\alpha = 2.2$ (cf. dashed lines in Fig. 4.9(b)). The labeled circles mark birth \textcircled{b} , outer turning point \textcircled{t} and recollision \textcircled{r} of the respective trajectories as in Fig. 4.8(b). (b) Time evolution of the single particle energies E_{sp} corresponding to the respective trajectories in (a). The solid blue curve represents the triangular trapping potential. Vertical dashed gray and blue lines indicate the surface and the end of the trapping potential, respectively. The inset in (b) shows the evolution of the single particle energies on a longer timescale. From [LS3].

4.2.2. Quenching of the material dependence

In the last section, the effect of the charge interaction mediated trapping field on the recollision process has been investigated. This section addresses its additional impact on the tunneling step. When considering that the trapping field counteracts the linear near-field and thus leads to a lowered effective field, two consequences on the tunneling can be expected. First, the ionization probability decreases due to the highly nonlinear scaling of the rate with the local intensity. Second, the classical tunneling exit $x_{te} = I_p/|\mathcal{E}_{nf}|$ increases. However, both the tunneling rate and the tunneling exit not only depend on the strength of the local near-field but also on the material-specific ionization energy. This motivates to explore the effects of charge interaction on the electron emission from different dielectric materials.

To begin the analysis, the combined impacts of the ionization energy and the intensity of the enhanced linear near-field on the electron emission are investigated systematically by performing a set of M³C simulations. Therefore, the ionization energy is varied between 4 eV and 10 eV to cover the range of typical dielectrics and semiconductors. The results of the systematic analysis are shown by the false color plot in Fig. 4.12 that represents a map of the extracted cut-off energies in dependence on ionization energy and peak surface intensity $I^{loc} = \gamma_0^2 I$. The energies are scaled to the ponderomotive energy U_p^{loc} of the maximally enhanced surface field. When assuming that the effects of tunneling exit and charge interaction were negligible this map would show a constant value of $10 U_p^{loc}$. However, as both effects are included in the simulations, the map is more complex. For low intensities ($I^{loc} \lesssim 4 \times 10^{13} \text{ W/cm}^2$), the cut-off energy depends strongly on the ionization energy. In particular, for the largest ionization energy, the cut-off energy approaches zero. This can be attributed to (i) the vanishing ionization rate and (ii) the increasing classical tunneling exit that can eventually quench electron recollisions completely. For low ionization energies, the cut-off strongly increases due to the combined effects of strong charge interaction and decreasing tunneling exit. This strong dependence on the ionization energy decreases for higher surface intensities, which can be explained as follows. At a critical intensity, the ionization-induced trapping field screens the linear near-field completely. Further

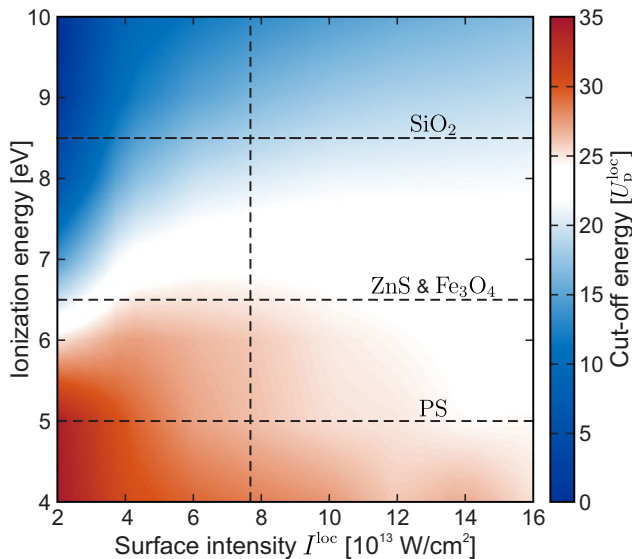


Figure 4.12. Cut-off energies of photoelectrons from $d = 100 \text{ nm}$ spheres under few-cycle pulses (5 fs, 720 nm) in dependence of ionization energy and peak intensity of the enhanced linear near-field as predicted by M³C. The vertical line marks the surface field intensity corresponding to a laser intensity of $3 \times 10^{13} \text{ W/cm}^2$ for SiO₂. Horizontal lines indicate the ionization energies of different dielectric nanoparticles (as indicated). Data published in [LS4].

4. Strong-field electron emission from small dielectric nanospheres

ionization is thus mainly limited by the mean-field instead of the specific impacts of the ionization energy or the local intensity. As the latter two depend both on the specific material, in the high intensity regime charge interaction therefore effectively quenches the material dependence of the photoemission process. For the considered parameters (i.e. nanoparticle size and pulse parameters), the simulations predict a material-independent cut-off around $22 U_p^{\text{loc}}$ for the highest considered local intensity.

Comparison with nanoparticle experiments

To substantiate the predicted quenching of the material dependence, the M³C results are compared to respective experiments where the photoemission has been investigated from four different dielectric materials³. The properties of the studied nanoparticle samples (SiO₂, ZnS, Fe₃O₄, Polystyrene (PS)) and the considered parameters for the simulations are summarized in Table 4.1. Photoelectron spectroscopy measurements revealed that the ionization energy of small silica nanoparticles is around 20 % lower compared to bulk (cf. Fig. 2.7). As the ionization energies of the other nanoparticles are unknown, in the simulations their values are adjusted within the same margin with respect to the literature bulk values for best agreement with the experimental results. The field enhancement factors γ_0 are determined from the enhanced linear near-fields obtained from Mie calculations for the corresponding relative permittivities ϵ_r . The utilized transport cross sections for the elastic collisions within the different materials are given in Appendix E.

The surface intensity-dependent cut-off energies measured for the four materials are shown as black symbols in Fig. 4.13. For comparison, the results of corresponding M³C simulations with and without charge interaction are indicated by the solid and dashed red curves, respectively. Without charge interaction the predicted cut-off energies converge to the classical $10 U_p^{\text{loc}}$ (dark gray area) for high intensities, where the effect of the tunneling exit becomes negligible. For lower intensities, slightly higher energies are possible as a result of the finite tunneling exit. When approaching the lowest intensities, the cut-off for SiO₂ decreases which might hint at the quenching of backscattering because of large tunneling exits due the high ionization energy. However, neglecting charge interaction severely underestimates the experimentally observed cut-off energies for all materials. Taking charge interaction into account results in better agreement of the simulated and

Material	Diameter [nm]	I_p (bulk) [eV]	I_p (np) [eV]	ϵ_r	γ_0
SiO ₂	$(80 - 100) \pm 8 \%$	10.2 [126]	8.5 [96]	2.12 [116]	1.60
ZnS	$136 \pm 33 \%$	7.5 [127]	6.5	5.44 [128]	2.55
Fe ₃ O ₄	$150 \pm 27 \%$	5.8 [129]	6.5	5.86 [130]	2.67
PS	$111 \pm 17 \%$	6.1 [131]/6.95 [132]	5.0	2.50 [133]	1.76

Table 4.1. Properties of studied nanoparticle samples and parameters for the M³C simulations. In the simulations for SiO₂ a diameter of 100 nm was considered. The nanoparticle (np) ionization energies for ZnS, Fe₃O₄ and PS have been extrapolated from the bulk values as stated in the text. The peak field enhancements γ_0 are determined from Mie calculations for the respective nanoparticle diameters and permittivities ϵ_r . From [LS4].

³The experiments have been carried out by the group of Matthias F. Kling at MPQ Garching.

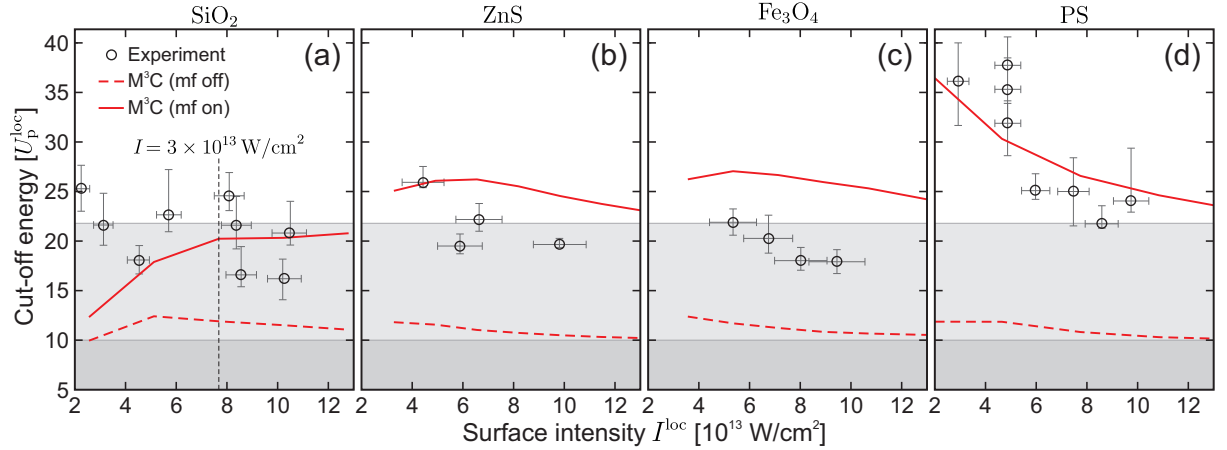


Figure 4.13. (a-d) Measured cut-off energies of electrons emitted from small (a) SiO₂, (b) ZnS, (c) Fe₃O₄ and (d) PS nanoparticles in dependence of the peak intensity at the surface I^{loc} (symbols) and as predicted by M³C simulations excluding (dashed curves) and including (solid curves) charge interaction. The relevant nanoparticle parameters correspond to the values given in Table 4.1. The experimental error bars reflect the uncertainties of the laser intensities and the extraction of the cut-off energies. Gray shaded areas visualize the $10 U_p^{\text{loc}}$ cut-off and an energy of $\approx 22 U_p^{\text{loc}}$. Data published in [LS4].

measured cut-offs. Best agreement is found for silica and polystyrene in the limit of high intensities, where ionization is determined by the mean-field rather than the distinct properties of the tunneling process. The deviations at low intensities could be attributed to both experimental and theoretical limitations. In particular, at low intensities the description of ionization transitions from the tunneling to the multiphoton regime which most likely results in deviations when considering a pure tunneling ionization model. The deviations for ZnS and Fe₃O₄ can most likely be traced back to strong deviations of the nanoparticles shape from spherical geometry, which might result in slightly different field enhancements. Beside the remaining small deviations between experiment and theory, the overall trends in the evolution with intensity are very similar. Most importantly, for the highest intensity, all results seem to converge to a common cut-off energy around 20 to 25 U_p^{loc} which supports the charge interaction induced quenching of the material dependence.

5. Field propagation effects at large dielectric nanospheres

In the last chapter, strong-field driven electron emission has been investigated for dielectric nanospheres that are small compared to the wavelength of the incident pulses. A particularly interesting additional parameter for tailoring the electron dynamics arises if electromagnetic field propagation becomes important. Typically (for non-resonant systems) this requires a size of the nanostructure comparable to the excitation wavelength. In this case, the dipole approximation fails as higher order multipole modes of the incident field contribute substantially to the induced polarization and the resulting linear near-field. For appropriate nanooptical targets, field propagation leads to nanofocusing effects that allow to manipulate the overall near-field structure, including its spatial profile, the position of the hot spots, and the phase evolution across the surface.

The focus of this chapter lies on investigating the influence of field propagation effects on the near-field mediated electron emission from large dielectric nanospheres under intense few-cycle pulses. [Section 5.1](#) is dedicated to systematically analyzing the evolution of the linear near-fields and the electron emission in dependence of the sphere size. After inspecting the structure of the linear near-fields at small and large spheres, the directionality, waveform-dependence and energy scaling of the electron emission are investigated. Particular focus lies on the size-dependent scaling of charge interaction mediated effects on the electron acceleration. [Section 5.2](#) provides a detailed analysis of the electron emission from particularly large nanospheres where the increasing impact of tangential near-field components and the resulting ellipticity of the local fields can result in interesting new physics. Here, a so far unknown acceleration mechanism that is enabled by double recollisions within strongly elliptic near-fields is presented. Some of the results in this chapter have been published in [\[LS5\]](#) and [\[LS6\]](#). The corresponding parts in the discussion follow the presentation in the original publications and include additional comments and background information.

5.1. Strong-field photoemission from nanospheres – from small to large

The spatio-temporal structure of the linear near-field at a dielectric sphere (with given optical properties) is only determined by the sphere size and the excitation wavelength and can be described conveniently by introducing the dimensionless propagation parameter¹ $\varrho = \pi d/\lambda$. Hence, when considering a fixed wavelength, the near-field structure can be

¹Note that this parameter already appeared in the derivation of the Mie solution for the linear near-field (cf. [Eq. 2.48](#)).

5. Field propagation effects at large dielectric nanospheres

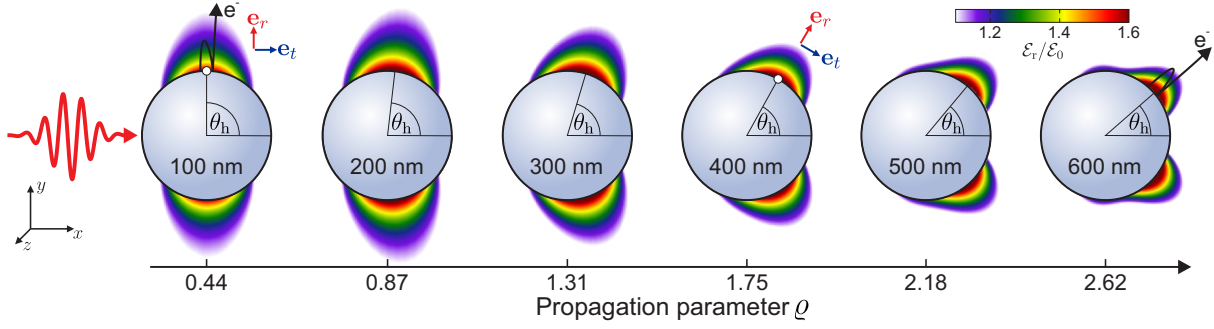


Figure 5.1. Enhancement of the radial linear near-field at silica spheres (false color plots) with respect to the incident 4 fs few-cycle pulse at 720 nm central wavelength (red curve) in dependence of sphere diameter (respective field propagation parameters ϱ as indicated). The characteristic angles θ_h indicates the hot spots (defined via the maximal enhancement at the surface). Red and blue arrows indicate radial and tangential unit vectors, respectively.

adjusted by varying the sphere size. Figure 5.1 shows the maximal relative enhancement of the radial near-field at silica nanoparticles with increasing diameters in the propagation-polarization plane of the driving few-cycle laser pulses. For the so far investigated small nanospheres ($\varrho \ll 1$) the linear near-field can be described well within Rayleigh's quasi-static dipole approximation [134], i.e. neglecting the influence of field propagation within the nanospheres. However, with increasing size this approximation fails and the spatio-temporal near-fields become strongly deformed resulting from the excitation of higher order modes for $\varrho \gtrsim 1$ [89]. The probably most notable effect is the gradual shift of the hot spots regions towards the rear side of the spheres.

5.1.1. Characterization of the linear near-fields

Before studying the impact of the field propagation induced near-field deformation on the electron emission, the main differences of the linear near-fields at small and large spheres are inspected. As the dominant contribution of photoelectrons can be expected to

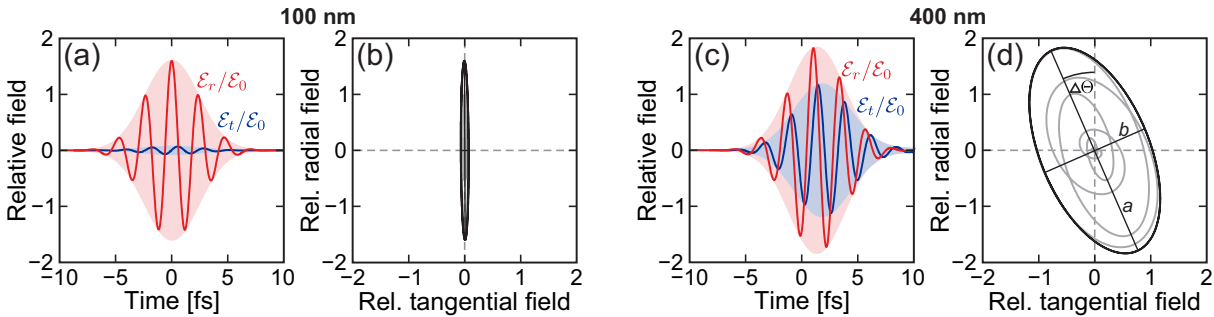


Figure 5.2. Evolution of the linear near-fields at small (a,b) and large (c,d) silica nanospheres. (a,c) Time-evolution of the radial (red curves) and tangential (blue curves) near-field components sampled at the respective hot spots (cf. Fig. 5.1). The individual components are obtained by projecting the vectorial near-field onto the radial and tangential unit vectors (e_r and e_t) as indicated in Fig. 5.1. Shaded areas indicate the field envelopes. (b,d) Combined radial and tangential evolution (gray curves). The polarization ellipses (black curves) yield the ellipticity parameter $\epsilon = b/a$, where a and b are the minor and major axis and the tilt $\Delta\Theta$.

5.1. Strong-field photoemission from nanospheres – from small to large

originate from the hot spot regions, the fields are characterized at the location of maximal enhancement, see white symbols for $d = 100$ and 400 nm in Fig. 5.1. The temporal evolution of the local fields is compared in Fig. 5.2. For the small sphere, the impact of the tangential near-field component is negligible in comparison to the radial field (compare blue and red curves in Fig. 5.2(a)) resulting in almost linear polarization of the local field (see Fig. 5.2(b)). For the large sphere, the enhancements of radial and tangential components are comparable (see Fig. 5.2(c)) and their phase shift leads to a pronounced ellipticity of the vectorial field (gray curve in Fig. 5.2(d)). This ellipticity is quantified via the ellipticity parameter $\epsilon = b/a$, where a and b are the field amplitudes along the major and minor axis of the polarization ellipse (black curve in Fig. 5.2(d)), and the tilt angle $\Delta\Theta$ of the major axis with respect to the local surface normal.

A systematic analysis of characteristic near-field properties in dependence on the nanoparticle diameter is displayed in Fig. 5.3. The map of the relative enhancement of the radial surface field in dependence of the angle θ and nanoparticle diameter in Fig. 5.3(a) clearly shows the field propagation induced near-field deformation. Starting from the upper

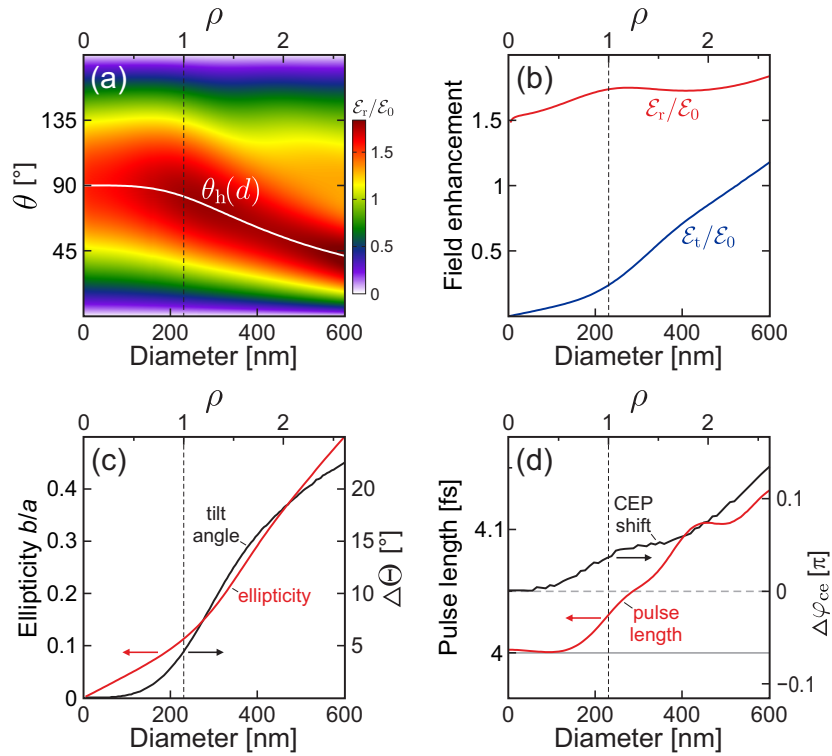


Figure 5.3. Characterization of the linear near-fields in dependence of sphere diameter. (a) Map of the radial surface fields ρ relative enhancement $\mathcal{E}_r(d, \theta)/\mathcal{E}_0$ with respect to the peak field strength \mathcal{E}_0 of the incident few-cycle laser pulse, in dependence of the angle θ sampled at the surface of the upper sphere half in the $z = 0$ plane. The white curve indicates the characteristic angle $\theta_h(d)$ of maximum enhancement. (b) Relative enhancements $\mathcal{E}_{r/t}(d, \theta_h)/\mathcal{E}_0$ of the radial (red) and tangential (blue) surface fields, sampled at the characteristic angle. (c) Ellipticity parameter (red) and tilt angle of the polarization ellipse (black), as defined in Fig. 5.2(d). (d) Effective pulse length (red) and CEP shift (black) of the local radial field. Arrows in (c) and (d) indicate the axis corresponding to the respectively colored curves. Published in [LS5].

5. Field propagation effects at large dielectric nanospheres

pole (90°) for small diameters, above $d \gtrsim 200$ nm ($Q \gtrsim 1$) the characteristic angle (white curve) decreases with sphere size and reaches around 45° for the largest diameter. The enhancements of the radial and tangential near-fields sampled at the characteristic angle in Fig. 5.3(b) reveal that the tangential fields are small for $Q \lesssim 1$ and rapidly increase for larger spheres. The increasing ellipticity parameter (red curve in Fig. 5.3(c)) reflects a gradual transition from linear to elliptic polarization of the local fields. Also the tilt angle of the polarization ellipse (black curve) increases for larger spheres. Further, both the pulse length and the CEP of the local field are robust with respect to the sphere size, see Fig. 5.3(d).

5.1.2. Field propagation mediated directional electron emission

Having characterized the size-dependent evolution of the linear near-field, the impact of the field propagation mediated near-field deformation on the electron emission can now be analyzed. In the previous chapter, the electron energy spectra from small nanoparticles were investigated only with respect to the emission into up- and downward direction. In experiments, such a measurement can for example be realized via a stereo-TOF³ setup [25, 135, 136]. However, in order to analyze the full emission directionality that approach is not sufficient. Instead, collecting the complete directional information, i.e. measuring the full three-dimensional momentum distribution of all emitted photoelectrons, is highly desirable. Unfortunately, this information is not easily accessible in respective strong-field experiments. Hence, in experiments that were performed by the group of

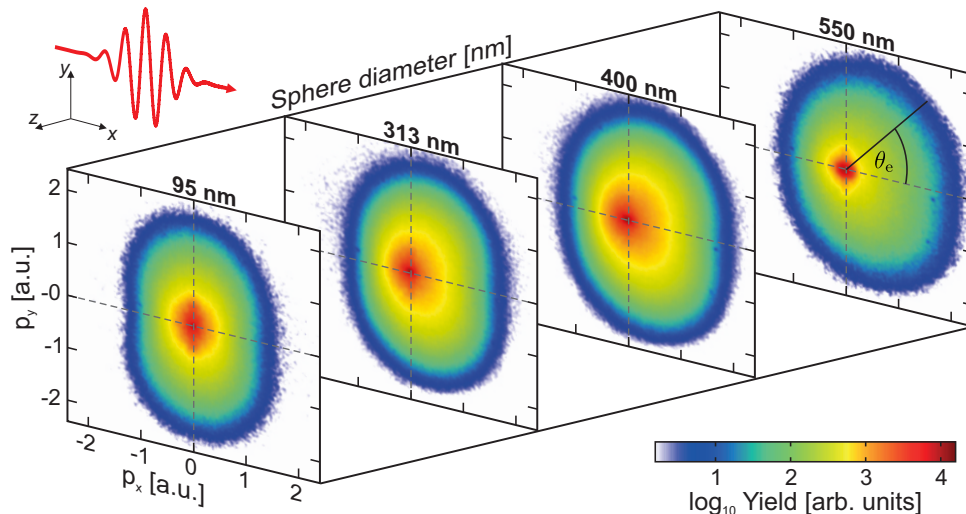


Figure 5.4. CEP-averaged projected momentum distributions measured from SiO₂ nanospheres with 95, 313, 400 and 550 nm diameter via velocity map imaging (averaged over millions of laser shots). Note that the intensity of the incident 4 fs NIR (720 nm central wavelength) laser-pulses (red curve in the top left corner) has been adjusted to reach maximal momenta around 2 a.u. for all sphere sizes². The final emission angle θ_e is defined with respect to the pulse propagation direction (x -axis), see 550 nm image. Experimental data courtesy of M. F. Kling.

²The atomic unit of momentum is 1 a.u. $\approx 2 \times 10^{-24}$ kg m/s. A momentum of 2 a.u. corresponds to a kinetic energy of ≈ 54 eV.

³Time Of Flight

5.1. Strong-field photoemission from nanospheres – from small to large

Matthias F. Kling at MPQ Garching the emitted photoelectrons were detected utilizing a velocity map imaging (VMI) spectrometer where the electrons are accelerated towards a two-dimensional detector by a static electric field (see e.g. [137, 138]). For the chosen geometry, this enabled to measure the momenta of all emitted electrons in the propagation direction (p_x) and polarization direction (p_y) of the laser field. The information on the z -components was lost due to the projection onto the two-dimensional detector.

Measured CEP-averaged momentum projections of the electron emission from SiO_2 spheres with increasing diameters are shown in Fig. 5.4. The peak laser intensities of the individual scans were chosen between $I = 2.8 - 3.7 \times 10^{13} \text{ W/cm}^2$ such that comparable cut-off momenta were obtained for all sizes. The laser pulses were propagating along the x -axis and were linearly polarized along the y -axis. While a symmetric electron distribution with respect to the polarization axis is observed for the smallest nanoparticles, the momentum distributions become increasingly deformed with increasing particle size. In particular, the spectral region including the highest momenta gradually shifts towards positive x -momenta. The corresponding decrease of the final emission angles θ_e of fast electrons from around 90° (in polarization direction) towards the rear-side of the nanospheres strikingly reveals the correlation between field propagation mediated near-field deformation and directional electron emission.

Electron emission as predicted by M^3C

As a first step to identify the physics underlying the experimentally observed directional electron emission and its connection to the near-fields, the electron emission predicted by M^3C is compared for small and large nanospheres. Although the full 3D-information on the emission directionality is accessible in the simulations, only projected momentum maps are analyzed for the sake of comparability to the respective experimental results. Figure 5.5(a,b) shows the calculated CEP-averaged projected momentum maps from a small (a) and a large (b) nanosphere. Similar to the experiment, the projected momentum

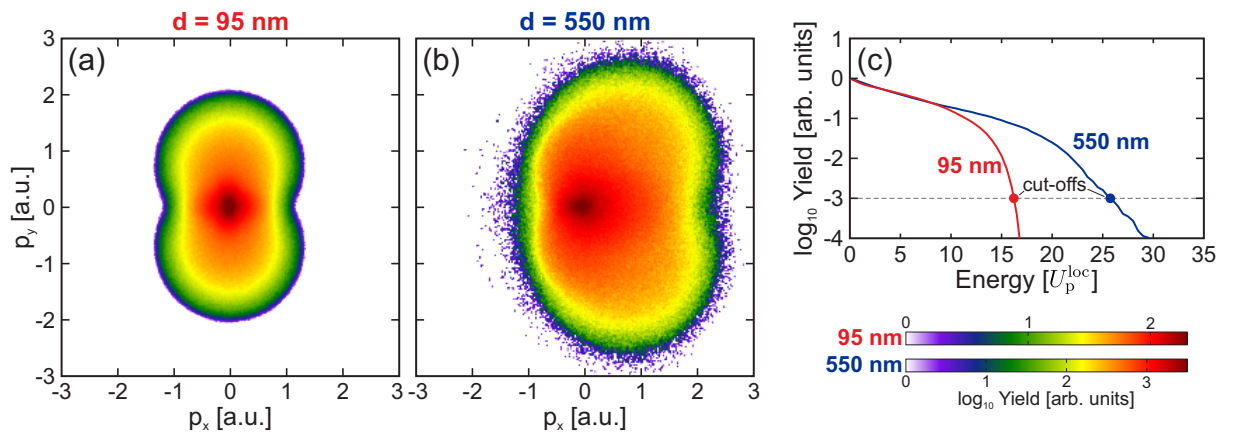


Figure 5.5. Electron emission from small and large silica nanospheres as predicted by M^3C . (a,b) CEP-averaged projected momentum maps of electrons emitted from $d = 95 \text{ nm}$ (a) and 550 nm (b) spheres under 4 fs, 720 nm few-cycle pulses at $3 \times 10^{13} \text{ W/cm}^2$. (c) Corresponding CEP-averaged energy spectra (as indicated). Red and blue symbols indicate the respective cut-off energies as defined in Fig. 4.3.

5. Field propagation effects at large dielectric nanospheres

map for the small sphere reveals a dipolar shape with most energetic electrons emitted along the polarization direction (y -axis). Most importantly, the emission is symmetric with respect to the propagation direction. For the larger sphere this symmetry is broken and the momentum map indicates pronounced emission towards the propagation direction of the incident pulse. The overall good qualitative agreement between experiment and theory motivates to compare the emission also quantitatively. Note that in the experiments the low momentum region may be contaminated with phase-independent contributions such as slow electrons due to thermal electron emission [14] or spurious contributions from residual gas in the vacuum chamber. Hence, for the following analysis only fast electrons close to the respective spectral cut-offs are considered. The latter are defined as those with projected momenta $p > \sqrt{2m_e E_{\text{th}}}$, where the threshold energy is defined as $E_{\text{th}} = 0.5E_c$ and the respective cut-off energies E_c are extracted from the energy spectra, see red and blue symbols in Fig. 5.5(c).

5.1.3. Phase-dependent directional switching

The few-cycle driven measured and predicted electron emission will now be compared quantitatively for small and large nanoparticles. Therefore, the yields of emitted near cut-off electrons in dependence of CEP and emission direction θ_e are analyzed in Fig. 5.6.

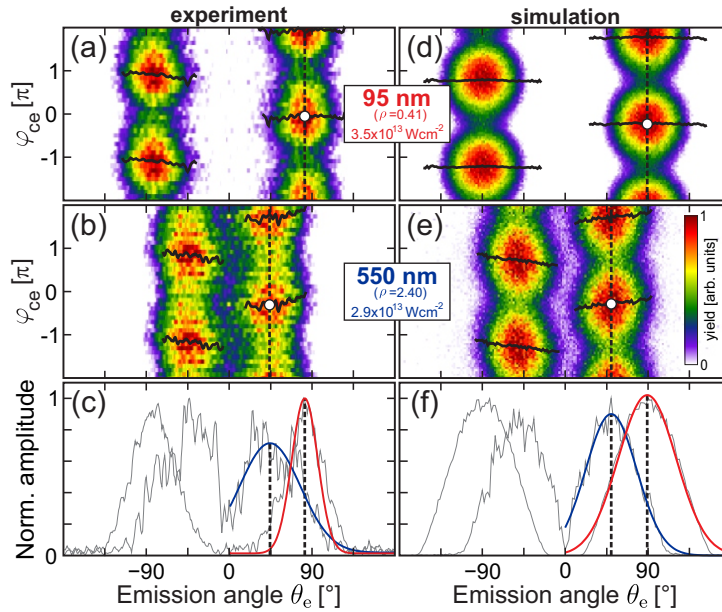


Figure 5.6. Directionality and phase-dependent switching. **(a,b)** Yields $Y(\theta_e, \varphi_{ce})$ of near-cut-off electrons (projected momenta $p > \sqrt{2m_e E_{\text{th}}}$ with threshold energy $E_{\text{th}} = 0.5E_c$) in dependence of final emission angle θ_e and CEP φ_{ce} , measured from small (a) and large (b) silica nanoparticles (parameters as indicated). **(c)** Amplitudes $A(\theta_e)$ (gray curves) extracted from harmonic fits $Y_{\text{fit}}(\theta_e, \varphi_{ce}) = Y_0(\theta_e) + A(\theta_e) \cos[\varphi_{ce} - \Delta\varphi(\theta_e)]$ of the data in (a) and (b). Maxima of the Gaussian fits to the amplitudes for upward emission (red and blue curves) define the critical emission angles θ_e^{crit} (vertical dashed lines). Black curves in (a) and (b) show the phase offsets $\Delta\varphi(\theta_e)$ extracted from the harmonic fits. The phase offsets at the critical emission angles define the critical phase $\varphi_{ce}^{\text{crit}}$ (white symbols). **(d-f)** M³C predictions for the experimental parameters as in (a-c). From [LS5].

For experiment and simulation and both sphere sizes the yields reveal (i) strong phase-dynamics and (ii) signal concentration in narrow angular ranges for up- and downward emission. However, while the phase-dependent up-down switching is similar for both sizes with preferred upward emission (i.e. $\theta_e > 0$) around $\varphi_{ce} = 0$, the emission directions are very different. The emission from the small particles (a,d) is peaked close to $\pm 90^\circ$, i.e. along the laser polarization direction, while the main emission direction is shifted towards the rear side for the larger nanoparticles (b,e) and peaks around $\pm 45^\circ$. To quantify the critical emission angles and phases, the CEP-dependent yields are fitted with harmonic functions (see figure caption). The resulting angle-dependent amplitudes for up- and downward emission and for both sizes are shown as gray curves in Fig. 5.6(c,f). The critical emission angles are defined as the centers of Gaussian fits to these amplitudes for upward emission (red and blue curves). The critical angles (vertical dashed black lines) for small and large particles are close to $\theta_e^{\text{crit}} \approx 90^\circ$ and 45° , respectively, with good agreement between experiment and theory. The critical emission phases $\varphi_{ce}^{\text{crit}}$ are defined as the values of the phase offsets $\Delta\varphi(\theta_e)$ extracted from the harmonic fits (solid black curves in Fig. 5.6(a,b,d,e)) at the critical emission angles and are marked by the white symbols. The measured and predicted critical phases are $\approx 1.9\pi$ for the small and $\approx 1.8\pi$ for the large nanoparticles.

5.1.4. Systematic comparison of simulation and experiment

The excellent qualitative and quantitative agreement of the predictions by the semi-classical simulations with the experimental data motivates a systematic analysis of the impact of the near-field deformation on the electron emission. Therefore, in Fig. 5.7 the evolution of the three previously defined characteristic emission parameters, i.e. (i) the critical emission angle θ_e^{crit} , (ii) the critical phase $\varphi_{ce}^{\text{crit}}$, and the cut-off energy E_c are investigated in dependence of nanoparticle size. First, the analysis of the critical emission angles in Fig. 5.7(a) reveals that the predictions of both SMM (black curve) and M³C (red curve) agree well with the experimental data (symbols). The remaining small offset is attributed to systematic errors in the experiment⁴. Comparing the critical emission angles to the characteristic angles θ_h of the radial Mie-field (solid green curve) and full Mie-field (dashed green curve) supports the dominant impact of the radial components of the surface field on the photoemission process.

Second, the measured critical phase varies only weakly with size and is well-reproduced by the M³C simulations (compare red curve to symbols in Fig. 5.7(b)). The SMM prediction shows the correct phase evolution (black curve) but exhibits an almost size-independent offset to M³C and experiment. The latter can be attributed to the impacts of the classical tunneling exit and charge interaction. For example, the lacking trapping field can result in slightly different timings for the generation of the optimal backscattering trajectories (cf. Fig. 4.11). However, the altogether small variations of the phase with the diameter support the possible application of robust attosecond control of the directional emission.

Finally, comparison of the predicted and measured cut-off energies in Fig. 5.7(c) reveals the following key results. First, the SMM cut-off (solid black curve) almost perfectly follows

⁴For example an inhomogeneous response of the VMI detector.

5. Field propagation effects at large dielectric nanospheres

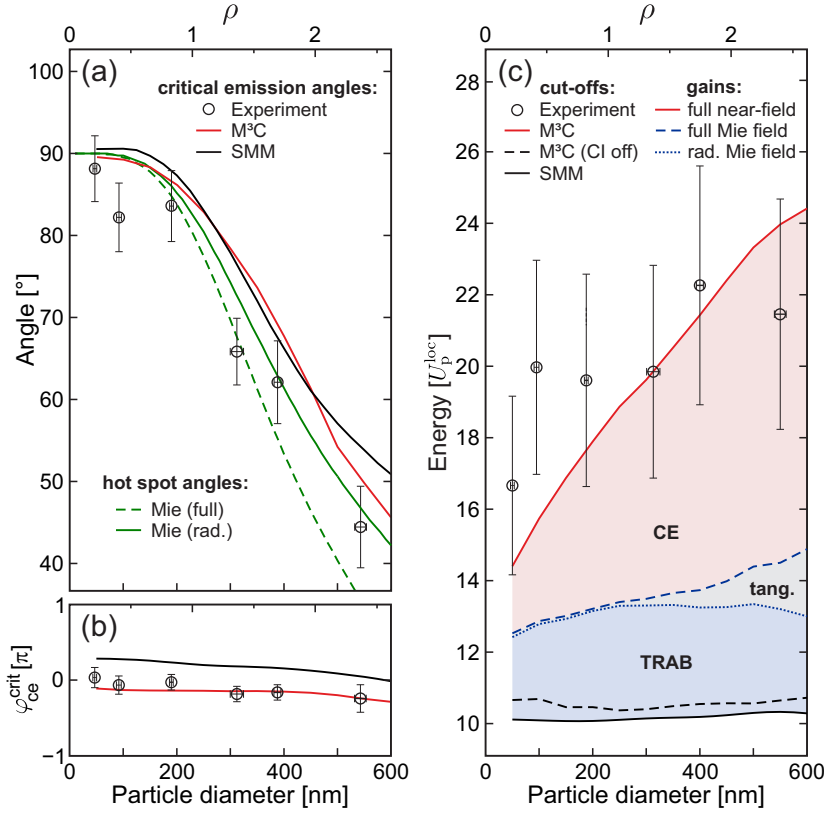


Figure 5.7. Evolution of measured characteristic emission parameters with sphere diameter (symbols) and respective predictions by SMM (solid black curves) and M³C (solid red curves). **(a)** Critical emission angles and angles of maximal enhancement of the radial (solid green) and full (dashed green) linear near-fields. **(b)** Critical phases. **(c)** Cut-off energies and selective energy gains from different field contributions (as indicated). Shaded areas represent the additional energy gains due to TRAB, CE and tangential field effects. Data published in [LS5].

the $10 U_p^{loc}$ law irrespective of sphere size. The cut-offs extracted from M³C simulations without charge interaction (dashed black curve) evolve similar to the SMM result. The small deviation can be attributed to the influence of the classical tunneling exit and small uncertainties in the cut-off evaluation. However, both predictions drastically underestimate the experimental cut-offs (symbols) which can only be reproduced by M³C when including charge interaction (red curve). In this case, the cut-off energies start around $15 U_p^{loc}$ for the smallest investigated spheres and increase almost linearly to around $24 U_p^{loc}$ for $d = 600$ nm. This increase is not attributed to the linear radial near-field as the energies are scaled with respect to the ponderomotive energy of the maximally enhanced radial near-field (cf. red curve in Fig. 5.3(b) for the respective size-dependent enhancement).

Selective energy gain analysis

In the semi-classical simulations, the additional acceleration due to trapping field assisted backscattering (cf. Section 4.2.1) and the Coulomb explosion of the escaping electron bunches is mediated via the self-consistent mean-field. The selective impacts of these acceleration effects and possible additional acceleration due to the increasing near-field ellipticity at large spheres can be disentangled via a selective energy gain analysis. To quantify the selective impacts, the kinetic energy gain

$$\Delta E_{kin} = \int_{t_b}^{\infty} \dot{\mathbf{r}}(t) \cdot \boldsymbol{\mathcal{E}}(\mathbf{r}(t)) dt \quad (5.1)$$

of electrons with final energies equal to the cut-off is evaluated, where t_b is the generation time of the respective trajectories. When taking into account the full near-field, the energy

gain reflects the final energy. Evaluating the integral for the specific contributions to the near-field allows to disentangle the energy gains mediated by the different acceleration mechanisms. The analysis of the selective gains reveals the impact of three specific contributions.

First, when including the radial component of the linear Mie field (dotted blue curve in Fig. 5.7(c)), only the energy gain due to the trajectory modification in the presence of the mean-field is included, while additional acceleration effects mediated by its dynamical evolution are excluded. This allows to isolate the effect of the trapping field assisted backscattering (blue shaded area). The analysis shows that the effect results mainly from the radial electron motion and leads to an additional energy gain of around $3U_p^{\text{loc}}$ which is in good agreement with the predictions of the simplified TRAB model (cf. Fig. 4.9(b)). The small variation with the sphere diameter suggests that the trapping potential depends only on the local charge density at the surface and that the TRAB mechanism is thus insensitive to the nanosphere size.

Second, the acceleration mediated by tangential components of the linear near-field can be studied when integrating over the full Mie field (dashed blue curve). The tangential field effect (gray shaded area) vanishes for small spheres ($d \lesssim 250$ nm) and remains small (but non-negligible) even for larger diameters where radial and tangential field components become comparably strong. This observation further substantiates that the rescattering process is mainly determined by the radial near-field.

Third, the remaining energy gain is attributed to the Coulomb explosion of escaping electron bunches (red shaded area). The impact of the CE increases strongly with sphere diameter and provides the dominant contribution to the overall energy gain for the largest spheres. This can be traced back to the increasing strength of the space-charge repulsion among the escaping electrons due to larger numbers of electrons within the bunches. In contrast to the local TRAB effect, the Coulomb explosion thus appears to be sensitive to the full (non-local) electron distribution.

Time-evolution of the selective energy gains

The timescales on which the additional acceleration via TRAB, due to the tangential fields and by Coulomb explosion of the escaping bunches takes place can be identified via the evolution of the respective selective energy gains. Note that the results of this analysis are similar to the results shown in Fig. 4.7(a). However, instead of comparing the kinetic energy evolution of cut-off electrons from simulations excluding the mean-field, investigating the selective energy gains allows a clear (and well-defined) separation of the contributing mechanisms. The results of the analysis for three different sphere sizes in Fig. 5.8 substantiate that the enhancement due to TRAB (blue shaded areas) evolves on a very short timescale during the recollision process (see blue arrows). The absence of additional energy gain in the later stages of the dynamics (including the later cycles of the field) are a clear indication that the TRAB process takes place close to the surface. Similarly, the additional energy gain from the tangential field components (gray shaded areas) that is only relevant for the largest investigated diameter also develops during the recollision phase (see black arrow in (c)). The Coulomb explosion mediated energy gains (red shaded areas) unfold on a substantially longer timescale, i.e. after the emitted electrons have left the vicinity of the surface.

5. Field propagation effects at large dielectric nanospheres

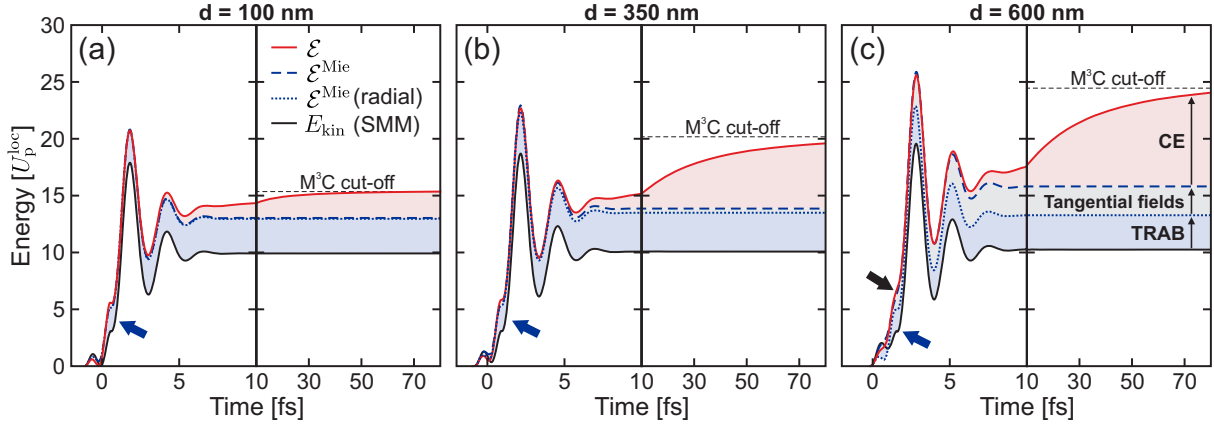


Figure 5.8. Time evolution of the selective kinetic energy gains for three sphere sizes (as indicated). Solid black curves indicate the evolution of the kinetic energies predicted by SMM. Blue and red curves represent the energy gains from selective contributions to the full near-field (as indicated) for cut-off electrons calculated via M³C (averaged for cut-off electrons). Shaded areas indicate the energy gains from TRAB (blue), Coulomb explosion (red) and tangential field effects (gray). Note the different scaling of the time axes before and after the vertical black lines. Data partially published in [LS5].

5.2. Tangential field effects and double recollisions

The selective energy gain analysis revealed that tangential components of the linear near-field start to notably affect the photoemission for large nanospheres ($d \gtrsim 400$ nm) and result in non-negligible contributions to the energy gains. This observation motivates a closer analysis of the electron emission from particularly large nanospheres ($d \gtrsim 600$ nm) where the near-field polarization becomes strongly elliptic (see evolution of the near-field polarization ellipses with sphere size in Fig. 5.9). It turns out that in this regime the spectral cut-off is enhanced by a so far unidentified double rescattering mechanism where the electrons undergo two surface recollision within a quarter-cycle of the field.

To investigate the impact of double recollisions on the photoemission, a systematic analysis of selective energy spectra for electrons emitted from small and large nanospheres at different intensities is shown in Fig. 5.10. As discussed before, direct electrons (gray

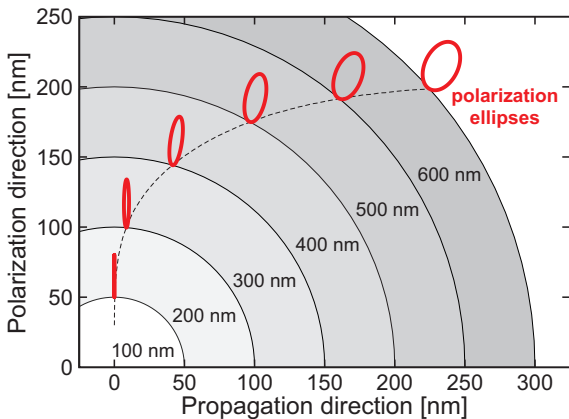


Figure 5.9. Sphere size-dependent near-field polarization at silica nanospheres. Gray circles reflect spheres with increasing diameters (light to dark shaded). The dashed black curve indicates the size-dependent location of the radial linear near-fields hot spots. Red curves visualize the polarization ellipses of the linear near-fields at the hot spots.

curves) dominate the low energy region (up to $2U_p^{\text{loc}}$) for small nanoparticles and low laser intensities (Fig. 5.10(a)). For increasing intensities (Fig. 5.10(b,c)), the emission of direct electrons is suppressed due the ionization induced trapping field. For the largest spheres (Fig. 5.10(g-i)), direct electrons can exceed the conventional $2U_p^{\text{loc}}$ cut-off energy which is attributed to the additional acceleration by tangential field components. For the following analysis, however, they are not of interest due to the comparably low yields and their minor impact on the high-energy spectral region. The latter is dominated by single recollision electrons (black curves) for $d = 100$ and 500 nm for all considered intensities. This changes for the largest spheres where double recollision electrons (red curves) prevail in the cut-off region irrespective of intensity.

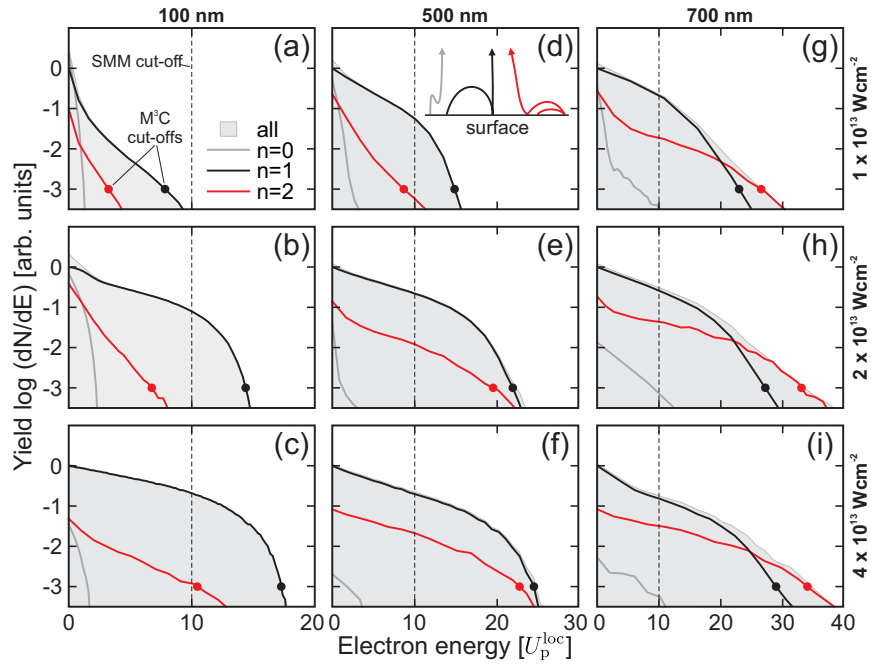


Figure 5.10. Recollision-resolved CEP-averaged M^3C energy spectra for different sphere diameters and laser intensities (as indicated). Gray shaded areas show the full spectra. Solid curves represent selective spectra for direct emission ($n = 0$, gray), single recollision ($n = 1$, black), and double recollision ($n = 2$, red), cf. schematic trajectories in (d). Spectra are normalized to the yield of single recollision electrons at $E = 0$. Energies are scaled to the ponderomotive potential of the maximally enhanced linear near-field and cut-offs of single and double recollision electrons (black and red symbols) are defined as in Fig. 4.3. Dashed vertical lines mark the conventional $10U_p^{\text{loc}}$ cut-off. Adapted from [LS6].

5.2.1. Evolution of electron yields and cut-off energies with size

Before inspecting the double rescattering mechanism in more detail, the scaling of single and double recollision electron yields and cut-off energies will be analyzed systematically in dependence of laser intensity and nanoparticle size. The analysis of the yields⁵ in Fig. 5.11 reveals two trends. First, the yields of single and double recollision electrons increase almost

⁵A quantitative comparison of measured and calculated yields for similar parameters is presented in [LS5] and supports the validity of the yields as predicted by the semi-classical simulations.

5. Field propagation effects at large dielectric nanospheres

linearly with the intensity of the incident laser field for all investigated sphere sizes, see black and red curves Fig. 5.11(a). This observation is in stark contrast to the predictions of the SMM, where the electron yield depends only on the local tunnel ionization rate. Since this rate typically scales exponentially with intensity, one would also expect an exponential increase of the overall electron yield. Hence, the linear scaling predicted by the M³C simulations supports the quenching of tunnel ionization due to charge separation at the surface.

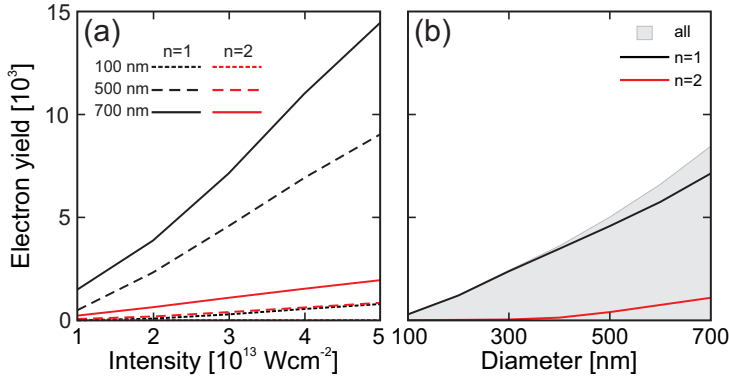


Figure 5.11. Single (black) and double (red) recollision electron yields. (a) Yields in dependence of laser intensity for three nanosphere diameters (as indicated). (b) Yields of all electrons (gray area) and selective yields against nanoparticle diameter for $I = 3 \times 10^{13} \text{ W/cm}^2$ (cf. vertical line in (a)). From [LS6].

Second, the yields increase nearly linearly also with the nanoparticle size when considering a fixed laser intensity (here, $I = 3 \times 10^{13} \text{ W/cm}^2$), see Fig. 5.11(b). This observation can as well be understood via space charge induced trapping in the following simplified picture. Assuming sequential emission of electrons, the total charge Q of the sphere increases with each escaping electron, resulting in the generation of an attractive Coulomb field. When considering that all electrons start with a given kinetic energy, their emission is quenched after reaching a critical charge $Q_{\text{crit}} = eN_{\text{crit}}$ where the respective Coulomb potential overcomes the electrons initial energy. As the Coulomb potential scales proportional to Q/R , this simplified picture predicts that the number of electrons N_{crit} that may be emitted before the onset of quenching scales linearly with the sphere radius⁶ R . The good agreement of the M³C results with the prediction of this simplified model signifies the space charge induced trapping effect.

The scaling of the cut-off energies for single and double recollision electrons in dependence of laser intensity is shown in Fig. 5.12(a) for three selected sphere sizes. Irrespective of the particular size, the cut-off energies of both single and double recollision electrons (black and red curves) first increase with intensity for $I \lesssim 2 \times 10^{13} \text{ W/cm}^2$. Further increasing the intensity results in no substantial enhancement due to the quenching of the ionization as discussed in Sec. 4.2.2.

Most importantly, when considering a fixed laser intensity, the simulations reveal that the cut-off energy of double recollision electrons increases faster with sphere size compared to the single recollision cut-off, see Fig. 5.12(b). Although for the so far investigated spheres with $d \lesssim 600 \text{ nm}$ the conventional single recollision process prevails, for larger spheres the double recollision process becomes more efficient and becomes dominant near the

⁶Please note that this simplified picture is similar to frustrated multistep ionization of XUV driven clusters [139–141].

cut-off. Note that despite the more efficient acceleration process, the overall yield of double recollision electrons is comparably small (compare red to black curve in Fig. 5.11(b)).

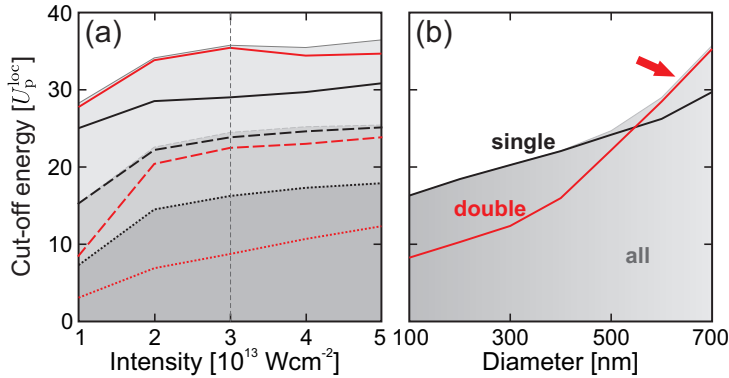


Figure 5.12. Cut-off energies of single and double recollision electrons. (a) Intensity-dependent cut-offs of selective single and double recollision energy spectra (legend as in Fig. 5.11(a)) and from respective full spectra (dark to light gray areas). (b) Cut-offs against sphere diameter for $I = 3 \times 10^{13} \text{ W/cm}^2$ (cf. vertical line in (a)). Adapted from [LS6].

5.2.2. Trajectory analysis of single and double rescattering

The origin of the increasing impact of double recollisions for the cut-off energies predicted for large nanospheres can be unraveled via a systematic trajectory analysis. Thereto, typical single and double recollision trajectories of electrons with final energies close to the respective cut-offs are analyzed for the largest investigated sphere with $d = 700 \text{ nm}$ (for $I = 4 \times 10^{13} \text{ W/cm}^2$ where the effect is most pronounced). To disentangle the selective impacts of their radial and tangential motion, the evolution of the two respective components of their positions, local electric fields and velocities are compared in Fig. 5.13.

As a starting point of the analysis, the evolution of the single recollision trajectory (black curves) is briefly discussed. It is launched (indicated by the black circles labeled with ⑥) at the classical tunneling exit (note the radial offset in Fig. 5.13(a)) close to the minimum of the local radial electric field (Fig. 5.13(b)) with zero initial velocity (Fig. 5.13(c)). Subsequently, the electron is accelerated by the radial and tangential fields, leading to large radial and tangential excursions before the recollision (indicated as ①). The timing of the recollision at the minimum of the tangential field and the zero-crossing of the radial field results in an almost purely radial recollision as the tangential velocity is small. This leads to an essentially radial jump of the velocity at the recollision (indicated by the gray line and ① in Fig. 5.13(c)) that allows for efficient radial acceleration during both the approach and the escape phase. After the recollision the electron undergoes a trivial radial and tangential quiver motion (see elliptical feature around $v_r \approx 5 \text{ \AA/fs}$ in Fig. 5.13(c)) followed by an additional almost purely radial acceleration due to the space charge repulsion within the escaping electron bunch (dotted black curve in Fig. 5.13(c)).

The double recollision trajectory (red curves) unveils a clearly different mechanism. Although it also starts at the classical tunneling exit (⑥ in Fig. 5.13(a)), the excursion in radial direction is significantly smaller in comparison to the single recollision trajectory during the full recollision process, while pronounced tangential motion is found between the two recollisions (① and ②). The timing of the second recollision is close to the zero-crossing of the radial field, resulting in efficient radial acceleration during the final escape similar to the single recollision case. The first recollision takes place close to the

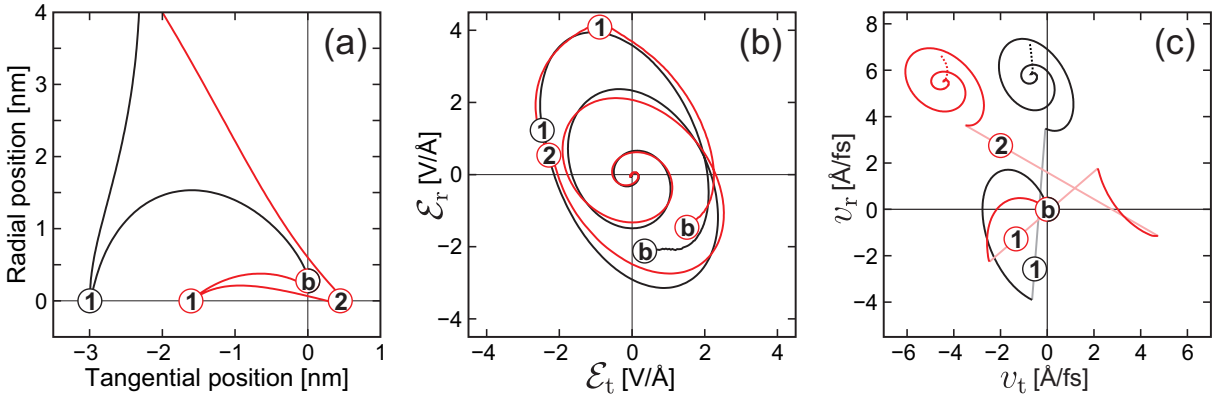


Figure 5.13. Trajectory analysis of single and double rescattering. (a) Evolution of radial and tangential excursion with respect to the birth position of typical trajectories extracted for cut-off electrons emitted from 700 nm silica spheres after single (black) and double (red) rescattering. Labeled circles indicate the moments of birth (b), the first (1) and second (2) recollision and correspond to (b) and (c). (b) Evolution of the elliptic local near-fields, sampled along the respective trajectories. (c) Evolution of the velocity components. Jumps in the velocities at the moments of recollision are indicated as light grey and light red lines. The elliptical features (around $v_r \approx 5 \text{ \AA/fs}$) reflect the trivial radial and tangential quiver motions after the recollision phase. The dotted ends of the curves show the additional (mainly radial) velocity gain mediated by the space-charge driven Coulomb explosion of the escaping bunches. The radial and tangential components of the properties shown in (a-c) are calculated with respect to the unit vectors as defined in Fig. 5.1. Adapted from [LS6].

zero-crossing of the tangential field (1 in Fig. 5.13(b)). This is the key for efficient tangential acceleration which requires the tangential velocity and the tangential field to have opposite signs for as long as possible. For the displayed trajectory, this is realized by the first recollision that flips the tangential velocity close to the zero-crossing of the tangential field (cf. 1 in Fig. 5.13(b,c)).

5.2.3. Selective energy gains for single and double rescattering

After inspecting the evolution of typical single and double rescattering trajectories, the temporal evolution of averaged trajectories and their respective energy absorption is depicted in Fig. 5.14. The averaged trajectories are calculated from ensembles of trajectories with final energies close to the respective single and double recollision cut-offs. While the averaged single recollision trajectory (black curve in Fig. 5.14(a)) resembles the conventional backscattering scenario (cf. Fig. 4.4), the averaged double rescattering trajectory reveals two subsequent recollisions that are separated by around 500 as with the second recollision being timed similarly to the single recollision process.

In order to substantiate the above introduced picture of strong energy gain from the tangential near-field components via double rescattering, the selective single-particle energy gains corresponding to the averaged trajectories are analyzed during the recollision phase, see Fig. 5.14(b). For the single recollision process, most of the energy is gained from the radial Mie field (dashed black curve) during approach to and escape from the surface (left and right of the vertical black line, cf. Fig. 5.14(a)). This results in two 'steps' (steep

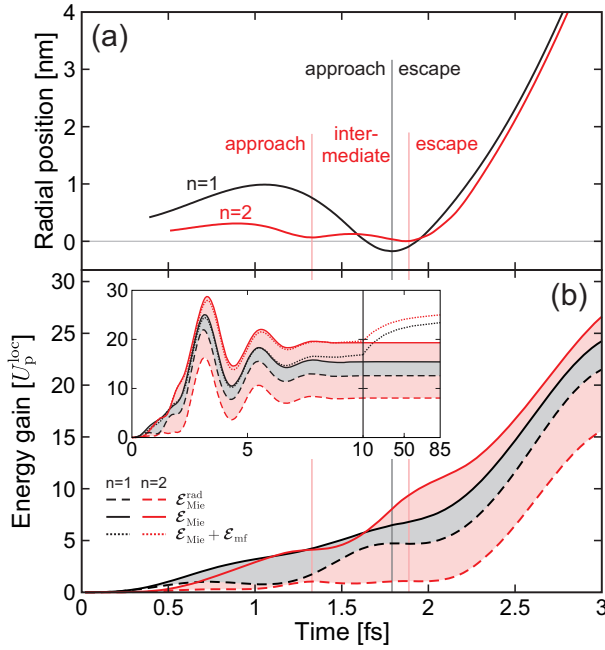


Figure 5.14. Energy absorption for single and double recollisions. **(a)** Averaged radial trajectories of electrons emitted from 700 nm silica spheres after one (black) and two (red) recollisions with final energies close to the cut-offs of the respective energy spectra ($\pm 1\%$ of the cut-off energy in Fig. 5.10(i)). Vertical lines indicate the average recollision timings, separating the phases of the recollision processes (as indicated). **(b)** Selective energy gains corresponding to the averaged trajectories in (a) during the recollision process, calculated from different near-field contributions (as indicated). Gray and red shaded areas reflect the energy gain from the tangential components of the Mie field. Inset: evolution on a longer timescale. From [LS6].

increases) of the energy gain before and after the recollision (see dashed black curve around $t \approx 1.5$ and 2.5 fs). The additional energy gain from the tangential component of the Mie field (gray area), i.e. the difference between the gains from the full (solid black line) and radial Mie field, is comparably small.

In the case of double rescattering, the energy gain from the radial component of the Mie field (dashed red curve) is small during the approach phase and in-between the two recollisions (cf. vertical red lines). Only after the second recollision, i.e. during the final escape, substantial energy is gained from the radial Mie field, similar to the single rescattering process (compare slopes of the dashed black and red curves during the escape phase). Despite the low energy gain from the radial field during the first two phases of the double recollision process, the final energy gained from the full Mie field (solid red curve) exceeds the energy gain in the single recollision process. The reason is the substantial energy gain from the tangential Mie field (red area) during the approach and intermediate phase. The combined effects of tangential and radial components thus lead to three 'steps' in the energy gain from the Mie field, resulting in the large impact of double recollisions for the cut-off energies predicted for large nanospheres.

For both, single and double rescattering, the energy gain from the full near-field (Mie field and mean-field) is comparable to the gain from the Mie field during the recollision phase (compare dotted to solid curves for small times in the inset of Fig. 5.14(b)). On a longer timescale, Coulomb explosion of the escaping bunches leads to an additional energy gain.

5.2.4. Emission directionality of single and double rescattering

After clarifying the impacts of the tangential fields on the acceleration dynamics and the energy spectra, now also their effect on the emission directionality of single and double recollision electrons will be inspected. Thereto, the correlation of their birth angles θ_b

5. Field propagation effects at large dielectric nanospheres

and emission angles θ_e is analyzed in Fig. 5.15. The two relevant limiting cases of the electron emission and the corresponding signatures in the correlation maps are illustrated schematically in Fig. 5.15(a). Undirected isotropic emission from a small surface region (red arrows), i.e. a sharp distribution of birth angles and a broad distribution of final angles, corresponds to a vertical signature in the correlation map. Radial emission, where birth and final angles are equal (blue arrows), corresponds to a diagonal correlation signature.

The correlation maps of fast electrons emitted from small and large nanoparticles at low and high intensities after one or multiple recollisions ($n > 0$) are compared in Fig. 5.15(b-e). For small nanoparticles, the correlation maps at both intensities (b,c) exhibit two signatures around $\pm 90^\circ$, indicating pronounced emission along the laser polarization axis. Although the overall directionality is robust with respect to intensity, the orientation of the features changes. In particular, the rotation from almost vertical alignment at low intensity to nearly diagonal alignment at high intensity reflects the transition from undirected to radial emission. This effect can be attributed to the increasing strength of the trapping potential acting as a filter for radial emission, as only electrons with a large radial velocity can escape the attractive trapping field. For large spheres (d,e) the emission is peaked around $\pm 40^\circ$ irrespective of intensity. In this case, however, the transition from undirected to radial emission is much less pronounced. This observation is a strong hint at the increasing importance of tangential field components that suppress emission of electrons with purely radial momenta.

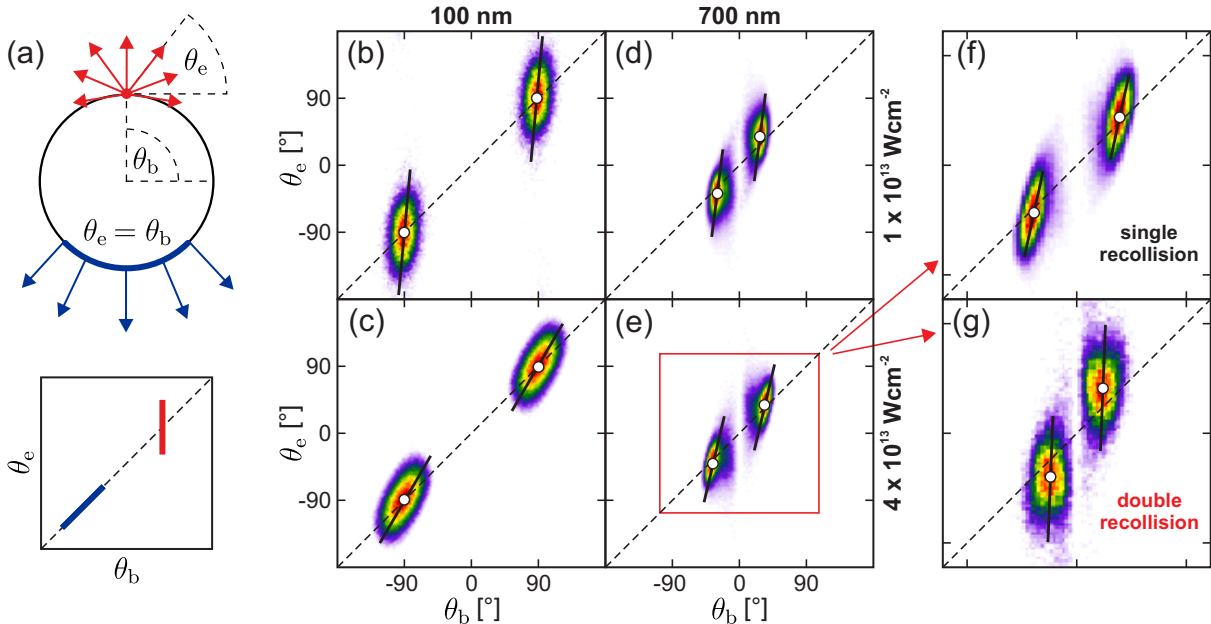


Figure 5.15. Correlation between birth angles θ_b and emission angles θ_e of electrons emitted from nanospheres. (a) Schematic visualization of the correlation between the two angles for undirected (red) and radial (blue) emission. (b-e) Correlation maps for fast ($E > 0.5E_c$) recollision electrons ($n > 0$) from small and large spheres under low and high intensities (as indicated) as predicted by M³C. Dashed diagonal lines indicate perfectly radial emission with $\theta_e = \theta_b$. Solid black lines visualize the tilts of the individual signatures. (f,g) Selective correlation maps for single (f) and double (g) recollision electrons for the scenario in (e), see red box. Adapted from [LS6].

The emission directionalities of single and double recollisions are disentangled in the selective correlation maps in Fig. 5.15(f,g). The analysis reveals two peculiar effects of the double recollision process. First, compared to the single recollision case, the signatures are oriented more vertical and second, they exhibit a small offset from the diagonal. Both characteristic features signify the deviation from purely radial emission due to stronger tangential acceleration.

Suggested strategy for verifying double recollisions experimentally

The so far experimentally unresolved double recollision mechanism might enable a better understanding of recollisions at surfaces of nanostructured solids and thus represents a promising perspective for future studies. For example, it could help to gain deeper insights into the microscopic features of the backscattering process or even reveal effects from surface roughness of the investigated materials. However, double recollisions have not yet been observed experimentally due to investigating only nanospheres with diameters up to 550 nm. Although the simulations predict that double recollisions influence the cut-off energy region for slightly larger nanoparticles, the cut-off enhancement alone might not be sufficient for the desired experimental verification. Therefore, the impact of double recollisions on other experimentally accessible observables is now briefly reviewed.

Based on the representation introduced in Fig. 5.6, the emission directionality and phase-dependent switching of single and double recollision electrons emitted from 700 nm silica spheres under few-cycle pulses at $I = 4 \times 10^{13} \text{ W/cm}^2$ is analyzed in Fig. 5.16(a,b). For the analysis, only fast electrons with energies above the threshold $E_{\text{th}} > 0.75E_c$ have been considered. Comparison of the single and double recollision yields reveals two key differences. First, the critical emission angle of double recollision electrons ($\approx 47^\circ$) is slightly larger as compared to the single recollision case $\approx 39^\circ$, compare vertical dashed lines in Fig. 5.16(a,b). Note that this is in good agreement with the larger emission angles observed in the correlation analysis (i.e. the offset from the diagonal in Fig. 5.15(g)). Second, for double rescattering, the critical CEP is lower ($\approx -0.5\pi$ for double recollision vs. $\approx -0.1\pi$ for single recollision).

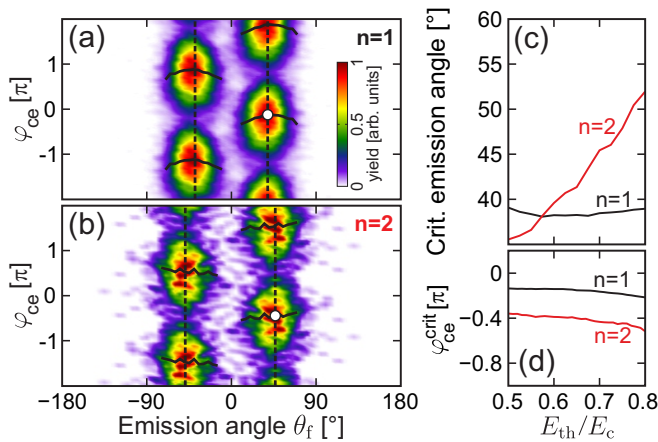


Figure 5.16. Directionality and phase-dependent switching of single and double recollision electrons from 700 nm nanospheres. (a,b) Yields of near-cut-off single (a) and double (b) recollision electrons in dependence of emission angle and CEP. Vertical lines, black curves and white dots indicate critical emission angles, phase offsets and critical CEPs as defined in Fig. 5.6. (c,d) Critical emission angles (c) and phases (d) of single and double recollision electrons in dependence of threshold energy. From [LS6].

5. Field propagation effects at large dielectric nanospheres

The difference of the critical emission angles is particularly promising for the experimental verification of double rescattering as it is easily accessible via VMI measurements. The dependence of emission angles and CEPs on the selected threshold energy E_{th} is compared for single and double recollision electrons in Fig. 5.16(c,d). For the single recollision case (black curves), the results signify the robustness of the analysis with respect to the threshold. Especially the weak variation of the critical emission angle with the threshold energy (black curve in (c)) substantiates the radial nature of the emission of single recollision electrons over a broad energy range. As opposed to that, the critical emission angle of double recollision electrons (red curve in Fig. 5.16(c)) increases strongly for larger thresholds. This reflects the strong impact of the tangential field on the electron acceleration, where stronger tangential acceleration results in higher energies but also leads to pronounced deviations from radial emission. This particular dependence might be important for the observation of double recollisions in future experiments.

6. Attosecond streaking on dielectric nanospheres

This chapter is dedicated to the theoretical investigation of attosecond streaking on dielectric nanospheres. The particular aim is to clarify the physical processes and their specific contributions to the streaking delay that was measured in the first streaking experiment for a dielectric material carried out recently by the groups of Matthias F. Kling and Francesca Calegari in Milano. The experimental setup and the strategy to discriminate signals from a gas reference and nanoparticles, that are simultaneously recorded within the same measurement, are presented in [Section 6.1](#). Afterwards, the streaking spectrograms obtained for the reference and the nanoparticles and their respective streaking delays are inspected. The processes that contribute to the delays are investigated via M³C streaking simulations in [Section 6.2](#). After establishing that the model captures the relevant physics by benchmarking the simulations against the experiment, the specific contributions to the streaking delay are studied individually. The particularly dominant contribution from electron transport in the dielectric is explored in [Section 6.3](#) where the selective impacts of elastic and inelastic electron-atom collisions are analyzed systematically. The simulations substantiate that the streaking delay is mainly sensitive to the inelastic scattering time in the case of dielectrics. To explain this observation, the underlying physical picture for the collisional delay is provided by a simplified model for attosecond streaking from surfaces. Note that substantial parts of the results are published in [[LS7](#), [LS8](#)] and are revisited here for convenience. The respective parts of the discussion follow that in the publications and include additional background information.

6.1. The attosecond streaking experiment

The setup of the attosecond streaking experiment is illustrated schematically in [Fig. 6.1](#). A beam of isolated $d = 50$ nm silica nanoparticles is delivered to the interaction region and

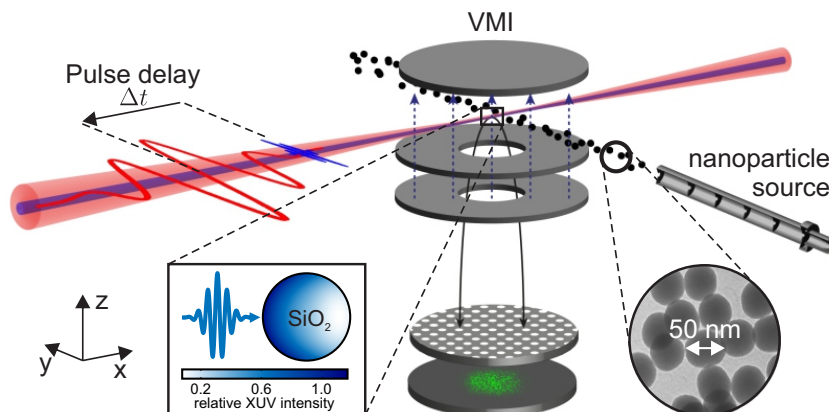


Figure 6.1. Schematic setup of the streaking experiment. Synchronized attosecond XUV and few-cycle NIR pulses are shot on a beam of isolated silica nanoparticles. Emitted electrons are detected using a velocity map imaging spectrometer. From [[LS7](#)].

6. Attosecond streaking on dielectric nanospheres

irradiated by isolated 250 as XUV pulses (central photon energy ≈ 28 eV, peak intensities $\approx 2 \times 10^{12}$ W/cm²) and synchronized 5 fs NIR pulses (central wavelength ≈ 720 nm, peak intensities $\approx 1 \times 10^{12}$ W/cm²) with adjustable pulse delay¹ Δt . Emitted electrons are recorded using a single-shot VMI spectrometer.

6.1.1. Data discrimination

A meaningful interpretation of the attosecond delays recorded in the streaking experiment requires a suitable reference measurement. The latter can be provided by a corresponding streaking experiment on gas targets. However, as the attosecond delays might be particularly sensitive to small variations of the experimental conditions, the gas reference and the nanoparticle signal have to be recorded simultaneously within the same experiment. Such a measurement can be realized by utilizing a very low density of silica particles in the nanoparticle beam, such that only a portion of laser shots hits one (or multiple) nanoparticles. In this way, the reference measurement is provided by laser shots that hit only residual gas while nanoparticle hits provide the signal. Evaluating such a simultaneous measurement requires a reliable method to distinguish gas from nanoparticle hits.

In this experiment, the discrimination of the measured data relies on the knowledge of how gas and nanoparticle hits contribute to the projected momentum distributions recorded in the VMI measurement. Figure 6.2(a,b) shows a comparison of two typical single-shot momentum distributions. The first one in Fig. 6.2(a) was recorded in an experiment where no silica particles were delivered to the interaction region, such that the detected events are attributed to electron emission from the residual gas. A significantly higher number of events can be recorded when performing the experiment with nanoparticles, see Fig. 6.2(b). Histograms of the events per shot recorded for millions of laser shots for the two respective experiments are depicted in Fig. 6.2(c). While both distributions are peaked around 50

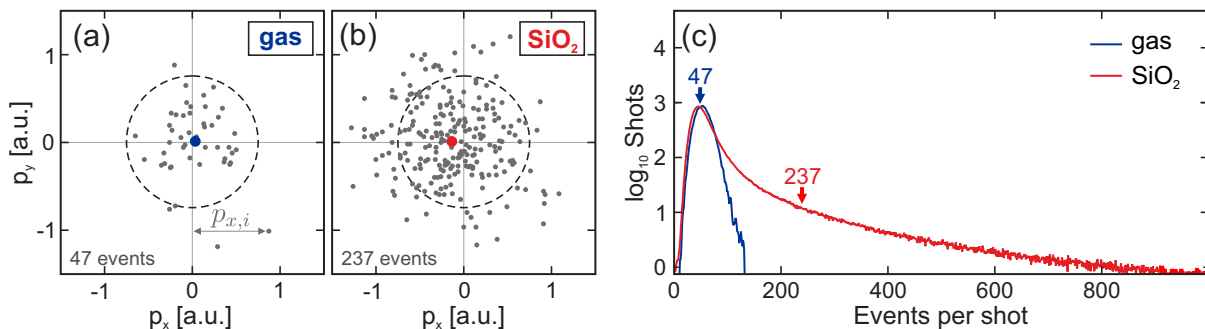


Figure 6.2. Discrimination of measured streaking data. (a,b) Typical single-shot VMI momentum projections recorded from a gas-only measurement (a) and when including silica nanoparticles (b). Dashed circles indicate the low momentum region (< 0.75 a.u.), where the measured signal contains additional contributions from residual gas background. The grey arrow in (a) illustrates the x-component of the projected momentum of the i -th measured event. Blue and red dots in (a) and (b) indicate the respective averaged projected momenta $\langle \mathbf{p} \rangle = \frac{1}{n} \sum_{i=1}^n \mathbf{p}_i$. (c) Histogram of detected events per shot for gas-only (blue) and with silica nanoparticles (red). Adapted from [LS7].

¹A positive pulse delay reflects that the NIR pulse arrives after the XUV pulse.

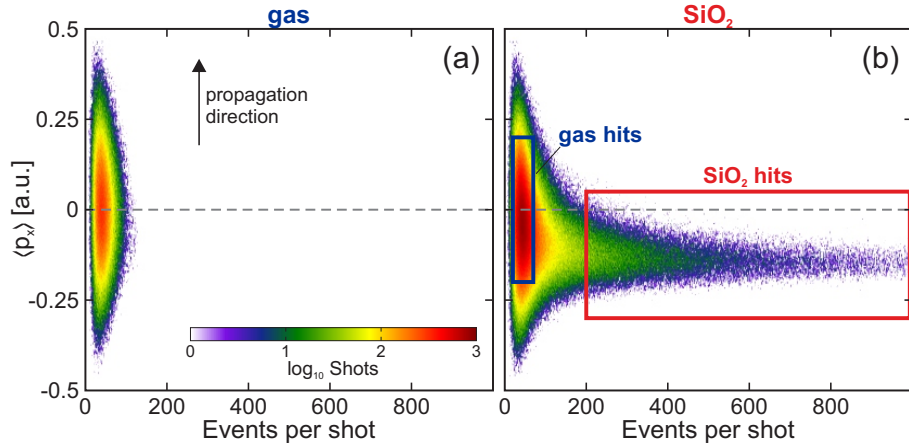


Figure 6.3. Maps of the correlation between the number of events (cf. Fig. 6.2(c)) and the x -components of the averaged momenta (cf. blue and red dots in Fig. 6.2(a,b)) $\langle p_x \rangle$ per shot for measurements only on gas (a) and when including silica nanospheres (b). Blue and red rectangles in (b) indicate the selected shots attributed to gas hits (blue) and nanoparticle hits (red). Adapted from [LS7].

events, the histogram for the gas-only experiment (blue curve) exhibits a sharp cut-off close to 150 events. For the experiment including nanoparticles (red curve), the histogram has a long tail extending to over 800 events per laser shot. This observation allows two conclusions. First, even when including nanoparticles, a significant amount of laser shots results only in a low number of measured events, suggesting that no nanoparticles were hit in the respective shots. Second, hitting a nanoparticle can result in a significantly higher number of recorded events. Hence, gas and nanoparticle hits could already be discriminated purely based on the number of measured events.

The discrimination can be further improved by considering the mean momentum in propagation direction

$$\langle p_x \rangle = \frac{1}{n} \sum_{i=1}^n p_{x,i} \quad (6.1)$$

averaged for each laser shot, where n is the number of events and $p_{x,i}$ is the x -component of the momentum of the i -th event (see blue and red symbols in Fig. 6.2(a,b)). The correlations of the recorded events and the mean x -momenta are depicted in Fig. 6.3. For the gas-only measurement, the distribution is symmetric with respect to the laser propagation direction, see Fig. 6.3(a). The distribution recorded for the nanoparticle measurement in Fig. 6.3(b) is more structured and includes two contributions. First, a signature at low event numbers ($\lesssim 150$ events) that is symmetric with respect to the p_x -momentum and resembles the gas-only measurement. Second, a signature at higher event counts $\gtrsim 150$ that is shifted towards negative momenta. This shift is attributed to a shadowing effect of the XUV pulses [142, 143, LS5], i.e. the absorption of the XUV-field at the front side of the nanosphere (cf. inset in Fig. 6.1) resulting in enhanced electron emission into the direction of the incident pulses.

Considering both criteria, i.e. the number of measured events and the x -component of the mean momenta, the VMI images recorded in the nanoparticle experiment can be

6. Attosecond streaking on dielectric nanospheres

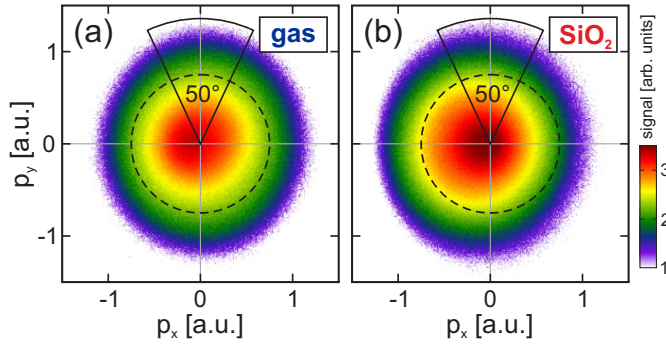


Figure 6.4. (a,b) Averaged momentum distributions recorded from gas (a) and SiO₂ (b) at $\Delta t = 0$ as. Dashed circles indicate the low momentum region as in Fig. 6.2(a,b). Adapted from [LS7].

assigned to gas hits (blue rectangle in Fig. 6.3(b)) and nanoparticle hits (red rectangle). This enables to evaluate averaged momentum distributions for the reference gas and the nanoparticle signal as shown in Fig. 6.4. Note that from here results labeled as 'gas' do not correspond to the gas-only measurement but to the gas-hits extracted from the experiment including nanoparticles.

6.1.2. Extraction of streaking spectrograms and delays

Investigating the evolution of the averaged momentum distributions for gas and nanoparticles (cf. Fig. 6.4) with the pulse delay Δt reveals periodic oscillations of the distributions within the polarization direction of the pulses as schematically illustrated in Fig. 6.5. The NIR field induced streaking effect is most pronounced for electrons emitted along the laser polarization direction. Hence, for the following analysis only electrons emitted in polarization direction are considered by integrating the signal within a small angle of $\pm 25^\circ$ around the polarization axis (cf. Fig. 6.4). Analyzing the energies that correspond to the projected momenta in dependence of the pulse delay yields a streaking spectrogram as illustrated in Fig. 6.5.

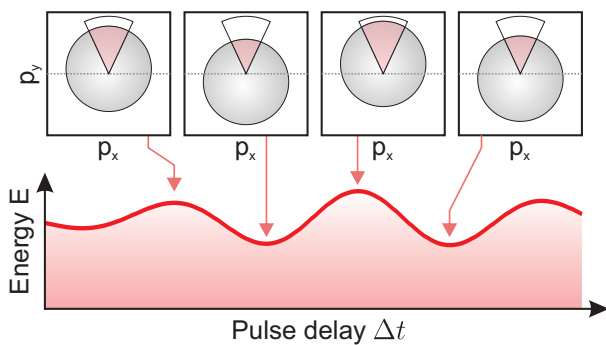


Figure 6.5. Illustration of the extraction of streaking spectrograms from VMI data. Integrating the signal within a small acceptance angle around the laser polarization direction in the pulse delay-dependent momentum projections (top) yields a delay-dependent streaking spectrogram of the respective energies (bottom).

The streaking spectrograms for gas and nanoparticles in Fig. 6.6(a,b) reveal pronounced delay-dependent oscillations and already hint at a relative delay of the nanoparticle data with respect to the gas (black arrows). To quantify the individual streaking delays, contour-lines (i.e. delay-dependent energies with equal signal strength) are determined from the streaking spectrograms. The contour lines were filtered to eliminate measurement-induced high frequency noise. The resulting filtered contour lines around energies of ≈ 25 eV are shown as blue and red dots in Fig. 6.6(a,b). To extract the streaking delay a contour-line

is fitted with the few-cycle waveform

$$E_{\text{fit}}(\Delta t) = E + A \cos(\omega [\Delta t - \delta t]) e^{-\frac{1}{2} \frac{(\Delta t - t_0)^2}{\tau^2}}, \quad (6.2)$$

where the asymptotic energy E , the streaking amplitude A and delay δt , and the peak t_0 and width τ of the envelope are determined via a least-squares fit (solid curves in Fig. 6.6(a,b)). The resulting energy-dependent streaking delays $\delta t(E)$ extracted for the high-energy spectral regions (20–30 eV) of the gas and nanoparticle streaking spectrograms are shown in Fig. 6.6(c). Note that each symbol corresponds to one parameter-pair (E and δt) from fitting a single contour line. The results unveil two prominent features. First, the streaking delays of both gas and silica particles increase linearly with energy, i.e. exhibit a tilt to the right. These tilts are mainly attributed to the chirp of the XUV pulses as discussed in more detail later. Second, and most importantly, the nanoparticle and gas data exhibit an almost energy-independent relative delay of around 100 as.

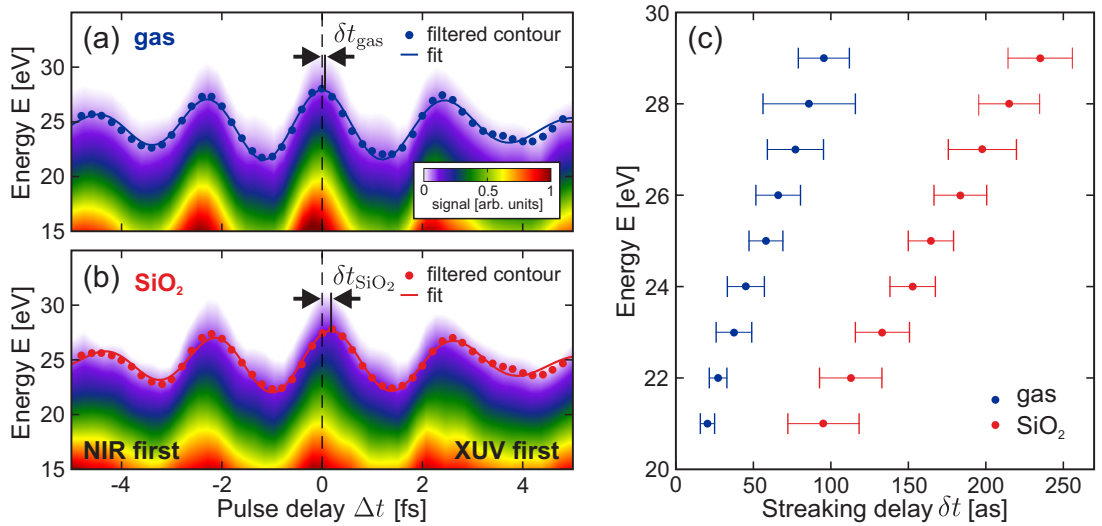


Figure 6.6. Measured streaking spectrograms and extracted delays (a,b) Attosecond streaking spectrograms obtained from angular integration of projected momentum maps over $\pm 25^\circ$ around the laser polarization direction (cf. Fig. 6.4) for gas (a) and silica nanoparticles (b). To extract the streaking delays energy-dependent frequency-filtered isolines (blue and red dots) were fitted with few-cycle waveforms (blue and red curves) as described in the text. The fits carrier phases define the respective streaking delays δt . (c) Streaking delays extracted from fits of isolines in the high energy range (20–30 eV) of the gas and nanoparticle streaking spectrograms (as indicated). The error bars reflect deviations of individually measured data sets. Adapted from [LS7].

6.2. Semi-classical streaking simulations

To clarify the origin and significance of the relative delay in the streaking experiment on silica nanospheres, corresponding semi-classical M³C simulations are employed. In particular, the freedom to systematically vary the strength of different simulation parameters is exploited to investigate the impacts of specific contributions to the streaking delay. However, as a first step the simulations are benchmarked against the experiment to ensure that the relevant physics is captured accurately. Therefore, a reference streaking

6. Attosecond streaking on dielectric nanospheres

simulation for the experimental parameters is analyzed. Small $d = 50$ nm nanospheres with relative permittivity $\epsilon_r = 2.12$ and bandgap $I_p = 9$ eV are considered to resemble the silica nanoparticles in the experiment. Inside the spheres, photoelectrons are generated in the near-field of a chirped XUV pulse² ($\tau = 250$ as, $\lambda = 44$ nm, $E_{\text{phot}} \approx 28$ eV, $I = 1 \times 10^{12}$ W/cm²) and propagated in the linear near-field induced by the synchronized NIR pulse ($\tau = 5$ fs, $\lambda = 720$ nm, $I = 2 \times 10^{12}$ W/cm²). As the XUV chirp could not be extracted accurately from the experiment it is determined by comparison of a streaking simulation for the reference gas to the experiment. Thereto, electrons are generated with initial energies that reflect the spectral intensity profile of the chirped XUV pulse and are propagated in the field of the incident NIR pulse. Best agreement is found for a chirp parameter of $\zeta = -7 \times 10^{-3}$ fs², compare blue curve to blue symbols in Fig. 6.7(a).

The comparison of the streaking delays extracted from gas and M³C simulations to the respective experimental values is shown in Fig. 6.7(a). While the experimental delay for the reference gas can be reproduced very well by the corresponding simulation (compare blue curve to blue symbols) the predicted delay for the nanoparticles exceeds that from the experiment (compare black curve to red symbols). This discrepancy is attributed to residual gas contributions in the nanoparticle signal³. Hence, the measured nanoparticle streaking delay actually reflects a mixture of the signals from nanospheres and reference gas. The respective energy-dependent ratio of nanoparticle and gas signal can be extracted from the experiment via background subtraction, see red symbols in Fig. 6.7(b). For a quantitative comparison of simulation and experiment this ratio is incorporated into the simulation results as follows. The individual streaking spectrograms for gas and nanoparticles are combined to a mixed spectrogram $S_{\text{mix}}(E, \Delta t) = S_{\text{SiO}_2}(E, \Delta t) + \eta S_{\text{gas}}(E, \Delta t)$ where the gas contribution is weighted with a single factor η . The latter is chosen such that the experimental SiO₂-gas ratio is reproduced best by the simulation results (compare black curve to red symbols in Fig. 6.7(b)). The good agreement of the streaking delay extracted

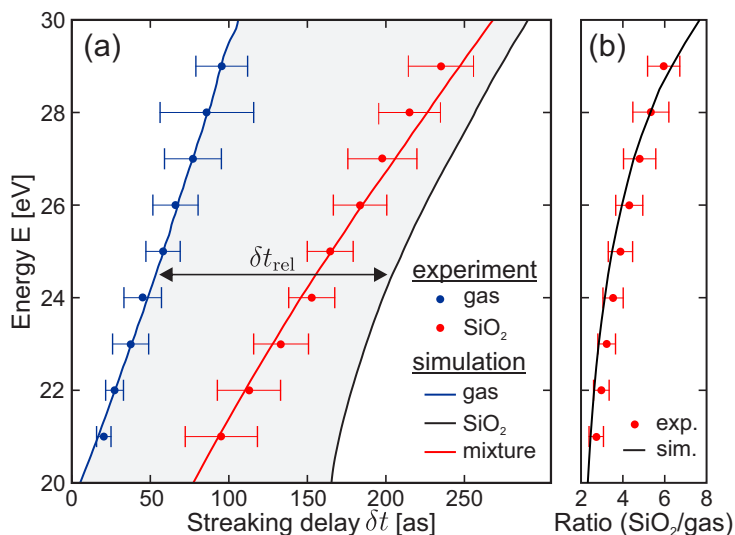


Figure 6.7. Comparison of measured and simulated streaking delays. **(a)** Energy-dependent delays from experiments for gas (blue symbols) and nanoparticles (red symbols) and as predicted by respective simulations for gas (blue curve) and nanoparticles (black curve). The red curve represents the delay extracted from a mixed spectrogram. **(b)** Ratio of nanoparticle to gas signal in dependence of energy, extracted from the experiment (red symbols) and from the simulations (black curve). Adapted from [LS7].

²To calculate the XUV near-field, the relative permittivity in the relevant spectral range is determined from the complex refractive index shown in Fig. 2.9.

³VMI images that are assigned to nanoparticle hits can still contain electrons from the gas surrounding the nanosphere.

from the mixed spectrogram with the experimental data (compare red curve to red symbols in Fig. 6.7(a)) supports that all important physical mechanisms are captured well by the semi-classical description when considering a scaling factor of $s = 2.1$ in the Lotz cross section. Therefore, the simulations can now be used to investigate the specific contributions to the essentially energy-independent relative streaking delay $\delta t_{\text{rel}} = \delta t_{\text{SiO}_2} - \delta t_{\text{ref}} \approx 150$ as between the (pure) nanoparticle delay δt_{SiO_2} and the delay of the reference δt_{ref} , see black arrow and gray shaded area in Fig. 6.7(a).

6.2.1. Contributions to the relative streaking delay

To clarify the specific contributions to the relative streaking delay, the individual contributions to the absolute delays for the reference and the nanoparticles are briefly outlined. For the reference, the absolute delay

$$\delta t_{\text{ref}} = \delta t_{\text{offset}} + \delta t_{\text{chirp}} \quad (6.3)$$

includes two contributions. First, a trivial shift (δt_{offset}) that is attributed to offsets of the XUV-NIR pulse delay axis and the CEP of the streaking field. Second, an additional contribution δt_{chirp} can be introduced by a chirp of the attosecond pulses, where spectrally varying arrival times of the intensity envelope can lead to energy-dependent photoionization timings. The absolute streaking delay

$$\delta t_{\text{SiO}_2} = \delta t_{\text{offset}} + \delta t_{\text{chirp}}^{\text{SiO}_2} + \delta t_{\text{fields}} + \delta t_{\text{coll}} \quad (6.4)$$

for the silica nanospheres also includes contributions from the offset and the XUV chirp. However, even when the chirps of the incident XUV pulses are the same for the reference and the nanoparticles, it has to be considered that field propagation could introduce additional modifications of the chirp in the XUV near-fields. To inspect this effect, the chirps of incident fields and near-fields are analyzed via their respective Wigner distributions in Sec. 6.2.3. The analysis supports that the modifications are small, such that streaking delays are similar ($\delta t_{\text{chirp}}^{\text{SiO}_2} \approx \delta t_{\text{chirp}}$) and thus cancel in the relative analysis. As compared to the reference, the nanoparticle delay includes two further contributions. On the one hand, field retardation and inhomogeneity effects of the local near-fields can result in an additional delay δt_{fields} . On the other hand, the electron transport governed by elastic and inelastic collisions within the material may result in an additional collisional streaking delay δt_{coll} . Further contributions such as Wigner delays and effects from Coulomb-laser coupling are excluded from the simulations since they are assumed to be comparable for the reference gas and the silica particles as their long-range potentials are both Coulomb-like and remaining short-range effects are considered to be negligible away from resonances [144].

After identifying the individual contributions to the absolute streaking delays for the reference and the nanoparticles, their specific impacts on the relative delay

$$\delta t_{\text{rel}} = \delta t_{\text{fields}} + \delta t_{\text{coll}} \quad (6.5)$$

are analyzed in detail. In particular, it will be shown in Sec. 6.2.2 that in the current scenario the near-field induced contribution is small, such that the relative streaking delay is in good approximation governed solely by the material-specific transport dynamics, i.e.

$$\delta t_{\text{rel}} \approx \delta t_{\text{coll}}. \quad (6.6)$$

6.2.2. Near-field induced contributions to the streaking delay

As opposed to atomic streaking, where XUV photoionization and acceleration in the NIR field are driven by the incident fields, nanoparticle streaking is mediated by the local near-fields. Hence, both the ionization and the subsequent acceleration are subject to field retardation effects due to the materials dispersion, i.e. its different optical properties in the two relevant spectral ranges. This near-field retardation reflects the first near-field mediated contribution to the streaking delay. In addition, a second contribution is expected due to the inhomogeneity of the NIR near-field, such that the overall near-field induced streaking delay is

$$\delta t_{\text{fields}} = \delta t_{\text{retard.}} + \delta t_{\text{inhom.}} \quad (6.7)$$

Below, the specific impacts of both effects are estimated for a $d = 50$ nm silica sphere.

Near-field retardation mediated delay

To estimate the retardation induced delay, the XUV and NIR near-fields are analyzed in the propagation-polarization ($x - y$) plane for $z = 0$, see Fig. 6.8(a). The NIR near-field reflects the typical dipole-shaped enhancement profile and the XUV near-field is subject to XUV shadowing [143], i.e. absorption of the incident field at the spheres front side. In general, the retardation of both near-fields is not homogeneous. Hence, the retardation effect on the streaking delay can be expected to depend on the particular ionization site of a selected electron. To estimate the averaged retardation effect for an ensemble of electrons it is necessary to account for the distribution of their ionization sites. The latter is quantified via the birth angle distribution $Y(\theta)$ of electrons that contribute to the nanoparticle streaking spectrogram and is shown in Fig. 6.8(b). The shift of the distributions peak from 90° to around 115° results from the XUV shadowing. In addition,

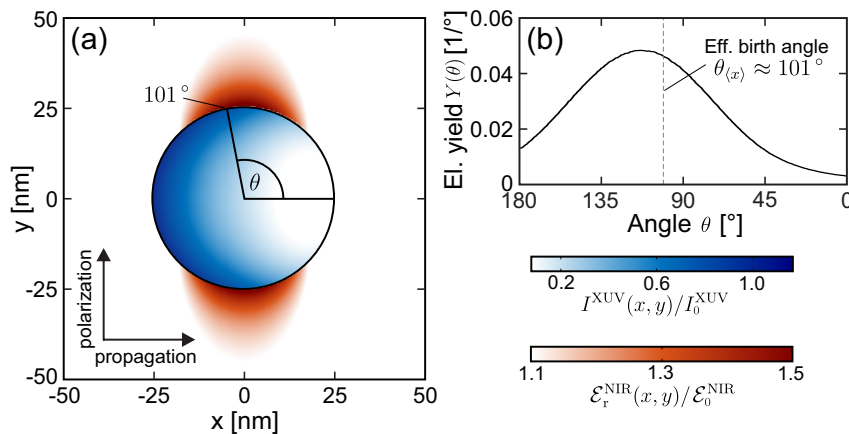


Figure 6.8. Near-fields and birth angle distribution. (a) Spatial distributions of the XUV (blue) and NIR (red) near-fields inside and outside of a $d = 50$ nm silica sphere sampled in the propagation-polarization (x - y) plane at $z = 0$. The shown XUV near-field intensity is normalized to the peak intensity of the incident XUV field while the NIR near-field shows the maximum relative enhancement of the radial NIR near-field normalized to the peak field strength of the incident NIR pulse. (b) Distribution of electrons contributing to a typical streaking spectrogram as function of birth angle θ as defined in (a). The vertical dashed line marks the effective birth angle $\theta_{\langle x \rangle} = \arccos(\langle \cos \theta \rangle)$. Adapted from [LS7, LS8].

the effective birth angle is defined via the ensemble average $\theta_{\langle x \rangle} = \arccos(\langle \cos \theta \rangle)$ and is $\approx 101^\circ$ for the considered scenario, see vertical dashed line.

To quantify the retardation effect, the timings of the XUV and NIR near-fields at the sphere surface are evaluated with respect to their respective plane wave solutions in vacuum. The XUV near-field enters the streaking via photoionization, where the respective rate is determined from the local intensity. Thus, the group delay $\Delta t_{\text{group}}^{\text{XUV}}$ reflects the XUVs arrival time and is determined from the center of mass of the near-fields envelope with respect to the corresponding vacuum solution, see blue curve in Fig. 6.9(a). Here, the XUV near-field is retarded with respect to the vacuum solution (reflected by positive group delays) at the spheres front side (180°) and at the upper pole (90°). To compensate the XUV retardation effect the incoming NIR pulse would have to be delayed by the XUV group delay. Hence, the streaking spectrogram is delayed by

$$\delta t_{\text{retard.}}^{\text{XUV}} = \Delta t_{\text{group}}^{\text{XUV}}. \quad (6.8)$$

The streaking of electrons is mediated by the full waveform of the NIR near-field. Thus its retardation is reflected by the phase delay $\Delta t_{\text{phase}}^{\text{NIR}}$ with respect to the corresponding vacuum reference, see red curve in Fig. 6.9(a). Note that here the y -component of the field is analyzed, as mainly electrons emitted along the polarization axis (y) contribute to the final streaking spectrograms. At the spheres front side, the near-fields y -component is advanced with respect to the vacuum solution, while it is retarded at the back side. To compensate the NIR near-fields phase delay, the incident NIR pulse needs to be advanced, such that the respective delay

$$\delta t_{\text{retard.}}^{\text{NIR}} = -\Delta t_{\text{phase}}^{\text{NIR}} \quad (6.9)$$

shifts the streaking spectrogram into negative direction, i.e. counteracts the XUV retardation effect. The combined retardation effect of the XUV and NIR near-fields thus contributes to the streaking delay via

$$\delta t_{\text{retard.}} = \Delta t_{\text{group}}^{\text{XUV}} - \Delta t_{\text{phase}}^{\text{NIR}} \quad (6.10)$$

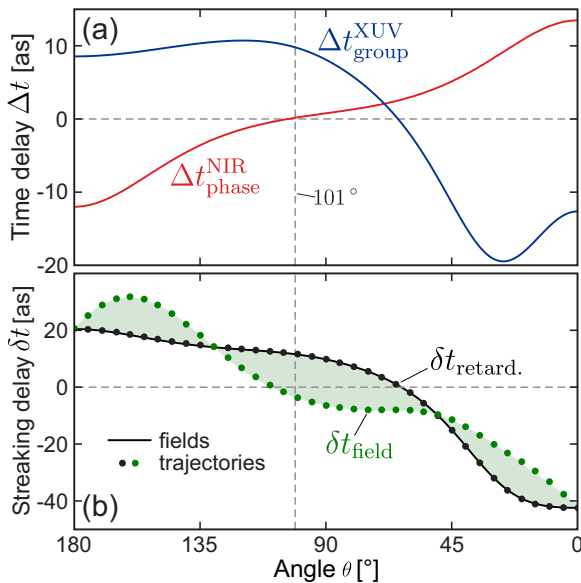


Figure 6.9. Near-field mediated streaking delays. **(a)** Angle-dependent group delay of the XUV near-field (blue curve) and phase delay of the NIR near-field (red curve) at a 50 nm silica sphere with respect to the respective vacuum solutions (Mie calculations). **(b)** Combined retardation delay $\delta t_{\text{retard.}} = \Delta t_{\text{group}}^{\text{XUV}} - \Delta t_{\text{phase}}^{\text{NIR}}$ (black curve) calculated from the curves in (a). Symbols indicate delays extracted from streaking spectrograms from trajectory simulations including the NIR near-field at the birth position (black) and including the full inhomogeneous NIR near-field (green). The green shaded area reflects the inhomogeneity effect alone. Adapted from [LS7, LS8].

6. Attosecond streaking on dielectric nanospheres

and is depicted by the black curve in Fig. 6.9(b). The analysis reveals that the retardation effect ranges from -40 to 20 as over the full angular range and is around 15 as at the effective birth angle (101° , see vertical dashed line). To take the full birth angle distribution into account, the mean streaking delay is defined as the weighted average

$$\overline{\delta t} = \frac{\int Y(\theta)\delta t(\theta)d\theta}{\int Y(\theta)d\theta}, \quad (6.11)$$

yielding $\overline{\delta t}_{\text{retard.}} \approx 7$ as for the mean retardation delay.

NIR near-field inhomogeneity induced delay

The previous analysis only addressed the retardation of the near-fields at the particle surface. However, in previous works it was shown that the electron emission may be strongly modified by the inhomogeneity of the NIR near-field [16]. Therefore, the effect of the acceleration in the inhomogeneous near-field outside the nanoparticle on the streaking delay will now be investigated. To quantify the delay, photoelectrons are launched on the surface of the sphere (in the $z = 0$ plane) with initial velocities in positive y -direction (corresponding to a typical excess energy of 19 eV as in the experiment and M³C simulations) at the peak of the local XUV near-field. The trajectories of electrons propagating in the NIR near-field outside of the sphere are calculated by integration of the classical EOM. The corresponding streaking spectrogram then only includes the above discussed retardation effect and the additional inhomogeneity effect of the NIR near-field. The extracted angle dependent streaking delay is indicated by the green symbols in Fig. 6.9(b) and reveals that the inhomogeneity effect (green shaded area) is on the same order as the retardation effect⁴. Both effects almost cancel around the pole such that the combined near-field induced delay almost vanishes around the effective birth angle (vertical dashed line). The respective mean delay $\overline{\delta t}_{\text{field}}$ is around 4 as.

Evolution of the near-field induced delay with nanoparticle size

As a last step, the evolution of the near-field induced contribution to the streaking delay with nanoparticle size is studied. The systematic analysis of the averaged field induced delays in Fig. 6.10 reveals strong oscillations of the retardation induced streaking delay (black curve and symbols) with nanoparticle size that are attributed to consecutive excitation of higher order modes of the NIR near-field. The offset of ≈ 10 as for $d \rightarrow 0$ does not result from field retardation but is an effect from the dispersion of SiO₂ in the XUV spectral range. The additional effect of the NIR near-field inhomogeneity (green shaded area) vanishes for large spheres but becomes increasingly important for small spheres with $d \lesssim 100$ nm. The analysis provides a first estimate for the field-induced delays for possible future studies at silica particles of various sizes. Most importantly, for the size considered in this study (vertical dashed line) the full field-induced delay (green symbols) is $\lesssim 5$ as and thus provides only a small contribution to the relative streaking delay.

⁴Including only the surface field in the trajectory integration (i.e. excluding inhomogeneity effects) perfectly reproduces the retardation induced delay (compare black symbols and curve in Fig. 6.9(b)).

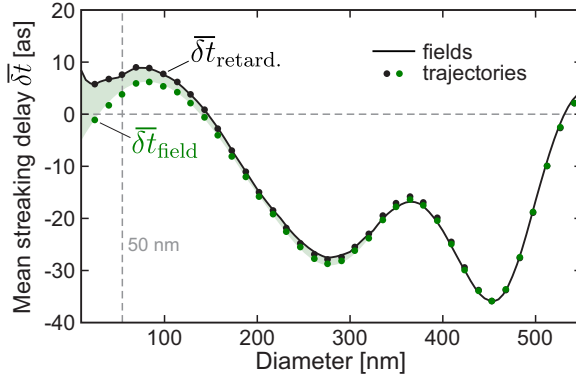


Figure 6.10. Size-evolution of the (birth angle averaged) mean streaking delays including field retardation (black curve and symbols) and the NIR near-field inhomogeneity (green symbols). The green shaded area visualizes the pure inhomogeneity effect. The vertical dashed line marks a sphere size of $d = 50$ nm. Adapted from [LS8].

6.2.3. Impact of the XUV chirp

In addition to the previously investigated field retardation and inhomogeneity effects, the simulated streaking delays are also modified by the chirp of the XUV pulses. To inspect how the latter affects the streaking delays for the gas reference and the nanoparticles, it is instructive to compare their respective Wigner-distributions. The distributions for XUV pulses in vacuum have already been discussed briefly in the methods section (cf. Fig. 2.3(a,b)). They revealed a chirp-dependent tilt of the temporal center of mass that characterizes the photon energy-dependent arrival delay $\Delta t_{\text{vac}}^{\text{XUV}}(E_{\text{ph}})$ of the spectral intensity envelope. Since the latter drives the photoionization, the arrival delay directly translates to an energy-dependent contribution to the streaking delay for the gas reference.

To investigate if the chirp of the near-fields is modified, Wigner distributions $W(\mathbf{r}, t, \omega)$ sampled for the near-fields at the upper pole of a nanoparticle are compared in Fig. 6.11(a,b) for two values of the chirp parameter ζ . The comparison reveals that the chirp effect on the spectral arrival delays is similar for vacuum (black curves, cf. Fig. 2.3(a,b)) and nanoparticles (blue curves), where in both cases the chirp results in a pronounced tilt. The relative arrival delays between the nanosphere and vacuum solutions $\Delta t_{\text{rel}}^{\text{XUV}}(E_{\text{ph}}) =$

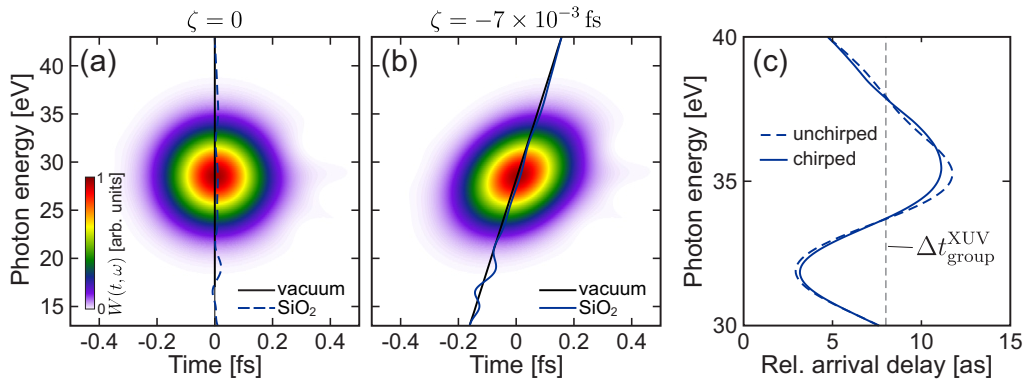


Figure 6.11. XUV chirp induced streaking delay. (a,b) Wigner distributions of unchirped (a) and chirped (b) 250 as XUV pulses used in the M³C simulations, sampled at the upper pole of a 50 nm silica sphere. Blue curves indicate the spectral arrival delays (defined as the temporal center of mass of the Wigner distributions). Black curves indicate the corresponding vacuum solutions as shown in Fig. 2.3(a,b). (c) Relative spectral arrival delays (silica minus vacuum) calculated from the data shown in (a) and (b). Adapted from [LS7].

$\Delta t_{\text{SiO}_2}^{\text{XUV}}(E_{\text{ph}}) - \Delta t_{\text{vac}}^{\text{XUV}}(E_{\text{ph}})$ are shown in Fig. 6.11(c) for the two chirps. In both cases, they exhibit small dispersion induced spectral variations on the order of a few attoseconds around the XUV group delay (gray line, corresponding to the blue curve at 90° in Fig. 6.9(a)). However, the relative delay does only depend weakly on the selected value of the chirp parameter. Hence, the chirp remains robust also in the near-fields and its effect essentially cancels in the relative streaking delay and can therefore be neglected for the further analysis.

6.3. The collisional streaking delay

To systematically explore the effect of electron transport within the material and its significance for the collisional streaking delay, full M³C simulations are performed with two central simplifications. First, the XUV pulses are considered to be unchirped in order to eliminate the energy-dependent tilt of the streaking delays. Second, electron scattering is modeled via fixed energy-independent scattering times for both elastic and inelastic collisions. The fixed scattering times are considered as $\tau_{\text{el}} = 100$ as and $\tau_{\text{inel}} = 300$ as to closely resemble the energy-dependent scattering times in the relevant energy range (cf. Fig. 2.12(c)). Both times are varied by factors of 1/3 and 3 leading to a set of nine M³C simulations for three elastic scattering times ($\tau_{\text{inel}} = 33, 100$ and 300 as) and three inelastic scattering times ($\tau_{\text{inel}} = 100, 300$ and 900 as). The nine corresponding energy-dependent streaking delays in Fig. 6.12(a) allow three key conclusions.

- First, neglecting the XUV chirp and assuming fixed scattering times results in essentially energy-independent streaking delays⁵.
- Second, the delays are strongly sensitive to the inelastic scattering time, where increasing the inelastic scattering time results in larger streaking delays (see three separated groups of curves indicated by the gray areas).
- Third, the sensitivity to the elastic scattering time is much weaker (compare colored curves within each gray group).

These observations support that the streaking delay can serve as a measure for the inelastic scattering time in the considered scenario. In particular, the streaking delay is roughly half of the inelastic scattering time for $\tau_{\text{inel}} = 100$ as and 300 as. For $\tau_{\text{inel}} = 900$ as the streaking delay is only approximately 30% of the inelastic scattering time which can be attributed to a wavelength-dependent saturation effect that is discussed in more detail later.

6.3.1. Impact of internal streaking

The semi-classical trajectory simulations for silica nanospheres have predicted a strong sensitivity of the streaking delays to the inelastic scattering time and only a weak dependence on the elastic scattering time. This observation raises the question if the behavior is

⁵To suppress additional energy dependencies due to the intercycle averaging effect that is discussed in Section 6.3.4, in this section the streaking delays are not extracted with the contour line method. Instead, energy-dependent delays are extracted by fitting the energetic center of mass of selective spectrograms which are calculated for photoelectrons with initial energies within small energy intervals.

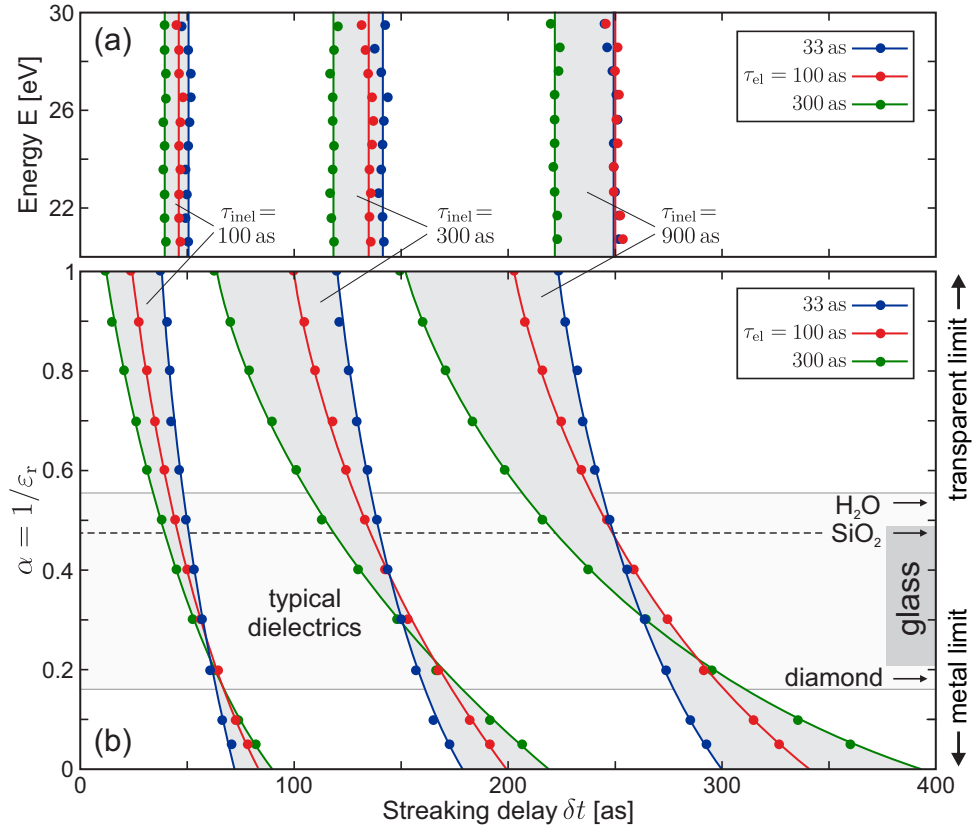


Figure 6.12. Systematic analysis of the collisional streaking delay calculated via M^3C assuming unchirped XUV pulses and energy-independent scattering times to eliminate energy-dependencies of the streaking delays. **(a)** Streaking delays in dependence of elastic and inelastic scattering times (as indicated). **(b)** Streaking delays as function of the material’s attenuation factor $\alpha = 1/\epsilon_r$, where ϵ_r is the relative permittivity at the wavelength of the NIR field. Gray shaded areas in both panels visualize the variation of the streaking delay in dependence of the elastic scattering time. The gray rectangle and the black arrows in (b) indicate permittivities of typical dielectric materials. The dashed black line marks the permittivity of SiO_2 . Adapted from [LS7].

general for solid-state attosecond streaking from arbitrary materials. As discussed in the introduction (cf. Fig. 1.8) the key difference between streaking at metallic and dielectric systems is the screening of the NIR field within the material and hence its effect on the internal streaking during the electron transport to the surface. To investigate the impact of the internal streaking quantitatively, the strength of the internal field is adjusted by varying the materials relative permittivity at the wavelength of the NIR streaking field. To systematically study the dependence of the collisional delay on the internal field, a set of nine simulations with elastic and inelastic scattering times similar to the example in Fig. 6.12(a) is performed in dependence of the permittivity. As the streaking delays are energy-independent in the considered scenario, each individual simulation for a set of parameters (τ_{el} , τ_{inel} and ϵ_r) results in one (energy-averaged) value for the streaking delay.

The results of the systematic analysis are depicted in Fig. 6.12(b) in dependence on the field attenuation factor $\alpha = 1/\epsilon_r$. For the case of SiO_2 where $\alpha \approx 0.5$ (see dashed black line in Fig. 6.12(b)) the delays reproduce the previously obtained results. In the two

6. Attosecond streaking on dielectric nanospheres

limiting cases $\alpha \rightarrow 0$ and 1 the delays are sensitive to both the inelastic and the elastic scattering time, as visualized by the broadening of the gray areas. The dependence on the latter, however, has opposite signs in the two limits. In the transparent case ($\alpha \rightarrow 1$, $\varepsilon_r \rightarrow 1$), the streaking delay decreases for larger elastic scattering times (compare blue to green curves at the top). In contrast, in the metal limit ($\alpha \rightarrow 0$, $\varepsilon_r \rightarrow \infty$) larger elastic scattering times result in larger streaking delays (compare blue to green curves at the bottom). The elastic collision effect reverses (and thus effectively vanishes) for permittivity values of typical dielectric materials (light gray shaded area). This nearly exclusive sensitivity of the streaking delays to the inelastic scattering time for dielectrics therefore enables the retrieval of quantitative scattering times by matching the simulation results to experimental data.

6.3.2. Intuitive physical picture for the collisional streaking delay

So far, the physical picture for the predicted almost exclusive sensitivity of the streaking delay to the inelastic scattering time for dielectrics is missing. This picture can be developed qualitatively from a simplified model for the collisional streaking delay for solids. As a starting point, a flat surface of a transparent material ($\varepsilon_r = 1$) is considered in order to suppress near-field induced effects on the streaking, see Fig. 6.13(a). Hence, the streaking

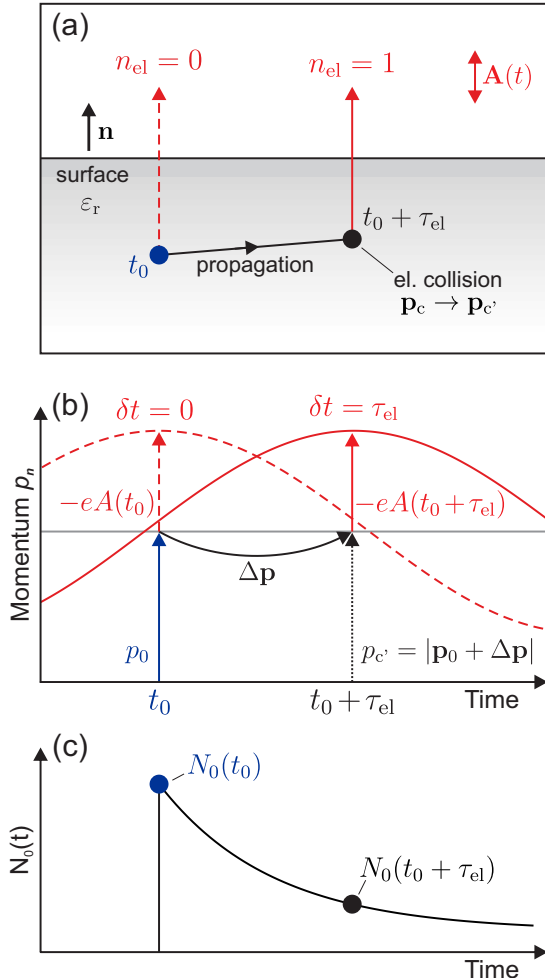


Figure 6.13. Simplified model for the collisional streaking delay. **(a)** Schematic representation of electrons generated inside a transparent material ($\varepsilon_r = 1$) at time t_0 (blue symbol) with initial momenta \mathbf{p}_0 and escaping without collisions (dashed red arrow) and after one elastic collision at $t_0 + \tau_{el}$ following propagation within the solid (black and solid red arrows). Note that only electrons escaping parallel to the surface normal \mathbf{n} are considered. **(b)** Final momenta (in \mathbf{n} -direction) $p_f = p_0 - eA(t_0)$ of directly escaping electrons (solid blue arrow and dashed red arrow) represent the NIR vector potential $\mathbf{A}(t) \parallel \mathbf{n}$ and correspond to a streaking trace with delay $\delta t = 0$ (dashed red curve). Electrons escaping after one elastic collision experience a momentum gain $\Delta \mathbf{p}$ during the propagation. At the collision, the ingoing collision momentum $\mathbf{p}_c = \mathbf{p}_0 + \Delta \mathbf{p}$ is directionally randomized and the final momentum is $\mathbf{p}_c' = |\mathbf{p}_c| \mathbf{n} - e\mathbf{A}(t_c)$. As discussed in the main text and illustrated in Fig. 6.14 for an ensemble of electrons with isotropic initial momenta, isotropic elastic collisions effectively act as a new birth such that $\langle p_f \rangle \approx p_0 - eA(t_0 + \tau_{el})$ and the corresponding streaking trace is delayed by $\delta t = \tau_{el}$ (solid red curve). **(c)** Depleting population of electrons with no inelastic collisions. Adapted from [LS7].

fields vector potential $\mathbf{A}(t)$ (that is considered to be aligned with the surface normal \mathbf{n}) is similar in- and outside of the material. Following XUV photoionization, an ensemble of electrons is generated inside the material at time t_0 with isotropic initial momenta \mathbf{p}_0 . In the first step, electrons are considered to escape from the material without elastic collisions. When assuming that only electrons leaving the material parallel to the surface normal can be detected, only electrons generated with initial momenta $\mathbf{p}_0 \parallel \mathbf{n}$ contribute to a respective streaking trace. The final momenta of these electrons are $p_f = p_0 - eA(t_0)$ (blue and dashed red arrows in Fig. 6.13(b)). The streaking trace corresponding to these electrons therefore directly characterizes the vector potential, see red dashed curve in Fig. 6.13(b). Hence, it is equivalent to traces for gas streaking and thus corresponds to a vanishing collisional streaking delay in a relative measurement.

Impact of elastic scattering

To inspect the effect of elastic scattering on the streaking delay, electrons are considered to be generated at the same time t_0 and scatter elastically after the elastic scattering time τ_{el} before leaving the material perpendicular to the surface (black and solid red arrows in Fig. 6.13(a)). It turns out that for an ensemble of such electrons an isotropic elastic collision effectively acts as a new birth and the electrons are indistinguishable from electrons generated at time $t_0 + \tau_{el}$ and escaping from the material with no elastic collision. The reason for this effect is illustrated schematically in Fig. 6.14. Electrons are generated with isotropic initial momenta \mathbf{p}_0 (blue arrows) and gain the momentum $\Delta\mathbf{p} = -e[\mathbf{A}(t_0) - \mathbf{A}(t_0 + \tau_{el})]$ during the propagation between their generation and the elastic collision (cf. black arrows in Fig. 6.13(a,b)). Thus, the distribution of ingoing collision momenta $\mathbf{p}_c = \mathbf{p}_0 + \Delta\mathbf{p}$ is shifted, generating momenta smaller and larger compared to the initial momentum p_0 (compare solid black to dashed blue circle in the middle of Fig. 6.14). Following the assumption that electrons can only be detected when leaving the material perpendicular to the surface, only electrons with outgoing collision momenta parallel to the surface normal have to be considered. For these electrons the elastic collision effectively rotates the momentum vectors into \mathbf{n} -direction and the outgoing collision momenta are determined as the modulus of the ingoing momenta $p_{c'} = |\mathbf{p}_c| \mathbf{n} = |\mathbf{p}_0 + \Delta\mathbf{p}| \mathbf{n}$. Assuming that $\Delta\mathbf{p} \ll \mathbf{p}_0$, which is well justified for the considered laser parameters, the ensemble-averaged outgoing collision momentum is $\langle p_{c'} \rangle \approx p_0$. Therefore, besides a broadening of the momentum distribution (see right picture in Fig. 6.14), the isotropic scattering event effectively acts as a new birth since the so far acquired momentum shifts average out. Therefore, an ensemble of electrons scattering elastically at time $t_0 + \tau_{el}$ has an average final momentum $\langle p_f \rangle \approx p_0 - eA(t_0 + \tau_{el})$ and the respective streaking trace is shifted by τ_{el} (see solid red curve in Fig. 6.13(b)).

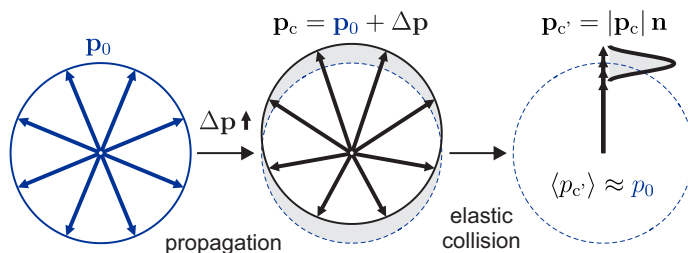


Figure 6.14. Schematic illustration of the effective cancellation of the momentum gain acquired by electrons propagating inside a material between generation with isotropic initial momenta \mathbf{p}_0 (left) and an elastic collision. Adapted from [LS7].

Impact of inelastic scattering

If the ensemble of electrons generated at t_0 is also subject to inelastic collisions, the initial population of electrons N_0 that have not scattered inelastically depletes as

$$N_0(t) = N_0 \exp(-t/\tau_{\text{inel}}) \quad (6.12)$$

determined by the inelastic scattering time, see Fig. 6.13(c). A final streaking spectrogram reflects the average of individual streaking traces that are shifted due to elastic collisions and weighted with the respective emission current. If only electrons with no inelastic collisions contribute to the spectrogram, the emission current reflects the population depletion via interband excitations. In that case the corresponding streaking delay is strongly sensitive to the inelastic scattering time. Key for analyzing only contributions from electrons without inelastic scattering in the experiment and the M³C simulations is to extract the streaking delays only in the high energy spectral region (here between 20 and 30 eV, cf. Fig. 6.6(c) and Fig. 6.7(a)). Since inelastic collisions reduce the electrons energy by at least the band gap (≈ 9 eV for silica nanoparticles), the high energy region only includes contributions from electrons without inelastic collisions, see Fig. 6.15.

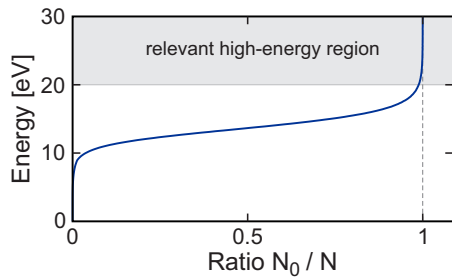


Figure 6.15. Energy-dependent ratio of electrons without inelastic collisions N_0 to the full electron population N extracted from M³C. The gray area indicates the relevant energy range for the streaking analysis that almost exclusively contains electrons with no inelastic collisions. Data published in [LS7].

6.3.3. Selective impacts of elastic and inelastic scattering in M³C

The simplified model has provided an intuitive picture for the effects of elastic and inelastic collisions on the streaking delay. To corroborate the validity of this picture, their selective impacts on the streaking delays extracted from full M³C simulations are analyzed in the next step. Figure 6.16 displays the results of a typical simulation utilizing an unchirped XUV pulse and energy-independent scattering times fixed at $\tau_{\text{inel}} = 300$ as and $\tau_{\text{el}} = 100$ as. Figure 6.16(a) shows selective streaking spectrograms calculated for electrons emitted without inelastic collisions and different numbers of elastic collisions. The extracted streaking delays (vertical black lines) increase linearly with the number of elastic collisions (black symbols in Fig. 6.16(b)) as predicted by the simplified model. The signal strength exhibits an exponential decrease with the number of elastic collisions driven by the population loss due to inelastic scattering, see Fig. 6.16(c). A corresponding full spectrogram (not shown) reflects the superposition of the shifted and weighted selective spectrograms and is thus 'smeared out' towards larger pulse delays. Hence, it contains the information on the population decay and thus the inelastic scattering time. The selective analysis allows to easily extract the streaking delay which corresponds to the value of a linear fit to the selective streaking delay (red curve in Fig. 6.16(b)) at the number of elastic collisions where the signal strength has decayed to a fraction of $1/e$ (dashed lines in Fig. 6.16(b,c)). For the considered scenario, the extracted streaking delay of $\delta t \approx 170$ as is

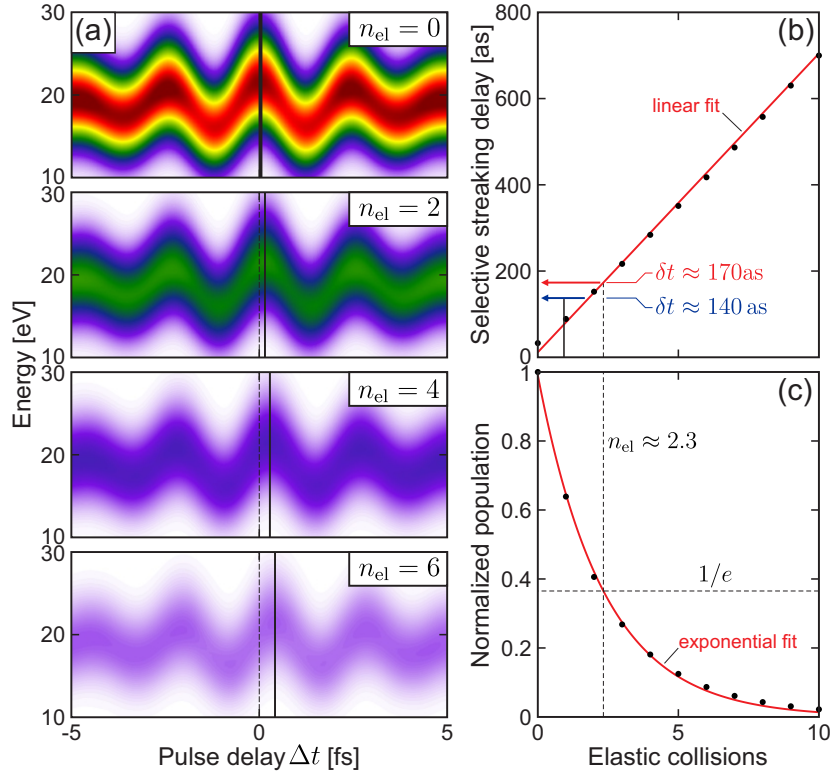


Figure 6.16. Impact of elastic and inelastic scattering on the streaking delay. (a) Selective streaking spectrograms for electrons without inelastic collisions and increasing number of elastic collisions (top to bottom, as indicated). Solid black lines represent the selective streaking delays. (b) Selective streaking delays as function of the number of elastic collisions (black symbols) and linear fit (red curve). (c) Normalized signal strength defined via the sum over each individual streaking spectrogram as function of elastic collisions (black symbols) and exponential fit (red curve). The number of elastic collisions after which the normalized signal decayed to $1/e$ is marked by the vertical dashed line. Adapted from [LS7].

slightly larger than the streaking delay of ≈ 140 as that can be extracted from the full streaking spectrogram (compare red to blue arrow in Fig. 6.16(b)). This deviation is caused by a NIR wavelength-dependent intracycle averaging effect that is discussed below.

6.3.4. Intercycle averaging and wavelength dependence

The analysis of selective streaking spectrograms (cf. Fig. 6.16) revealed a discrepancy between the streaking delays extracted from selective spectrograms and the respective full spectrogram. This deviation can be attributed to an intracycle averaging effect that can intuitively be understood as the 'smearing out' of parts of the full spectrogram into the following cycles. The resulting deformation of the spectrogram can lead to modifications of the extracted streaking delays that can be expected to become non-negligible when the inelastic scattering time (and thus the smear-out effect) is large. The impact of the intercycle averaging effect is estimated by considering a generic streaking spectrogram (see Fig. 6.17(a)) obtained by superimposing individual spectrograms that are shifted in time by t' and weighted by $\exp(-t'/\tau)$ to mimic the respective effects of elastic and inelastic collisions. Here, the decay coefficient is chosen as $\tau = 500$ as. Extracting the streaking

6. Attosecond streaking on dielectric nanospheres

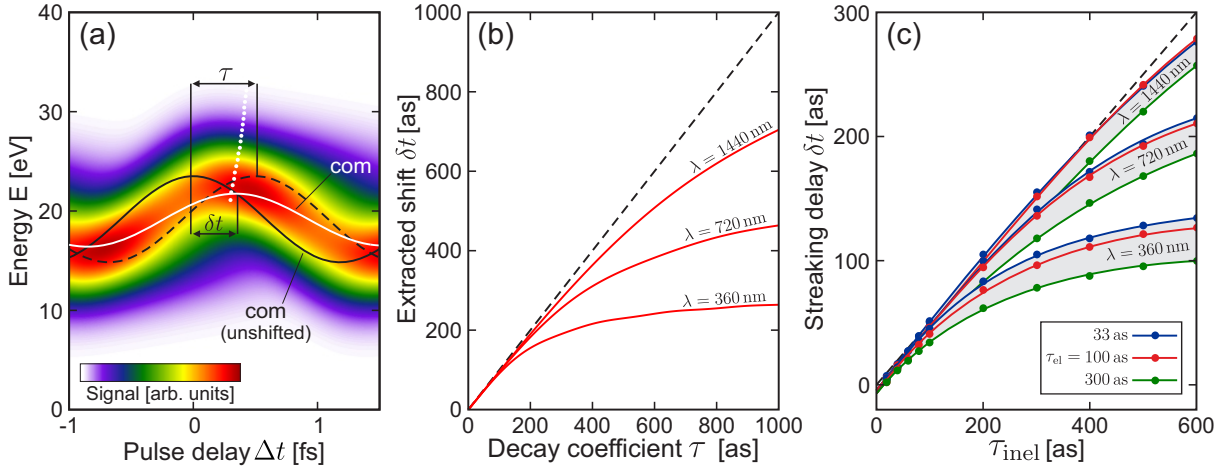


Figure 6.17. Intracycle averaging and wavelength dependence of the streaking delays. **(a)** Generic streaking spectrogram $S(\Delta t, E) = \int_0^\infty s(\Delta t + t', E) \exp(-t'/\tau) dt'$, generated by superimposing individual spectrograms $s(\Delta t, E) = \exp\left(-\frac{1}{2} \frac{(E - E(\Delta t))^2}{\Delta E^2}\right)$ with decreasing weight as determined by the decay coefficient $\tau = 500$ as. Here, $E(\Delta t)$ reflects a streaking trace with asymptotic energy $E_0 = 19$ eV that oscillates corresponding to a wavelength of 720 nm. The amplitude of the oscillation and the spectral width ΔE are chosen to yield a spectrogram similar to those extracted from the full simulations. The solid black curve indicates the streaking trace and also reflects the energetic center of mass (com) of an unshifted individual spectrogram $s(\Delta t, E)$. The dashed black curve visualizes a streaking trace that is delayed by the decay coefficient. The white curve represents the com of the full generic spectrogram $S(\Delta t, E)$ and is delayed by $\delta t \approx 350$ as. White symbols reflect energy-dependent delays extracted via the contour line method. **(b)** Delays extracted from the center of mass of generic streaking spectrograms as in (a) in dependence of the decay coefficient for three wavelengths (as indicated). The dashed black curve indicates $\delta t = \tau$. **(c)** Streaking delays extracted from M³C calculations (no XUV chirp, fixed scattering times) in dependence of the inelastic scattering time and for different elastic scattering times and wavelength of the NIR field (as indicated). Gray areas indicate the variation of the streaking delay with the elastic scattering time for each wavelength. The dashed black curve indicates $\delta t = \tau_{\text{inel}}/2$.

delay via a selective analysis of the individual spectrograms as discussed in the previous section would yield a delay δt equal to the decay coefficient τ (dashed black curve). The streaking delay obtained by fitting a waveform (cf. Eq. 6.2) to the energetic center of mass (solid white curve) of the full generic spectrogram is only $\delta t \approx 350$ as. Note that the intercycle averaging effect also results in an additional energy dependence of delays extracted via the contour line method (white symbols). The qualitative agreement of the observed deviation for the generic streaking spectrogram with the results from M³C spectrograms supports that the intercycle averaging effect emerges only from the delay extraction method.

A systematic analysis of the extracted delay in dependence of the decay coefficient reveals that the deviation is weak for small decay coefficients ($\tau \lesssim 200$ as, compare red curve for $\lambda = 720$ nm to dashed black curve in Fig. 6.17(b)). For larger decay coefficients, the deviation increases and shows a saturation effect that suggests that in this region the streaking spectrograms are significantly smeared out into the following cycles. Although this effect cannot be circumvented in the current way of analyzing the data, the region where the deviation is small can be extended by using longer wavelength driving fields

(compare red curves in Fig. 6.17(b)). For driving fields with smaller wavelength, the saturation starts already at smaller decay coefficients.

Similar to the shifts extracted from the generic streaking spectrograms, also the streaking delays extracted from full M³C simulations indicate the intercycle averaging effect and the effect of the streaking pulse wavelength when analyzed as function of the inelastic scattering time, see Fig. 6.17(c). Here, the dashed black curve represents $\delta t = \tau_{\text{inel}}/2$, since for dielectrics the collisional streaking delay reflects roughly half of the inelastic scattering time (cf. Fig. 6.12). Besides explaining the deviation between the streaking delays extracted from the selective analysis and the full streaking spectrogram (cf. arrows in Fig. 6.16(b)) the intercycle averaging effect also clarifies why the streaking delays extracted for an inelastic scattering time of 900 as in Fig. 6.12 are considerably smaller than $\tau_{\text{inel}}/2 = 450$ as.

6.3.5. Extracted IMFP in comparison with literature

Identifying the vanishing impact of the elastic scattering time on the streaking delay is probably the most important result of this thesis, as it opens the route for the direct extraction of inelastic scattering times for typical dielectric materials. For SiO₂, the M³C simulations reproduce the measured streaking delays when assuming a scaled Lotz cross section and allow to extract an inelastic scattering time of $\tau_{\text{inel}} \approx 370$ as for electron energies around 25 eV. The respective energy-dependent inelastic mean free path of approximately 10 Å is compared to literature data from previous experiments and simulations in Fig. 6.18. Best agreement is found with the IMFP calculated from optical data by Tanuma *et al.* [103]⁶ and obtained from Monte-Carlo simulations by Kuhr *et al.* [102].

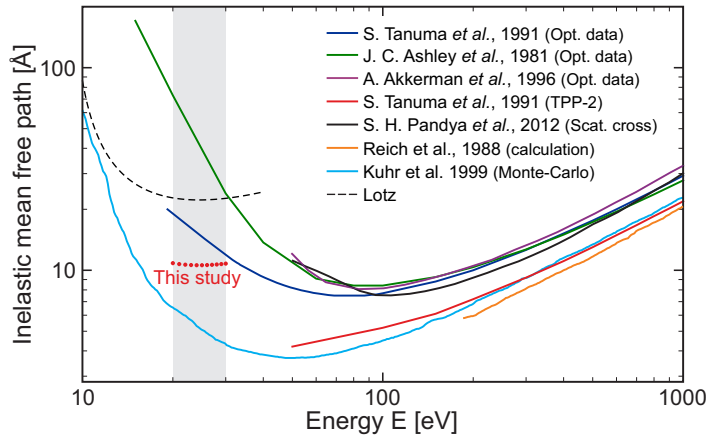


Figure 6.18. Energy-dependent IMFP obtained from this study (red symbols) in comparison with literature data from Tanuma *et al.* [103], Ashley *et al.* [104], Akkerman *et al.* [145], Pandya *et al.* [146], Reich *et al.* [105] and Kuhr *et al.* [102] (curves, as indicated). Adapted from [LS7].

⁶Note that the authors state that their 'IMFP values are shown for 10 – 40 eV electrons to illustrate trends but these results are not considered to be reliable'.

7. Conclusions and outlook

The main goal of this work was to theoretically explore novel aspects of the ultrafast electron dynamics at nanostructures under ultrashort intense laser pulses. A particular aim was the identification of the central physical mechanisms underlying the strong-field induced electron dynamics of recent experiments for the three scenarios of (i) CEP-controlled photoemission from dielectric nanospheres, (ii) coherent electron emission from metal nanotips under bichromatic laser fields, and (iii) attosecond streaking on dielectric nanospheres. As a complete quantum description was not feasible for these scenarios, the theoretical investigations in this work were based on a combination of classical, semi-classical and quantum descriptions of the electron dynamics for corresponding model systems. In particular, near-field driven electron backscattering as well as attosecond streaking at dielectric nanospheres were simulated via the semi-classical Mean-field Mie Monte-Carlo model. The latter combines a continuum description of the local near-fields at a laser-excited nanosphere with modelling the electron motion via classical trajectories. Ionization and electron-atom scattering were included via respective effective rates extracted from simplified quantum models. Near-field mediated coherent electron emission from metal nanotips was studied via a simplified quantum model by solving the time-dependent Schrödinger equation numerically.

The first part was dedicated to the investigation of coherent photoemission from metal nanotips under bichromatic fields. Quantum simulations for a simplified one-dimensional nanotip model revealed strong effects of the near-field inhomogeneity. In particular, the analysis has shown quenching of the quiver motion as observed in earlier nanotip experiments as well as ponderomotive shifts of the coherent HATI signatures due to the finite near-field extension. The main objective was the identification of the dominant control mechanisms that result in changes of the electron spectra as function of the relative phase between the spectral components of the two-color field. The simulations have shown that this phase-dependence is different for low, intermediate, and high electron energies. The dominating processes behind the specific phase modulations were disentangled by employing semi-classical SMM simulations. Comparison of TDSE and SMM results substantiated that the backscattering plateau acquires its phase sensitivity from two-color mediated modifications of the ionization rate. In contrast, modulations of the cut-off are mainly sensitive to modifications of the electron trajectories and were found to be robust with respect to the near-field inhomogeneity. These results could be relevant for future applications measuring and calibrating the two-color phase via nanotip phasemeter devices.

The second objective was to explore the emission of recollision electrons from dielectric nanospheres under CEP-controlled few-cycle pulses. The semi-classical trajectory simulations unveiled the large impact of charge interaction. In particular, the separation of electrons and ions at the surface generates a trapping field that affects the photoemission in two ways. On the one hand, the trapping field quenches the material dependence of the

7. Conclusions and outlook

emission process at high laser intensities where tunneling becomes solely limited by the trapping field. On the other hand, the trapping field suppresses the direct electron emission but enhances the energies of recollision electrons via trapping field assisted backscattering. Besides these trapping field effects, charge interaction can further accelerate emitted electrons via Coulomb explosion of the escaping bunches. Extending the studies to large spheres, where field propagation results in substantial deformations of the local near-fields, revealed the possibility of efficient directional control of the photoemission as well as waveform-controlled switching. For particularly large spheres, the simulations predict a so far unknown and experimentally not yet observed double rescattering mechanism. The latter competes with the conventional single recollision mechanism and is expected to dominate the cut-off of photoelectron spectra for sphere sizes where the local near-field polarization becomes strongly elliptic.

In the third part, attosecond streaking on dielectric nanospheres was investigated. The goal was to unravel the origin of a relative delay measured between the streaking spectrograms from silica nanospheres and a gas reference in a streaking experiment recently performed in the groups of our collaborators Matthias F. Kling and Francesca Calegari. Semi-classical streaking simulations revealed that different effects contribute to the relative delay. It could be shown that contributions due to charge interaction, retardation and inhomogeneities of the local near-fields, and the chirp of the applied attosecond pulses are negligibly small. The dominant contribution could be attributed to the attosecond electron transport dynamics within the dielectric material. A systematic analysis of the specific impacts of elastic and inelastic electron-atom collisions revealed that for a broad range of dielectric materials the streaking delays are essentially insensitive to elastic scattering and can serve as a clock for the inelastic scattering time, providing direct access to the measurement of the inelastic mean free path of electrons in an energy range that was so far inaccessible to direct methods. This conclusion is likely to be the most important one from this thesis, as it may open the door for systematic characterization of attosecond electron transport in various dielectrics.

Outlook

Motivated by recent experiments on metal nanoparticles performed by Matthias F. Kling and Artem Rudenko, an interesting perspective is to make the existing M³C code applicable to metals. This could be realized by including image charge effects and utilizing improved tunneling models. Another promising approach could be to develop Quantum-Vlasov models that combine a trajectory-based description of tunneling for conduction electrons with a quantum-statistical treatment of dissipation via dynamical electron-electron correlations, which represents a so far unresolved problem in time-dependent density-functional theory. Including interference effects in the trajectory approach could enable unprecedented insight into the combined classical and quantum features in the electron emission from nanospheres.

The first proof-of-principle study for attosecond streaking on SiO₂ nanoparticles presented in this work opens numerous routes for future research. For example, further experiments are required to substantiate the results for a broader energy range and other dielectrics. Another remaining issue is to unravel the missing parts of the physical picture behind the collisional delay. A possible approach could be to describe the impacts of elastic

and inelastic collisions and the material's optical properties in a linked analytical model by combining diffusive transport and two-stage streaking. This might enable reliable quantitative predictions for arbitrary materials and allow systematic characterization of material parameters via streaking experiments. Future studies could be performed for water droplets or jets to unravel the transport in a material close to tissue and enable better understanding of radiation induced DNA-damage.

Appendix

A. Quiver motion & ponderomotive energy

The one-dimensional classical motion of an electron in a harmonic electric field $\mathcal{E}(t) = \mathcal{E}_0 \cos(\omega t)$ is determined by the equation of motion

$$m_e \ddot{x}(t) = -e\mathcal{E}(t). \quad (\text{A.1})$$

Considering an electron born into the field at time t_0 , position x_0 and with initial velocity \dot{x}_0 , reorganization of the EOM and integration yields the acceleration, velocity and position

$$\ddot{x}(t) = -\frac{e\mathcal{E}_0}{m_e} \cos(\omega t) \quad (\text{A.2})$$

$$\dot{x}(t) = -\frac{e\mathcal{E}_0}{m_e\omega} [\sin(\omega t) - \sin(\omega t_0)] + \dot{x}_0 \quad (\text{A.3})$$

$$x(t) = -\frac{e\mathcal{E}_0}{m_e\omega^2} [-\cos(\omega t) + \cos(\omega t_0) - \omega \sin(\omega t_0)(t - t_0)] + x_0. \quad (\text{A.4})$$

The prefactors define the characteristic scales of the motion and termed quiver acceleration $a_q = \frac{e\mathcal{E}_0}{m_e}$, quiver velocity $v_q = \frac{e\mathcal{E}_0}{m_e\omega}$ and quiver amplitude $x_q = \frac{e\mathcal{E}_0}{m_e\omega^2}$. The respective energy-scale of the (drift-free) quiver motion is defined as the cycle-averaged kinetic energy and is termed ponderomotive potential or ponderomotive energy

$$U_p = \frac{m_e}{2} \langle \dot{x}(t) \rangle \quad (\text{A.5})$$

$$= \frac{e^2 \mathcal{E}_0^2}{2m_e \omega^2} \langle \sin^2(\omega t) \rangle \quad (\text{A.6})$$

$$= \frac{e^2 \mathcal{E}_0^2}{4m_e \omega^2} \quad (\text{A.7})$$

B. Derivation of the spectral photoionization cross section

The spectral photoionization cross section is derived by considering the absorption of an incident plane wave¹ $e^{ik_0 x}$ by a cubic medium (edge length l) with complex refractive index $n = n_r + in_i$, see [Figure B.1](#). Here, $k_0 = \omega/c_0$ is the wave number in vacuum, corresponding to the angular frequency ω , and c_0 is the vacuum speed of light. Inside the medium the wavenumber is $k = nk_0$ and the field strength hence reads

$$E(x) = e^{ikx} = e^{ink_0 x} = e^{in \frac{\omega}{c_0} x} = e^{in_r \frac{\omega}{c_0} x} \cdot e^{-n_i \frac{\omega}{c_0} x}. \quad (\text{B.1})$$

¹Note that the time-dependent part is omitted here for the sake of readability

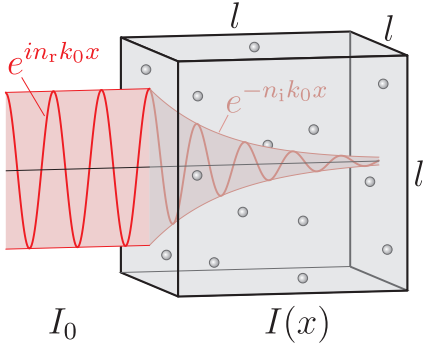


Figure B.1. Absorption of an incident plane wave (from the left) by a box of volume l^2 filled with N atoms. Note that for better visualization the real part n_r of the complex refractive index is chosen to be unity.

The second part $e^{-n_i \frac{\omega}{c_0} x}$ describes the absorption of the field driven by the extinction coefficient n_i . The corresponding intensity is given by

$$I(x) \sim I_0 e^{-\frac{2n_i \omega}{c_0} x} = I_0 e^{-\frac{x}{x_0}}, \quad (\text{B.2})$$

with the decay length $x_0 = \frac{c_0}{2n_i \omega}$.

Considering a finite pulse of length τ being absorbed by the cube, the incident energy is given by $W_{\text{inc}} = I\tau l^2$. The absorbed energy is given by $W_{\text{abs}} = -I\tau\sigma N$, where σ is the atomic photoionization cross section, and N is the number of atoms in the volume l^3 . Considering the atom density $n = N/l^3$ yields $W_{\text{abs}} = -I\tau\sigma n l^3$. The fraction of energy lost compared to the incident energy is given by

$$\frac{W_{\text{abs}}}{W_{\text{inc}}} = -\frac{I\tau\sigma n l^3}{I\tau l^2} = -\sigma n l. \quad (\text{B.3})$$

In an infinitesimal small absorption length dx the ratio of the absorbed intensity dI to the incident intensity I is given by

$$\frac{dI}{I} \sim \frac{dW}{W} = -\sigma n dx \quad (\text{B.4})$$

yielding that $\frac{dI}{dx} = -\sigma n I$. Integrating results in

$$I = I_0 e^{-\sigma n x}. \quad (\text{B.5})$$

Comparing Eq. B.2 and Eq. B.5 yields that $1/x_0 = \sigma n$ and therefore

$$\sigma(\omega) = \frac{2n_i \omega}{nc_0}. \quad (\text{B.6})$$

C. Impact of anisotropic elastic scattering in typical simulations

The differential scattering cross section in Fig. 2.10(b) shows that forward scattering prevails for electron energies above ≈ 5 eV. To justify assuming isotropic elastic scattering for the M³C simulations in this work, a comparison of typical simulation results obtained for isotropic and anisotropic elastic scattering is shown in Fig. C.1.

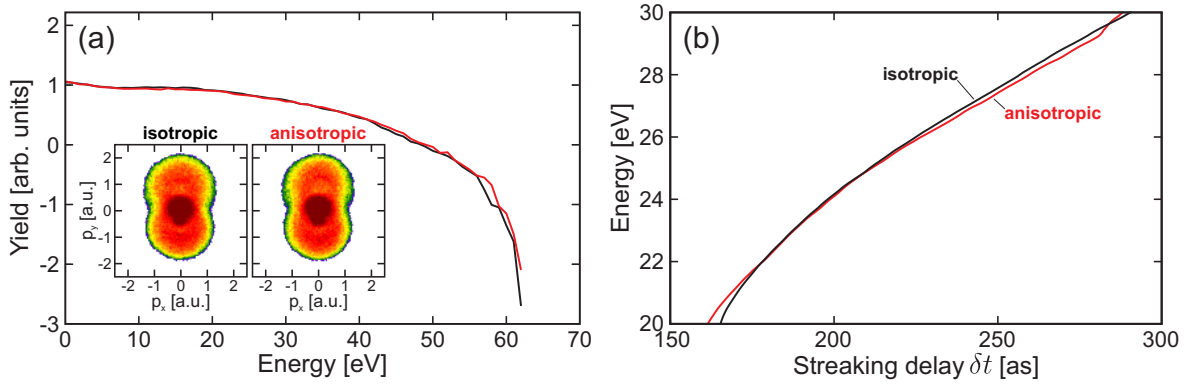


Figure C.1. Comparison of M^3C simulations with isotropic (black curves) and anisotropic (red curves) elastic scattering. **(a)** Energy spectra from $d = 100$ nm silica spheres under NIR few-cycle pulses ($\lambda = 720$ nm, $\tau = 4$ fs, $I = 3 \times 10^{13}$ W/cm², $\varphi_{ce} = 0$). Insets show the respective projected momentum images (as indicated). **(b)** Absolute streaking delay from silica nanoparticles as in Fig. 6.7(a). The black curve represents the data shown in the main part of the thesis and the red curve reflects the results of a corresponding simulation with anisotropic elastic scattering. Data published partially in [LS7].

The energy spectra of electrons emitted from $d = 100$ nm reveal no significant difference when considering isotropic (black curve) or anisotropic (red curve) elastic scattering. Also the respective projected momentum images (see inset) remain robust under the effect of anisotropic scattering. This supports the assumption of isotropic elastic scattering for the recollision studies in Chapter 4 and Chapter 5 of this thesis.

The streaking simulations presented in Chapter 6 of this thesis have been performed assuming isotropic elastic collisions. Also the cancellation of the momentum gain acquired before an elastic collision has been motivated considering isotropic scattering. To check if these assumptions are justified the impact of anisotropic scattering on the attosecond streaking is inspected, by comparing the streaking delays from simulations with isotropic and anisotropic elastic collisions (compare black and red curves in Fig. C.1(b)). The good agreement supports that the assumption of isotropic elastic scattering is justified for the streaking analysis.

D. Impact of charge interaction on attosecond streaking

To inspect the effect of charge-interaction on the attosecond streaking at nanospheres, the streaking delay from M^3C simulations excluding the mean-field (as shown in Fig. 6.7(a) in the main part of the thesis) is compared to respective result from a simulation including the mean-field in Fig. D.1. The comparison shows that the streaking delay is only weakly affected by charge-interaction over the full energy range of interest. Due to the high numerical effort for performing the simulations including charge-interaction, the statistics close to the spectral cut-off ($\gtrsim 27$ eV) was low and the extracted streaking delay is not considered to be reliable in this region (see dotted part of the red curve). For lower energies, the modification of the delay when including charge-interaction is $\lesssim 5$ as and thus much

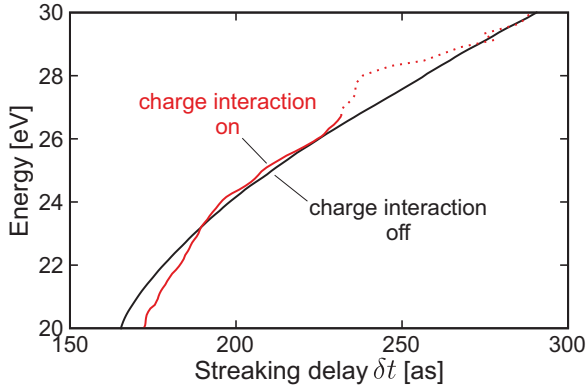


Figure D.1. Energy-dependent streaking delays for $d = 50$ nm silica spheres as predicted by M³C simulations excluding (black curve, cf. Fig. 6.7(a)) and including (red curve) charge-interaction. The dotted part of the red curve indicates the high energy region, where the streaking delay is subject to strong variations due to low statistics.

smaller than the dominant collisional delay (≈ 150 as). Hence, the main conclusions of this thesis remain robust also when taking charge-interaction into account.

E. Transport cross sections for SiO₂, ZnS, Fe₃O₄ and PS

Figure E.1 shows the calculated transport cross sections for the elastic scattering in the different materials investigated in Section 4.2.2.

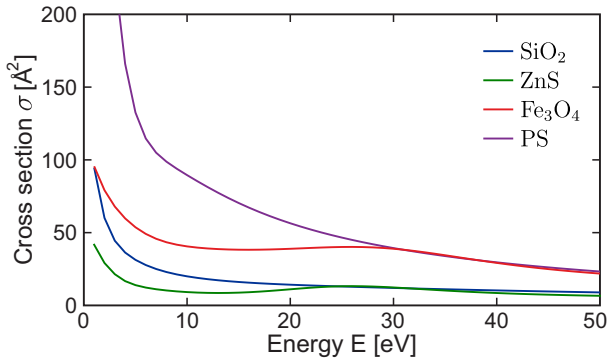


Figure E.1. Elastic scattering transport cross sections for SiO₂, ZnS, Fe₃O₄ and PS as considered for the M³C simulations presented in Section 4.2.2.

Bibliography

- [1] L. V. Keldysh, *Ionization in the field of a strong electromagnetic wave*, *Sov. Phys. – JETP* **20**, 1307–1314 (1965).
- [2] P. B. Corkum, *Plasma perspective on strong field multiphoton ionization*, *Phys. Rev. Lett.* **71**, 1994–1997 (1993).
- [3] K. Schafer, Z. Wei and M. Vrakking, *Special issue celebrating 25 years of re-collision physics*, *J. Phys. B: At., Mol. Opt. Phys.* **50**, 170201 (2017).
- [4] G. G. Paulus, W. Nicklich, H. Xu, P. Lambropoulos and H. Walther, *Plateau in above threshold ionization spectra*, *Phys. Rev. Lett.* **72**, 2851–2854 (1994).
- [5] G. G. Paulus, W. Becker, W. Nicklich and H. Walther, *Rescattering effects in above-threshold ionization: a classical model*, *J. Phys. B: At., Mol. Opt. Phys.* **27**, L703 (1994).
- [6] W. Becker, S. P. Goreslavski, D. B. Milosevic and G. G. Paulus, *The plateau in above-threshold ionization: the keystone of rescattering physics*, *J. Phys. B: At., Mol. Opt. Phys.* **51**, 162002 (2018).
- [7] A. McPherson, G. Gibson, H. Jara, U. Johann, T. S. Luk, I. A. McIntyre, K. Boyer and C. K. Rhodes, *Studies of multiphoton production of vacuum-ultraviolet radiation in the rare gases*, *J. Opt. Soc. Am. B* **4**, 595–601 (1987).
- [8] M. Ferray, A. L’Huillier, X. F. Li, L. A. Lompre, G. Mainfray and C. Manus, *Multiple-harmonic conversion of 1064 nm radiation in rare gases*, *J. Phys. B: At., Mol. Opt. Phys.* **21**, L31 (1988).
- [9] X. F. Li, A. L’Huillier, M. Ferray, L. A. Lompré and G. Mainfray, *Multiple-harmonic generation in rare gases at high laser intensity*, *Phys. Rev. A* **39**, 5751–5761 (1989).
- [10] J. L. Krause, K. J. Schafer and K. C. Kulander, *High-order harmonic generation from atoms and ions in the high intensity regime*, *Phys. Rev. Lett.* **68**, 3535–3538 (1992).
- [11] A. L’Huillier, M. Lewenstein, P. Salières, P. Balcou, M. Y. Ivanov, J. Larsson and C. G. Wahlström, *High-order Harmonic-generation cutoff*, *Phys. Rev. A* **48**, R3433–R3436 (1993).
- [12] M. Lewenstein, P. Balcou, M. Y. Ivanov, A. L’Huillier and P. B. Corkum, *Theory of high-harmonic generation by low-frequency laser fields*, *Phys. Rev. A* **49**, 2117–2132 (1994).

- [13] S. Zharebtsov, T. Fennel, J. Plenge, E. Antonsson, I. Znakovskaya, A. Wirth, O. Herwerth, F. Süßmann, C. Peltz, I. Ahmad, S. A. Trushin, V. Pervak, S. Karsch, M. J. J. Vrakking, B. Langer, C. Graf, M. I. Stockman, F. Krausz, E. Rühl and M. F. Kling, *Controlled near-field enhanced electron acceleration from dielectric nanospheres with intense few-cycle laser fields*, *Nat. Phys.* **7**, 656–662 (2011).
- [14] S. Zharebtsov, F. Süßmann, C. Peltz, J. Plenge, K. J. Betsch, I. Znakovskaya, A. S. Alnaser, N. G. Johnson, M. Kübel, A. Horn, V. Mondes, C. Graf, S. A. Trushin, A. Azzeer, M. J. J. Vrakking, G. G. Paulus, F. Krausz, E. Rühl, T. Fennel and M. F. Kling, *Carrier-envelope phase-tagged imaging of the controlled electron acceleration from SiO₂ nanospheres in intense few-cycle laser fields*, *New J. Phys.* **14**, 075010 (2012).
- [15] M. Krüger, M. Schenk and P. Hommelhoff, *Attosecond control of electrons emitted from a nanoscale metal tip*, *Nature* **475**, 78–81 (2011).
- [16] G. Herink, D. R. Solli, M. Gulde and C. Ropers, *Field-driven photoemission from nanostructures quenches the quiver motion*, *Nature* **483**, 190–193 (2012).
- [17] D. J. Park, P. Björn, S. Slawa, K. Heiko, M. Manfred, G. Petra and L. Christoph, *Characterizing the optical near-field in the vicinity of a sharp metallic nanoprobe by angle-resolved electron kinetic energy spectroscopy*, *Ann. Phys.* **525**, 135–142 (2013).
- [18] B. Piglosiewicz, S. Schmidt, D. J. Park, J. Vogelsang, P. Gross, C. Manzoni, P. Farinello, G. Cerullo and C. Lienau, *Carrier-envelope phase effects on the strong-field photoemission of electrons from metallic nanostructures*, *Nat. Phot.* **8**, 37–42 (2014).
- [19] H. Yanagisawa, S. Schnepf, C. Hafner, M. Hengsberger, D. E. Kim, M. F. Kling, A. Landsman, L. Gallmann and J. Osterwalder, *Delayed electron emission in strong-field driven tunnelling from a metallic nanotip in the multi-electron regime*, *Sci. Rep.* **6**, 35877 (2016).
- [20] P. Dombi, A. Hörl, P. Rácz, I. Márton, A. Trügler, J. R. Krenn and U. Hohenester, *Ultrafast Strong-Field Photoemission from Plasmonic Nanoparticles*, *Nano Lett.* **13**, 674–678 (2013).
- [21] P. Hommelhoff and M. F. Kling, *Attosecond Nanophysics: From Basic Science to Applications*, Wiley-VCH (2015), ISBN: 978-3-527-41171-9.
- [22] F. Krausz and M. I. Stockman, *Attosecond metrology: from electron capture to future signal processing*, *Nat. Photonics* **8**, 205 (2014).
- [23] W. Becker, F. Grasbon, R. Kopold, D. B. Milošević, G. G. Paulus and H. Walther, *Above-Threshold Ionization: From Classical Features to Quantum Effects*, *Adv. At. Mol. Opt. Phys.* **48**, 35–98 (2002).
- [24] D. G. Arbó, K. L. Ishikawa, K. Schiessl, E. Persson and J. Burgdörfer, *Intracycle and intercycle interferences in above-threshold ionization: The time grating*, *Phys. Rev. A* **81**, 021403 (2010).

-
- [25] G. G. Paulus, F. Lindner, H. Walther, A. Baltuška, E. Goulielmakis, M. Lezius and F. Krausz, *Measurement of the Phase of Few-Cycle Laser Pulses*, *Phys. Rev. Lett.* **91**, 253004 (2003).
- [26] M. Kitzler and M. Lezius, *Spatial Control of Recollision Wave Packets with Attosecond Precision*, *Phys. Rev. Lett.* **95**, 253001 (2005).
- [27] S. Skruszewicz, J. Tiggesbäumker, K.-H. Meiwes-Broer, M. Arbeiter, T. Fennel and D. Bauer, *Two-Color Strong-Field Photoelectron Spectroscopy and the Phase of the Phase*, *Phys. Rev. Lett.* **115**, 043001 (2015).
- [28] L. Medišauskas, J. Wragg, H. van der Hart and M. Y. Ivanov, *Generating Isolated Elliptically Polarized Attosecond Pulses Using Bichromatic Counterrotating Circularly Polarized Laser Fields*, *Phys. Rev. Lett.* **115**, 153001 (2015).
- [29] D. B. Milošević, *Generation of elliptically polarized attosecond pulse trains*, *Opt. Lett.* **40**, 2381–2384 (2015).
- [30] M. Hentschel, R. Kienberger, C. Spielmann, G. A. Reider, N. Milosevic, T. Brabec, P. Corkum, U. Heinzmann, M. Drescher and F. Krausz, *Attosecond metrology*, *Nature* **414**, 509 (2001).
- [31] P. B. Corkum and F. Krausz, *Attosecond science*, *Nat. Phys.* **3**, 381–387 (2007).
- [32] F. Krausz and M. Ivanov, *Attosecond physics*, *Rev. Mod. Phys.* **81**, 163–234 (2009).
- [33] S. Harris, J. Macklin and T. Hänsch, *Atomic scale temporal structure inherent to high-order harmonic generation*, *Opt. Commun.* **100**, 487–490 (1993).
- [34] P. M. Paul, E. S. Toma, P. Breger, G. Mullot, F. Augé, P. Balcou, H. G. Muller and P. Agostini, *Observation of a Train of Attosecond Pulses from High Harmonic Generation*, *Science* **292**, 1689–1692 (2001).
- [35] Y. Mairesse, A. de Bohan, L. J. Frasinski, H. Merdji, L. C. Dinu, P. Monchicourt, P. Breger, M. Kovačev, R. Taïeb, B. Carré, H. G. Muller, P. Agostini and P. Salières, *Attosecond Synchronization of High-Harmonic Soft X-rays*, *Science* **302**, 1540–1543 (2003).
- [36] H. Muller, *Reconstruction of attosecond harmonic beating by interference of two-photon transitions*, *Appl. Phys. B* **74**, s17–s21 (2002).
- [37] D. Baykusheva and H. J. Wörner, *Theory of attosecond delays in molecular photoionization*, *J. Chem. Phys.* **146**, 124306 (2017).
- [38] R. Locher, L. Castiglioni, M. Lucchini, M. Greif, L. Gallmann, J. Osterwalder, M. Hengsberger and U. Keller, *Energy-dependent photoemission delays from noble metal surfaces by attosecond interferometry*, *Optica* **2**, 405–410 (2015).
- [39] Z. Tao, C. Chen, T. Szilvási, M. Keller, M. Mavrikakis, H. Kapteyn and M. Murnane, *Direct time-domain observation of attosecond final-state lifetimes in photoemission from solids*, *Science* **353**, 62–67 (2016).

- [40] D. Rattenbacher, I. Jordan, A. Schild and H. J. Wörner, *Nonlocal mechanisms of attosecond interferometry and implications for condensed-phase experiments*, *Phys. Rev. A* **97**, 063415 (2018).
- [41] A. Baltuška, T. Udem, M. Uiberacker, M. Hentschel, E. Goulielmakis, C. Gohle, R. Holzwarth, V. S. Yakovlev, A. Scrinzi, T. W. Hänsch and F. Krausz, *Attosecond control of electronic processes by intense light fields*, *Nature* **421**, 611 (2003).
- [42] E. Goulielmakis, M. Uiberacker, R. Kienberger, A. Baltuška, V. Yakovlev, A. Scrinzi, T. Westerwalbesloh, U. Kleineberg, U. Heinzmann, M. Drescher and F. Krausz, *Direct Measurement of Light Waves*, *Science* **305**, 1267–1269 (2004).
- [43] E. Gagnon, I. Thomann, A. Paul, A. L. Lytle, S. Backus, M. M. Murnane, H. C. Kapteyn and A. S. Sandhu, *Long-term carrier-envelope phase stability from a grating-based, chirped pulse amplifier*, *Opt. Lett.* **31**, 1866–1868 (2006).
- [44] I. P. Christov, M. M. Murnane and H. C. Kapteyn, *High-Harmonic Generation of Attosecond Pulses in the “Single-Cycle” Regime*, *Phys. Rev. Lett.* **78**, 1251–1254 (1997).
- [45] R. Kienberger, E. Goulielmakis, M. Uiberacker, A. Baltuška, V. Yakovlev, F. Bammer, A. Scrinzi, T. Westerwalbesloh, U. Kleineberg, U. Heinzmann, M. Drescher and F. Krausz, *Atomic transient recorder*, *Nature* **427**, 817–821 (2004).
- [46] G. Sansone, E. Benedetti, F. Calegari, C. Vozzi, L. Avaldi, R. Flammini, L. Poletto, P. Villoresi, C. Altucci, R. Velotta, S. Stagira, S. De Silvestri and M. Nisoli, *Isolated Single-Cycle Attosecond Pulses*, *Science* **314**, 443–446 (2006).
- [47] P. B. Corkum, N. H. Burnett and M. Y. Ivanov, *Subfemtosecond pulses*, *Opt. Lett.* **19**, 1870–1872 (1994).
- [48] C. Altucci, C. Delfin, L. Roos, M. B. Gaarde, A. L’Huillier, I. Mercer, T. Starczewski and C.-G. Wahlström, *Frequency-resolved time-gated high-order harmonics*, *Phys. Rev. A* **58**, 3934–3941 (1998).
- [49] F. Calegari, G. Sansone, S. Stagira, C. Vozzi and M. Nisoli, *Advances in attosecond science*, *J. Phys. B: At., Mol. Opt. Phys.* **49**, 062001 (2016).
- [50] E. Constant, V. D. Taranukhin, A. Stolow and P. B. Corkum, *Methods for the measurement of the duration of high-harmonic pulses*, *Phys. Rev. A* **56**, 3870–3878 (1997).
- [51] M. Drescher, M. Hentschel, R. Kienberger, G. Tempea, C. Spielmann, G. A. Reider, P. B. Corkum and F. Krausz, *X-ray Pulses Approaching the Attosecond Frontier*, *Science* **291**, 1923–1927 (2001).
- [52] J. Itatani, F. Quéré, G. L. Yudin, M. Y. Ivanov, F. Krausz and P. B. Corkum, *Attosecond Streak Camera*, *Phys. Rev. Lett.* **88**, 173903 (2002).
- [53] D. Hoff, M. Krüger, L. Maisenbacher, A. M. Saylor, G. G. Paulus and P. Hommelhoff, *Tracing the phase of focused broadband laser pulses*, *Nat. Phys.* **13**, 947 (2017).

-
- [54] L. Wimmer, G. Herink, D. R. Solli, S. V. Yalunin, K. E. Echternkamp and C. Ropers, *Terahertz control of nanotip photoemission*, *Nat. Phys.* **10**, 432 (2014).
- [55] G. Herink, L. Wimmer and C. Ropers, *Field emission at terahertz frequencies: AC-tunneling and ultrafast carrier dynamics*, *New J. Phys.* **16**, 123005 (2014).
- [56] A. Feist, K. E. Echternkamp, J. Schauss, S. V. Yalunin, S. Schäfer and C. Ropers, *Quantum coherent optical phase modulation in an ultrafast transmission electron microscope*, *Nature* **521**, 200 (2015).
- [57] K. E. Priebe, C. Rathje, S. V. Yalunin, T. Hohage, A. Feist, S. Schäfer and C. Ropers, *Attosecond electron pulse trains and quantum state reconstruction in ultrafast transmission electron microscopy*, *Nat. Photonics* **11**, 793–797 (2017).
- [58] K. E. Echternkamp, G. Herink, S. V. Yalunin, K. Rademann, S. Schäfer and C. Ropers, *Strong-field photoemission in nanotip near-fields: from quiver to sub-cycle electron dynamics*, *Appl. Phys. B* **122**, 80 (2016).
- [59] J. Schötz, S. Mitra, H. Fuest, M. Neuhaus, W. A. Okell, M. Förster, T. Paschen, M. F. Ciappina, H. Yanagisawa, P. Wnuk, P. Hommelhoff and M. F. Kling, *Nonadiabatic ponderomotive effects in photoemission from nanotips in intense midinfrared laser fields*, *Phys. Rev. A* **97**, 013413 (2018).
- [60] S. Thomas, G. Wachter, C. Lemell, J. Burgdörfer and P. Hommelhoff, *Large optical field enhancement for nanotips with large opening angles*, *New J. Phys.* **17**, 063010 (2015).
- [61] M. Förster, T. Paschen, M. Krüger, C. Lemell, G. Wachter, F. Libisch, T. Madlener, J. Burgdörfer and P. Hommelhoff, *Two-Color Coherent Control of Femtosecond Above-Threshold Photoemission from a Tungsten Nanotip*, *Phys. Rev. Lett.* **117**, 217601 (2016).
- [62] T. Paschen, M. Förster, M. Krüger, C. Lemell, G. Wachter, F. Libisch, T. Madlener, J. Burgdörfer and P. Hommelhoff, *High visibility in two-color above-threshold photoemission from tungsten nanotips in a coherent control scheme*, *J. Mod. Opt.* **64**, 1054–1060 (2017).
- [63] T. V. Liseykina, S. Pirner and D. Bauer, *Relativistic Attosecond Electron Bunches from Laser-Illuminated Droplets*, *Phys. Rev. Lett.* **104**, 095002 (2010).
- [64] L. Di Lucchio and P. Gibbon, *Relativistic attosecond electron bunch emission from few-cycle laser irradiated nanoscale droplets*, *Phys. Rev. ST Accel. Beams* **18**, 023402 (2015).
- [65] J. M. Dahlström, A. L’Huillier and A. Maquet, *Introduction to attosecond delays in photoionization*, *J. Phys. B: At., Mol. Opt. Phys.* **45**, 183001 (2012).
- [66] R. Pazourek, S. Nagele and J. Burgdörfer, *Attosecond chronoscopy of photoemission*, *Rev. Mod. Phys.* **87**, 765–802 (2015).

- [67] M. Schultze, M. Fieß, N. Karpowicz, J. Gagnon, M. Korbman, M. Hofstetter, S. Neppl, A. L. Cavalieri, Y. Komninos, T. Mercouris, C. A. Nicolaides, R. Pazourek, S. Nagele, J. Feist, J. Burgdörfer, A. M. Azzeer, R. Ernstorfer, R. Kienberger, U. Kleineberg, E. Goulielmakis, F. Krausz and V. S. Yakovlev, *Delay in Photoemission*, [Science](#) **328**, 1658–1662 (2010).
- [68] S. Nagele, R. Pazourek, J. Feist, K. Doblhoff-Dier, C. Lemell, K. Tókési and J. Burgdörfer, *Time-resolved photoemission by attosecond streaking: extraction of time information*, [J. Phys. B: At., Mol. Opt. Phys.](#) **44**, 081001 (2011).
- [69] P. Hockett, E. Frumker, D. M. Villeneuve and P. B. Corkum, *Time delay in molecular photoionization*, [J. Phys. B: At., Mol. Opt. Phys.](#) **49**, 095602 (2016).
- [70] L. Eisenbud, *The Formal Properties of Nuclear Collisions*, PhD thesis, Princeton University (1948).
- [71] E. P. Wigner, *Lower Limit for the Energy Derivative of the Scattering Phase Shift*, [Phys. Rev.](#) **98**, 145–147 (1955).
- [72] F. T. Smith, *Lifetime Matrix in Collision Theory*, [Phys. Rev.](#) **118**, 349–356 (1960).
- [73] O. Smirnova, M. Spanner and M. Y. Ivanov, *Coulomb and polarization effects in laser-assisted XUV ionization*, [J. Phys. B: At., Mol. Opt. Phys.](#) **39**, S323 (2006).
- [74] O. Smirnova, A. S. Mouritzen, S. Patchkovskii and M. Y. Ivanov, *Coulomb–laser coupling in laser-assisted photoionization and molecular tomography*, [J. Phys. B: At., Mol. Opt. Phys.](#) **40**, F197 (2007).
- [75] C.-H. Zhang and U. Thumm, *Electron-ion interaction effects in attosecond time-resolved photoelectron spectra*, [Phys. Rev. A](#) **82**, 043405 (2010).
- [76] Y. Mairesse and F. Quéré, *Frequency-resolved optical gating for complete reconstruction of attosecond bursts*, [Phys. Rev. A](#) **71**, 011401 (2005).
- [77] J. Gagnon, E. Goulielmakis and V. Yakovlev, *The accurate FROG characterization of attosecond pulses from streaking measurements*, [Appl. Phys. B](#) **92**, 25–32 (2008).
- [78] A. L. Cavalieri, N. Müller, T. Uphues, V. S. Yakovlev, A. Baltuška, B. Horvath, B. Schmidt, L. Blümel, R. Holzwarth, S. Hendel, M. Drescher, U. Kleineberg, P. M. Echenique, R. Kienberger, F. Krausz and U. Heinzmann, *Attosecond spectroscopy in condensed matter*, [Nature](#) **449**, 1029–1032 (2007).
- [79] S. Neppl, R. Ernstorfer, E. M. Bothschafter, A. L. Cavalieri, D. Menzel, J. V. Barth, F. Krausz, R. Kienberger and P. Feulner, *Attosecond Time-Resolved Photoemission from Core and Valence States of Magnesium*, [Phys. Rev. Lett.](#) **109**, 087401 (2012).
- [80] S. Neppl, R. Ernstorfer, A. L. Cavalieri, C. Lemell, G. Wachter, E. Magerl, E. M. Bothschafter, M. Jobst, M. Hofstetter, U. Kleineberg, J. V. Barth, D. Menzel, J. Burgdörfer, P. Feulner, F. Krausz and R. Kienberger, *Direct observation of electron propagation and dielectric screening on the atomic length scale*, [Nature](#) **517**, 342 (2015).

- [81] F. Siek, S. Neb, P. Bartz, M. Hensen, C. Strüber, S. Fiechter, M. Torrent-Sucarrat, V. M. Silkin, E. E. Krasovskii, N. M. Kabachnik, S. Fritzsche, R. D. Muiño, P. M. Echenique, A. K. Kazansky, N. Müller, W. Pfeiffer and U. Heinzmann, *Angular momentum-induced delays in solid-state photoemission enhanced by intra-atomic interactions*, *Science* **357**, 1274–1277 (2017).
- [82] P. Balling and J. Schou, *Femtosecond-laser ablation dynamics of dielectrics: basics and applications for thin films*, *Rep. Prog. Phys.* **76**, 036502 (2013).
- [83] B. C. Garrett, D. A. Dixon, D. M. Camaioni, D. M. Chipman, M. A. Johnson, C. D. Jonah, G. A. Kimmel, J. H. Miller, T. N. Rescigno, P. J. Rossky, S. S. Xantheas, S. D. Colson, A. H. Laufer, D. Ray, P. F. Barbara, D. M. Bartels, K. H. Becker, K. H. Bowen, S. E. Bradforth, I. Carmichael, J. V. Coe, L. R. Corrales, J. P. Cowin, M. Dupuis, K. B. Eisenthal, J. A. Franz, M. S. Gutowski, K. D. Jordan, B. D. Kay, J. A. LaVerne, S. V. Lymar, T. E. Madey, C. W. McCurdy, D. Meisel, S. Mukamel, A. R. Nilsson, T. M. Orlando, N. G. Petrik, S. M. Pimblott, J. R. Rustad, G. K. Schenter, S. J. Singer, A. Tokmakoff, L.-S. Wang, and T. S. Zwier, *Role of Water in Electron-Initiated Processes and Radical Chemistry: Issues and Scientific Advances*, *Chem. Rev.* **105**, 355–390 (2005).
- [84] C. Caleman, C. Ortiz, E. Marklund, F. Bultmark, M. Gabrysch, F. G. Parak, J. Hajdu, M. Klintenbergl and N. Timneanu, *Radiation damage in biological material: Electronic properties and electron impact ionization in urea*, *Europhys. Lett.* **85**, 18005 (2009).
- [85] L. H. Toburen, S. L. McLawhorn, R. A. McLawhorn, K. D. Carnes, M. Dingfelder and J. L. Shinpaugh, *Electron Emission from Amorphous Solid Water Induced by Passage of Energetic Protons and Fluorine Ions*, *Radiat. Res.* **174**, 107–118 (2010).
- [86] M. A. Hill, P. O’Neill and W. G. McKenna, *Comments on potential health effects of MRI-induced DNA lesions: quality is more important to consider than quantity*, *Eur. Heart J. Cardiovasc. Imaging* **17**, 1230–1238 (2016).
- [87] G. Wachter, C. Lemell, J. Burgdörfer, M. Schenk, M. Krüger and P. Hommelhoff, *Electron rescattering at metal nanotips induced by ultrashort laser pulses*, *Phys. Rev. B* **86**, 035402 (2012).
- [88] J. D. Jackson, *Classical electrodynamics*, Wiley (New York) (1999), ISBN: 978-0-471-30932-1.
- [89] G. Mie, *Beiträge zur Optik trüber Medien, speziell kolloidaler Metallösungen*, *Ann. Phys.* **330**, 377–445 (1908).
- [90] J. A. Stratton, *Electromagnetic theory*, John Wiley & Sons (2007), ISBN: 978-0-470-13153-4.
- [91] C. F. Bohren and D. R. Huffman, *Absorption and scattering of light by small particles*, John Wiley & Sons (1998), ISBN: 978-0-471-29340-8.
- [92] E. Wigner, *On the Quantum Correction For Thermodynamic Equilibrium*, *Phys. Rev.* **40**, 749–759 (1932).

- [93] L. Cohen, *Time-frequency distributions – a review*, *Proc. IEEE* **77**, 941–981 (1989).
- [94] K.-H. Hong, J.-H. Kim, Y. Kang and C. Nam, *Time-frequency analysis of chirped femtosecond pulses using Wigner distribution function*, *Appl. Phys. B* **74**, 231–236 (2002).
- [95] M. V. Ammosov, N. B. Delone and V. P. Krainov, *Tunnel ionization of complex atoms and of atomic ions in an alternating electromagnetic field*, *Sov. Phys. JETP* **64**, 1191–1194 (1986).
- [96] E. Antonsson, *Photoexcitation, Photoionization, and X-Ray Scattering of Free Nanoparticles Prepared in a Beam*, PhD thesis, Freie Universität Berlin (2011).
- [97] G.-L. Tan, M. F. Lemon and R. H. French, *Optical Properties and London Dispersion Forces of Amorphous Silica Determined by Vacuum Ultraviolet Spectroscopy and Spectroscopic Ellipsometry*, *J. Am. Ceram. Soc.* **86**, 1885–1892 (2003).
- [98] E. Schreiber and H.-J. Fitting, *Monte Carlo simulation of secondary electron emission from the insulator SiO₂*, *J. Electron Spectrosc. Relat. Phenom.* **124**, 25–37 (2002).
- [99] L. Verlet, *Computer "Experiments" on Classical Fluids. I. Thermodynamical Properties of Lennard-Jones Molecules*, *Phys. Rev.* **159**, 98–103 (1967).
- [100] W. C. Swope, H. C. Andersen, P. H. Berens and K. R. Wilson, *A computer simulation method for the calculation of equilibrium constants for the formation of physical clusters of molecules: Application to small water clusters*, *J. Chem. Phys.* **76**, 637–649 (1982).
- [101] M. Siegfried, *Einfluss von harten Elektron-Atom-Stößen auf die Ionisationsdynamik atomarer Cluster in intensiven Laserfeldern*, Master's thesis, University of Rostock (2014).
- [102] J.-C. Kuhr and H.-J. Fitting, *Monte Carlo simulation of electron emission from solids*, *J. Electron Spectrosc. Relat. Phenom.* **105**, 257–273 (1999).
- [103] S. Tanuma, C. J. Powell and D. R. Penn, *Calculations of electron inelastic mean free paths. III. Data for 15 inorganic compounds over the 50–2000 eV range*, *Surf. Interface Anal.* **17**, 927–939 (1991).
- [104] J. C. Ashley and V. E. Anderson, *Energy Losses and Mean Free Paths of Electrons in Silicon Dioxide*, *IEEE Trans. Nucl. Sci.* **28**, 4131–4136 (1981).
- [105] T. Reich, V. G. Yarzhemski and V. I. Nefedov, *Calculation of inelastic mean free path of photoelectrons in some solids*, *J. Electron Spectrosc. Relat. Phenom.* **46**, 255–267 (1988).
- [106] W. Lotz, *An empirical formula for the electron-impact ionization cross-section*, *Zeitschrift für Physik* **206**, 205–211 (1967).
- [107] D. Bauer and P. Koval, *Qprop: A Schrödinger-solver for intense laser-atom interaction*, *Comput. Phys. Commun.* **174**, 396–421 (2006).

-
- [108] J. Crank and P. Nicolson, *A practical method for numerical evaluation of solutions of partial differential equations of the heat-conduction type*, *Math. Proc. Cambridge Philos. Soc.* **43**, 50–67 (1947).
- [109] D. Neuhasuer and M. Baer, *The time-dependent Schrödinger equation: Application of absorbing boundary conditions*, *J. Chem. Phys.* **90**, 4351–4355 (1989) (Note, that the correct first author name is D. Neuhauser).
- [110] K. J. Schafer and K. C. Kulander, *Energy analysis of time-dependent wave functions: Application to above-threshold ionization*, *Phys. Rev. A* **42**, 5794–5797 (1990).
- [111] K. J. Schafer, *The energy analysis of time-dependent numerical wave functions*, *Comput. Phys. Commun.* **63**, 427–434 (1991).
- [112] M. Krüger, C. Lemell, G. Wachter, J. Burgdoerfer and P. Hommelhoff, *Attosecond physics phenomena at nanometric tips*, *J. Phys. B: At., Mol. Opt. Phys.* **51**, 172001 (2018).
- [113] E. W. Müller, *Work function of tungsten single crystal planes measured by the field emission microscope*, *J. Appl. Phys.* **26**, 732–737 (1955).
- [114] L. F. Mattheiss, *Fermi surface in tungsten*, *Phys. Rev.* **139**, A1893 (1965).
- [115] P. H. Bucksbaum, R. R. Freeman, M. Bashkansky and T. J. McIlrath, *Role of the ponderomotive potential in above-threshold ionization*, *J. Opt. Soc. Am. B* **4**, 760–764 (1987).
- [116] I. H. Malitson, *Interspecimen Comparison of the Refractive Index of Fused Silica*, *J. Opt. Soc. Am.* **55**, 1205–1209 (1965).
- [117] F. Lindner, G. G. Paulus, H. Walther, A. Baltuška, E. Goulielmakis, M. Lezius and F. Krausz, *Gouy Phase Shift for Few-Cycle Laser Pulses*, *Phys. Rev. Lett.* **92**, 113001 (2004).
- [118] M. F. Kling, J. Rauschenberger, A. J. Verhoef, E. Hasović, T. Uphues, D. B. Milošević, H. G. Muller and M. J. J. Vrakking, *Imaging of carrier-envelope phase effects in above-threshold ionization with intense few-cycle laser fields*, *New J. Phys.* **10**, 025024 (2008).
- [119] M. Kling, C. Siedschlag, I. Znakovskaya, A. Verhoef, S. Zherebtsov, F. Krausz, M. Lezius and M. Vrakking, *Strong-field control of electron localisation during molecular dissociation*, *Mol. Phys.* **106**, 455–465 (2008).
- [120] I. Znakovskaya, P. von den Hoff, S. Zherebtsov, A. Wirth, O. Herrwerth, M. J. J. Vrakking, R. de Vivie-Riedle and M. F. Kling, *Attosecond Control of Electron Dynamics in Carbon Monoxide*, *Phys. Rev. Lett.* **103**, 103002 (2009).
- [121] I. Znakovskaya, P. von den Hoff, G. Marcus, S. Zherebtsov, B. Bergues, X. Gu, Y. Deng, M. J. J. Vrakking, R. Kienberger, F. Krausz, R. de Vivie-Riedle and M. F. Kling, *Subcycle Controlled Charge-Directed Reactivity with Few-Cycle Midinfrared Pulses*, *Phys. Rev. Lett.* **108**, 063002 (2012).

Bibliography

- [122] M. Kübel, K. J. Betsch, N. G. Johnson, U. Kleineberg, R. Moshhammer, J. Ullrich, G. G. Paulus, M. F. Kling and B. Bergues, *Carrier-envelope-phase tagging in measurements with long acquisition times*, *New J. Phys.* **14**, 093027 (2012).
- [123] B. Wang, X. Li and P. Fu, *The effects of a static electric field on high-order harmonic generation*, *J. Phys. B: At., Mol. Opt. Phys.* **31**, 1961 (1998).
- [124] J. Köhn, *Wechselwirkung von intensiven Laserfeldern mit Metallclustern - Energieabsorption durch Streuprozesse*, PhD thesis, University of Rostock (2009).
- [125] J. Passig, S. Zhrebetsov, R. Irsig, M. Arbeiter, C. Peltz, S. Göde, S. Skruszewicz, K.-H. Meiwes-Broer, J. Tiggesbäumker, M. F. Kling and T. Fennel, *Nanoplasmonic electron acceleration by attosecond-controlled forward rescattering in silver clusters*, *Nat. Commun.* **8**, 1181 (2017).
- [126] T. DiStefano and D. Eastman, *The band edge of amorphous SiO₂ by photoinjection and photoconductivity measurements*, *Solid State Commun.* **9**, 2259 - 2261 (1971).
- [127] R. K. Swank, *Surface Properties of II-VI Compounds*, *Phys. Rev.* **153**, 844–849 (1967).
- [128] M. Debenham, *Refractive indices of zinc sulfide in the 0.405–13- μ m wavelength range*, *Appl. Opt.* **23**, 2238–2239 (1984).
- [129] M. Fonin, R. Pentcheva, Y. S. Dedkov, M. Sperlich, D. V. Vyalikh, M. Scheffler, U. Rüdiger and G. Güntherodt, *Surface electronic structure of the Fe₃O₄ (100): Evidence of a half-metal to metal transition*, *Phys. Rev. B* **72**, 104436 (2005).
- [130] M. R. Query, *Optical constants*, Contractor Report AD-A158-623, U.S. Army Chem. Res. and Dev. Eng. Cent., Aberdeen Proving Ground, Md. (1985).
- [131] C. B. Duke, W. R. Salaneck, T. J. Fabish, J. J. Ritsko, H. R. Thomas and A. Paton, *Electronic structure of pendant-group polymers: Molecular-ion states and dielectric properties of poly(2-vinyl pyridine)*, *Phys. Rev. B* **18**, 5717–5739 (1978).
- [132] M. Fujihira, T. Hirooka and H. Inokuchi, *Photoemission from compounds containing benzene, naphthalene and anthracene ring systems*, *Chem. Phys. Lett.* **19**, 584–587 (1973).
- [133] N. Sultanova, S. Kasarova and I. Nikolov, *Dispersion properties of optical polymers*, *Acta Phys. Pol. A* **116**, 585 (2009).
- [134] H. J. W. Strutt, *On the scattering of light by small particles*, *Lond. Edinb. Dubl. Phil. Mag.* **41**, 447–454 (1871).
- [135] G. G. Paulus, F. Lindner, H. Walther, A. Baltuška and F. Krausz, *Measurement of the phase of few-cycle laser pulses*, *J. Mod. Opt.* **52**, 221–232 (2005).
- [136] T. Wittmann, B. Horvath, W. Helml, M. G. Schätzel, X. Gu, A. L. Cavalieri, G. G. Paulus and R. Kienberger, *Single-shot carrier-envelope phase measurement of few-cycle laser pulses*, *Nat. Phys.* **5**, 357 (2009).

-
- [137] A. T. J. B. Eppink and D. H. Parker, *Velocity map imaging of ions and electrons using electrostatic lenses: Application in photoelectron and photofragment ion imaging of molecular oxygen*, *Rev. Sci. Instrum.* **68**, 3477–3484 (1997).
- [138] F. Süßmann, S. Zhrebtsov, J. Plenge, N. G. Johnson, M. Kübel, A. M. Sayler, V. Mondes, C. Graf, E. Rühl, G. G. Paulus, D. Schmischke, P. Swrschek and M. F. Kling, *Single-shot velocity-map imaging of attosecond light-field control at kilohertz rate*, *Rev. Sci. Instrum.* **82**, 093109 (2011).
- [139] C. Bostedt, H. Thomas, M. Hoener, E. Eremina, T. Fennel, K.-H. Meiwes-Broer, H. Wabnitz, M. Kuhlmann, E. Plönjes, K. Tiedtke, R. Treusch, J. Feldhaus, A. R. B. de Castro and T. Möller, *Multistep Ionization of Argon Clusters in Intense Femtosecond Extreme Ultraviolet Pulses*, *Phys. Rev. Lett.* **100**, 133401 (2008).
- [140] M. Arbeiter and T. Fennel, *Ionization heating in rare-gas clusters under intense XUV laser pulses*, *Phys. Rev. A* **82**, 013201 (2010).
- [141] B. Schütte, F. Campi, M. Arbeiter, T. Fennel, M. J. J. Vrakking and A. Rouzée, *Tracing Electron-Ion Recombination in Nanoplasmas Produced by Extreme-Ultraviolet Irradiation of Rare-Gas Clusters*, *Phys. Rev. Lett.* **112**, 253401 (2014).
- [142] K. R. Wilson, S. Zou, J. Shu, E. Rühl, S. R. Leone, G. C. Schatz and M. Ahmed, *Size-Dependent Angular Distributions of Low-Energy Photoelectrons Emitted from NaCl Nanoparticles*, *Nano Lett.* **7**, 2014–2019 (2007).
- [143] R. Signorell, M. Goldmann, B. L. Yoder, A. Bodi, E. Chasovskikh, L. Lang and D. Luckhaus, *Nanofocusing, shadowing, and electron mean free path in the photoemission from aerosol droplets*, *Chem. Phys. Lett.* **658**, 1–6 (2016).
- [144] J. Dahlström, D. Guénot, K. Klünder, M. Gisselbrecht, J. Mauritsson, A. L’Huillier, A. Maquet and R. Taïeb, *Theory of attosecond delays in laser-assisted photoionization*, *Chem. Phys.* **414**, 53–64 (2013).
- [145] A. Akkerman, T. Boutboul, A. Breskin, R. Chechik, A. Gibrekhterman and Y. Lifshitz, *Inelastic Electron Interactions in the Energy Range 50 eV to 10 keV in Insulators: Alkali Halides and Metal Oxides*, *Phys. Status Solidi B* **198**, 769–784 (1996).
- [146] S. H. Pandya, B. G. Vaishnav and K. N. Joshipura, *Electron inelastic mean free paths in solids: A theoretical approach*, *Chin. Phys. B* **21**, 093402 (2012).

Academic curriculum vitae

Not included in the online version.

Statement of authorship

Erklärung

gemäß §4 der Promotionsordnung
der Mathematisch-Naturwissenschaftlichen Fakultät
der Universität Rostock

Ich gebe folgende Erklärung ab:

1. Die Gelegenheit zum vorliegenden Promotionsvorhaben ist mir nicht kommerziell vermittelt worden. Insbesondere habe ich keine Organisation eingeschaltet, die gegen Entgelt Betreuerinnen/Betreuer für die Anfertigung von Dissertationen sucht oder die mir obliegenden Pflichten hinsichtlich der Prüfungsleistungen für mich ganz oder teilweise erledigt.
2. Ich versichere hiermit an Eides statt, dass ich die vorliegende Arbeit selbstständig angefertigt und ohne fremde Hilfe verfasst habe. Dazu habe ich keine außer den von mir angegebenen Hilfsmitteln und Quellen verwendet und die den benutzten Werken inhaltlich und wörtlich entnommenen Stellen habe ich als solche kenntlich gemacht.

Rostock, den 24.08.2018

Lennart Seiffert

Acknowledgments

An dieser Stelle möchte ich mich herzlich bei allen bedanken, die mich auf dem Weg zu dieser Arbeit begleitet und unterstützt haben. An erster Stelle gilt mein Dank natürlich Thomas, der mir die Möglichkeit geboten hat nach der Masterarbeit auch die Promotion in seiner Gruppe anzufertigen. Danke für die große Hilfe bei allen Problemen in den vergangenen Jahren und auch für die unzähligen anregenden fachlichen und nicht-fachlichen Diskussionen. Danke auch für die Durchsicht dieser Arbeit.

Weiterhin möchte ich mich bei allen aktuellen und früheren Mitgliedern unserer Arbeitsgruppe für die entspannte und vor allem freundschaftliche Arbeitsatmosphäre bedanken. Danke Christian, Mathias, Kathi, Björn, Benjamin und Phillip für das spannende Fachsimpeln und die vielen lustigen Stunden während der Arbeit und bei privaten Aktivitäten. Danke Björn und Benjamin für die kurzfristige und dennoch akribische Fehlersuche in dieser Arbeit.

Natürlich danke ich auch den vielen Wissenschaftlern und Wissenschaftlerinnen, die mit ihrer Zusammenarbeit maßgeblich zur erfolgreichen Fertigstellung dieser Arbeit beigetragen haben. Für die langjährige und fruchtbare Zusammenarbeit und die vielen fachlichen Diskussionen danke ich besonders Matthias Kling und seiner Gruppe. Insbesondere Frederik, Max, Philipp und Sergey haben wesentlich zum Veröffentlichen der Ergebnisse dieser Arbeit beigetragen. Für die Zusammenarbeit am Attostreaking Projekt danke ich Francesca Calegari und ihrer Crew. Weiterhin danke ich Peter Hommelhoff und Timo Paschen für die tolle Zusammenarbeit bei der Spitzenforschung. Ich danke auch allen anderen, mit denen ich in den letzten Jahren wissenschaftlich zusammenarbeiten durfte. Danke Artem, Jeff, Hans-Jakob, Inga, Elefterios und Manish.

Danke an Franzi, Alex, Steffen, Matthias, Robin, Sergej und alle anderen, mit denen ich in den letzten Jahren zusammen die Lehre in Übungen und Praktika bestreiten durfte. Danke an die Haages für die kühlen Biere und das gemütliche Zusammensitzen nach (!) der Arbeit.

Zu guter Letzt danke ich natürlich meiner Freundin Josepha und meiner Familie, insbesondere meiner Mutter, für die seelische und moralische Unterstützung in den letzten Jahren und besonders während der finalen Phase der Promotion.